





Universitat Autònoma de Barcelona

ADVERTIMENT. L'accés als continguts d'aquesta tesi queda condicionat a l'acceptació de les condicions d'ús establertes per la següent llicència Creative Commons:  http://cat.creativecommons.org/?page_id=184

ADVERTENCIA. El acceso a los contenidos de esta tesis queda condicionado a la aceptación de las condiciones de uso establecidas por la siguiente licencia Creative Commons:  <http://es.creativecommons.org/blog/licencias/>

WARNING. The access to the contents of this doctoral thesis it is limited to the acceptance of the use conditions set by the following Creative Commons license:  <https://creativecommons.org/licenses/?lang=en>

Towards the therapeutic use of nanoparticles in cancer: a cellular perspective.

October 2021

Antonio Aranda Ramos

**Unitat de Biologia Cel·lular
Departament de Biologia Cel·lular, Fisiologia i Immunologia.**

**Tesi doctoral
Programa de Doctorat en Biologia Cel·lular**



Universitat Autònoma de Barcelona

Departament de Biologia Cel·lular, Fisiologia i Immunologia



Towards the therapeutic use of nanoparticles in cancer: a cellular perspective.

Cap a l'ús terapèutic de nanopartícules contra el càncer: una perspectiva cel·lular.

Hacia el uso terapéutico de nanopartículas contra el cáncer: una perspectiva celular.

Antonio Aranda Ramos

**Unitat de Biologia Cel·lular
Departament de Biologia Cel·lular, Fisiologia i Immunologia.**

Directora: Dra. Carme Nogués Sanmiquel

Tutora: Dra. Carme Nogués Sanmiquel

**Unitat de Biologia Cel·lular
Departament de Biologia Cel·lular, Fisiologia i Immunologia.**

Tesi presentada per optar al grau de Doctor per la Universitat Autònoma de Barcelona.

Report submitted to qualify for the Doctor of Philosophy Degree in Cell Biology at the
Universitat Autònoma de Barcelona

Bellaterra, 28 d'Octubre 2021



Universitat Autònoma de Barcelona
Departament de Biologia Cel·lular, de Fisiologia i
d'Immunologia
Unitat de Biologia Cel·lular

La Dra. **Carme Nogués Sanmiquel**, professora catedràtica del Departament de Biologia Cel·lular, de Fisiologia i d'Immunologia de la Universitat Autònoma de Barcelona,

CERTIFICA:

Que **Antonio Aranda Ramos** ha realitzat sota la seva direcció el treball d'investigació que s'exposa en la memòria titulada "Towards the therapeutic use of nanoparticles in cancer: a cellular perspective" per optar al grau de Doctor per la Universitat Autònoma de Barcelona.

Que aquest treball s'ha dut a terme a la Unitat de Biologia Cel·lular del Departament de Biologia Cel·lular, de Fisiologia i d'Immunologia de la Universitat Autònoma de Barcelona.

I per tal que així consti, firma el present certificat.

Bellaterra, 28 d'Octubre de 2021,

Maria del Carme
Nogués
Sanmiquel - DNI
33863533N
(TCAT)

Firmado digitalmente
por Maria del Carme
Nogués Sanmiquel -
DNI 33863533N (TCAT)
Fecha: 2021.10.28
15:47:17 +02'00'

Dra. Carme Nogués Sanmiquel

This Thesis has been performed with the support of the projects:

2014 SGR 524 SGR Project, Unitat de Biologia Cel·lular. Departament d'Universitats, Recerca i Societat de la Informació.

MINAHE 4, MicroNanotools for Life Sciences, Plan Nacional de Investigación, Desarrollo e Innovación científica (Ministerio de Ciencia e Innovación)

MAT2014-57960-C03-3-R, Biocompatibilidad y efectividad de aleaciones porosas para aplicaciones biomédicas. Ministerio de Economía y Competitividad.

MAT2017-86357-C3-3-R, Materiales porosos accionados electricamente para tecnologías sostenibles de ingeniería tisular. Ministerio de Economía y Competitividad.

MAGPLADRUG, Magnetoplasmonic control (actuation and monitoring) of drug release using Fe/Au Semi-shells on biodegradable nanoparticles. Fundación Ramón Areces.

Abstract

For the past three decades, nanotechnology has been an ever-growing field, including its application to medicine, what is known as nanomedicine. Despite the promising potential applications of nanomedicine, translation to effective therapeutic and diagnostic alternatives is still very low. This is in part, due to a lack of knowledge of the mechanisms in which nanomaterials interact with the organisms, beginning with their biointeraction at the cellular level. This information is often over-looked when characterising new engineered nanomaterials and can contribute to their efficient and safe development. In this scenario, the goal of this thesis is to provide an in-depth clear perspective from a cellular point of view of these nanomaterial bio-interactions and how they might affect their expected therapeutic outcome. We also point out the importance of using compatible methods to study the cytotoxicity of new nanomaterials to avoid potential assay interferences and to evaluate the uptake and intracellular fate of nanomaterials quantitatively. Works presented in this thesis highlight the importance of in vitro characterisation of the biointeraction of nanomaterials using different cell lines. First, we proved the biocompatibility and antioxidant properties of cerium oxide nanoparticles, achieving antioxidant results close to those obtained with commercially available antioxidant products. Second, we demonstrated the biocompatibility of silica nanoparticles and provided new insights into their biointeraction using confocal laser scanning and scanning electron microscopy techniques and a novel quantifiable analysis of the obtained internalisation data. It also led new quantitative information on how time-dependent internalisation can critically affect the uptake and intracellular fate of nanomaterials. Lastly, we analysed the biointeraction, cytotoxicity, magnetic targeting capabilities and hyperthermia-triggered therapeutic use of iron and gold magnetoplasmonic polystyrene nanodomains to selectively treat tumoral cell lines (SKBR-3) and leave non-tumoral cell lines (MCF10a) unaffected. The efficiency to magnetically manipulate this kind of nanoparticles and the increase of the uptake efficiency in cells is proved in static and flow conditions. We also highlight the differential cell death mechanisms induced by hyperthermia after near-infrared laser irradiation between tumoral and non-tumoral cell lines. In conclusion, the present thesis provides new knowledge towards the development of better nanomaterials and new generation diagnostic and therapeutic agents for the selective destruction of malignant cells.

Resum

Durant les últimes 3 dècades, la nanotecnologia s'ha convertit en un camp en constant creixement, incloent la seva aplicació a la medicina, la qual coneixem com a nanomedicina. Tot i les prometedores aplicacions potencials de la nanomedicina, la seva traducció a alternatives terapèutiques i diagnòstiques efectives és encara molt baixa. Això és degut, en part, a la falta de coneixement dels mecanismes amb els que els nanomaterials interaccionen amb els organismes, així com la seva biointeracció a nivell cel·lular. Aquesta informació és freqüentment ignorada quan es caracteritzen nous dissenys de nanomaterials i pot contribuir substancialment al seu desenvolupament eficient i segur. En aquest escenari, l'objectiu d'aquesta tesi és proporcionar un anàlisi en profunditat des d'una perspectiva cel·lular de les nano-biointeraccions dels nanomaterials i com aquestes poden afectar al potencial terapèutic dels mateixos. També posem en relleu la importància de caracteritzar amb mètodes compatibles la citotoxicitat de nanomaterials per evitar potencials interferències amb els mètodes emprats i de la quantificació de la internalització i destí intracel·lular de nous nanomaterials. Els estudis presentats en aquesta tesi també destaquen la rellevància de la caracterització in vitro de les biointeraccions dels nanomaterials fent servir diferents línies cel·lulars. Primer, hem comprovat la biocompatibilitat i propietats antioxidants de les nanopartícules d'òxid de ceri, aconseguint resultats propers als efectes d'antioxidants disponibles a nivell comercial. En segon lloc, hem demostrat la biocompatibilitat de les nanopartícules d'òxid de silici i aportat nova informació rellevant de la seva biointeracció amb cultius cel·lulars fent servir microscòpia làser d'escaneig confocal i microscòpia electrònica d'escaneig, així com un anàlisi quantificable de les dades d'internalització obtingudes. Aquest estudi aporta nova informació quantitativa sobre com els temps d'incubació poden afectar dràsticament a l'eficiència d'internalització i el destí intracel·lular dels nanomaterials. Finalment, hem analitzat la biointeracció, la citotoxicitat, les possibilitats de direcció a través de manipulació magnètica i l'ús pel tractament per hipertèrmia de nanopartícules magnetoplasmòniques d'or i ferro sobre poliestirè de forma selectiva en una línia cel·lular tumoral (SKBR-3) i una línia cel·lular no tumoral (MCF10a). Hem comprovat l'eficiència de manipulació magnètica de les nanopartícules magnetoplasmòniques i com afecten incrementant l'eficiència d'internalització per part de les cèl·lules en condicions de cultiu estàtiques i dinàmiques. També destaquem els mecanismes diferencials de mort cel·lular entre línies tumorals i no tumorals induïts pel tractament per hipertèrmia mitjançant l'estimulació de les nanopartícules magnetoplasmòniques amb un làser amb longitud d'ona propera al infraroig. En conclusió, la present tesi aporta nous coneixements que ajudaran al desenvolupament de nous nanomaterials i el desenvolupament de nous agents basats en nanomaterials pel diagnòstic i teràpia contra cèl·lules tumorals.

Abbreviation list

ACS	American Chemistry Society
AM	Acetoxymethyl
AMD	Advanced Micro Devices
AMF	Alternating Magnetic Field
AND	AND Operator in Fiji
AOBS	Acousto-Optical Beam Splitter
ATCC	American Type Culture Collection
BD	Beckton-Dickinson
BIST	Barcelona Institute of Science and Technology
BRCA	Breast Cancer Gene
BSA	Bovine Serum Albumin
CAF	Carcinoma-associated fibroblasts
CH	Channel
CLIJ	Fiji plugin for GPU-accelerated image processing
CLSM	Confocal Laser Scanning Microscopy/Microscope(s)
CNT	Carbon Nanotube(s)
COLOC	Co-localised signal or channel
COVID	Coronavirus disease (COVID-19)
CPU	Central Processing Unit
CROPS	Cropped images
CSIC	Consejo Superior de Investigaciones Científicas
CTR	Control(s)/sample(s)/group(s)
CYTO	Cytoskeleton signal channel
DEAD	Dead cell(s)
DECON	Deconvolution process in macros
DECONV	Deconvolution signal(s)/channel(s)
DLS	Dynamic Light Scattering
DMEM	Dulbecco's Modified Eagle Medium
DMSO	Dimethyl sulfoxide
DNA	Deoxyribonucleic acid
ECM	Extracellular matrix
EDTA	Ethylenediaminetetraacetic acid
EEA1/EEA-1	Early Endosome antigen-1
ELISA	Enzyme-linked immunosorbent assay
ENM	Engineered nanomaterial
ENMs	Engineered nanomaterial(s)
EPR	Enhanced permeability and retention
EU	European Union

FBS	Foetal Bovine Serum
FDA	Food and Drug Administration of the United States
FFT	Fast Fourier Transform
FIB-SEM	Focused ion beam-Scanning microscopy/microscope
FITC	Fluorescein isothiocyanate
FSC	Forward Scattering
GPU	Graphical processing unit
H2DCF-DA	Dichlorofluorescein diacetate
HBSS	Hank's Balanced Salt Solution
HER-2	Receptor tyrosine-protein kinase erbB-2
HIF-1a	Hypoxia inducible factor 1-alpha
HMDS	Hexamethyldisilazane
HPLC	High-performance liquid chromatography
HRTEM	High-resolution transmission electron microscopy
ICMAB-CSIC	Institut de Ciència de Materials de Barcelona
ICN2	Institut Català de Nanociències i Nanotecnologia
ICP-AES	Inductively coupled plasma atomic emission spectroscopy
IL	Interleukin
INSIDE	Channel or signal inside the cells in macro
ISO	International Organization for Standardization
LAMP-1	Lysosomal-associated membrane protein 1
LDH	Lactate dehydrogenase
LIVE	Live cell
LUT	Look-up table
MASK	Mask in image processing macro
MAX	Maximum
MEM	Minimum Essential Media
MCF10a	MCF10a non-tumoral human breast cell line
MNP	Magnetic nanoparticle
MPND	Magnetoplasmonic nanoparticle
MPNDs	Magnetoplasmonic nanoparticle(s)
MRI	Magnetic resonance imaging
MSNs	Mesoporous Silica Nanoparticle
MTS	(3-(4,5-dimethylthiazol-2-yl)-5-(3-carboxymethoxyphenyl)-2-(4-sulfophenyl)-2H-tetrazolium)
MTT	(3-(4,5-dimethylthiazol-2-yl)-2,5-diphenyltetrazolium bromide

NAC	N-acetylcysteine
NIR	Near-infrared
NMR	Nuclear magnetic resonance
NP	Nanoparticle
NPs	Nanoparticles
NT	Nanotube
OD	Optical density
PBS	Phosphate Buffer Saline
PDT	Photo-dynamic therapy
PEG	Polyethylene glycol
PEI	Polyethylenimine
PFA	Paraformaldehyde
PI	Propidium iodide
PM	Plasma membrane
PROJ	Projection
PSF	Point Spread Function
QD	Quantum dot
RES	Reticulo endothelial system
RL	Richardson-Lucy deconvolution algorithm
RNA	Ribonucleic acid
ROI	Region of interest
ROS	Reactive oxygen species
CellROX	CellROX® Green Reagent
RT	Room temperature
SEM	Scanning electron microscopy/microscope
SiNP	Silica Nanoparticle
SiNPs	Silica Nanoparticles
SKBR-3	SKBR-3 Human breast cancer cell line
SPION	Superparamagnetic iron oxide nanoparticles
SRB	Sulforodamine B assay
SSC	Side scattering
STED	Stimulated emission depletion (STED) microscopy
TB	Trypan blue
TBHP	Tert-Butyl hydroperoxide
TDDS	Targeted drug delivery system
TEM	Transmission electron microscopy
TEOS	Tetraethyl orthosilicate
TGA	Thermogravimetric analysis

TM	Trademark
TMOS	Tetramethyl orthosilicate
TNF-α	Tumour necrosis factor alpha
UAB	Universitat Autònoma de Barcelona
UV	Ultraviolet
WHO	World Health Organization
WSTS	Water soluble tetrazolium salts
XPS	and X-ray photoelectron spectroscopy
XRD	X-ray diffraction
XRPD	X-ray powder diffraction
XTT	(2,3-bis-(2-methoxy-4-nitro-5-sulfophenyl)-2H-tetrazolium-5-carboxanilide)
XYZ	XYZ planes in confocal datasets

Table of contents

1 Introduction	1
1.1 Engineered nanomaterials in medicine	3
1.2 The engineered nanomaterials zoo	7
1.3 Engineered nanomaterials applications	12
1.3.1. Drug delivery	12
1.3.2. Hyperthermia	13
1.4 Engineered nanomaterials and biological interaction	16
1.4.1. Biodistribution and immunological response	17
1.4.2. Tumour microenvironment	18
1.4.3. Extracellular matrix	19
1.4.4. Plasma Membrane	21
1.4.5. Endolysosomal system	24
1.5 Future perspectives on engineered nanomaterials	26
2. Objectives	29
3. Results	31
3.1 Chapter 1: Simple synthesis of biocompatible stable CeO₂ nanoparticles as antioxidant agents	33
3.2 Chapter 2: Seeing is believing: robust characterisation of nanomaterial-cell interactions	61
3.3 Chapter 3: Biointeraction and hyperthermia effects of magnetoplasmonic nanodomains on cancer cells.	113
4 General discussion	147
5 Conclusions	159
6 References	161

1 Introduction

Cancer is not a single disease, but a group of malignancies characterised by the uncontrolled growth and propagation of abnormal cells through the body. It remains one of the world's worst diseases and a great challenge for those working in the health sciences community. It strikes our population at an alarming growing pace, increasing an 36,9 % its incidence from 14.1 million in 2012 (Ferlay et al., 2015) to 19.3 million in 2020 (Sung et al., 2021). This trend was projected in 2020 to continue growing, with the number of new cases expected to rise a further 47%, enlarging the number of cancer cases to 28,4 million over the next two decades worldwide (Sung et al., 2021). According to estimates from the World Health Organization (WHO) in 2019, cancer was the first or second leading cause of death before the age of 70 years in 112 of 183 countries and ranks third or fourth in a further 23 countries (Sung et al., 2021) representing a 16,7% of the total deaths worldwide in 2019.

Although the incidence and mortality of certain kind of cancers is being lowered by the development of pre-clinical diagnostic methods and good habits in highly developed countries, it is observed that this trend might not be equal in low- and in-development countries where preventive measures fail to extend in the population (Sung et al., 2021). In low- and in-development countries, incidence of particular tumours may be relatively low, but corresponding mortality data often reflect late-stage diagnosis as the norm and consequently poor clinical outcomes.

Aggregated data from 2020 shows that the prevalence of colorectal cancer is the 3rd highest among the population, regardless of gender with over 1.9 million cases representing a 10% of total cancer cases. It ranks 2nd in terms of mortality (Sung et al., 2021). It is the 3rd (10,6%) most prevalent kind of cancer in men, only under lung (14.3%) and prostate cancer (14,1%). Meanwhile, in women, the prevalence rank is led by breast cancer (24,5%), followed by colorectal cancer (9,4%), lung (8,4%) and being the cervical-uteri cancer the 4th in place (6,5%) (Sung et al., 2021). The diagnosis and prognosis of all of these types of cancer is heavily affected by pre-clinical policies and screenings. New, highly specific and cheaper strategies that enhance the early detection of cancer are of fundamental need, especially in low-resource countries where investment in pre-clinical policies is scarce and treatable cancers are often overlooked with fatal consequences.

Traditional therapies against cancer include surgery, radiation and the use of chemotherapeutic drugs which are usually associated with undesired side-effects to surrounding and/or distant normal tissues. This is the reason why the development of alternative therapeutic strategies that overcome these drawbacks is of fundamental need.

In 2004, the National Cancer Institute committed \$144 million toward the development of novel nanotechnologies for improving cancer mortality focusing on six areas that included (1) detection of molecular changes responsible for disease pathogenesis; (2) disease diagnosis and imaging; (3) drug delivery and therapy; (4) multifunctional systems for combined therapeutic and diagnostic applications; (5) vehicles to report the in vivo efficacy of a therapeutic agent; and (6) nanoscale enabling technologies, which will accelerate scientific discovery and basic research (RF, 2005).

One of the desired goals of the application of nanotechnology into medicine is the early detection of pathological changes in the organism at a molecular level thanks to individually engineered nanotheranostic tools that offer an unambiguous method to diagnose, monitor and treat the disease in a single non-invasive procedure.

1.1 Engineered nanomaterials in medicine

Nanomaterials are defined by their inner and/or outer dimensions, being either of them of up to 100 nm. Nanoparticles (NPs) are commonly defined by its outer dimensions only, and therefore should not exceed the range of 1-100 nm in diameter. Despite this classic cut-off of the upper limit in size, depending on the NPs' material the so-called quantum effect of their size starts at a higher size. Therefore, depending on the application of the engineered nanomaterials (ENMs), sizes that slightly surpass the upper size limit can also be considered and described as NPs. Examples on the non-triviality of the size and shape of these materials are gold NPs, which heavily change their properties around 100 nm in size (their excitation and emission changes at this critical size) (Eustis & El-Sayed, 2006) or titanium NPs which change their properties from inert to explosive at 300-500 nm in size (Boilard et al., 2013). Therefore, toxicologists and pharmacologists commonly refer to particles below 250 nm in size as NPs and federal institutions like the Food and Drug Administration (FDA) of the United States of America classify as NPs those particles that are up to 1000 nm in size if the particle exhibits distinct physical, chemical or biological properties to that of the bulk material (Administration, 2014). Currently, there are more than 1800 consumer products according to the Project on Emerging Nanotechnologies inventory that are made of or contain NPs since 2005, with a wide range of applications and industries such as energy, automotive, electronics and computing, food and beverages, health and construction materials (Vance et al., 2015). With such a product penetration level on products already on the market and their promising application to medicine, ENMs characterisation and analysis of their biointeraction with biological systems is of fundamental need, to assess not only the risks of their application, but also the plethora of benefits they could represent to our society.

Due to the ability to manipulate these ENMs it is possible to choose what properties they should have depending on their use in nanomedicine. For example, depending on the chosen diagnostic or therapeutic strategy according to the tumour biology and location, multiple active moieties can be added to the ENMs surface. One of the most common surface modification is the ENMs conjugation to targeting molecules such as antibodies against malignant molecules on target (Kirpotin et al., 2006) or ligands to receptors over-expressed in malignant cells (Ishida et al., 2001) to increase the chances and specificity of the ENMs' interaction with targeted cells. Other modifications include stability stealth molecules such as Polyethylene glycol (PEG) (Wang & Thanou, 2010), glucans as dextran (Coty et al., 2017) or dendrimers (which expand the active surface of NPs) (Aurelia Chis et al., 2020) to increase their circulation times by hampering unspecific protein interactions, protein corona formation and ENMs opsonisation. Several strategies focus on the addition of charged molecules, for example polyethylenimine (PEI) (Patiño et al., 2012) (a vector molecule commonly used in DNA transfection strategies), as surface modifications that mask the polarity and charges of the

therapeutic compounds inside the ENMs and allow a programmed internalisation when in contact with the plasma membrane of targeted cells.

These modifications help nanomedicine-oriented ENMs to reach their target site with their full therapeutic potential intact and therefore contribute to unravel the potential benefits of their use (listed in Table 1).

Table 1. Main advantages of nanotechnology in diagnosis, imaging and cancer therapy.

Advantages of nanotechnology in diagnostics and imaging	Advantages of nanotechnology for cancer therapy
Increased sensitivity and specificity which results in optimised patient sample needs.	Increased drug delivery to tumour cells
Early bird detection of cancer biomarkers in patient samples (RNA/DNA, exosomes, proteins...)	Increased tumoral specificity through tumour cell targeting moieties decoration
Ability to monitor treatment response via biomarker detection and/or imaging using theranostic probes.	Potential to decrease off-target systemic drug toxicity and side effects
Increased sensitivity to detect small local and distant metastases or circulating tumour cells.	Potential to deliver virtually any therapeutics to target cells protecting their composition. and activity
Potential to target and non-invasively differentiate between tumoral and surrounding healthy tissue	Provide increase solubility, stability and circulation half-life for existing chemotherapeutic drugs.

Profiting from the array of advantages presented in Table 1, ENMs can be used as nano-diagnostic tools and/or nano-carriers for new and existing chemotherapeutic drugs (to mask their hydrophobicity, protect their active moieties, protect them from metabolisation...), solving some of their present limitations in delivery and enhancing their therapeutic outcome.

Despite the promise ENMs represent in health sciences, their translation from basic research to the clinic has been poor. As of 2020, the number of nanomaterials approved as nanomedicines for human use by the United States' FDA was approximately 250 either on the market or in clinical trial phase (Albalawi et al., 2021). The majority of these approved products are polymeric, liposomal and nanocrystal formulations, despite the current interest in the production of more complex ENMs like micelles, protein-based NPs and metallic and inorganic NPs. Some of the limitations' scientist face in the translation of nanoparticle-based therapies to the clinic are the diversity of geometries, materials, coatings, surface modifications and chemistries that complicate the standardisation of their validation for human use and raise safety concerns.

The versatility of ENMs in terms of chemistry and structure makes them a perfect tool to achieve a multi-modal/multi-plexed tool that combines multiple functions that can be useful along their transit through the system up to their final destination.

The chemistry and chassis of these materials can be critical in their therapeutic action. ENMs can be engineered taking advantage of the elemental properties of their primary components like the reactive oxygen species (ROS)-quenching activity of lanthanides (Podolski-renic et al., 2015) like cerium, which can add antioxidant properties to the ENMs. Or use more common elements like iron and take advantage of its ability to trigger cell death due to an accumulation of iron in cells (a process known as ferroptosis (Yan et al., 2020)). Or explore their magnetic abilities to drive and retain them at the targeted point of action thanks to the magnetic properties of iron in their composition. It is common to not only focus on one chemistry to generate new NPs, but to combine elements in their structure to take advantage of their isolated or combined properties. Therefore, adding metal elements like gold or iron to the NP core/chassis to add plasmonic and magnetic capabilities to them is easily achievable. This would allow to trigger an hyperthermic effect right were nanoparticles accumulate due to the plasmon surface resonance ability of gold when electromagnetically stimulated with specific light wavelengths or magnetic fields exciting the iron in their core.

As explained before, ENMs can be chemically tuned and decorated with a wide variety of moieties from chemical groups like PEG that increase their circulation times, to antibodies or receptor ligands that enhance their internalisation once they reach their target's cell membrane.

Nanomaterials offer a large surface area despite their small volume, this opens the possibility of targeted drug delivery, by adding targeting molecules to their surface to enhance their selectivity and internalisation that promote what's described as active targeting or receptor-ligand kind of interaction between the cell and the drug delivery systems. This improvement helps to reduce the dosage needed for the therapy to be effective as well as its side-effects, as less active substance is spread through the healthy tissues of the organism. However, recent publications have doubted of the efficiency of this method and concluded that only 0.7% of the injected dose reaches the tumour mass (Wilhelm et al., 2016).

With the ever-expanding research of nanotechnology propelled by the new characterisation techniques, the 1980s was a key decade for the ideation and expansion of nanomedicine. The use of nanocompounds in medicine was proposed as a 2nd generation of drug delivery systems that takes the place of oral and transdermal drug release systems. Even though their application in nanomedicine is still fighting over the traditional therapies that have been used for long, they are currently used in diagnostics from at-home pregnancy test to clinical procedures as contrast agents in diagnostic techniques like magnetic resonance imaging or intra-operational contrast agents for tumoral and cardiovascular affectations.

The first nanomedicine approved by the FDA in 1995 was Doxil®, after approximately 15 years of development. It consists on a reformulation of the classic doxorubicin compound into PEGylated

liposomes. The main reason for its approval was the improvement in cardiotoxicity while maintaining an equivalent efficiency in ovarian cancer treatment of Doxorubicin in its free form (Barenholz, 2012).

Abraxane®, another FDA-approved nanomedicine for the treatment of Non-small-cell lung carcinoma and breast cancer, consists on albumin-coated Paclitaxel NPs obtained after the evaporation of its oil/water emulsion. The main reason for its approval was the enhanced biodistribution of the hydrophobic compound Paclitaxel enhancing its therapeutic effect (Gradishar et al., 2005).

Previously-mentioned nanotherapeutic drugs led the way and increased the interest of scientists and the pharmaceutical industry in generating new therapies and new strategies to deliver their available products taking advantage of new delivery strategies and formulations. Some examples are the anti-emetic Emend® (the nanocrystalline form of a previously commercialised anti-emetic drug Aprepitant®), the PEGylated blocker of tumour necrosis factor alpha (TNF- α) Cimzia® used for autoimmune and inflammatory diseases (like Chron's disease, psoriatic arthritis or ankylosing spondylitis), Feraheme® an intravenous drug formulation with neutral pH for treatment of anemia (Farjadian et al., 2019) or the recent use of nanosized liposomes in COVID-19 mRNA vaccines from Pfizer/BioNTec® and Moderna® (Buschmann et al., 2021).

The truth is that even though nanoparticle formulations showed an 100-400% increase of drug accumulation in the tumour area, more than a 95% of the nanoparticles end up at sites other than the tumour.

Once most drugs are administrated, it is common to lose track and perspective on their biodistribution and location. This hinders the scientists' ability to understand their behaviour and crucial information for their enhancement is lost. By combining these drug delivery systems with imaging/detection capabilities a theranostic probe is obtained. The word theranostic is a neologism to describe a system that combines therapeutic and diagnostic abilities. Thanks to their imaging/detection properties, their biodistribution and fate can be tracked inside the organism in vivo. Therefore, a theranostic system can detect, help diagnose or monitor a disease as well as give us information about the progress and efficacy of a therapeutic agent in real-time (Muthu et al., 2014).

1.2 The engineered nanomaterials zoo

Since scientists gained ability to characterise materials at such a nanoscopic and atomic scale, nanomaterials of different sizes, compositions, geometries, electrical charges and multiple surface functionalisations have appeared (Fig 1); contributing to the formation of what Gubala et al. named the 'nanoparticle zoo' (C. J. Moore et al., 2015).

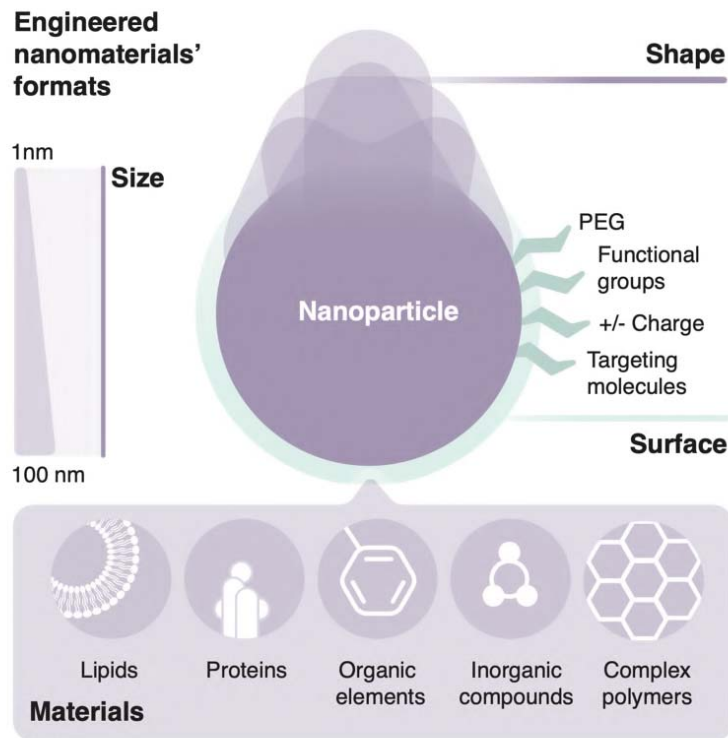


Figure 1. Engineered nanomaterials' formats. Size, shape, material and surface modifications are key points of NP design that can be tuned to allow a better therapeutic outcome or delivery strategy. PEG (Polyethylene glycol).

Here are listed some of the most important ENM (Fig 2) classifications according to their properties:


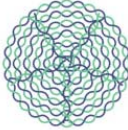








					
Name	Liposome	Polymer NPs	Dendrimer NPs	Polystyrene NPs	Gold NPs
Composition	Lipid bilayer + contents	PLGA, DNA, PCL, PEG hydrogels, monomers	PAMAM, Diphenylacetylene	Polystyrene	Gold spheres, rods, shells, spikes...
Applications	Drug delivery	Drug delivery, release and targeting, imaging	Drug delivery, controlled release	Drug delivery, diagnostics	Hyperthermia, drug delivery, imaging, diagnostics
					
Name	Cerium oxide NPs	Silica NPs	Magnetic NPs	Quantum dots	Carbon NPs or nanotubes
Composition	Cerium oxide	Spheres, mesoporous, microporous,	Iron oxide or cobalt-based	CdSe, CdTe	Graphene, buckyballs, nanotubes,
Applications	Antioxidant, solar cells, supermaterials	Drug delivery, imaging and contrast agents	Drug delivery, controlled release, hyperthermia	Drug delivery, imaging diagnostics	Hyperthermia, drug delivery, water decontamination

Figure 2. Engineered nanomaterials' classification. Some of the most common ENMs include organic and inorganic nanoparticle designs. Multiple compositions, combinations and shapes lead to unique properties of these and their most common applications.

Liposomes.

Liposomes are ENMs of around 100 nm in diameter consisting of a bilayer of phospholipids with hydrophilic heads and hydrophobic tails that are self-assembled (due to their polarity) into membrane structures leaving an aqueous nucleus in the middle. Due to their structural properties, liposomes can host hydrophobic drug molecules on their hydrophobic membranes which also act preventing the leakage of encapsulated hydrophilic drugs and siRNA inside their nucleus (Schroeder et al., 2010). The first FDA-approved nanomedicine Doxil® (Barenholz, 2012) is based on this kind of ENMs, consisting on a liposomal form of doxorubicin used as a chemotherapeutic drug.

Polymer micelles.

Polymer micelles are ENMs in the range of 10-100 nm in size, formed from the self-assembly of amphiphilic block co-polymers in an aqueous environment. Their structure is usually formed by a hydrophilic corona (usually by PEG) and a hydrophobic core that allows the solubilisation of lipophilic drugs (Ghezzi et al., 2021).

Several polymer micelle systems have been studied in clinical phase, one example is Genexol-PM, a polymeric micelle formulation of paclitaxel with block copolymers that include poly-(ethylene glycol) (useful for nonimmunogenic carriers) and biodegradable core-forming poly-(d,l-lactic acid) required for the solubilization of the hydrophobic drug. It was evaluated in a phase I study in patients with advanced malignancies with emphasis on pharmacokinetics evaluation (T.-Y. Kim et al., 2004). It reached a phase II clinical trial for patients with metastatic breast cancer (Lee et al., 2008) and advanced non-small-cell lung cancer (D. W. Kim et al., 2007).

Dendrimers.

Dendrimers consist of nano-sized materials that are approximately 10 nm in size composed of a highly repetitive structural units of terminal groups that branch from a central core. One of the advantages of this kind of ENMs is their controlled depolymerisation that allows a highly tailored release profile of the drug administered (Wong et al., 2012). They can either form the NPs themselves or can be used to functionalise ENMs' surfaces. They have been used for a wide variety of nanomedicine applications: cancer therapy, bioimaging, gene/protein/enzyme delivery or photodynamic therapy (Sherje et al., 2018).

Silica nanoparticles.

This kind of nanoparticles are made of silicon dioxide. Silicon (Si) and oxygen (O), two of the most abundant elements found in nature, normally combine in the form of silicon dioxide (SiO₂) forming covalent bonds. The high abundance of these elements is a major advantage for its industrial exploitation and development of new technologies.

In addition, the low toxicity (*EU Regulation (EC) No. 1272/2008 of the European Parliament and of the Council on Classification, Labelling and Packaging of Substances and Mixtures*, 2008) of silicon dioxide when in amorphous form have been previously described, both in colloidal and nanoparticle form, when in contact to biological models and acute contact tests.

Nano-structured silica.

Silica nanoparticles can be obtained through a base-catalysed sol-gel production process that involves a silane precursor, such as alkoxydes tetraethyl orthosilicate (TEOS) or tetramethyl orthosilicate (TMOS), which undergoes hydrolysis and condensation reactions in the presence of a catalyst, such as acetic acid or hydrochloric acid. Depending on the proportions, order and agitation conditions the molecules will structure in a different conformation and result in different NP conformations and sizes (Lim et al., 2016).

Mesoporous silica nanoparticles.

This kind of silica nanoparticles contain a porous (2–50 nm pores) honeycomb-like structure tunable in size. They keep the biocompatibility due to their silica composition and offer a large surface

area due to the pores that allows the attachment of the functional groups on the NPs. They are commonly used as a drug delivery nanomaterial, due to their high load capacity. There are mainly three types of mesoporous silica nanoparticles (MSNs) i.e., ordered, hollow or rattle type and core/shell MSNs (Alothman, 2012). This kind of nanoparticles have been proved to be a potential theranostic tool for future drug delivery compositions and to be successful in cancer-imaging, targeting, specificity and photodynamic therapy (Benachour et al., 2012; Cheng et al., 2010). The application of gadolinium-loaded silica NPs and a chlorin photosensitiser to facilitate dual-functional MRI and PDT by Benachour et al. is a clear example of the integral solution that this kind of nanoparticles offer for theranostic applications (Benachour et al., 2012).

Microporous silica nanoparticles.

In this case the pores created by nano-structured silica are less than 2 nm in size so they can encapsulate small cargoes like small hydrophobic drugs, photosensitising components and or fluorescent dyes (C. Moore, 2016). Their pore-size and high capacity profile makes a perfect candidate for their application to bioimaging and diagnostics (Gubala et al., 2020) and to prospective cancer therapies by drug loading or photodynamic treatment.

Latex/polystyrene nanoparticles.

These kinds of nanoparticles are commonly available in the market in various sizes, forms and surface chemistries. Their core is made of latex/polystyrene that has been proved to be biocompatible and non-toxic for a long time (Hesler et al., 2019). They have been studied as a way to characterise bio-nano interactions in the past and have demonstrated their versatility in assessing the possible toxicity changes due to surface modifications (Loos et al., 2014).

Cerium oxide nanoparticles.

CeO₂ NPs can be produced with high control in morphology and size through different synthetic methods. This kind of NPs take advantage of the high redox ability and safety of cerium in nanocrystalline form to enable its application as pharmacological and antioxidant agent for human cells in preventing the oxidative process associated with age-related degenerative diseases including arthritis, cardiovascular disease, inflammation, Alzheimer's disease, Parkinson's disease, diabetes, or cancer (Kumar et al., 2014). Ceria NPs have been proposed not only as an antioxidant agent that enables cancer therapy radioprotection in the healthy tissues but also as a radiosensitiser and potential anticancer treatment thanks to their pro-apoptotic behaviour in cancerous cells (Gao et al., 2014).

Magnetic nanoparticles.

Magnetic NPs are usually made with the iron oxides magnetite (Fe_3O_4) or maghemite ($\gamma\text{-Fe}_2\text{O}_3$) and can be used to target chemotherapeutic drugs to tumours. They can be injected in the organism and retained at a specific site using an external magnetic field (Häfeli, 2004). Magnetic NPs can also be used for cancer hyperthermia (Jordan et al., 1999), photodynamic therapy or as contrast agents for magnetic resonance imaging. In addition, super-paramagnetic iron NPs present low cytotoxicity and their surface can be functionalised with several molecules for targeting and/or drug delivery (Gupta et al., 2007).

Gold NPs.

These kinds of particles are made of gold, a metal that has been proved to be innocuous due to its lack of reactivity to common biological and chemical compounds. It is easily tunable in terms of size and shape (spheres, nanoshells, nanorods or nanocages) and can carry different molecules simultaneously, like therapeutic drugs and targeting agents. Due to their optical and conductive properties, gold NPs and their surface plasmon resonance activity can be used for cell imaging, detection and photothermal ablation triggering hyperthermia or drug activation, making them a good candidate for cancer theranostics (Pissuwan et al., 2006) despite the price of its primary source.

Quantum dots.

QDs are spherical NPs smaller than 100 nm in diameter consisting of a crystalline semiconductor core coated by a shell with optical properties and covered by a cap to enable water solubility. They can be functionalised to target specific cells and are really resistant to photobleaching in contrast to common fluorophores and dyes, so they are excellent for imaging and diagnostic purposes as explored by Montón et al. in 2009 (Montón et al., 2009).

Carbon Nanotubes.

These are cylindrical structures made of a rolled graphene sheet (single walled) or sheets (multi-walled), having 1 nm in diameter and between 1 and 100 nm in length. Graphene is a hexagonal network of carbon atoms that has a high mechanical strength, thermal resistance and conductivity (electric and thermal). Carbon nanotubes (CNTs) are easily functionalised thanks to their available large surface. When structured in a multiwalled conformation, CNTs their high optical absorbance in the near-infrared makes them a potential tool for hyperthermia induced treatments (Sobhani et al., 2017).

1.3 Engineered nanomaterials applications

Despite the plethora of applications that ENMs offer, the focus of this thesis will be to investigate the biointeraction between tumoral and normal cell lines and NPs with antioxidant, drug delivery or hyperthermia-inducing capabilities.

1.3.1. Drug delivery

One of the most important applications of ENMs is drug delivery. Drug delivery systems are therapeutic strategies that use formulations, technologies and transportation systems to safely achieve a therapeutic effect such as a targeted tissue or a pharmacokinetic activity in an organism. Therefore, ENMs like nanoparticles can act as a vehicle to deliver a therapeutic component to a tumoral region, as part of a drug delivery systems.

Targeted drug delivery refers to a predominant drug accumulation within a target zone that is independent of the method of administration (Bae & Park, 2011). It aims to specifically target a drug or drug carrier to minimise drug-originated systemic toxic and secondary effects. Effective targeted drug delivery systems should feature the following requirements:

Retention. In order to reach a therapeutic dose in situ, drugs and drug carriers should have a high blood circulation rate and retention. This depends on metabolisation of such therapeutic strategies and clearance by lymphatic system and detoxifying organs like kidneys and liver.

Evasion. Targeted drug delivery systems should aim to evade the reticuloendothelial system (see page 17) so they can reach the tumour while still functional (Huang & Guo, 2011).

Targeting. Specific moieties on the surface of the drug delivery system should aim to increase the specificity of interaction with targeted tissues and cells.

Both, the so-called 'passive targeting' and 'active targeting' strategies for drug delivery take profit of the body circulation to distribute the drug and the enhanced permeability and retention (EPR) effect (see page 19) to localise the drug in the vicinity of the tumour. The misnomer 'active targeting' simply refers to the cases in which there is a specific ligand-receptor interaction thanks to the decoration of the drug delivery system with active moieties aiming to interact with the target (Bae & Park, 2011).

Release. The release of the drug should be coordinated with the specific interaction with the target, so that the therapeutic outcome is optimised and the secondary effects and interference with the rest of the body are limited.

Therefore, nanoparticles offer a strategic gateway into the tumour, acting as a Trojan horse when encapsulating chemotherapeutic drugs that may be hard to administer due to their hydrophobicity or short-life once in the bloodstream due to their size or predisposition for metabolic inactivation.

1.3.2. Hyperthermia

The use of heat in tumour treatment dates to back to the beginnings of the 20th century. Heat has a direct cytotoxic effect on cells due to the small margin of temperature in which the molecular structures and components of the cell remain stable and functional. Whilst the first uses of heat as a treatment involved contact with a heat source, nowadays, a non-contact approach is preferred to avoid system side-effects. In this sense, magnetic hyperthermia, or thermotherapy, one of the latest technologies developed for the matter is applied. It consist of the use of magnetic nanoparticles (iron, iron/gold, gold/palladium...) sensitive to electromagnetic fields and specific wavelengths across the spectrum to produce heat (Rajan & Sahu, 2020).

Magnetic nanoparticles (MNPs) can be used to generate heat locally using triggers as an alternate magnetic field (AMF). The production of heat happens due to the coupling of the magnetic moments of the MNPs with the oscillating fields of the AMF and the transformation of the energy absorbed into heat on the targeted tumour cells.

Combining materials with both magnetic and plasmonic properties, such as iron oxide and gold into a single ENM design, what is called a magnetoplasmonic NP, allows to take advantage of two different triggering strategies (that can be vital depending on the ability to reach the tumour with the selected electromagnetic trigger). Once, these NPs are exposed to an electromagnetic stimulus like an alternating magnetic field, or the irradiation with a laser of a particular wavelength, the plasmonic atoms of gold or the magnetic atoms of iron on their design are triggered into an excited state from which they can only escape dissipating the energy absorbed through heat production. This energy dissipation locally heats the liquid around the NP and can induce damage in biological structures in close contact with them (Fig 3).

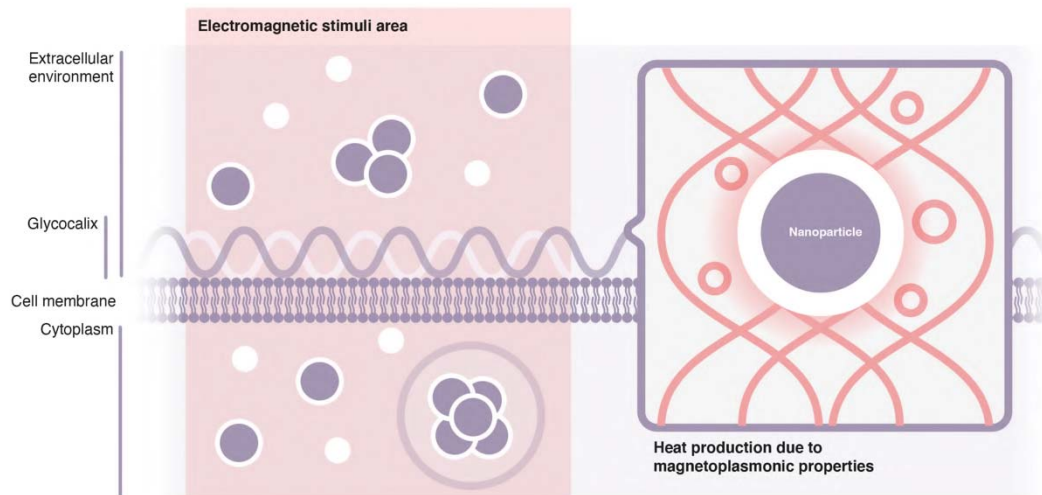


Figure 3. Magnetic nanoparticles' heat production mechanisms. When magnetoplasmonic NPs are exposed to an electromagnetic stimulus energy is produced and its dissipation locally heats the liquid around the NP, producing damage in the nearby biological structures.

Effects of heat on cells.

Close contact between heat-producing NPs and the cell membrane leads to the apparition of membrane pores/holes after hyperthermia is triggered as analysed by scanning electron microscopy and transmission electron microscopy. This means that local heat-damaging effects in the membrane produce membrane destabilisation that can trigger necrosis. Cells exposed to hyperthermia typically exhibit complete vacuolisation of all organelles in the cytosol, including mitochondria and the endoplasmic reticulum, and ruptures on the plasma membrane (Sanz et al., 2017).

In case NPs can't escape the endolysosomal system (see page 17), death can be triggered during magnetic hyperthermia treatment by the release of countless enzymes from the destructed lysosomes into the surrounding cell space. This leakage will trigger intracellular damage, lipid structure peroxidation, structure degradation and promote the activation of cell death programmes (Clerc et al., 2018).

Exposure to hyperthermia conditions can lead to very different cell death triggering outcomes depending on several factors concerning the NPs. Size, concentration and localisation are key to the aggressiveness of the selected therapeutic strategy when performing hyperthermia. NP size will affect the heat production level, as explained before. The selected concentration will be key to produce mild or strong hyperthermia in the targeted cells (logically the more NPs in contact or inside the targeted cells, the better). The selected time of exposure will also affect the aggressiveness of the local-heat treatment. Localisation within the tumour and the targeted cells also determine the outcome of the local heat-damage strategy. NPs that are outside the cell may heat the tumour

microenvironment and induce a damaging response from outside the targeted cells, meanwhile NPs on the cell surface or within the cytoplasm and its organelles will cause direct damage to intracellular structures and trigger unregulated (necrosis) or regulated (apoptosis, necroptosis, parthanatos, pyroptosis...) (Galluzzi et al., 2018) cell death programs from within.

Hyperthermia has been proved to induce nuclei modifications. The cell nucleus is normally a rounded structure formed by a double lipid bilayer encapsulating the DNA content of the cell at different degrees of condensation. When stressed the degree of condensation of the cell nucleus is modified and structures like the nucleoli are modified. If the stress is high enough it may induce changes in the nuclei membrane, chromatin condensation and even generate DNA breaks. All of this can lead to the formation of irregularly shaped nuclei and occasional compacted chromatin spots and/or aberrant nuclear shapes indicative of karyolysis, pyknosis and karyorrhexis (Sanz et al., 2017). These processes are critical in the functionality of the whole cell and a major indicator of cell death. Due to these effects, NPs with hyperthermia-inducing properties are a great candidate as a coadjuvant for radio- or chemotherapy, as cancer cells are more sensitive to these treatments when they have been previously subjected to high temperatures (42-45°C), and the combination has a synergistic effect on their elimination (Abe et al., 1986).

1.4 Engineered nanomaterials and biological interaction

Cancer is a complex disease, but there's key hallmarks that may serve as a target when aiming to fight it. Since their administration, drugs will face complex barriers (Fig 4) that will affect their therapeutic outcome. First, their biodistribution and how they reach the vicinity of the targeted tissue, second, the tumour microenvironment and its complexity, third, the extracellular matrix (ECM), fourth, the plasma membrane of the cell and finally, the endolysosomal system.

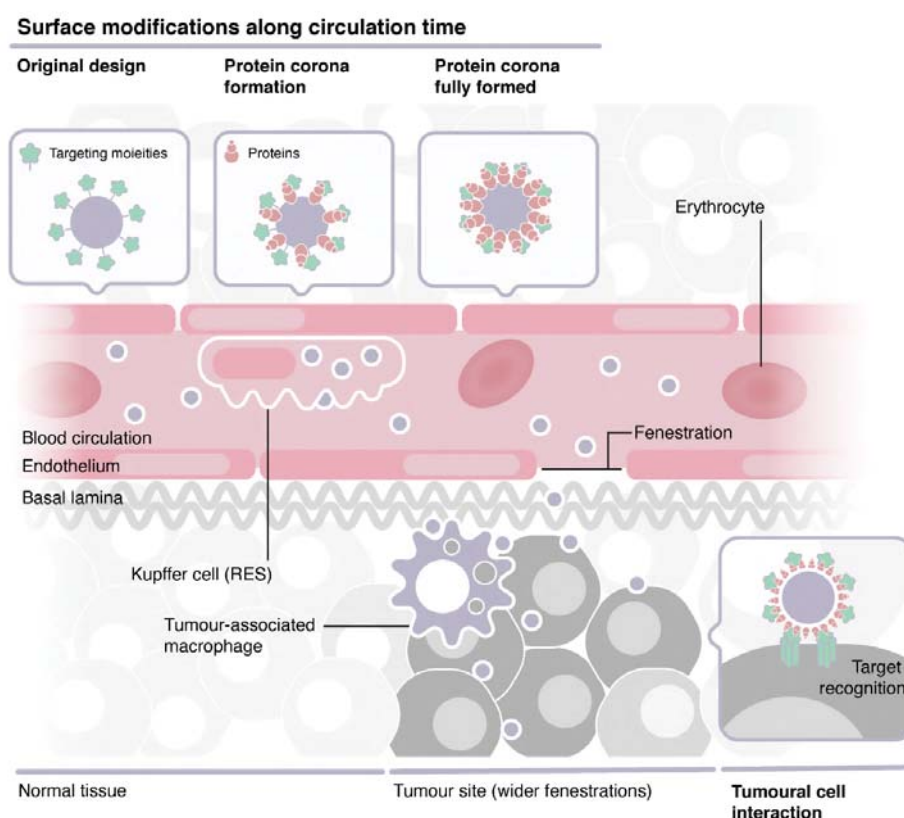


Figure 4. Biological barriers for ENMs reaching the tumour milieu. NPs' original design is easily modified upon administration when in contact with biological compounds (serum, blood, saliva, mucus...). The figure depicts one of the above-mentioned modifications, the formation of a protein corona around the NPs along its circulation time in blood, that could hinder the targeting moieties ability to interact with their targeted molecules and receptors. Within the blood vessels the Kupffer cells (part of the Reticuloendothelial system (RES) patrol the surrounding areas of a tumour, engulfing NPs that could be recognised as stranger bodies. Wider fenestrations between the endothelial cells of the blood vessels surrounding the tumour lead to the EPR (enhanced permeability and retention) effect, so NPs can leak to the tumour milieu, cross the basal lamina (rich in proteins like collagen) and interact with tumour cells passively or through target recognition strategies. Inside the tumour, tumour-associated macrophages can also engulf nanoparticles preventing their interaction with targeted cells.

The clinical success of nanomedicine may be hindered by biological barriers, that affect their distribution through the body, their possible toxic effects on non-targeted tissues and their fate. In this sense, the assessment of the NPs biointeraction with each biological barrier is of fundamental need for optimal therapeutic application and outcomes.

1.4.1. Biodistribution and immunological response

Chemotherapeutic drugs usually have high polarity and therefore their administration and biodistribution within the body is difficult and highly unspecific, leading to high impact side-effects when in free-form. In this sense, encapsulation on ENMs can be beneficial to increase solubility, biodistribution and specificity of the above-mentioned problematic compounds. It is known that injected materials suffer from sequestration by the immune system's reticuloendothelial system (RES), a network of macrophages and monocytes that patrol the body, clearing it from foreign bodies and materials (Peer et al., 2007). The recognition that NPs face when circulating depends on their interaction with the complement system that can opsonise the particles once their foreign nature is identified and facilitates their phagocytosis and clearance. Moreover, this response activates a pro-inflammatory reaction via complement mediators or anaphylotoxins that can cause an allergic reaction in sensitive patients (Peer et al., 2007).

In this sense, it is important to create therapies and drug delivery systems that minimise the interaction with the RES to enhance their therapeutic outcome. It has been previously described, for example, that materials above 100 nm hardly escape the RES (Peer et al., 2007). It is also well-known that particle size affects the rate of clearance from the bloodstream. In general, smaller particles (50-300 nm) have a slower removal from circulation compared to those with higher sizes. To achieve a better therapeutic outcome, it is important that targeted drug delivery systems (TDDS) sustain the circulation time and release of the drug as much as possible, without compromising the drug activity on the way. The use of nanotherapies encapsulating the drugs in their cores is an effective strategy to increase circulation times, reduce drug clearance by biliary, urinary and liver excretion systems, and enhance its biodistribution and retention, while protecting drug integrity and activity.

Other strategies to lengthen circulation times in TDDS include NP interaction with PEG molecules (Ginader Timothy, 2016) that can reduce opsonisation and therefore their recognition as a threat by the immune system (Halamoda-Kenzaoui & Bremer-Hoffmann, 2018). Another is the previous decoration of NPs with a corona that hinders the ability of complement molecules to attach to their surface (Coty et al., 2017).

By contrast, immune response can be used to promote tumour destruction. That is, by the interaction of ENMs with tumour associated macrophages. These macrophages have a 'healing' phenotype around the tumour, promoting angiogenesis and cell proliferation and therefore its progression. They can uptake ENMs that trigger an inflammatory reaction that may reprogram them into a 'cytotoxic' phenotype, and therefore reverse their behaviour to promote tumour destruction instead (Anchordoquy et al., 2017).

1.4.2. Tumour microenvironment

The tumour milieu is complex, both in structure as in physico-chemical, immunological and metabolic characteristics. The tumour microenvironment is formed by tumour cells, their stromal cells and all the proteins and fluids produced by them and confined in the tumour vicinity. Tumour's stromal cells are non-malignant cells present in the tumour that contribute to its formation. There are different stromal cells like carcinoma associated fibroblasts (CAFs), specialised mesenchymal cell types specific to the tissue, immune cells from the innate and adaptive systems and vasculature cells. In addition, the ECM contributes to the tumour microenvironment with its structural proteins (collagen and elastin), glycoproteins (fibronectin and fibrillin) and proteoglycans (decorin, heparan, etc.) (Kamińska et al., 2015).

The tumour microenvironment is very important in cancer development and the efficiency of therapies against it. The tumour microenvironment is responsible for the deregulation of the extracellular matrix, the cell metabolism, the continually activated proliferative signalling, the inhibition of tumour suppressors and apoptosis (regulated cell death mechanism), the tissue invasion and metastasis and the evasion of the immune action on the tumour (Kamińska et al., 2015). Most of these processes also promote the colonisation of distant organs through factor secretion altering the microenvironment of the tissue where a metastatic cell from the primary tumour may develop a secondary tumour.

All the elements contributing to the tumour mass and forming the tumour micro-environment act as a trap for therapeutic agents that get lost in the way to find their therapeutic target. Like a tightly-knit mesh of elements (stromal, tumoral and extracellular matrix compounds produced by cancer cells) act as a network that surrounds and protects the tumour from the therapeutic strategies against them. The application of nano-engineered solutions to the delivery of chemotherapeutic agents allows the use of sequential and programmed drug delivery strategies. Thanks to ENMs design we can create strategies that escape the RES and immune tumour-protecting cells thanks to their surface modifications, are able to disaggregate and cross the complex extracellular matrix (due to their enzymatic activity or their ability to induce movement or locally produce heat) and reach the target for delivery of the therapeutic attack.

One of the consequences of the abnormally grown tissue and the 'healing' phenotype of the immunological entities in the tumour, is the rapid vascularisation of the tumour. It is well known that the vasculature of the tumour has bigger fenestrations. These fenestrations led to the definition of the enhanced permeability and retention (EPR) effect: the fenestrated vessels allow macromolecules and NPs to permeate through the tumour and due to the lack of a functional lymphatic system, the NPs leak to the interstitial space within the tumour and are retained there due to low lymphatic clearance (Seleci et al., 2017). Scientists saw as an opportunity to deliver ENM to the tumours using passive distribution and targeting strategies thanks to this EPR effect. Passive distribution and targeting of nanomaterials taking advantage of the tumour's EPR effect was proposed in the 1980s Maeda et al. realised that the theory behind the use of radioactive gallium in scintigraphy for tumour detection (something that was routinely applied in clinical settings) was based on the EPR mechanism due to leaky vasculature within the tumour region and low clearance due to abnormal lymphatic action (Maeda et al., 2000). Using this logic, theranostic ENMs can use this entry strategy to reach the vicinity of the tumour where they can perform their reporting or therapeutic strategy.

1.4.3. Extracellular matrix

It has been previously described that stromal cells, such as CAFs, can work together with cancer cells to modify physical properties of the ECM. Such modifications can affect the stiffness, pore size and viscoelasticity of the ECM surrounding cancerous cells which conforms the microenvironment of the tumour (Calvo et al., 2013). Stiff tumour microenvironment caused by such modifications and increased ECM deposition has been shown to promote tumour progression and malignancy via alterations in integrins' cell signaling (Spill et al., 2016). Moreover, these changes in the ECM make very difficult for free drugs and TDDS to reach the target cells, and sometimes only reach the vicinity of the tumour and accumulate in its surroundings.

One possibility to overcome this barrier is the use of active TDDS. One example is the magnetically-mediated TDDS. Even if TDDS can't achieve the targeted cell inside the tumour, scientists may take advantage of the NPs closeness to it. Inducing a lithic activity, for example by externally triggering heat production locally, causes a decrease in the density of the ECM and tumour microenvironment. This may help NPs to reach and treat the tumour producing hyperthermia ablation or enhance the ability of other drugs to cross the dense tumour milieu and reach their therapeutic target.

In addition, mechanical resistance, that is, the ECM density and increased confinement due to the high collagen concentrations (promoted by local hypoxia (Riching et al., 2015)) has been recently shown to have a role in stimulating cancer cell migration and tissue invasion promoting the activity of metalloproteinases and protease-dependent invasion (Riching et al., 2015). The production of

ROS due to hypoxic conditions inside the tumour environment leads to sustain carcinogenic behaviours of the transformed cells thanks to the stabilisation and activation of molecular effectors like HIF1 α which trigger survival, growth, motility, metastasis, and metabolic changes of transformed cells (Fluegen et al., 2017).

In addition to this, the treatment through conventional chemotherapeutics and radiotherapy induce pro-inflammatory response on and around the tumour, leading to a modification of the affected area where ROS are highly abundant (Grivennikov et al., 2010). The use of adjuvant nano-therapies like antioxidants in combination with such therapies can be beneficial to ensure that not only the therapeutic effect is efficient, but also to control the secondary effects on the surroundings of the affected area. Antioxidants may protect normal cells indirectly by priming cells to respond to ROS insult or directly by scavenging cellular ROS, meanwhile they can be toxic to cancer cells, inhibit their invasion ability and sensitise them for radiotherapy (Gao et al., 2014). This is the case of the described radioprotective effect of cerium oxide NPs in combination with radiotherapy by Madero-Visbal et al. in mice after head and neck radiation, when a decrease in xerostomia and radiation-induced dermatitis was observed (Madero-Visbal et al., 2012).

As explained, altered ECM properties can also promote cancer cell migration. It has been previously described the preference of cells for stiffer substrates, an effect called durotaxis. However, recent findings highlight the ability of some cells to reverse the durotaxis effect and migrate to soft matrices instead.

Stiffness and mechanical resistance have been described to play a role in collective cell migration, a process in which migrating cells follow a population of leader cells that exhibit an increased proteolytic activity that enhances tumoral's cell scape from the primary tumour mass and may lead to metastasis (Lintz et al., 2017). Compressive forces within the tumour from uncontrolled growth and interstitial fluid accumulation and flow from the leaky vasculature promote an invasive phenotype in tumoral cells activating a mechanotransductive mechanism that leads to cellular migration upstream of the interstitial flow, that is known as rheotaxis (Polacheck et al., 2014) which also facilitates the scape of cancerous cells from the tumoral mass triggering metastasis.

Such pressure inside the tumour environment and the possible escape of highly dynamic and migrating cell types are common problems for therapeutic agents to reach their desired target populations. Multiplexed ENMs therapies make the co-adjuvant strategies, that enhance the delivery in such areas, vital to prevent tumour growth and expansion. Promoting the accumulation of the therapeutic agent on-site, can be vital to control this factor. Therefore, strategies to deliver and retain apparently innocuous agents on the tumour and its surroundings can be used as a Trojan horse fighting strategy (MG et al., 2015), in which after accumulation a coordinated attack can be unleashed using a highly controllable trigger such as magnetic stimulation, laser irradiation or other

electromagnetic stimuli. This is one strategy being explored by magnetic and magnetoplasmonic NPs, which can be magnetically traced within an organism, attracted and retained in a specific target area and triggered by an AMF or specific laser wavelengths to locally induce heat production and cause tumour/target ablation by local hyperthermia. This way the amount of NPs interacting inespecifically with other tissues and their side-effect is lowered. All the hyperthermia effects are isolated to the targeted region exclusively due to the high accumulation and the concentration of the trigger with the magnets on-site.

Cell migration and proliferation is also enhanced by changes in the components of the cell plasma membrane. Tumoral cells' membrane has been described to vary in their cell membrane fluidity and expression of proteins. Some of the proteins under-expressed in malignant processes are the cadherin family which keep cells attached to their neighbour cells and are responsible of the cell's contact inhibition effect (that prevents cells from proliferating when the surrounding space is taken by other cells). The loss of this kind of cell-cell interaction leads to abnormal cell growth and proliferation and can promote metastasis.

1.4.4. Plasma Membrane

Once ENMs reach the tumour environment and cross the ECM the next barrier they should cross to enter the cell is the cell membrane. This process can be passive or active depending on the mechanism that the ENMs trigger when in contact with the plasma membrane.

The plasma membrane is a selectively permeable membrane that transfers materials that are critical for the cell's life. Naturally, such compounds, as ions and nano-sized proteins, can pass through the lipid bilayer using specialised membrane-transport protein channels. Depending on their size, shape, and surface chemistry NP would entry the cells through different endocytic pathways.

NP internalisation can be accomplished i) passively, by diffusion, a mechanism for molecules that are not charged and smaller than 1 kDa (Petros & Desimone, 2010) and energy is not required o ii) actively, by endocytosis, a process that generates small (60–120 nm) membrane vesicles that in eukaryotic cells transport various cargo molecules from the plasma membrane into the cytoplasm. These cargoes (transmembrane proteins and their extracellular ligands) are involved in a broad range of physiological processes, including nutrient uptake, cell signalling, developmental regulation through morphogens, cell adhesion, etc.

The term endocytosis includes a wide variety of specific endocytic pathways and processes that have been described in cells, such as phagocytosis, pinocytosis, macropinocytosis, clathrin-mediated endocytosis, caveolin-mediated endocytosis and clathrin- and caveolin-independent endocytosis.

Phagocytosis.

A mechanism to internalise molecules and complexes larger than 200 nm in size, including foreign materials like NPs and bodies like bacteria and other microorganisms or remnants of other cells. This mechanism is common on phagocytic cells like macrophages and neutrophils of the immunological system, specialised in the surveillance of the system and detecting foreign materials and organisms in it. Despite that, some other cell types can display phagocytic activity under certain conditions (Patiño et al., 2012). For phagocytosis to happen we need an extrinsic activation of the cell surface receptors or an indirect recognition of the foreign body thanks to its opsonisation. Once this recognition is activated actin polymerises and protrusions form on the cell surface, wrapping and internalising the foreign body forming a vesicle in the cytosol known as the phagosome. Usually, this phagosome contents are further processed by the hydrolytic digestion of its contents and acidification of the compartment through its maturation, ending up in a lysosome. These phagocytic processes that occur in the RES and immune cells patrolling living organisms are detrimental to the ENMs delivery strategies because they clear active therapeutic drug delivery systems from circulation while they haven't reached the tumour vicinity yet (as mentioned in section 1.4.1., page 17). Therefore, size and surface modification mechanisms that inhibit opsonisation and molecular recognition by these surveillant cells is of fundamental need to enhance the therapeutic outcome of the treatment.

Pinocytosis.

In 1931, Warren H. Lewis observed the uptake of extracellular fluid by cells in vitro and coined the term pinocytosis, or "cell drinking" (Schmid et al., 2014). Nowadays, after years of studying this process through membrane dynamics, the protein structures involved in membrane protrusions and invaginations and the discovery and use of inhibitors, this process has been subdivided in several pathways that use different strategies to internalise extracellular materials into the cells.

a. Macropinocytosis.

Macropinocytosis is a process independent of receptor recognition, initiated by the actin-driven extension of the plasma membrane in form of ruffles that occasionally form a cup-like structure or nascent macropinosome that seals at its distal tips to form a relatively large (>250 nm) endosome (a macropinosome) engulfing extracellular components. Subsequent membrane fusion and fission interactions with various organelles, primarily components of the endocytic pathway, result in the formation of a mature, acidic, and often tubular structure termed a macropino-lysosome. In this process they gain early endosome markers like the early endosome antigen 1 (EEA-1) and fuse with other late endosomes and lysosomes (Canton, 2018). Due to their size (>1000 nm), macropinocytosis is the predominant mechanism for the internalisation of microparticles (Patiño et al., 2012).

b. Clathrin-mediated endocytosis.

This is a receptor-mediated mechanism present in all eukaryotic cells. It involves a wide variety of membrane receptor and cytosolic proteins that form an endocytic event by their clustering in a highly regular sequence in which they arrive and leave in a specific order, forming the nucleus for the assembly of the vesicle coat of an specific internalisation complex. Clathrin-mediated endocytosis starts with a signal promoted by some of these macromolecules when binding specific transmembrane receptors, and it is followed by the recruitment of clathrin, a soluble intracellular protein that assembles on the inner hemimembrane of the plasma membrane. Clathrin recruitment is led by the adaptor proteins, which bind on the one side to the receptor with the cargo and, on the other side, to clathrin, also mediating the selective gain of membrane and soluble cargo molecules into the vesicle. Its assembly stabilises the membrane curvature, which results in a clathrin-coated pit. Later, dynamin polymerises forming a coil that constricts the pit neck until clathrin-coated pit scission. Clathrin-coated vesicle formation lasts for about a minute (Cocucci et al., 2012).

The resulting clathrin-coated vesicles are 120 nm in diameter and the clathrin coat is lost after membrane detachment. From then on, they can fuse with one another, or with other vesicles resulting from endocytic processes, generating an early endosome. In the early endosome the pH decreases until a range of 6.1-6.8. Early endosomes have two distinguishable parts: a tubular side from where recycling endosomes are formed; and a bulbous, vacuolar region that drives the cargo to the degradative endolysosomal pathway. Non-recycled molecules remain in the bulbous region, which matures into a multivesicular body and, then, a late endosome, an organelle with a highly acidic lumen with pH values of down to 4.8 (El-Sayed & Harashima, 2013). Finally, the late endosome fuses with a lysosome to form an endolysosome, where the cargo starts to be degraded at a pH of around 4.5, when hydrolases are able to start their enzymatic activity.

Receptors previously needed to initiate clathrin-mediated endocytosis can follow the endolysosomal pathway and be degraded or be recycled and sent back from the tubular region of the early endosome to the plasma membrane.

This internalisation method is often used by NP designs that are surface modified using ligands and antibodies against receptors on the surface of targeted cells. After the receptor's surface targeted recognition NPs are internalised following clathrin-mediated endocytosis if they are small enough to be inserted into the vesicle that is formed.

c. Caveolin-mediated endocytosis.

It's a receptor-dependent endocytic mechanism, that is thought to be associated with lipid rafts (membrane domains rich in cholesterol and sphingolipids) through the dimerisation of the membrane protein caveolin. Caveolin drives the formation of small invaginations called caveolae while the cytosolic side of caveolins is linked to large complexes of proteins that are likely stabilizing the

membrane curvature. Contrary to clathrin-mediated endocytosis, caveolae usually remain static, unless their pinch off is induced by a signal that causes caveolin phosphorylation. The vesicles resulting from this endocytic mechanism have an approximated diameter of 60-80 nm (El-Sayed & Harashima, 2013). This has been described as the predominant uptake pathway of ~13 nm gold NPs in human alveolar epithelial type II A549 cell line (Rothen-Rutishauser et al., 2014)

Different vesicles formed from caveolae can fuse to form a caveosome, which is able to avoid the endolysosomal pathway and transfer its cargo to the endoplasmic reticulum or even the Golgi apparatus. It can also undergo the endolysosomal pathway directly fusing with an endosome instead.

d. Clathrin- and caveolin-independent endocytosis.

Despite the above-mentioned mechanisms are the most common, there are clathrin- and caveolae-independent pathways that are cholesterol-sensitive and contribute to compound internalisation in the cell.

1.4.5. Endolysosomal system

The endolysosomal system is a complex structured membranous organelle that has high pH variation depending on their maturation phase. The hydrolases inside the endolysosomal compartments can digest molecules like DNA, RNA, lipids, polysaccharides and proteins making the digestion products available for the cell. Those products that cannot be digested or the cells can't profit from are secreted back to the ECM through exocytosis. ENMs protect their therapeutic compound inside when entering this system keeping it protected from the action of these hydrolases in order to reach their therapeutic target while still active. ENMs design take advantage of this system to release their therapeutic agent and be degraded into innocuous compounds that can easily be cleared from the body. Escaping from the endolysosomal system is one of the last biological barriers some of the delivered therapeutic strategies must cross before reaching their therapeutic target. Therapeutic strategies must be able to survive these changes in pH or take advantage to ensure a good delivery strategy. Some TDDS such as dendrimers and polymer-based ENMs start to degrade to innocuous structural compounds while releasing the drugs that diffuse through the membranes into the cytosol where they can access their targets such as the cell nucleus, the mitochondria or enzymes and nucleic acids within the cytoplasm (Perrigue et al., 2021).

Other delivery strategies use the ability to functionalise ENMs with mixed-charged surfaces so once inside the lysosome crystallise in a programmed manner and act as disruptors of their membranes so both the TDDS and the lysosome contents can escape the membranous endolysosomal system and access their final therapeutic active sites within the cytosol, leading to cell death (Borkowska et al., 2020).

On the other hand, some of the ENMs used to trigger a therapeutic response can be manipulated using specific waves from the electromagnetic spectrum to produce heat and disrupt the membranes of the endolysosomal pathway they might be trapped in. This produces a direct therapeutic effect based on heat production on intracellular organelles and structures, causing ROS, instability of their limiting membranes and the release of the contents of these compartments (Clerc et al., 2018) into the cytosol, which promotes cell death (Clerc et al., 2018).

1.5 Future perspectives on engineered nano-materials

According to Feynman's early idea that tiny nanorobots could be designed, manufactured, and introduced into the human body to perform cellular repairs at the molecular level (Mestre et al., 2021), new generation of ENMs have increasingly complex abilities (common to computer-like communication, information recording and transmission, swarm behaviour, reprogramming and surveillance (Hortelao et al., 2021)). For the past three decades, nanotechnology has been an ever-growing field. As it happens with every emerging technology, it has spread rapidly into new applications and markets, but it has not started to translate into technologies beneficial in medicine until recently. This could be not only due to some of the underlying effects of their nature (desired or not) but also to the lack of knowledge of the mechanisms in which these therapies interact with the organisms, which are not normally studied in an integral way. Many details of this interactions are often overlooked from inception to keep up with the publication rhythm of the field or because of a lack of tools for in-depth biological characterisation. Despite that, NPs are a great promise to revolutionise how we diagnose and treat disease in the future. They are majorly explored to benefit challenging areas of modern medicine such as the enhancement of the biodistribution and delivery of drugs to targeted sites, what is known as drug delivery, the diagnosis and/or trigger of local responses against malignant cells, reducing side-effects. In this sense, due to the interdisciplinary nature of the field, in vitro studies at the cellular level are often over-looked or performed superficially when describing new materials with nanomedicine potential. It is our goal to provide an in-depth clear perspective from a cellular point of view of these nano-bio-interactions and how they might affect the expected therapeutic outcome.

2. Objectives

The general objective of this thesis is to analyse the biointeraction of different NPs and their capacity to treat and/or destroy malignant cells using different approaches. The specific objectives are defined as follows:

- I. To assess the biointeraction, toxicity and putative antioxidant effect of cerium dioxide nanoparticles on tumoral cell cultures.
- II. To evaluate the biointeraction and toxicity of silicon dioxide nanoparticles on cell cultures to explore their potential as theranostic tools for biological applications.
- III. To investigate the biointeraction, toxicity and ability to induce cell death of magneto-plasmonic latex iron/gold nanodomains when triggered externally by a magnetic field or near-infrared laser.

3. Results

3.1 Chapter 1: Simple synthesis of biocompatible stable CeO₂ nanoparticles as antioxidant agents

Simple Synthesis of Biocompatible Stable CeO₂ Nanoparticles as Antioxidant Agents

A. Garzón-Manjón,^{†,‡,§,||} A. Aranda-Ramos,^{§,#} B. Melara-Benítez,^{‡,¶} I. Bensarghin,[§] J. Ros,[‡] S. Ricart,^{*,†} and C. Nogués^{*,§}

Affiliations:

[†]Institut de Ciència de Materials de Barcelona, ICMA-B-CSIC

[‡]Departament de Química, Universitat Autònoma de Barcelona, Campus de la UAB, 08193 Bellaterra, Catalonia, Spain

[§]Departament de Biologia Cel·lular, Fisiologia i Immunologia, Universitat Autònoma de Barcelona, Campus de la UAB, 08193 Bellaterra, Catalonia, Spain

* Corresponding authors ricart@icmab.es, carne.nogues@uab.cat

Present Addresses

^{||}Max-Planck-Institut für Eisenforschung GmbH, Max-Planck-Straße 1, 40237 Düsseldorf, Germany.

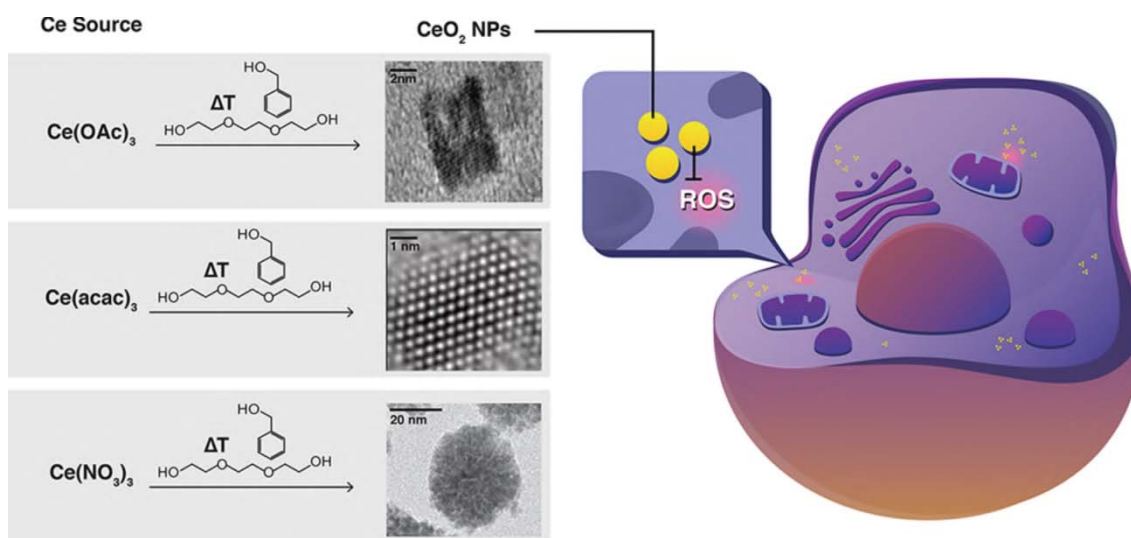
[¶]Geschäftsführung des Departments für Chemie, Greinstrasse 6, 50939 Köln, Germany.

Author Contributions

[#]Alba Garzón-Manjón and Antonio Aranda-Ramos contributed equally to this work.

Reprinted (adapted) with permission from 'Simple Synthesis of Biocompatible Stable CeO₂ Nanoparticles as Antioxidant Agents' **Authors:** A. Garzón-Manjón, A. Aranda-Ramos, B. Melara-Benítez, I. Bensarghin, J. Ros, S. Ricart, and C. Nogués **Publisher:** American Chemical Society **Date:** 1 July 2018 **Copyright 2018 American Chemical Society**

Abstract



Cerium oxide (IV) nanoparticles offer a high redox ability, while maintaining nontoxicity and high stability. Thus, dispersed nanocerium is a promising candidate as antioxidant material for human cells. In this work, we report on a fast and simple one-pot process that yields a final nanoparticle size of 2–4 nm in polar solvents such as water and alcohols. High boiling point solvents, namely, benzyl alcohol and triethylene glycol, are used to obtain high crystalline nanoparticles by thermal and microwave activation. Transmission electron microscopy investigations prove the narrow size distribution of the CeO₂ nanoparticles and show that the shape can be tuned from spherical to cubic using an appropriate precursor. The main objective of this work is to produce nanoparticles, which are well-defined, biocompatible, and stable in highly concentrated colloidal solutions (up to 90 mM) for a long period of time to study their behavior as antioxidant agents in human cells under oxidative stress.

Introduction.

Nanocrystalline cerium (IV) oxide (CeO_2) has a unique atomic structure and the 4f electronic configuration provides special luminescent¹, magnetic² and electronic³ properties. This 4f electronic configuration makes CeO_2 ⁴ of interest to design new applications, which are not possible with transition or main group metals. CeO_2 nanomaterials can be used in different fields of engineering and technology⁵ such as solid-oxide fuel cells⁶, catalytic materials⁷, solar cells⁸, three-way catalyst for automobile exhaust-gas treatments⁹, and oxidative coupling of methane and the water–gas shift reaction¹⁰. Furthermore, its high redox ability and nontoxicity enable its application as pharmacological and antioxidant agent for human cells^{11–13}. There are different types of nanoparticles that can be used to decrease the level of reactive oxygen species (ROS)^{14,15}, but the capacity of CeO_2 to remove and prevent their formation during the oxidative stress process in cell cultures is well-known¹⁶. It has been demonstrated that ROS and oxidative stress are associated with age-related degenerative diseases including arthritis, cardiovascular disease, inflammation, Alzheimer's disease, Parkinson's disease, diabetes, or cancer. For this reason, CeO_2 nanoparticles (NPs) – directly or indirectly – can play a vital role in human cells hampering the oxidative process.¹¹

CeO_2 NPs can be produced with high control in morphology and size. Several techniques such as hydrothermal¹⁷, solvothermal¹⁸, aqueous precipitation¹⁹, reversed micelles²⁰, thermal decomposition²¹, and flame spray methods²² are used to synthesize CeO_2 NPs with specific characteristics. The different synthetic methodologies determine the solubility, size, nature of capping ligand, charge, structural arrangement, and morphology of NPs and, thus, their properties. CeO_2 NPs for biological applications require a stable dispersion in water²³, polyethylene glycol²⁴ or glucose²⁵ and a narrow size distribution of the NPs below 10 nm.

Recently, we presented two synthetic routes²⁶, using thermal and microwave-assisted preparation of different metal oxide NPs controlling their growth process to obtain the desired shape and size²⁷. Using the microwave-assisted synthesis we were able to synthesize CeO_2 NPs (<10 nm) which were incorporated into functional ceramic nanocomposites to obtain improved superconducting properties^{28,29}.

In this work, we present an optimized preparation process, based on the thermal decomposition route previously described for other oxides that allows us to produce small CeO_2 NPs for biological applications, which are stable in polar solvents such as alcohols and

water. The main feature of this optimized process is the use of high-boiling-point solvents, that are, at the same time, ligand stabilizers thus hampering the growth of the nanoparticles at the very early stage. No other reactants are introduced in the reaction. That also allows us to clearly reduce or even eliminate secondary reaction products. Moreover, two different activation systems (thermal and micro- wave) are presented and three different sources of Ce, Ce(III) nitrate ($\text{Ce}(\text{NO}_3)_3$), Ce(III) acetylacetonate ($\text{Ce}(\text{acac})_3$), and Ce(III) acetate ($\text{Ce}(\text{OAc})_3$) in benzyl alcohol (BnOH) or triethylene glycol (TEG), as high boiling point solvents. We focus on the CeO_2 NPs characterization and on its antioxidant property to rescue cells under oxidative stress.

Results and discussion

The decomposition of metalorganic salts (MOD approach such as $\text{Ce}(\text{acac})_3$, $\text{Ce}(\text{Oac})_3$, and also $\text{Ce}(\text{NO}_3)_3$) using thermal or microwave activation has been chosen among the different possible synthetic routes to produce CeO_2 NPs. Two different types of high boiling point solvents were used (TEG²⁷ and BnOH³⁰). From our previous study²⁶, we know that for the synthesis of metal oxide NPs, the use of a unique compound as solvent and stabilizer produces small NPs with a very narrow dispersion in size.

CeO_2 NPs Characterization.

Our first approach was the use of TEG as solvent and stabilizer and cerium(III) acetylacetonate as starting salt, where NP nucleation and growth is initiated by thermal and microwave activation. In this case, CeO_2 NPs of 2.5 ± 0.3 nm (thermal and microwave) with a narrow dispersion in size were produced (Figure 1).

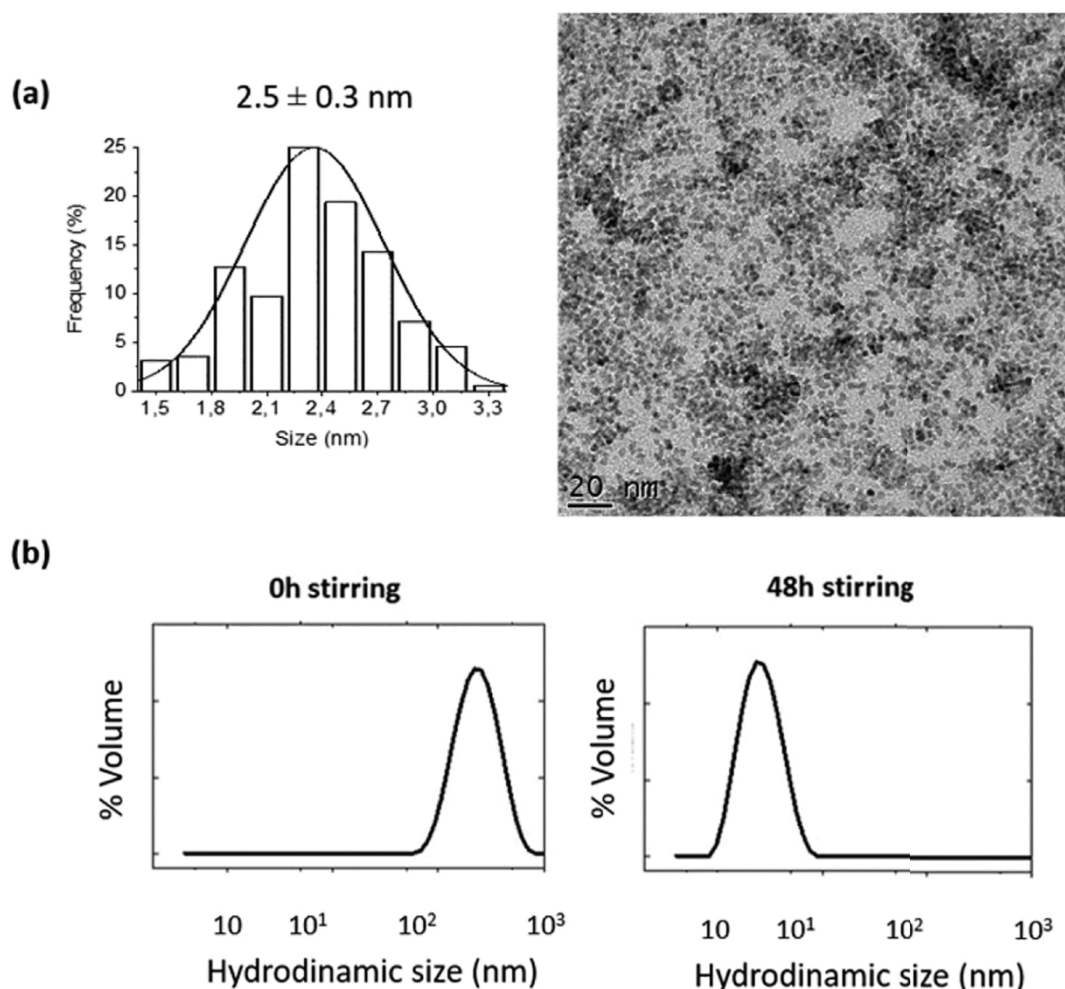


Figure 1. (a) Transmission electron microscopy image of the CeO₂/TEG NPs after 48 h stirring by thermal process. (b) DLS of the CeO₂/TEG before and after 48 h stirring.

In order to reduce the number of agglomerations of NPs (Figure 1b) an additional stirring (48 h) at room temperature is required before the cleaning and redispersion process. This can account for the presence of oligomeric products coming from the solvent/ligand used (TEG). As observed by gas chromatography– mass spectroscopy (GC-MS) analysis (Table S1), di- and trimerization TEG subproducts are present after the NPs synthesis. These subproducts interact weakly with the nanoparticle surfaces generating temporary agglomerations in the colloidal solution³¹. The microwave activation process³² was also used to synthesize CeO₂ NPs with a clear reduction in time from ~7h to ~1.5 h and reduced temperature from 280 to 220 °C for the synthesis. This process also suppresses the formation of TEG subproducts.

However, if both approaches are used, thermogravimetric analysis (TGA) showed a high amount of organic material (Figure S1) as a shell after the end of the cleaning process. The presence of high amounts of organic shell (more than 50% in weight) can be reduced (to

14%) by repetitive cleaning procedures (10 times cleaning) (Figure S1). However, after this long cleaning process the final colloidal solution presents nanoparticle agglomeration which produce a decrement in its stability.

Hence, a different approach was undertaken and BnOH was used instead of TEG as high boiling point solvent. Using BnOH as a solvent and stabilizing agent it can be expected that no oligomeric reactions appear. In this approach, the three starting cerium salts $\text{Ce}(\text{acac})_3$, $\text{Ce}(\text{OAc})_3$, and $\text{Ce}(\text{NO}_3)_3$ were used (Figure 2).

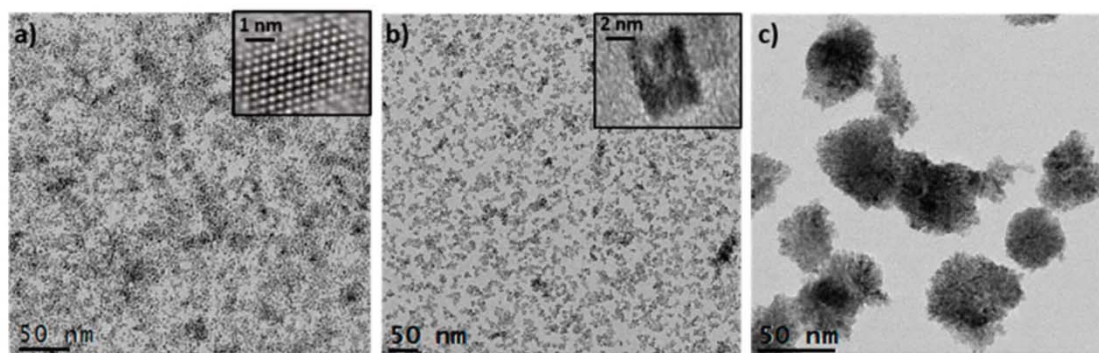


Figure 2. Transmission electron microscopy images of the CeO_2/BnOH NPs from (a) $\text{Ce}(\text{acac})_3$, (b) $\text{Ce}(\text{OAc})_3$, and (c) $\text{Ce}(\text{NO}_3)_3$.

The transmission electron microscopy (TEM) characterization of the three NPs obtained, using BnOH as a solvent, shows that the starting salt clearly influences the size and shape of the NPs. Spherical NPs of around 2–3 nm in diameter (Figure 2a) are obtained from the $\text{Ce}(\text{acac})_3$ salt, whereas cubic NPs (inset of Figure 2b) of around 4–5 nm in size are produced when starting from the $\text{Ce}(\text{OAc})_3$ salt. In the case of $\text{Ce}(\text{NO}_3)_3$, heterogeneously agglomerated groups with a diameter of 50 nm were obtained (Figure 2c). When zooming in to one of these agglomerates, it seems to consist of smaller spherical NPs of ~5 nm. In this case, the use of nitrate as the counterion decreases the stabilization of the NPs, which generates aggregates in contrast to $\text{Ce}(\text{OAc})_3$ or $\text{Ce}(\text{acac})_3$ salts. After TEM and GC-MS characterization, our efforts were focused in the X-ray powder diffraction (XRPD) and X-ray photoelectron spectroscopy (XPS) analysis of CeO_2 NPs, which are synthesized from the acetate and acetylacetonate. NPs from $\text{Ce}(\text{NO}_3)_3$ starting salt yield large aggregates of 50 nm, which makes them incompatible with cellular studies in terms of stability. Furthermore, BnOH was chosen as a high-boiling- point solvent to decrease the amount of organic shell formed around the NPs from ~50% (TEG) to ~35% after the cleaning process (Figure S2).

XRPD analysis confirms that for all the cases the synthesized NPs are composed of cerium oxide with a typical fluorite (face-centered cubic) structure (JCPDS 34-0394, space group $Fm\bar{3}m$)³³. All samples exhibit peaks corresponding to (111), (200), (220), (311), (222), (400), (331), and (420) planes. However, they are much broader than the reference spectrum due to the small NPs size (Figure S3).

To confirm the CeO_2 phase of the NPs, XPS analysis³⁴ was carried out. Figure 3 shows the Ce 3d spectra for CeO_2 NPs obtained from $Ce(OAc)_3$ and $Ce(acac)_3$ using BnOH as solvent, where in both cases the same results are obtained. These present two sets of multiplets (u and v) corresponding to the spin-orbit split of 3d 5/2 and 3d 3/2 core holes.

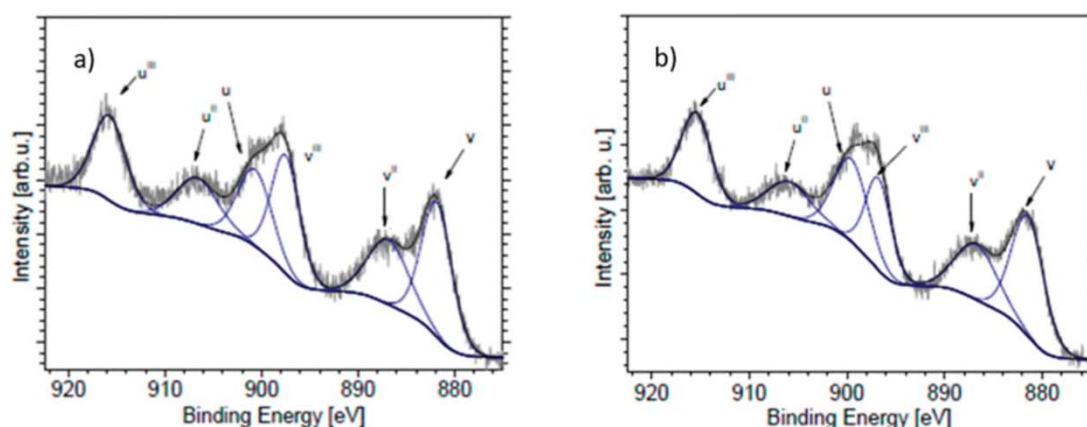


Figure 3. X-ray photoelectron spectroscopy of the CeO_2 NPs in BnOH form (a) $Ce(acac)_3$ and (b) $Ce(OAc)_3$.

The spin-orbit splitting, measured by the difference between the main peaks for 3d 5/2 and 3d 3/2, is about 18.1 eV for the sample obtained from $Ce(OAc)_3$ and about 18.9 eV for the one from $Ce(acac)_3$. For Ce(IV) compounds, each spin-orbit component (3d 5/2, 3d 3/2) is dominated by three features in contrast to Ce(III), which is dominated by two features. These three features from Ce(IV) are visible as six peaks corresponding to the spin-orbit doublets. The highest binding energy peaks of u''' and v''' appear at 915.5 and 896.9 eV for CeO_2 obtained from $Ce(OAc)_3$ and at 915.9 and 897.6 eV for CeO_2 obtained from $Ce(acac)_3$. These are the result of a $Ce\ 3d^9\ 4f^0\ O\ 2p^6$ final state and the u''' associated with the $Ce\ 3d_{3/2}$ is characteristic of the presence of tetravalent Ce (Ce^{4+} ions) in the compound. Hence, the (+IV) oxidation state of Ce in the synthesized CeO_2 NPs is hereby confirmed.

By comparing all the NPs growth process studies, the high boiling point solvent/thermal decomposition approach for the formation of NPs show two main advantages. First, the solvent acts at the same time as diluent solution and stabilizing ligand, where only small amounts of secondary products, mainly organics originating from the metal-organic salt decomposition, are produced, which can be easily eliminated by the cleaning process.

Second, using this approach, high concentrations of stable NPs in polar solvents (up to 90 mM) can be obtained in a highly reproducible way. DLS experiments confirm the stability for a month of CeO₂ NPs without the formation of big aggregates (Figure S4). Thus, this protocol is a good and simple way to prepare small-sized NPs with a narrow dispersion in size.

Internalization of CeO₂ NPs by SKBR-3 Cells.

Internalization was measured by quantifying the NP absorbance³⁵. It has been described that CeO₂ shows a strong absorption band at 210–350 nm in the UV range³⁶, and absorption depends on the oxidation state of Ce, i.e., Ce³⁺ has its maximum absorption at 250 nm, while Ce⁴⁺ has its maximum at 298 nm^{37,38}. CeO₂ NPs absorption was recorded at 210, 250, 280, and 293 nm, and in all wavelengths analyzed, the absorption was higher in samples incubated with NPs compared with control samples (Figure S5), confirming the CeO₂ NPs uptake by SKBR-3 cells.

NPs Antioxidant efficiency of CeO₂ NPs.

Among the different CeO₂ NPs synthesized in the present work, the most promising candidate as antioxidant for human cells is the nanoceria synthesized by Ce(acac)₃ in BnOH using thermal activation due to the high stability in cell culture conditions. Furthermore, due to their small size (2.5 ± 0.3 nm) there are more active seeds to react with the unwanted reactive oxygen species (ROS). Regarding the cytotoxicity of CeO₂ NPs, different results were obtained when using the Vybrant MTT Cell Proliferation Assay (MTT) and the Sulforhodamine B (SRB) cytotoxicity assays. MTT, a widely used assay, showed no cytotoxicity effect with increasing concentration of NPs. In fact, an increase in cell viability was observed with respect to control cultures. No cytotoxicity or even increases in cell viability was observed by other groups using MTT assay^{12,13,39–41}. However, when cell cultures were analyzed under an inverted microscope, after MTT incubation an increase in formazan crystals formation was detected, but not an increase in cell density. Thus, CeO₂ NPs produced either an increase in the cell activity without proliferation or a direct reduction of the MTT. For this reason, the stoichiometric assay SRB was used to quantify the cytotoxicity of CeO₂ NPs. SRB results showed that there was a significant decrease in cell viability with increasing NP concentration (Figure 4).

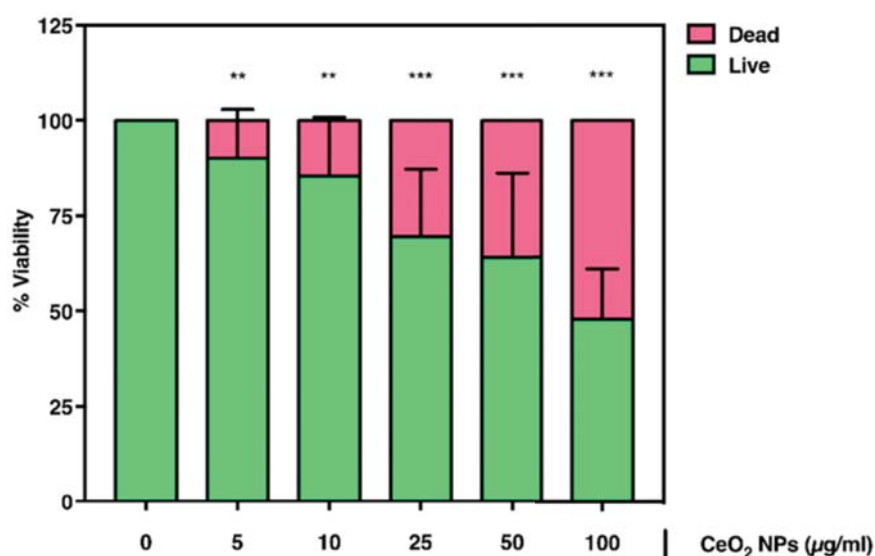


Figure 4. Percentage of viability of SKRB-3 cells after incubation in the presence of different concentrations of CeO₂ NPs. Asterisks denote significant differences compared to the control culture. (**p < 0.03 and ***p < 0.01).

Other groups, using exclusion dye assays (trypan blue or propidium iodide) instead of MTT, also reported a decrease in the viability of cells cultured in the presence of CeO₂ NPs with increasing concentration⁴². Discrepancies between the values obtained using direct and indirect methods for cell viability determination have been described before⁴³ when working with Fe-based materials or redox-active molecules⁴⁴.

The concentration of 25 µg/mL of CeO₂ NPs was chosen to test the antioxidant properties of CeO₂ NPs. According to the statistical comparison analyses of green fluorescence, once the threshold was applied the level of ROS was very low in control cells (4%), N-acetylcysteine (NAC) incubated cells (3%), or NP incubated cells (6%), but very high in cells incubated with tert-butyl hydroperoxide (TBHP) (28%). ROS levels in the presence of TBHP were lower when incubated with NAC (18%) than incubated with CeO₂ NPs (22%), but the differences found between them were not statistically significant (Figure 5).

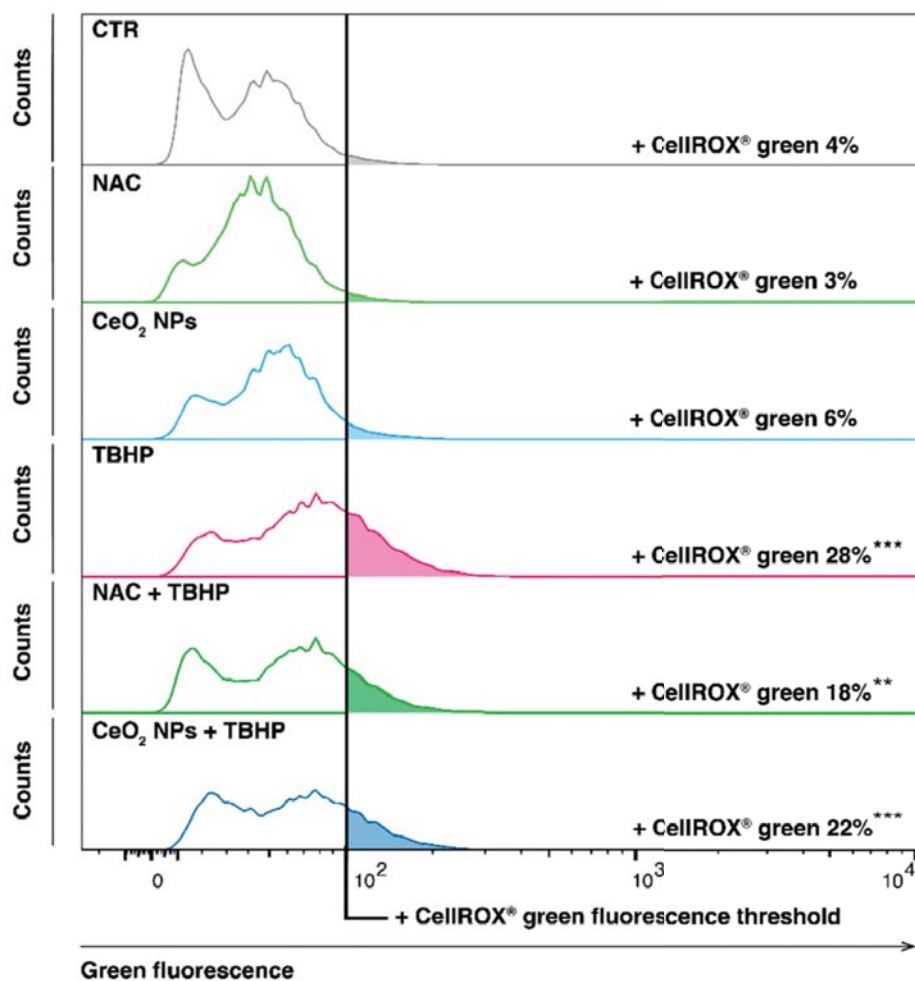


Figure 5. Detection of ROS levels in SKBR-3 cells. Data for each histogram corresponds to a concatenated population of 30000 cells from the triplicates of each condition. A threshold corresponding to the basal level of ROS in control cells was set at 10^2 (arbitrary units) of CellIROX green fluorescence. Percentages stated in each histogram correspond to the population that exceeds the established fluorescence threshold and are computed considering the single-cell population for each condition. X-axis in logicle scale. Y-axis in linear scale, ranging from 0 to 1000 green fluorescence signal arbitrary units for each histogram (** $p < 0.03$ and *** $p < 0.01$).

We first quantified the basal ROS of SKBR-3 cells, because elevated rates of ROS have been observed in almost all cancer cell lines⁴⁵. Then, we compared the effect of the commercial antioxidant NAC with the synthesized CeO₂ NPs. When the obtained values were normalized to the control value, NAC lowered the basal ROS level by 0.8 times, while the CeO₂ NPs increased it by 1.7 times compared to the basal ROS (Figure 5), though these differences were not statistically significant. However, increments of ROS in the presence of ceria NPs have also been reported by other groups using lung adenocarcinoma cells⁴³ or normal lung epithelial cells.¹⁶ Cells incubated with TBHP to induce oxidative stress presented 7.8 times ROS compared to the basal level. When cells were incubated with NAC

or CeO₂ NPs, the induced-ROS level decreased 0.8 times (34%) in the presence of NAC or 0.7 (23%) times in the presence of CeO₂ NPs (Figure 6), but these differences were not statistically significant.

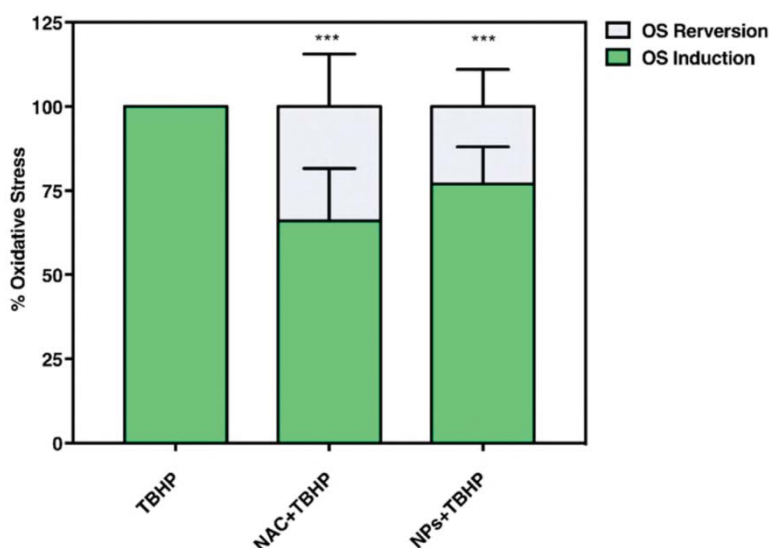


Figure 6. ROS reversion. Effect of NAC and NPs on the ROS reversion produced by TBHP (p < 0.01).**

Thus, in terms of oxidative stress reversion NAC and NPs are equally effective. Our results agree with those obtained in a previous study⁴⁰, which compared the antioxidant properties of two sizes, namely, 7 and 94 nm, of ceria NPs and found that the smaller NPs were able to reverse the induced ROS by ~20% after 24 h of incubation. However, 94 nm NPs were more effective than the 7 nm NPs in ROS reversion. Similar results were also reported for 5 to 25 nm large ceria NPs, showing a low reversion of basal ROS in the presence of 5 nm NPs compared to 25 nm¹². Thus, the size of CeO₂ NPs seems to play an important role for the antioxidant properties. The NPs used in this study had a mean diameter of 2.5 nm, which is smaller than the previously mentioned ceria NPs, even though they were able to partially reverse the oxidative stress produced by TBHP.

Conclusions

In the present study, the different combinations of precursors (Ce(acac)₃, Ce(OAc)₃), high boiling point solvents (TEG and BnOH), and activation (thermal and microwave) for the synthesis of CeO₂ NPs were investigated. The results presented show the importance of the decomposition step on the final size of the formed NPs, which is determined by the starting salt as described by our group. Spherical and cubic NPs were produced via thermal and microwave activation using Ce(acac)₃ (2 nm) and Ce(OAc)₃ (4 nm) as precursors in two

different high-boiling-point solvents: TEG and BnOH. Shape, size, structure, and phase of CeO₂ NPs were thoroughly studied by XRD, TEM, and XPS techniques. The relationship between the chemical nature of the different precursors and the final shape and size of the NPs has been demonstrated. Furthermore, a simple synthesis strategy for bioapplication of CeO₂ NPs was developed and the efficiency of the obtained NPs as antioxidants proved. The nanoceria NPs synthesized by Ce(acac)₃ in BnOH were able to decrease 23% the ROS induced level in human tumor cells demonstrating a similar efficiency than the commercial products.

Experimental procedures

CeO₂ NPs.

Cerium(III) nitrate (Ce(NO₃)₃ · 6H₂O) (Ce-(NO₃)₃) (Aldrich), cerium(III) acetylacetonate hydrate (Ce(C₅H₇O₂)₃ · xH₂O) (Ce(acac)₃) (Aldrich), cerium(III) acetate hydrate (Ce(CH₃CO₂)₃ · xH₂O) (Ce(OAc)₃) (Aldrich), triethylene glycol (HO(CH₂CH₂O)₂CH₂CH₂OH) (TEG) (Aldrich, 99%), benzyl alcohol (C₆H₅CH₂OH) (BnOH) (Aldrich 99%), ethanol (CH₃CH₂OH) (Panreac, 96%, absolute), and diethyl ether (CH₃CH₂)₂O) (Panreac 96%) were used as purchased without further purification.

Cell Cultures.

The human tumor mammary epithelial cell line SKBR-3 was used (ATCC) to conduct the biological studies. Cells were cultured in McCoy's 5A modified medium (Gibco) supplemented with 10% fetal bovine serum (Gibco) and maintained at 37 °C in a humidified atmosphere of 5% CO₂ (standard cell culture conditions).

Synthesis of CeO₂ NPs.

The decomposition of metal-organic was obtained by using thermal or microwave activation²⁶. Two different types of high boiling point solvents were used (TEG and BnOH³⁰).

*Thermal Process (T)*²⁷. Ce(acac)₃, Ce(OAc)₃, or Ce(NO₃)₃ (2.25 mM) was suspended in TEG²⁷ or BnOH (25 mL) using an ultrasonic bath. The mixture was deposited into a round bottomed flask equipped with a condenser, a magnetic stirrer, a thermograph, and a heater. The system was heated at 220 °C (1 K/min) for BnOH and at 280 °C (1 K/min) when TEG was used as a solvent. After 2.5 h the mixture was cooled and stirred for 48 h at room temperature.

For the final precipitation product, the viscosity of the media was lowered by washing the NPs (with ethanol, acetone, or diethyl ether) using centrifugation, which additionally removes remaining solvents. Then, the nanocrystals were dispersed in sterile Milli-Q water (up to 90 mM) yielding a stable dispersion. *Microwave Process (MW)*.²⁷ Ce(acac)₃, Ce(OAc)₃, or Ce(NO₃)₃ (2.25 mM) was suspended in TEG or BnOH solution (25 mL) and transferred to a microwave vial. After ultrasonication, the solution was heated under magnetic stirring by microwave radiation (300 W) to 210 °C in BnOH or 220 °C in TEG. After 1 h at final temperature, the mixture was cooled under nitrogen atmosphere and stirred for 48 h at room temperature. CeO₂ nanocrystals were separated and washed thoroughly by repeated centrifugation and dispersed in sterile Milli-Q water (up to 90 mM).

NPs Characterization.

Transmission electron microscopy (TEM) and selected area diffraction (SAD) measurements were performed on a Jeol 2011 microscope to analyze the size, shape, structure, and composition of the nanocrystalline CeO₂ NPs. High-resolution TEM (HRTEM) images were recorded on a Jeol 2017F field emission gun microscope (200 kV) with a point-to-point resolution of 0.19 nm. X-ray powder diffraction (XRPD) patterns were recorded on a Rigaku D diffractometer equipped with a rotating anode and a Cu Kα' ($\lambda = 0.154056$ nm). The chemical composition was determined by X-ray photoelectron spectroscopy (XPS) on an ESCA M-Probe (Al Kα) with an energy resolution of 0.8 eV. The charge calibration was performed by correcting C 1s peak of adventitious carbon setting to 284.8 eV to compensate the charge effect. Particle size distribution was analyzed by dynamic light scattering (DLS) measurement using Zetasizer Nano Zs (Malvern Instruments) with a maximum size range from 0.6 nm to 6 μm, minimum sample volume 12 μL, and a maximum sample concentration of 40% w/V.

Cytotoxicity Assay.

Cytotoxicity was assessed using two different methods: (a) the Vybrant MTT Cell Proliferation Assay Kit (ThermoFisher Scientific), which evaluates the cell metabolic activity by quantifying the reduction of 3-(4, 5-dimethylthiazolyl-2)-2,5-diphenyltetrazolium bromide (MTT) to formazan; (b) the Sulforhodamine B cytotoxicity assay (SRB, Canvax Biotech), a stoichiometric assay based on cell mass quantification instead of cell activity.

Cells were seeded overnight on six-well plates and then incubated with different concentration of CeO₂ NPs (5, 10, 25, 50, and 100 μg/mL) for 24 h. Afterward, MTT or SRB assay

was performed according to the manufacturer's instructions. Each experiment was performed in triplicate.

NPs Internalization.

NPs internalization was evaluated using an UV–vis spectrophotometer (Nanodrop 2000) by quantifying the absorbance at different wavelengths (210, 250, 280, and 298 nm).

Cells were seeded overnight and then incubated with CeO₂ (10 µg/mL) for 24 h. Next, cells were washed thoroughly in saline solution, detached by trypsin treatment, and resuspended in Milli-Q water. Cells were centrifuged at 1100 rpm and the supernatant containing non-internalized NPs was discarded, whereas pellet was resuspended in Milli-Q water and kept at –80 °C to break the plasma membrane. To ensure cell lysis, cells were sonicated after thaw for 5 min and the solution was centrifuged at 1100 rpm to pellet the cellular debris. The supernatant, containing the released NPs, was evaluated using the spectrophotometer. For each measure, a control culture without having been incubated with NPs was also evaluated. Each experiment was performed in triplicate.

Oxidative Stress Induction and Effect of CeO₂ NPs as Antioxidant.

Oxidative stress was assessed using the CellROX Flow Cytometry Assay kit (ThermoFisher Scientific) according to the manufacturer's instructions. The kit contains tert-butyl hydroperoxide (TBHP) an oxidative stress inductor, N-acetylcysteine (NAC) an antioxidant compound that scavenges ROS, and the reagent CellROX Green Fluorescence, which is a non-fluorescent compound in its reduced form that becomes fluorescent upon oxidation due to interaction with intracellular ROS. The effect of the antioxidant NAC was tested in the absence (control cultures) and in the presence of TBHP (200 µM) (ROS-induced cultures). After 1 h of incubation with NAC (250 mM) the solution was replaced with fresh medium to test the effect of NAC in control cells, or with TBHP to test its effect in ROS-induced cells and incubated for another hour. To assess the antioxidant properties of CeO₂ NPs, cells were previously incubated with a concentration of 25 µg/mL for 3 h. Afterward TBHP was added to induce ROS as explained before. Oxidative stress was analyzed by quantifying CellROX reagent fluorescence using a flow cytometer (FACSCanto, BD Biosciences). Per each condition and experiment 10000 events were recorded, and each experiment was performed in triplicate.

Statistical Analysis.

The Fisher's exact test was used for cytotoxicity evaluation results comparisons. To differentiate the effect of induction and/or reversion of ROS, a threshold corresponding to the basal level of ROS in control cells was set to 10^2 (arbitrary units) of CellROX green fluorescence. Values above this threshold were considered as positive for ROS and were compared using the Fisher's exact test to the control cultures. The values with $p < 0.05$ were considered statistically significant.

Associated content

Supporting information

The Supporting Information is available free of charge on the ACS Publications website at DOI: 10.1021/acs.bioconjchem.8b00300.

Supplementary data regarding gas chromatography–mass spectroscopy (GC-MS) analysis, as well as results obtained by the use of Ce(acac)₃

Acknowledgments

The authors thank the funding of the European Union's Seventh Framework Program (FP7/2007-2013 under the Grant Agreement number 280432) EUROTAPES and the Spanish Government "MINECO2 (MAT2011-28874-C02, MAT2017-86357-C3-3-R, CSD 2007-0041, IPT-2011-1090- 920000 and Generalitat de Catalunya (2017-SGR-503). Alena Folger, Joohym Lim, and in particular Torsten Schwarz and Eduardo Solano are also recognized for his contribution to the writing of this manuscript. The authors wish to thank the Scientific-Technical Services of SCAC and LLEB at the UAB, the Scientific-Technical Services at ICMAB and SHOOK Studio for the graphical abstract.

Notes

The authors declare no competing financial interest

References

1. Masalov, A. *et al.* Formation of luminescent centers in CeO₂ nanocrystals. *J. Lumin.* **145**, 61–64 (2014).
2. Coey, M., Ackland, K., Venkatesan, M. & Sen, S. Collective magnetic response of CeO₂ nanoparticles. *Nat. Phys.* **12**, 694–699 (2016).
3. Skorodumova, N. V. *et al.* Electronic, bonding, and optical properties of CeO₂ and Ce₂O₃ from first principles. *Phys. Rev. B - Condens. Matter Mater. Phys.* **64**, 1151081–1151089 (2001).
4. Xu, C. & Qu, X. Cerium oxide nanoparticle: a remarkably versatile rare earth nanomaterial for biological applications. *NPG Asia Mater.* **6**, e90–e90 (2014).
5. Nanoparticles, B., Bouzigues, C., Gacoin, T. & Alexandrou, A. Biological Applications of Rare-Earth. 8488–8505 (2011).
6. Harthøj, A., Holt, T. & Møller, P. Oxidation behaviour and electrical properties of cobalt/cerium oxide composite coatings for solid oxide fuel cell interconnects. *J. Power Sources* **281**, 227–237 (2015).
7. Walkey, C. *et al.* Catalytic properties and biomedical applications of cerium oxide nanoparticles. *Environ. Sci. Nano* **2**, 33–53 (2015).
8. Corma, A., Atienzar, P., García, H. & Chane-Ching, J. Y. Hierarchically mesostructured doped CeO₂ with potential for solar-cell use. *Nat. Mater.* **3**, 394–397 (2004).
9. Haneda, M., Kaneko, T., Kamiuchi, N. & Ozawa, M. Improved three-way catalytic activity of bimetallic Ir-Rh catalysts supported on CeO₂-ZrO₂. *Catal. Sci. Technol.* **5**, 1792–1800 (2015).
10. Zhang, Z. & Baerns, M. Hydrogen formation by steam-reforming and water-gas shift reaction in the oxidative methane coupling reaction over calcium oxide-cerium dioxide catalysts. *Appl. Catal.* **5**, 299–310 (1991).
11. Celardo, I., Pedersen, J. Z., Traversa, E. & Ghibelli, L. Pharmacological potential of cerium oxide nanoparticles. *Nanoscale* **3**, 1411–1420 (2011).
12. Lyu, G. M. *et al.* Hydrophilic CeO₂ nanocubes protect pancreatic β -cell line INS-1 from H₂O₂-induced oxidative stress. *Nanoscale* **8**, 7923–7932 (2016).
13. Vassie, J. A., Whitelock, J. M. & Lord, M. S. Endocytosis of cerium oxide nanoparticles and modulation of reactive oxygen species in human ovarian and colon cancer cells. *Acta Biomater.* **50**, 127–141 (2017).
14. Zhao, H. *et al.* Polydopamine nanoparticles for the treatment of acute inflammation-induced injury. *Nanoscale* **10**, 6981–6991 (2018).
15. Fu, P. P., Xia, Q., Hwang, H.-M., Ray, P. C. & Yu, H. Mechanisms of nanotoxicity: Generation of reactive oxygen species. *J. Food Drug Anal.* **22**, 64–75 (2014).
16. Park, E.-J., Choi, J., Park, Y.-K. & Park, K. Oxidative stress induced by cerium oxide nanoparticles in cultured BEAS-2B cells. *Toxicology* **245**, 90–100 (2008).
17. Yu, S.-H., Cölfen, H. & Fischer, A. High quality CeO₂ nanocrystals stabilized by a double hydrophilic block copolymer. *Colloids Surfaces A Physicochem. Eng. Asp.* **243**, 49–52 (2004).
18. Gu, H. & Soucek, M. D. Preparation and Characterization of Monodisperse Cerium Oxide Nanoparticles in Hydrocarbon Solvents. *Chem. Mater.* **19**, 1103–1110 (2007).
19. Sreeremya, T. S., Thulasi, K. M., Krishnan, A. & Ghosh, S. A Novel Aqueous Route To Fabricate Ultrasmall Monodisperse Lipophilic Cerium Oxide Nanoparticles. *Ind. Eng. Chem. Res.* **51**, 318–326 (2012).
20. Sathyamurthy, S., Leonard, K. J., Dabestani, R. T. & Paranthaman, M. P. Reverse micellar

synthesis of cerium oxide nanoparticles. *Nanotechnology* **16**, 1960–1964 (2005).

21. Miyazaki, H. *et al.* Synthesis of CeO₂ nanoparticles by rapid thermal decomposition using microwave heating. *Adv. Appl. Ceram.* **109**, 123–127 (2010).
22. Schulz, H., Stark, W. J., Maciejewski, M., Pratsinis, S. E. & Baiker, A. Flame-made nanocrystalline ceria/zirconia doped with alumina or silica: structural properties and enhanced oxygen exchange capacity. *J. Mater. Chem.* **13**, 2979 (2003).
23. Hirst, S. M. *et al.* Anti-inflammatory Properties of Cerium Oxide Nanoparticles. *Small* **5**, 2848–2856 (2009).
24. Karakoti, A. S. *et al.* PEGylated Nanoceria as Radical Scavenger with Tunable Redox Chemistry. *J. Am. Chem. Soc.* **131**, 14144–14145 (2009).
25. Li, M., Shi, P., Xu, C., Ren, J. & Qu, X. Cerium oxide caged metal chelator: anti-aggregation and anti-oxidation integrated H₂O₂-responsive controlled drug release for potential Alzheimer's disease treatment. *Chem. Sci.* **4**, 2536 (2013).
26. Solano, E. *et al.* Facile and efficient one-pot solvothermal and microwave-assisted synthesis of stable colloidal solutions of MFe₂O₄ spinel magnetic nanoparticles. *J. Nanoparticle Res.* **14**, 1034 (2012).
27. Garzón-Manjón, A. *et al.* Induced shape controllability by tailored precursor design in thermal and microwave-assisted synthesis of Fe_3O_4 nanoparticles. *J. Nanoparticle Res.* **17**, 291 (2015).
28. Cayado, P. *et al.* Epitaxial YBa₂Cu₃O_{7-x} nanocomposite thin films from colloidal solutions. *Supercond. Sci. Technol.* **28**, 124007 (2015).
29. Obradors, X. & Puig, T. Coated conductors for power applications: materials challenges. *Supercond. Sci. Technol.* **27**, 044003 (2014).
30. Niederberger, M. Aqueous and Nonaqueous Sol-Gel Chemistry. in *Metal Oxide Nanoparticles in Organic Solvents* 7–18 (2009). doi:10.1007/978-1-84882-671-7_2.
31. Duan, F., Kwek, D. & Crivoi, A. Viscosity affected by nanoparticle aggregation in Al₂O₃-water nanofluids. *Nanoscale Res. Lett.* **6**, 248 (2011).
32. Solano, E. *et al.* Neutron and X-ray diffraction study of ferrite nanocrystals obtained by microwave-assisted growth. A structural comparison with the thermal synthetic route. *J. Appl. Crystallogr.* **47**, 414–420 (2014).
33. Babitha, K. K., Sreedevi, A., Priyanka, K. P., Sabu, B. & Varguese, T. Structural characterization and optical studies of CeO₂ nanoparticles synthesized by chemical precipitation. *Indian. J. Appl. Phys.* 596–603 (2015).
34. Channei, D., Inceesungvorn, B., Wetchakun, N. & Phanichphant, S. Kinetics Study of Photocatalytic Activity of Flame-Made Unloaded and Fe-Loaded CeO₂ Nanoparticles. *Int. J. Photoenergy* **2013**, 1–9 (2013).
35. Mazzolini, J. *et al.* Protein Corona Modulates Uptake and Toxicity of Nanoceria via Clathrin-Mediated Endocytosis. *Biol. Bull.* **231**, 40–60 (2016).
36. Reyes-Acosta, M. A. *et al.* Thermal, mechanical and UV-shielding properties of poly(methyl methacrylate)/cerium dioxide hybrid systems obtained by melt compounding. *Polymers (Basel)*. **7**, 1638–1659 (2015).
37. Pulido-Reyes, G. *et al.* Untangling the biological effects of cerium oxide nanoparticles: the role of surface valence states. *Sci. Rep.* **5**, 15613 (2015).
38. Inerbaev, T. M. *et al.* Aqueous medium induced optical transitions in cerium oxide nanoparticles. *Phys. Chem. Chem. Phys.* **17**, 6217–6221 (2015).
39. Zholobak, N. M. *et al.* Direct monitoring of the interaction between ROS and cerium dioxide nanoparticles in living cells. *RSC Advances* vol. 4 (2014).

40. Bhushan, B., Nandhagopal, S., Rajesh Kannan, R. & Gopinath, P. Biomimetic nanomaterials: Development of protein coated nanoceria as a potential antioxidative nano-agent for the effective scavenging of reactive oxygen species in vitro and in zebrafish model. *Colloids Surfaces B Biointerfaces* **146**, 375–386 (2016).
41. Zhang, X. *et al.* Surfactant modification of aggregation-induced emission material as biocompatible nanoparticles: Facile preparation and cell imaging. *Nanoscale* **5**, 147–150 (2013).
42. Mittal, S. & Pandey, A. K. Cerium Oxide Nanoparticles Induced Toxicity in Human Lung Cells: Role of ROS Mediated DNA Damage and Apoptosis. *Biomed Res. Int.* **2014**, 1–14 (2014).
43. Chan, G. K. Y., Kleinheinz, T. L., Peterson, D. & Moffat, J. G. A Simple High-Content Cell Cycle Assay Reveals Frequent Discrepancies between Cell Number and ATP and MTS Proliferation Assays. *PLoS One* **8**, (2013).
44. Moravej, M., Purnama, A., Fiset, M., Couet, J. & Mantovani, D. Electroformed pure iron as a new biomaterial for degradable stents: In vitro degradation and preliminary cell viability studies☆. *Acta Biomater.* **6**, 1843–1851 (2010).
45. Liou, G.-Y. & Storz, P. Reactive oxygen species in cancer. *Free Radic. Res.* **44**, 479–496 (2010).

Supporting information

Table S1. GC-MS of mother solution after the CeO₂NPs synthesis by Ce(acac)₃ in TEG.

Peak	Ret. time (min)	Width (min)	Area (arb.u)	Start time (min)	End time (min)	% Area
Ethanol	1.313	0.058	86789644	1.144	1.432	1.686
Ethyl Acetate	1.817	0.085	403383692	1.742	1.982	7.837
2-(2-methoxyethoxy)	7.976	0.277	187980979	7.549	8.173	3.652
2-(2-Hydroxyethoxy) ethyl acetate	10.206	0.055	8109104	10.172	10.350	0.158
Triethylene glycol	13.611	1.319	4046528098	11.872	14.150	78.621
2-[2-[2-(2-Hydroxyethoxy) ethoxyl] ethyl acetate	14.402	0.137	414098546	14.242	14.988	8.046
Tetraethylene glycol	15.954	0.027	23788877	15.916	16.048	0.462

Results obtained by the use of Ce(acac)₃ precursor show that the precursor reacted with the solvent to form different TEG polymerization subproducts.

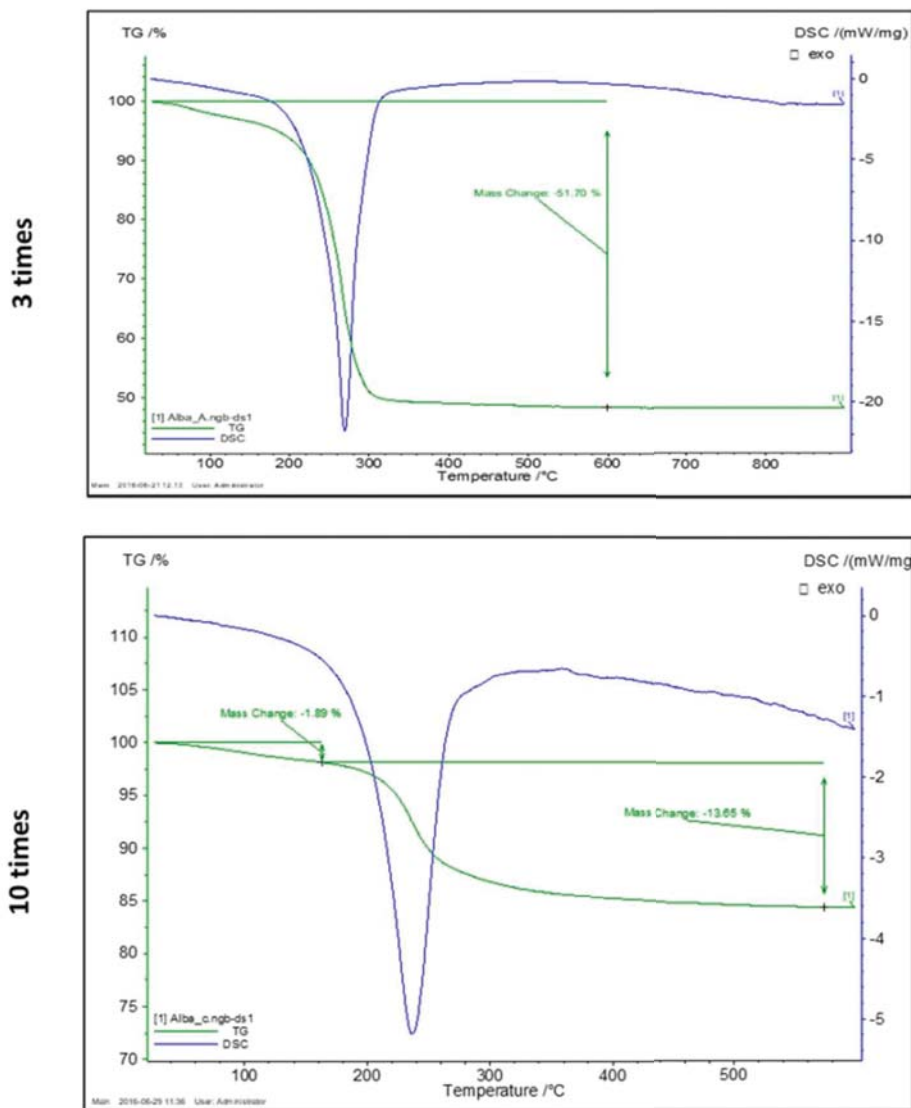


Figure S1. Thermogravimetric analysis of the CeO₂/TEG NP.

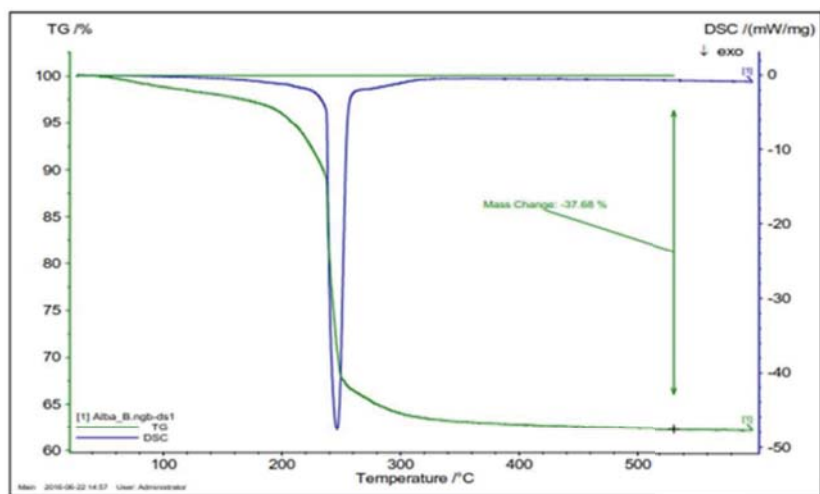


Figure S2. Thermogravimetric analysis of the CeO₂/BnOH NPs.

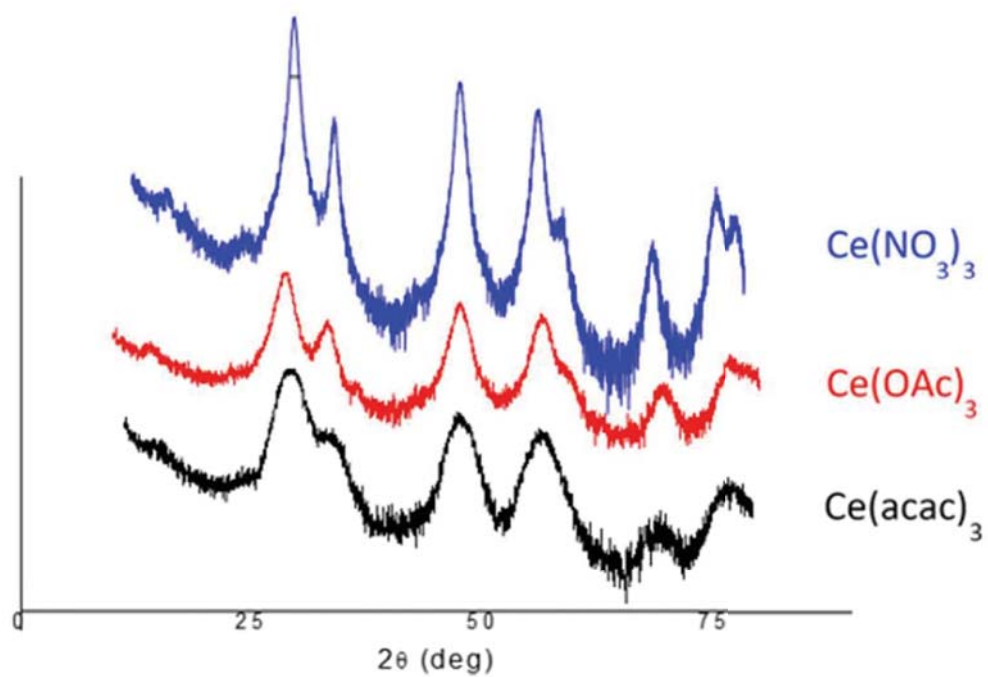
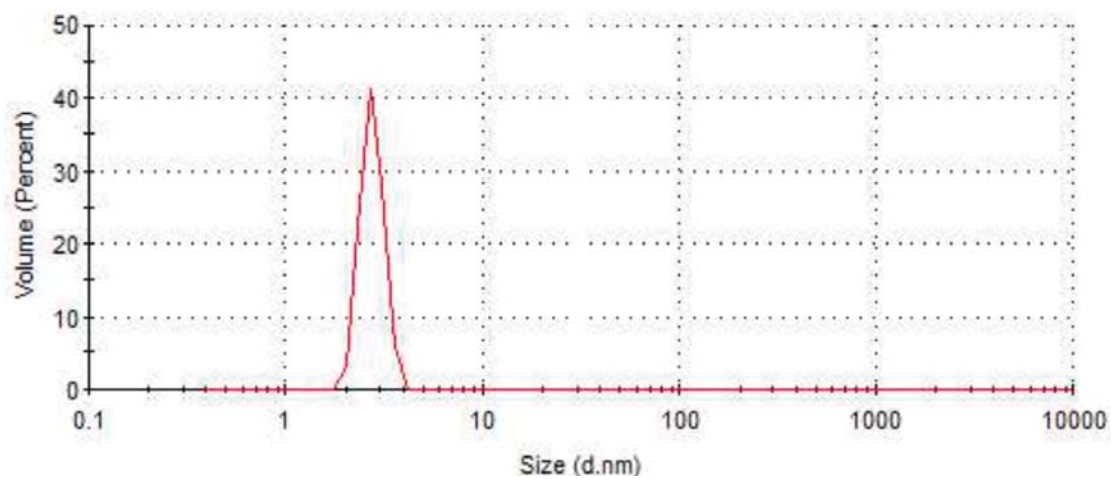
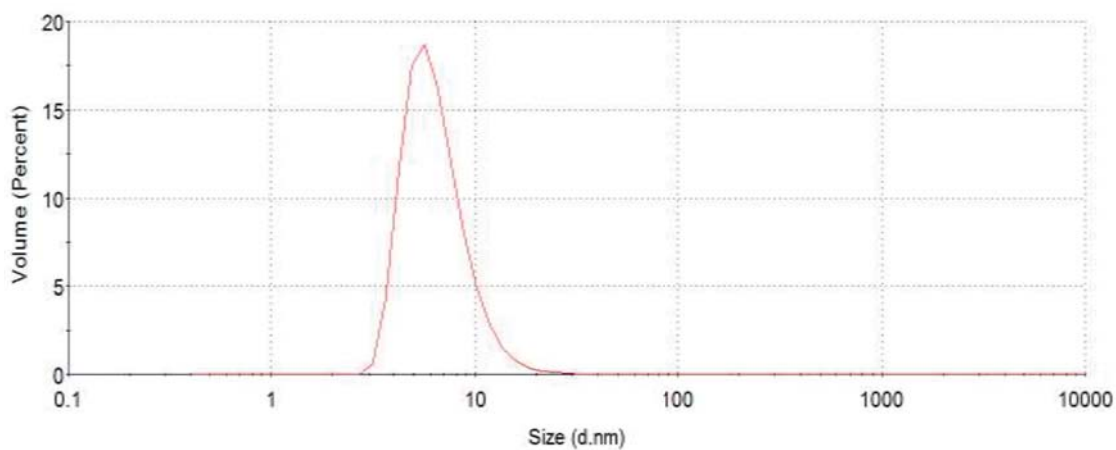


Figure S3. XRD analysis of the CeO₂NPs obtained from the three precursors.

NPs by $\text{Ce}(\text{acac})_3$



NPs by $\text{Ce}(\text{OAc})_3$



NPs by $\text{Ce}(\text{NO}_3)_3$

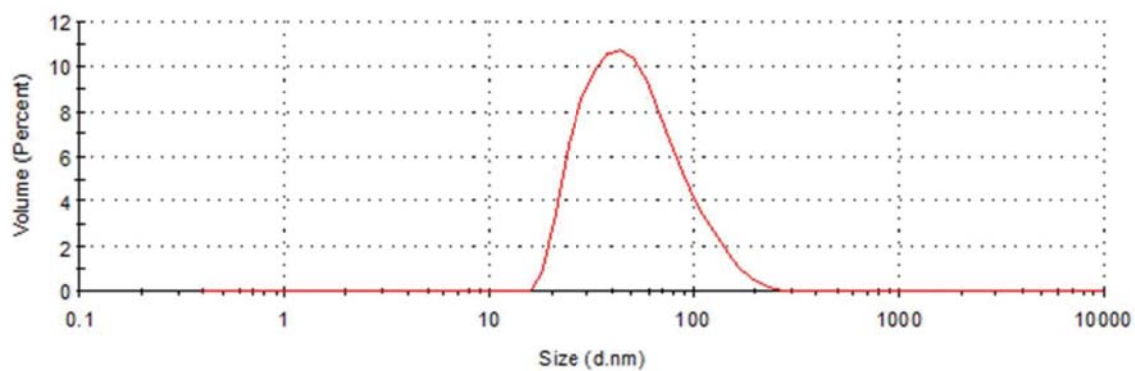


Figure S4. DLS of CeO_2 NPs obtained from $\text{Ce}(\text{acac})_3$, $\text{Ce}(\text{OAc})_3$ and $\text{Ce}(\text{NO}_3)_3$ after 1 month dispersed in polar solvents.

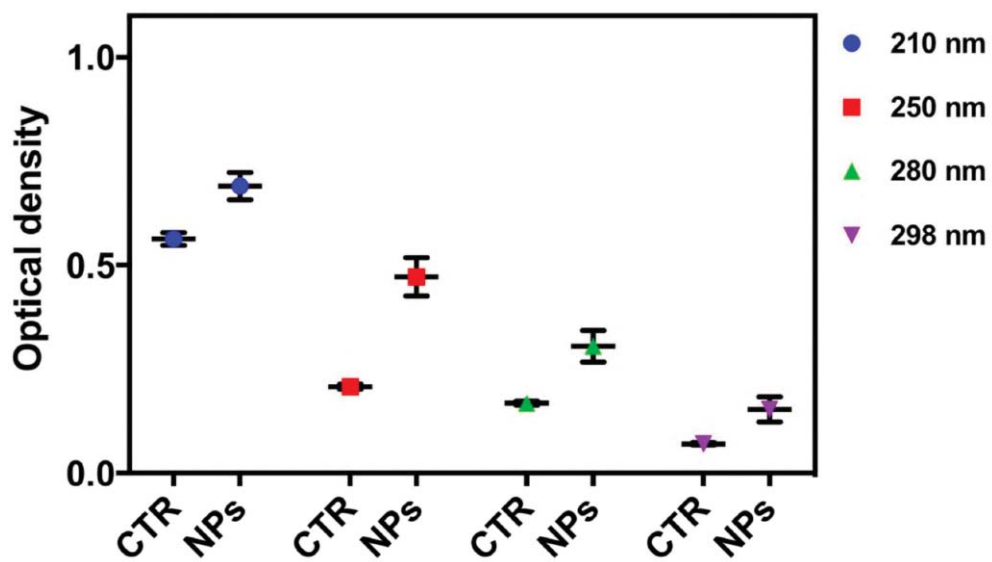


Figure S5. Absorbance of internalized CeO₂ NPs in SKBR-3 cells after cell lysis. Optical density was measured at different wavelengths. In all wavelength tested, absorbance was higher in culture cells containing NPs (NPs) than in control ones (CTR).

3.2 Chapter 2: Seeing is believing: robust characterisation of nanomaterial-cell interactions

Seeing is believing: robust characterisation of nanomaterial-cell interactions.

A. Aranda-Ramos^a, C. J. Moore^b, V. Gubala^c, and C. Nogués^{a*}

Affiliations:

^a Departament Biologia Cel·lular, Fisiologia i Immunologia. Unitat Biologia Cel·lular. Facultat Biociències. Campus de la UAB, 08193, Bellaterra (Cerdanyola del Vallès) Barcelona, Spain.

^b Istituto Italiano Tecnologia, 30 Via Morego, 16163 Genoa, Italy.

^c Medway School of Pharmacy, University of Kent, Chatham Maritime, Kent ME4 4TB, United Kingdom.

* Corresponding author carne.nogues@uab.cat

Introduction

There has been a plethora of publications over the past two decades describing new nanomaterials with exciting functionalities for biological applications. Such is the extent with which new materials are reported in the literature, we are now faced with a 'nano-Particle Zoo'¹. This 'Zoo' contains such a broad range of engineered materials they can be categorised based on different criteria, for example: by their composition (gold, carbon, silica, polymers, liposomes, iron oxide, etc.); their architectural design (spheres, rods, plates, bubbles, disks, stars etc.) or in terms of their physicochemical characteristics (positive/negative charge, plasmonics, fluorescence, magnetic properties). This 'nano-Particle Zoo' now contains such a variety of particles that they are almost difficult to keep track of. Considering the frequency at which scientists claim nanotechnology will revolutionise healthcare, we are yet to realise the potential benefits predicted by the assortment of engineered nanomaterials (ENMs) reported. In fact, at the time of writing, the number of nanomaterials approved as nanomedicines for human use by the United States' Federal Drug Administration is approximately 250² (either on the market or in clinical trial phase), yet 245,907 hits appear when searching for full texts on National Institutes of Health's Pubmed database only.

This situation suggests the scientific community needs to reconsider and improve the current approaches used to assess interactions between ENM and biological systems. A bottom-up strategy is needed, which means revising how researchers first elucidate cellular association, uptake and cytotoxicity of ENMs *in vitro*. These essential analyses must therefore be performed robustly to allow scientists to confidently claim their material is, for instance, non-toxic when internalised in a cell. Without appropriate ENM-cell characterisation *in vitro*, researchers may progress too promptly to *in vivo* analyses and find themselves in the situation where the materials they claim to be 'exciting' are in fact underperforming for unknown reasons, which could have been ruled out previously. This will also contribute to a more sustainable research and development processes by lowering the resources, economic and environmental impact and reducing the number of animals used for research.

However, performing robust *in vitro* analysis does not need to reinvent the wheel. It should involve using established characterisation techniques that complement each other to provide an accurate examination of ENM-cell interactions. We believe that 'seeing is believing' is an important facet of this interrogation method, that is, if there is a method to visualise

nanomaterial-cell interactions, then we recommend doing it. For example, scanning electron microscopy (SEM) can be used to investigate the state of nanomaterial aggregation as they interact with the cell membrane. Material scientists often presume that because their ENM is nanosized upon synthesis it remains that way. It has been widely reported that nanomaterial size is a key parameter in cytotoxicity² and internalisation pathways³ of nanoparticles (NPs). SEM allows to visualise the size of nanomaterials as they interact with the cell surface. This can lead researchers to critically assess if their nanomaterial is stable in the presence of salts or if the nanomaterial has been appropriately handled to ensure maximal dispersion in solution. SEM can also be used as a qualitative method of studying nanomaterial internalisation. This information can be used to supplement the information that flow cytometry analysis could provide of cellular association and internalisation of nanomaterials. Using a similar approach, it is also important to use more than one method for evaluating cell viability. The Methylthiazolyldiphenyl-tetrazolium-bromide (MTT) assay is the most common method for elucidating nanomaterial toxicity in literature, but it has been shown to have its drawbacks such as the direct reduction of the MTT reagent depending on ENM composition or the inability to discern between an increase in the cell viability or an increase in the metabolic cell activity resulting on the increased product obtained⁴. It is therefore important to use a second method to analyse cell viability to verify the results of this commonly used assay.

Here we demonstrate a robust *in vitro* analysis of the cytotoxicity and internalisation of fluorescent microporous silica nanoparticles (SiNPs) incubated in HeLa and Caco-2 cell cultures. Several commonly used characterisation tools have been used to assess SiNPs interactions with these cells: from the ones that focus on visual and volumetric analyses at the nanoscale of single cell populations like SEM and confocal laser scanning microscopy (CLSM), to the ones that can be used as high-throughput methods for quantification of whole cell populations like flow cytometry, the MTT assay and LIVE/DEAD® Viability Assay. These studies, conducted in a specific order, can serve as a guide for scientists on how to better analyse their ENMs in early *in vitro* studies and provide new insights into the biological interrogation of ENMs. Each analysis gives accurate information on the status of the ENMs at a specific experimental point and allows to decide whether the ENMs behave as expected and thus the study can continue or if the ENMs are not suitable for their use, and thus, they must be discarded. We also highlight some pitfalls of how ENMs can behave undesirably in biological conditions and how they can be explored and avoided through

the imaging and complementary techniques proposed for the examination of the NP-cell biointeraction which allow accurate data interpretation.

Materials and methods

SiNPs characterisation and handling

Nanoparticles of SiO₂ (SiNPs) were supplied by Dr. Gubala from the University of Kent. SiNPs were around 120 nm in diameter with an electrical charge of -25/-20 mV when incubated in complete medium. Due to the FITC, loaded onto the microporous matrix of the SiNPs, they presented an absorbance peak at 488 nm and an emission peak at 525 nm, respectively.

SiNPs solutions were freshly prepared before exposure to cell cultures by centrifugation in water for 5 min at 14000 rpm twice and finally resuspended in cell culture media to fit the desired concentration. Bad handling conditions were considered when resuspension of the pellet was performed by actively micropipetting in 1 ml of complete media before its further dilution for experiment. Good handling conditions were considered when before micropipetting and preparing the incubation solutions, SiNPs pellets were exposed to an ultrasonication bath (FisherBrand) (with just enough volume inside the Eppendorf to cover the SiNPs pellet) for 3 min at room temperature (RT). Effects on bad handling or good handling of the SiNPs were analysed through SEM and CLSM.

Cell Culture maintenance.

Human Epithelial Cervical Adenocarcinoma Cells (HeLa) and Human Epithelial Colorectal Adenocarcinoma Cells (CaCo-2, ATCC®) were cultured in complete medium 1X MEM (Gibco by Life Technologies) supplemented with 10% foetal bovine serum (FBS) (Biowest) and 2 mM L-Glutamine (Life Technologies). All cell lines were maintained at 37°C and humidified atmosphere of 5% CO₂ (standard conditions).

SiNPs cytotoxicity evaluation

For cytotoxicity assays, Caco-2 and HeLa cells were seeded in 24-well plates (Thermo Scientific) at a density of 1.5×10^4 cells per well. After 24 h, cell media were replaced with a solution of 500 µl of 50 µg/mL SiNPs in complete medium. Cell cultures were washed

twice with Hanks' Balanced Salt Solution (HBSS, Biowest) after 60 min of SiNPs incubation and were kept for 0 h, 6 h, 24 h, 72 h and 7 days post-incubation time in complete MEM. For MTT (Life Technologies) assay, 1 mg/mL of stock solution in MilliQ water (Merck Millipore) was prepared and filtrated using a 0.22 μm filter (Whatman), which was kept refrigerated and preserved from direct light until use. After each post-incubation time, media was removed and 500 μl of MTT working solution (0.1 mg/mL MTT diluted in complete MEM) were added and incubated for 3.5 h until the formation of formazan crystals was observable under an inverted contrast phase microscope (Olympus IX71). Lastly, the MTT solution was removed and cultures were let to dry while stored at RT in the dark until evaluated. Before carrying out the measures of absorbance, 500 μl of Dimethylsulfoxide (DMSO, Sigma Aldrich) were added to each well. A well containing DMSO was used as a blank. The absorbance at 550 nm was read in a Victor™ X3 Multilabel Plate Reader (Perkin Elmer) and data were processed using Excel worksheets (Microsoft) and Prism 9.0 (Graphpad) software. The experiment was done in triplicate.

For LIVE/DEAD® kit cytotoxicity assay evaluation, after each post-incubation time, cells were stained directly (without washing steps to avoid losing possible dead cells in suspension) with Live/Dead Kit® for mammalian cells (Life Technologies). A volume of 0.1 μl of Calcein AM (which stains metabolically active, viable cells' cytoplasm) and 1 μl of Ethidium Homodimer 1 (which stains dying cells' nuclei) was added directly to the medium (1 mL). Incubation was carried out for 15 min in an incubator at 37°C. Finally, cell cultures were observed under an inverted fluorescence microscope (Olympus IX71) equipped with a green (488 nm) and red (550 nm) filter to observe Calcein AM and Ethidium Homodimer 1 stains, respectively. The experiment was done in triplicate.

Analysis of SiNPs-cell interactions through scanning electron microscopy. Assessment of SiNPs interaction with HeLa and Caco-2 cells was first evaluated through SEM. Cells were seeded in round glass coverslips (Knittel glass) in 4-well plates (Thermo Scientific) at a density of 1.5×10^4 cells per well. After 24 h, cell media were replaced with a solution of 500 μl of 50 $\mu\text{g}/\text{mL}$ SiNPs in complete medium. Cells were incubated with SiNPs for either 20 min, 60 min or 24 h. Afterwards, cell cultures were washed twice with a 0.1 M cacodylate buffer (TAAB) and fixed with a 2.5% glutaraldehyde (Merck) in 0.1 M cacodylate buffer solution for 45 min. Samples were then dehydrated through a series of increasingly

graded ethanol (Merck Millipore) incubations for 7 min: 50%, 70% and 90% once and 100% twice. Finally, samples were incubated for 15 min with Hexamethyldisilazane (Electron Microscopy Sciences) after which the coverslips were removed from the 4-well plate, mounted onto SEM stubs and analysed by SEM (Carl Zeiss Merlin) using a secondary electron detector.

Internalisation of SiNPs by flow cytometry

The internalisation of SiNPs in both cell lines was quantified through flow cytometry. Cells were first seeded onto 6-well plates at a cell density of 1.5×10^5 per well. After 24 h cells were exposed to 2.5 mL of a 100 $\mu\text{g}/\text{mL}$ SiNPs (to keep the SiNPs-cell ratio) in complete medium solution for 20 min, 60 min, 6 h and 24 h. After incubation time the solutions were removed and cell cultures were washed twice with HBSS. They were further trypsinised with 1x Trypsin-Ethylenediaminetetraacetic acid (EDTA) (Biowest) diluted in HBSS and neutralised after 5 min with complete MEM. The cellular suspensions were analysed using a FACSCalibur (Becton Dickinson) equipment and FACSDiva® Software (Becton Dickinson). At least 10^4 cells (events) were included in each analysis. Control cell cultures were used to establish the negative and positive association gates and thus to delimit the SiNPs-cell positive association area. Data obtained were processed using FACSDiva® 7.0 Software (Becton Dickinson). The experiment was done in triplicate.

Internalisation, quantification and localisation of SiNPs by CLSM

The internalisation of SiNPs in both cell lines was visualised through CLSM. First cells were seeded in 3.5 mm diameter glass bottom dishes (MatTEK) for CLSM at a cell density of 1.5×10^4 per dish. Cells were only placed on the glass coverslip located on the centre of the dish. After 24 h cells were exposed to 500 μL of a 50 $\mu\text{g}/\text{mL}$ SiNPs in complete medium solution (keeping the NPs-cell ratio) for 20 min, 60 min, 6 h and 24 h. After incubation time, incubation solutions were withdrawn, and cell cultures were washed twice with HBSS. One millilitre of complete medium was added to the samples, that were later labelled with Life Technology's Cell mask (Texas Red reagent) to visualise the limit of the cell and Hoechst 33342 (Life Technologies) to visualise the nucleus, according to manufacturer's instructions, and observed under CLSM to confirm internalisation.

For quantification and localisation experiments, cells were seeded in round glass coverslips (Knittel glass) in 4-well plates (Thermo Scientific) at a density of 1.5×10^4 cells per well. After 24 h, cell media were replaced with a solution of 500 μ l of 50 μ g/mL SiNPs in complete medium for 1 or 3 h. To localise SiNPs inside the cells an immunofluorescence staining was performed after incubation time. Cell cultures were washed twice with PBS, fixed with 4% paraformaldehyde in PBS for 15 min and permeabilised with 0.1 % Triton X-100 in PBS for 15 min at RT. Later, cell cultures were blocked with 5% PBS-bovine serum albumin (BSA) (Sigma-Aldrich) for 40 min at RT. After blocking, cell cultures were incubated for 1 h at RT with mouse anti-LAMP-1 polyclonal antibody (1:500 in PBS/BSA 5%; BD Biosciences 611043) or with mouse anti-EEA-1 monoclonal antibody (BD Biosciences 610457). Samples were sealed using parafilm (avoiding bubble formation) and kept at 4°C overnight in a humid chamber. Next day, samples were washed 3x with PBS, incubated for 1 h at RT with goat anti-mouse IgG antibody 647 (1:500; Life Technologies) while sealed with parafilm (avoiding bubble formation). Finally, cell cultures were washed twice with PBS before being labelled with 2 drops of ActinRed™ 555 (ReadyProbes™) Reagent (Rhodamine phalloidin) to reveal the actin cytoskeleton of the cell and 0.5 μ L of Hoechst 33342 (Life Technologies) to visualise nuclei, according to manufacturers' instructions. Samples were finally mounted in Prolong Glass® antifade mounting media and let to cure at RT according to manufacturer's instruction at least 48 h before observation. Quantification and localisation experiments were done in triplicate.

Images were captured with a confocal laser scanning microscope (Leica TCS-SP5 AOBS spectral; Leica Microsystems) using a Plan-Apochromatic 63x Oil objective (NA 1.4). Image acquisition of the cells was carried out sequentially with a 405 nm blue diode for the cell nucleus, a 488 nm Argon laser for the SiNPs, a 594 nm HeNe laser for the cytoskeleton and a 633 nm HeNe laser for LAMP-1/EEA-1 labelled compartments. Stacks of images along the z-axis were obtained for a selected area using the xyz mode of the microscope at the highest resolution level available. Pinhole was set to 1 Airy disk units. Image size was set at 3296x3296, resulting in 37,3 nm/pixel size. Z-Depth size was set at 125,9 nm. Fiji⁵ was used to obtain overlapped images including all channels (nuclei, actin cytoskeleton and SiNPs) and to visually evaluate internalisation of SiNPs within the cells datasets were observed through the 69rtogon viewer and 69rtogonal projections.

To quantify more precisely the SiNPs internalisation, as well as the co-localisation with the endolysosomal system, a post-processing deconvolution, segmentation and 3D object evaluation method was applied. Each image stack captured was processed as follows:

A The original CLSM signal (Fig 1A) was quality evaluated and Z-Projections of maximum intensities on all channels were obtained for each 3D stack corresponding to a field. Cells were manually segmented according to their cytoskeleton limits using the free hand area selections. Selections were stored as regions of interest (ROIs) and were saved for each individual cell. Image stacks were automatically processed using the 'ROI splitter' macro. (Supporting information). For every stack corresponding to one segmented cell, channels were split and saved as individual stacks per channel. The cytoskeleton signal was automatically thresholded using the MinError (I) algorithm available in Fiji and further processed using the fill holes algorithm to obtain the complete area for each slice and therefore segment the whole volume of the cell. The thresholded signal was later saved as a mask (Fig 1B) for further processing the SiNPs and endosome/lysosome compartments. This process was performed using the ROI extractor and cytoskeleton segmentation macro (Supporting information).

B SiNPs and endosome/lysosome single channel stacks were automatically deconvolved (Fig 1C) using the 'Green AUTO PSF Deconvolution' macro and 'Far red AUTO PSF Deconvolution' ImageJ macros. The deconvolution process was optimised using fast Fourier transform-based deconvolution to reconstruct the degraded signal using the CLIJ2 'Richardson-Lucy Deconvolution algorithm' by R. Haase and B. Northan⁶ and using a theoretical PSF calculated from the CLSM acquisition settings thanks to Dr. Dougherty's 'Diffraction 3D PSF' plugin on Fiji⁵.

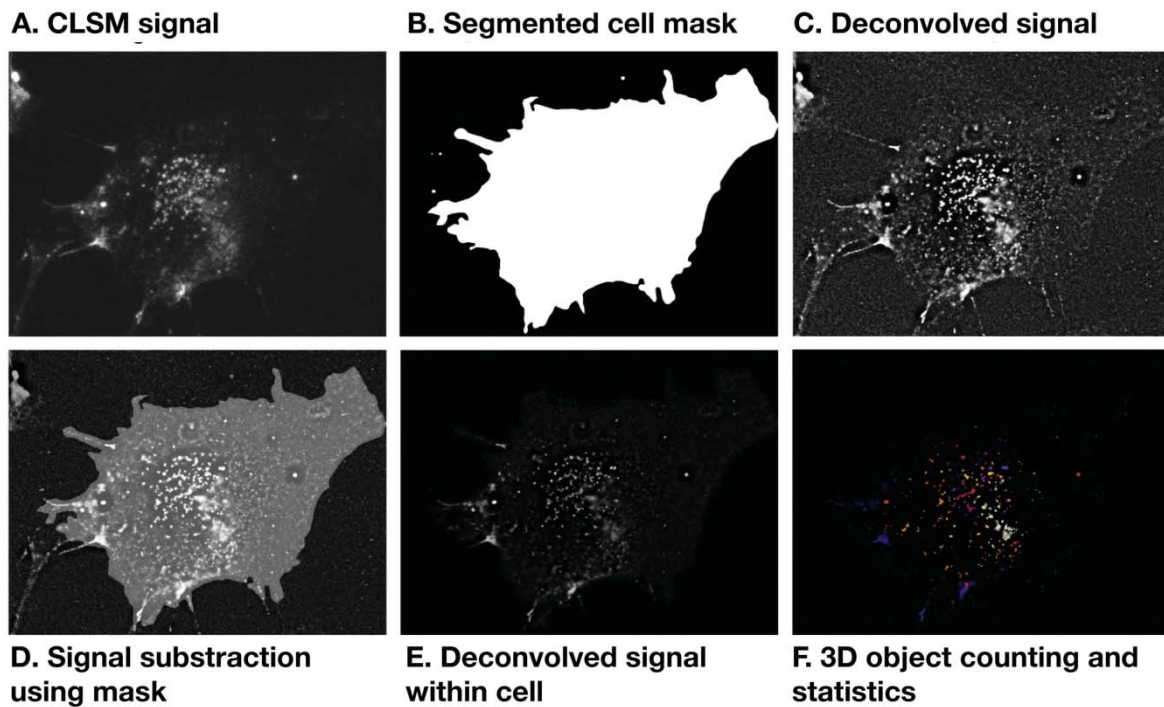


Figure 1. Representative images of the post-processing workflow for CLSM dataset quantification of a HeLa cell exposed to SiNPs for 1 h at a 50 $\mu\text{g}/\text{mL}$ concentration. A Original CLSM signal from one cell corresponding to its SiNPs' green fluorescence (488 nm). **B** Deconvolved SiNPs signal **C** Segmented cell mask computed from actin cytoskeleton staining (555 nm). **D** Superposition of the segmented cell mask with deconvolved signal to illustrate the process of image calculation for each slice in the dataset volume to keep only the signal coming from within the cell. **E** Resulting deconvolved signal from segmented cell mask's image calculation. **F** 3D Object counting output of objects detected volumetrically that have been statistically analysed.

C The resulting stacks were further analysed using the Complete_quantification.ijm macro (including 3D object detection on graphics processing unit (GPU) by CLIJ2's 3D Object Count on GPU⁶ plugin for ImageJ). SiNPs and endosome/lysosome channels were filtered through image calculation processing (Fig 1D) using the masks from the cytoskeleton obtained in Step A to retain only the signal within the cell limits (defined by the cytoskeleton staining and its masks) (Fig 1E). Image calculation was performed again to calculate the co-localisation signal between SiNPs and compartments (endosomes/lysosomes) using the 'AND' Image operator algorithm in ImageJ. For quantification of resulting deconvolved and co-localisation signals, filtering for 16-voxel-sized objects (the minimum number of voxels corresponding to a SiNPs signal according to their average size) was performed (Fig 1F). Pixels which values were between 0-25 values of intensity were also discarded from

the analysis and only pixels with intensities from 25-Maximum intensity values were considered to avoid segmentation and 3D object detection issues. Data obtained for each analysis were processed using Excel worksheets (Microsoft) and Prism 9.0 (Graphpad) software.

Statistical Analyses.

Viability proportions from MTT and LIVE/DEAD assays, flow cytometry internalisation population proportions and co-localisation experiments were analysed using the Kruskal-Wallis test for multiple comparisons using Dunn's correction. Internalisation data did not pass normality testing and therefore ranks were compared using the Mann-Whitney test.

Alpha was set at 0,05 and therefore significance levels were reported as follows: * when $p < 0.05$, ** when $p < 0.01$, *** when $p < 0.001$ and **** when $p < 0.0001$ unless stated otherwise on the figure footer.

Results and discussion

The results hereby presented are classified into essential and advanced analyses in a bottom-up strategy workflow illustrated in figure 2. Essential analyses cover the basics for NP characterisation in terms of their interaction with the biointerface: cytotoxicity, association and internalisation. Advanced analyses go one step further in the NP-cell interaction and provide nanoscaled volumetric data for quantitative internalisation and localisation of SiNPs from single-cell population data. These advanced analyses are time consuming in terms of data acquisition, but the analysis proposed in the present study have been optimised to be reliable, quantifiable and semi-automatised while providing very valuable visual and volumetric data to support the conclusions presented. In this proposal, every analysis is prioritised from top to bottom depending on the urgency and value of the data that can be extracted from each step, and their relevance to the predetermined biological questions and the new ones that may arise while exploring each step's results. Following this logic, each step is to be performed and analysed before continuing further in the workflow. If

problems arise in any of the proposed analyses it is advisable to solve them, before advancing on the exploration of more complex levels of interaction between NPs and cells in biological conditions.

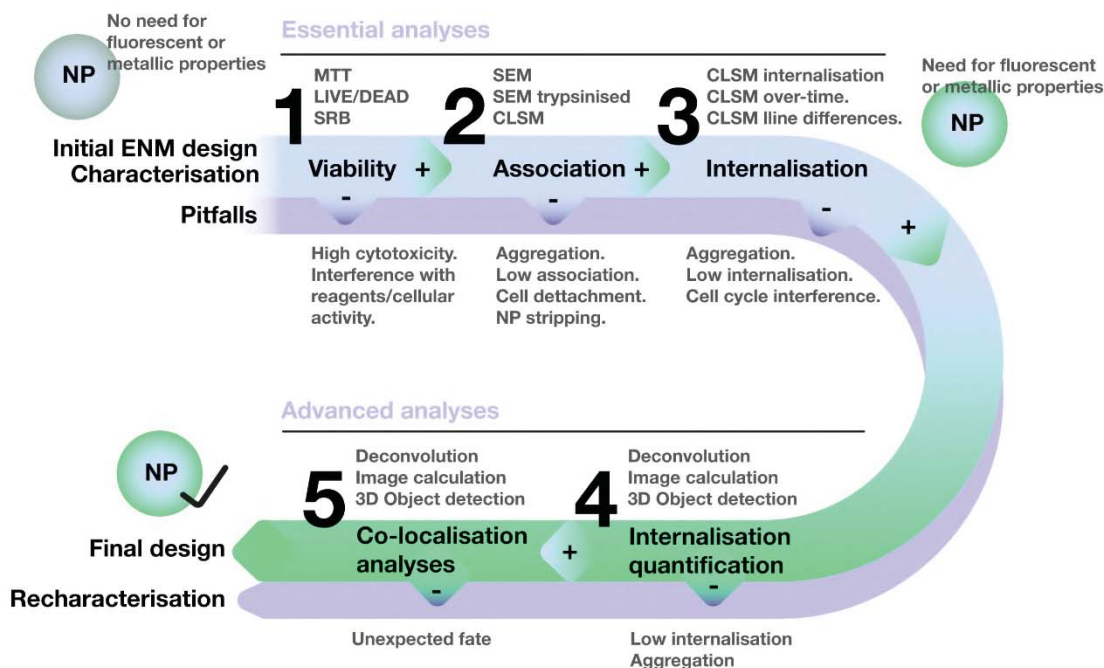


Figure 2. Workflow of analyses proposed for the investigation of ENMs at the biointerface. The workflow is proposed following the numeration in the scheme starting with **1** viability analysis by different compatible methods, then the **2** association of ENMs with cells by SEM and CLSM visualisation, followed by their **3** internalisation, its **4** quantification and finally the **5** co-localisation to determine the intracellular fate of the ENMs. Depicted along the characterisation workflow are the common pitfalls for each characterisation step, which require going back to the previous step or several steps to re-characterise the ENMs.

Essential analyses

Cell viability.

Concerning *in vitro* studies of viability, the kit or assay scientist choose to perform to investigate the interaction between ENMs and cell cultures can be crucial on the outcome of the experiments performed. Measuring the viability of cells after incubation with chemicals is a routinely made method, in material sciences and toxicology laboratories, in order to assess toxicity information of the tested ENMs⁷. The MTT assay is a test where a yellowish salt is reduced by mitochondrial dehydrogenases to water-insoluble violet MTT-formazan

crystals, which are later solubilised with solvents like DMSO and photometrically quantified at 550 nm. Untreated cells for each incubation time are used as control (100% viable) and SiNPs-exposed cultures' values are correlated with this set of data. In our case, SiNPs are stable in solution and non-reactive to media conditions and MTT reagents exposure as characterised by Dr. Moore (data not shown). Therefore, the results of assays based on a reagent being reduced or oxidised can be allegedly trusted in terms of NP-assay reactive interaction. If an ENM has a potential antioxidant or oxidative effect, for example, or it is formed of stable element compositions but without a strong bind that could be easily lost when in a polar solution, that means that this kind of ENM could potentially interfere⁸ with the results of a common MTT cell viability assay.

Regarding the obtained results (Fig 3), no statistical differences (ns; $p > 0.05$) were found between control and SiNPs-treated groups for any of the tested post-incubation times in HeLa cells after 0 h, 20 min, 60 min, 6 h, 24 h, 72 h and 7 d post-incubation times. However, statistically significant differences were found between control and SiNPs-exposed groups in Caco-2 cells after 0 h and 24 h post-incubation times, in both cases, viability was higher in SiNPs-exposed cell cultures, so accordingly, no negative effects in viability were found on SiNPs-exposed cultures in comparison to the control groups.

The differences observed in Caco-2 cells after 0 h post-incubation time, where the viability of the cell cultures exposed to SiNPs is twice of that of the control group, might be attributable to an activation of the redox metabolic activity⁹ or the endocytic uptake^{10,11} in these cell lines due to their epithelial nature and specific transcytosis activity when they sense foreign objects on their membranes. SiNPs in contact with Caco-2 cells might temporarily stimulate the cell metabolism and endocytic and transcytotic activity and therefore, cause a spike in MTT absorbance detection due to high metabolic activity right after exposure. The temporality of such effects is also something that will determine the interpretation of the results and the affectation to the cells' ability to survive. In our specific case, this increase in the activity is not related to an increase of proliferation but must be demonstrated.

Viability assays through MTT reduction reactions have been described in the past to be affected by ENMs like nanotubes¹² which interfered with the formazan crystals formed as a product of the reduction by live cells during incubation and affected their solubilisation and posterior quantification. There have also been described materials such as TiO₂ NPs¹³

interfering with the MTT assay by directly reducing the substrate and producing the formazan reporter product. Therefore, it is advisable to test the viability by at least two methods, especially if the materials tested have strong absorptions within the wavelengths used to detect the viability product of the assay used, have reductive/oxidative activity themselves or could interact with the solubility of the product used as viability reporter. Sulforhodamine B¹⁴, a stoichiometric-based assay that uses total protein levels in cell cultures has been proposed as a great quantitative alternative to tetrazolium salts reduction-based assays such as MTT, MTS ((3-(4,5-dimethylthiazol-2-yl)-5-(3-carboxymethoxyphenyl)-2-(4-sulphophenyl)-2H-tetrazolium), XTT (2,3-bis-(2-methoxy-4-nitro-5-sulphophenyl)-2H-tetrazolium-5-carboxanilide), or water soluble tetrazolium salts (WSTs).

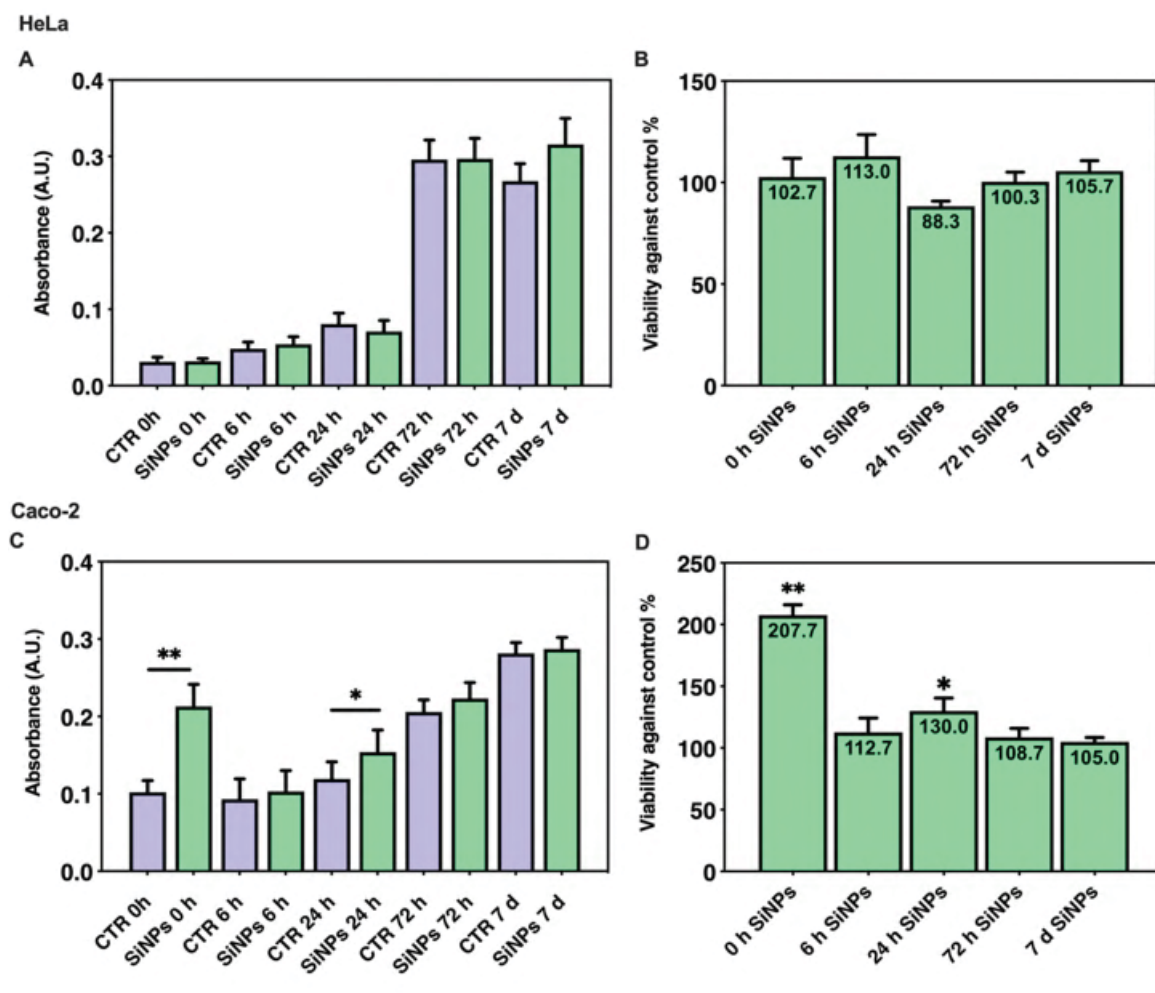


Figure 3. Post-incubation time viability A. Bars plotted depict mean values of MTT absorbance +/- standard deviation of the mean in arbitrary units per condition in HeLa cells. Plotted data shows increasing values over time as cell cultures grow in both SiNPs-treated and CTR groups, plateauing after 72 h in culture. No statistical differences were found between viability control and SiNPs-treated groups for any of the tested post-

incubation times. **B.** SiNPs-treated normalised data against control group per condition depicts the percentage of viable cells between conditions in HeLa cells. **C.** Bars plotted depict mean values of MTT absorbance +/- standard deviation of the mean in arbitrary units per condition in Caco-2 cells. Plotted data shows increasing values over time as cell cultures grow in both SiNPs-treated and CTR groups. Statistical differences found between viability control and SiNPs-treated groups for 0 h (**, $p < 0.01$) and 24 h (*, $p < 0.05$) post-incubation times. **D.** SiNPs-treated normalised data against control group per condition depicts the percentage of viable cells between conditions in Caco-2 cells. Statistically significant different values against control group are depicted with ** (when $p < 0.01$) and * (when $p < 0.05$). Control samples/group (CTR) All experiments done in triplicate.

Since the sensitivity of the metabolic assays chosen for cytotoxicity assessment has been previously described to be affected by the stressor or death inducing mechanism by the ENMs by Cortés-Ciriano et al¹⁵, the values estimated might significantly diverge, and compound cytotoxicity might be over- or underestimated. Therefore, providing complementary biological information through an alternative cytotoxicity evaluation method is likely to palliate these issues, at the expense of higher experimental cost. Accordingly, and due to the high sensitivity of MTT results to cells' metabolic state, a second viability method was performed to confirm the obtained results. Image analyses of LIVE/DEAD kit[®] stained cultures, after incubation with SiNPs and several post-treatment times (up to 7 days), revealed that no cytotoxic, neither proliferative action is attributable to SiNPs on HeLa and Caco-2 cell lines when compared to control cell cultures (Fig 4). As previously described by our group, cell status visualisation via LIVE/DEAD[®] assay or trypan blue tests to confirm the viability and possible proliferative interference of the materials tested is of vital importance to corroborate the results obtained of the MTT assay, otherwise, the conclusions obtained from MTT data could be unreliable¹⁶. The differences observed in Caco-2 cell lines 0 h post-incubation were not observed using the LIVE/DEAD[®] assay, since it's not depending on the reducing metabolic activity of the cell. LIVE/DEAD[®] assay allows to distinguish live from dead cells because only live cells can cleave, using their own esterase, the substrate provided by the kit; once cleaved the product emits green fluorescence.

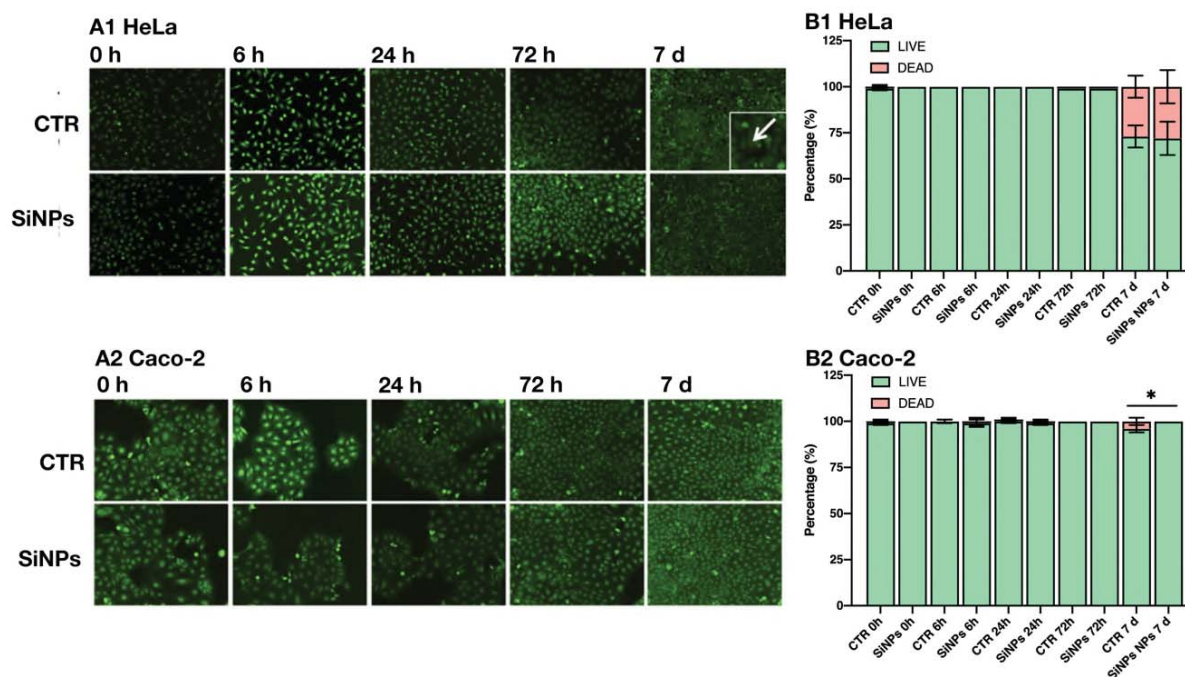


Figure 4. LIVE/DEAD® Viability/Cytotoxicity assay. A1 HeLa and **A2** Caco-2 cells from control and SiNPs-treated groups stained with calcein AM (positive=green viable cells) and Ethidium Homodimer-1 (positive=red dead cells). White arrow shows dying cells/cell remnants. **B1** and **B2** depict the proportion of live vs dead cells in stated conditions. Statistically significant different values against control group are depicted with * (for $p < 0.05$). Control samples/group (CTR). All experiments done in triplicate.

Therefore, with the complementary results from both tests, we can confirm that no negative or positive effect on viability of HeLa and Caco-2 cell cultures can be found after the exposure for 1 h of incubation to a concentration of 50 $\mu\text{g/ml}$ SiNPs in cell media up to 7 days post-treatment. We also want to highlight the importance of visualisation of ENMs-exposed cell cultures to assess the reliability of the obtained viability results depending on the reduction of products such as MTT, MTS, XTT or WSTS, due to the possible interferences of the materials used with such tests.

Viability differences found after 7 days post-incubation are mainly observed in high confluent cell cultures and attributable to nutrient competition and growth area limitations after long time in culture without reducing population size by splitting.

SiNPs-cell association.

SEM analyses of the cell surface at each incubation time revealed the contact and internalisation kinetics of the interaction of SiNPs with HeLa and Caco-2 cell cultures. SiNPs were

abundantly attached to cell plasma membranes at early incubation times (20 and 60 min) but almost none was observed attached after 24 h of incubation (Fig 5).

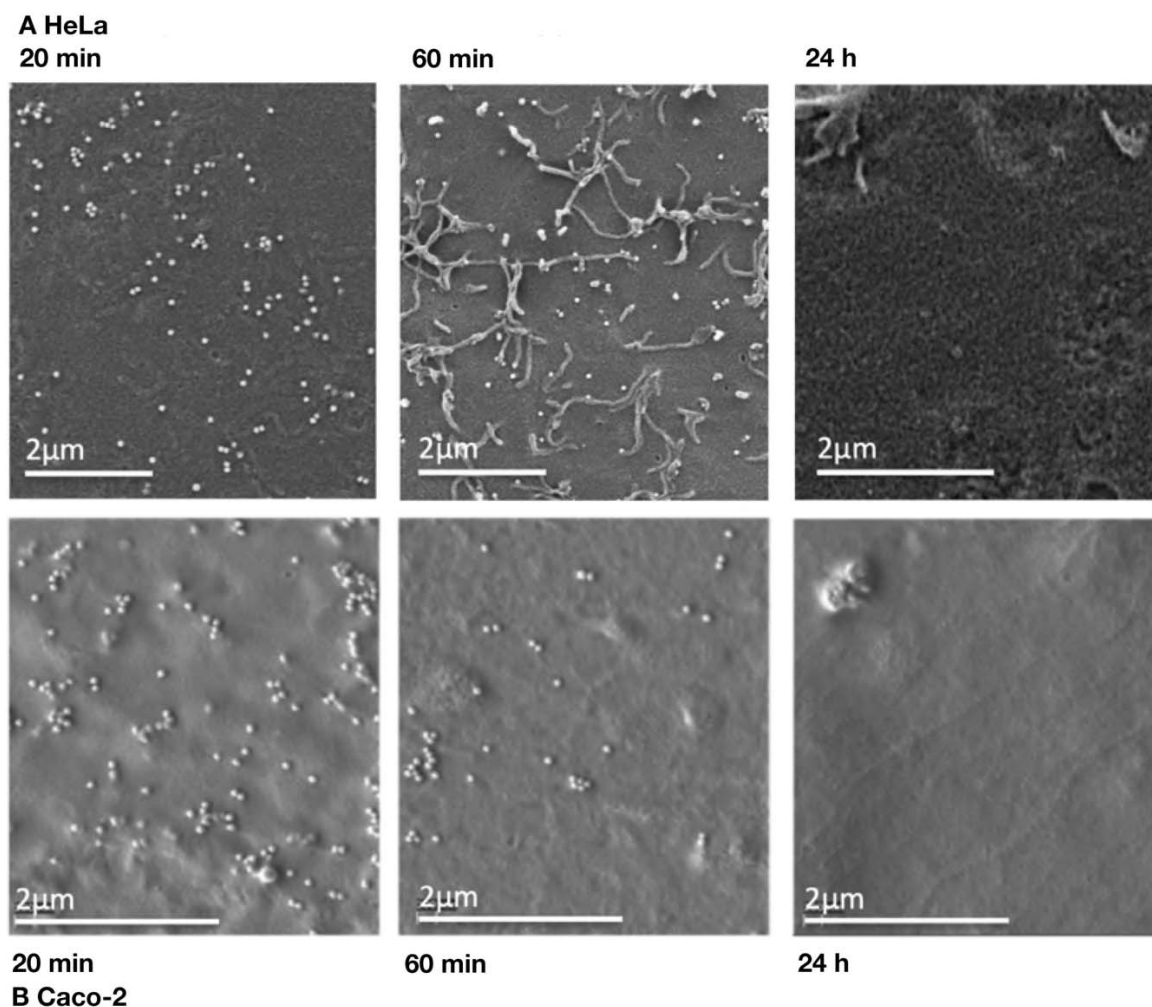


Figure 5. Representative scanning electron microscopy images of cells incubated with SiNPs over time. Images display high SiNPs-plasma membrane association in early incubation times (20 and 60 min) and lower or almost inexistent association in long incubation times (24 h) due to SiNPs internalisation in both cell lines.

SEM was also used to detect the effects of “bad handling conditions” prior to cell culture exposure. Big aggregates appeared on HeLa cell cultures exposed to badly handled SiNPs solutions after 20 min of exposure, as observed in figure 6. Moreover, the cells appearance changed drastically in terms of plasma membrane protuberances and ruffles, cell’s morphology (roundness) and detachment from growing substrate. All of this indicates that exposure to big aggregates, and therefore higher number of NPs/cell can lead to cell distress, detachment from growth surface (as marked with arrows) in figure 6 that could be an indicator or leading factor to cell death. The effect of NP aggregation on uptake¹⁷ and cell

viability has been previously described both *in vitro*¹⁸ and *in vivo*¹⁹. Therefore, once the aggregation is confirmed by SEM either the ENMs lot should be re-evaluated and re-characterised in terms of stability and aggregation on biologically compatible solutions, or its handling and colloidal suspension preparation protocol must be optimised. If upon inspection of these parameters the NPs fail to provide good stability in biological conditions or in contact with cells, their application should be re-evaluated, or the lot should be discarded. The SEM ‘bad handling conditions’ results highlight the importance of the preparation of the colloidal suspensions prior to exposure, as they should be freshly prepared and sonicated prior to each experiment in order to minimize the effects of NP aggregation on cells. *In vitro* tests concerning the visualisation of cell cultures after exposure offer a good understanding of the processes underlying bio-interaction of the ENMs. There are a lot of morphological features to assess the status of the cells in culture after treatment: cell area, volume, morphology, membrane roughness and ruffles, filopodia and lamellipodia formations, detachment from surface, presence of mitotic cells, plasma membrane blebbing, cell fragmentation, vacuole formation, nuclei fragmentation or nucleoli organisation. Most of these features can be visualised extracellularly through SEM and provide good information around the cell status in contact with the ENMs.

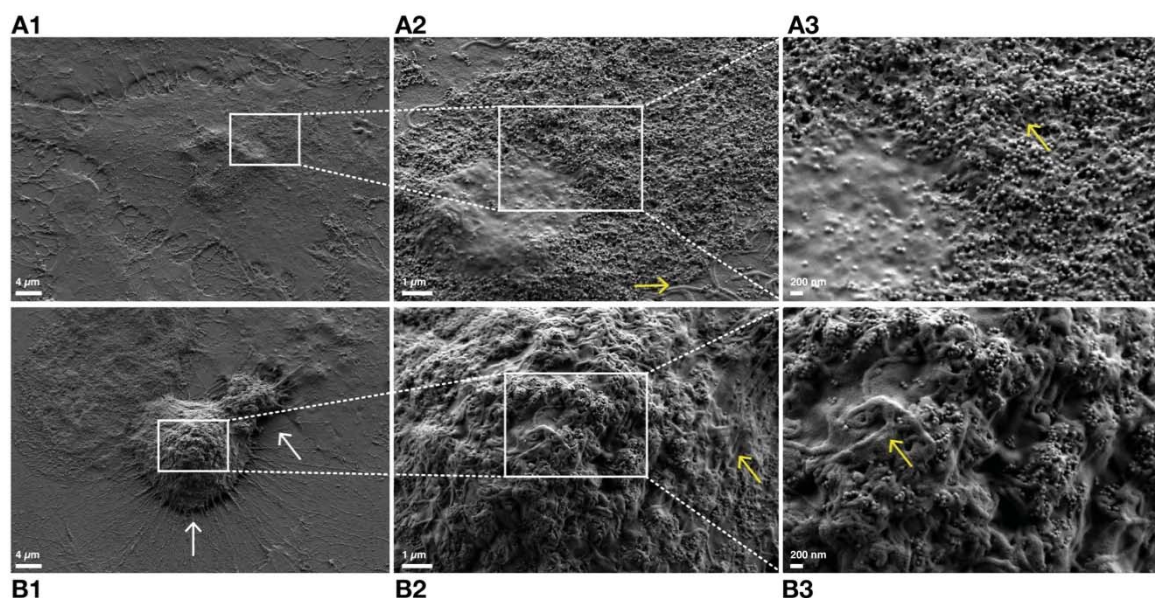


Figure 6. SEM analysis of cells exposed to SiNPs (50 µg/ml) not properly handled (bad handling) after 60 min incubation with HeLa cells. A1 general view of a cell presenting high aggregates of NPs, **A2** enlarged view of the area in **A1** and **A3** enlarged view of the area in **A2** showing high membrane roughness (yellow arrows). **B1**. General view of a HeLa cell detaching from the growth surface (white arrows). **B2** enlarged view

of the area shown in **B1** and **B3** enlarged view of the area in **B2** showing high membrane roughness and ruffling (yellow arrows)

SEM was also used to check if SiNPs remain attached to the cell surface once trypsinised. As previously described, this is an especially important step, when analysing the aggregation status and adsorption to the cell membrane of ENMs but especially when evaluating the internalisation results using other methods like flow cytometry. Cell detachment with trypsin is a requirement of high-throughput methods like flow cytometry where cells must be in suspension to be analysed. Trypsin action can cause, in addition, a complete stripping of the ENMs attached/adsorbed to the cell membrane.

If a targeting strategy, like the addition of anti-EpCAM antibodies to the SiNPs design is used, the SEM analysis can be essential to evaluate if the ligand/receptor-mediated association is sensitive to trypsin's digestion (Fig 7) and therefore the analysis of their internalisation by flow cytometry is reliable or not²⁰. Making sure that NPs are not present in the membrane is very important when flow cytometry is used to evaluate internalisation, to be sure that the fluorescence detected comes from SiNPs inside the cells and not from mixed signal from outside (associated to cell membrane) and inside the cells.

The effect of trypsinisation was tested on EpCAM-functionalised SiNPs after 20 min exposure in HeLa and Caco-2 cells and can be observed in figure 7. Results show that SiNPs attached to the cell membrane after 20 min post-incubation times do not resist the trypsinisation process and are stripped from the cell membrane. Therefore, fluorescence detected in flow cytometry assays (after trypsinisation) comes predominantly from SiNPs that have been internalised by the cells.

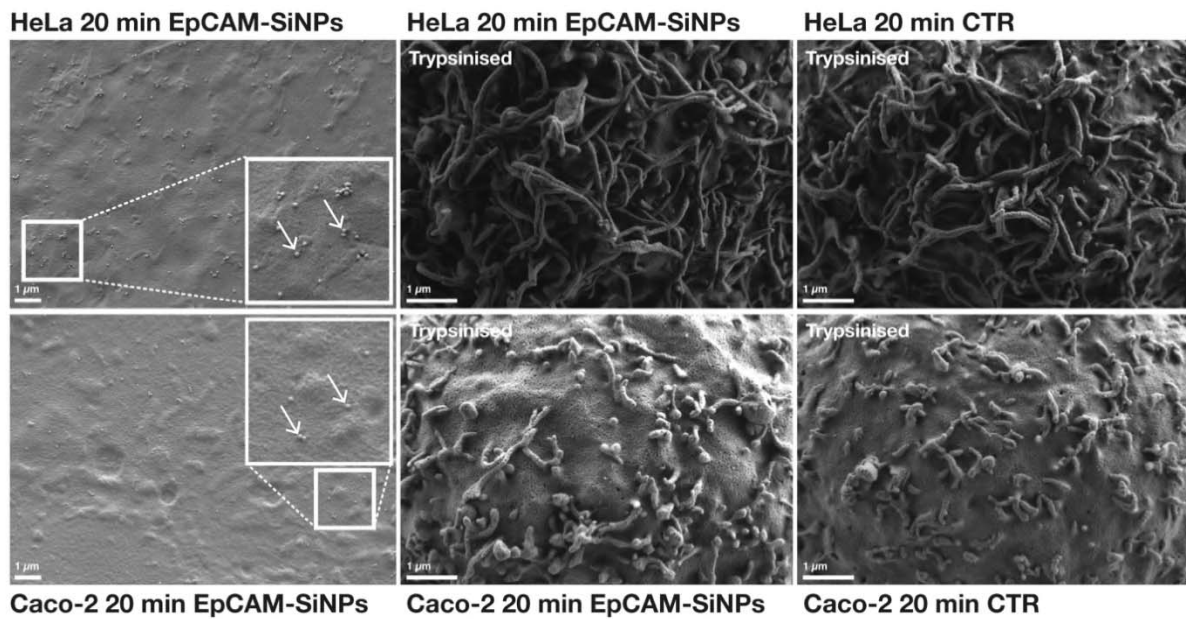


Figure 7. SEM analysis of cells incubated 20 min with EpCAM-functionalised SiNPs (50 µg/ml) and trypsinised. HeLa (top) and Caco-2 (bottom). Left column shows a detail of a cell still attached to the surface, the membrane is nearly flat and NPs can be seen (arrows). Middle column shows a detail of the membrane after trypsinisation, the cells have become round and the membrane is completely rough with no visible SiNPs on the surface. Right column shows a detail of control trypsinised cell membranes (not incubated with SiNPs) at the same magnification. Control samples (CTR).

Internalisation

Internalization has been analysed using two different methods, on one hand by cytometry, which allows to quantify a large number of cells (around 10.000 events/sample), on the other hand by confocal microscopy that gives a visual information about the distribution of NPs inside the cells (diffuse distribution or pointed distribution).

SiNPs positive internalisation was observed using flow cytometry analysis (Fig 8) after every post-incubation time tested (20 min, 60 min, 6 h and 24 h), both in HeLa and Caco-2 cell lines. SiNPs positive association increased over time reaching a plateau after 60 min incubation time in both, HeLa and Caco-2 cell cultures (Fig 9).

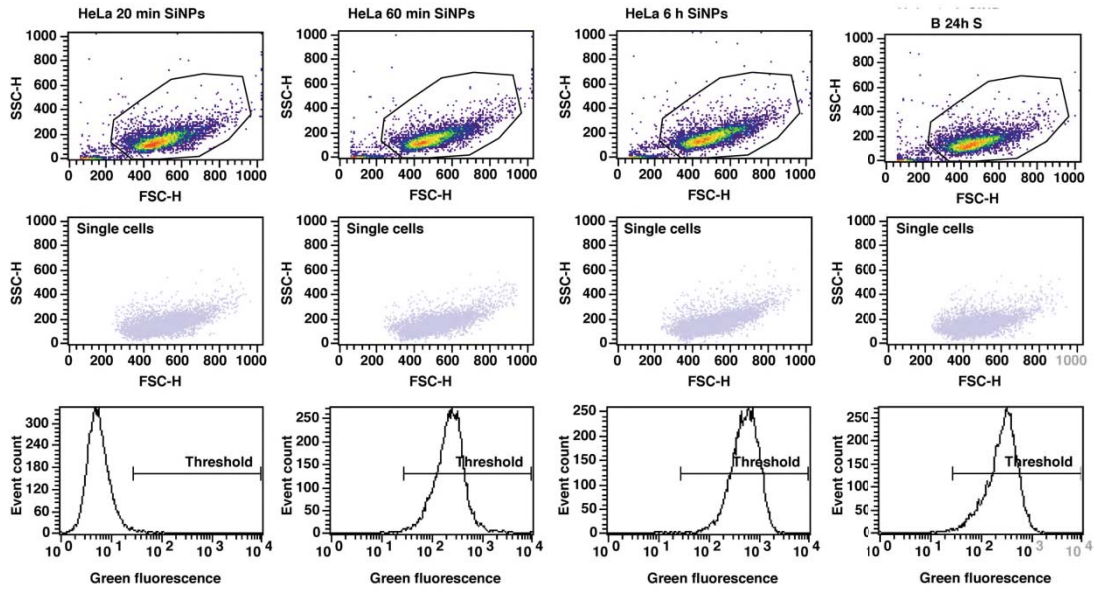
These results are in accordance with the ones observed in SEM, where, after 60 min incubation we see a reduction of the SiNPs adsorbed to the cell plasma membrane, indicating

their internalisation. Flow cytometry allowed to quantify the cells with internalised SiNPs (positive internalisation) in both cell lines just 60 min post-incubation with a 99,79% SiNPs-positive cells in HeLa and 91,58% SiNPs-positive cells in Caco-2. After 24 h incubation time, almost no SiNPs can be observed in SEM, and accordingly, the positive internalisation percentage detected in flow cytometry is 98,93% SiNPs-positive cells in HeLa and 96,74% SiNPs-positive cells in Caco-2 cell line.

Despite the ability to extract information from large populations using flow cytometry data to quantify internalisation, this technique has been pointed to have several drawbacks²⁰. The first drawback is that most of these analyses are done assuming they are detecting only the NPs inside the cells, without evaluating if there might be NPs remaining bound to the surface. One way to eliminate the signal emitted by outside NPs is using trypan blue, which can quench the fluorescence coming from outside the cell, as shown previously in our group using microparticles²¹. Despite this method is easy-to-use and proven useful in the case of big materials like microparticles and NPs²², this technique can have an effect on other molecules, especially surface markers required for other analyses, that could be analysed simultaneously (each single cell is exposed to all the excitations wavelengths at the same time, excitation and detection cannot be done sequentially as in CLSM). Moreover, trypan blue binds unspecifically to proteins and exhibits significant autofluorescence signal when excited at 488 nm²³, which can increase autofluorescence of the cells and the signal to noise ratio might be compromised, affecting the efficiency of the ENMs' detection. Taking together all the problems that can arise using trypan blue, we strongly recommend corroborating the lack of NPs outside the cell by SEM.

Another limitation is the inability to know the number of particles internalised. Their mean fluorescence intensity gives information about the whole population, despite the single-cell nature of the technique, and it does not distinguish between cells that have a high number of NPs internalised or the ones that have very few. Differences on the basal autofluorescence signal between different cell lines have previously identified²⁴. It also assumes that the intensity values of NPs will not change depending on intracellular parameters like the local environment, especially the pH²⁵, granularity and intracellular compounds or the presence of other markers that could diminish the detection or quench the signal.

A Representative HeLa cells cytograms and histograms



B Representative Caco-2 cells cytograms and histograms

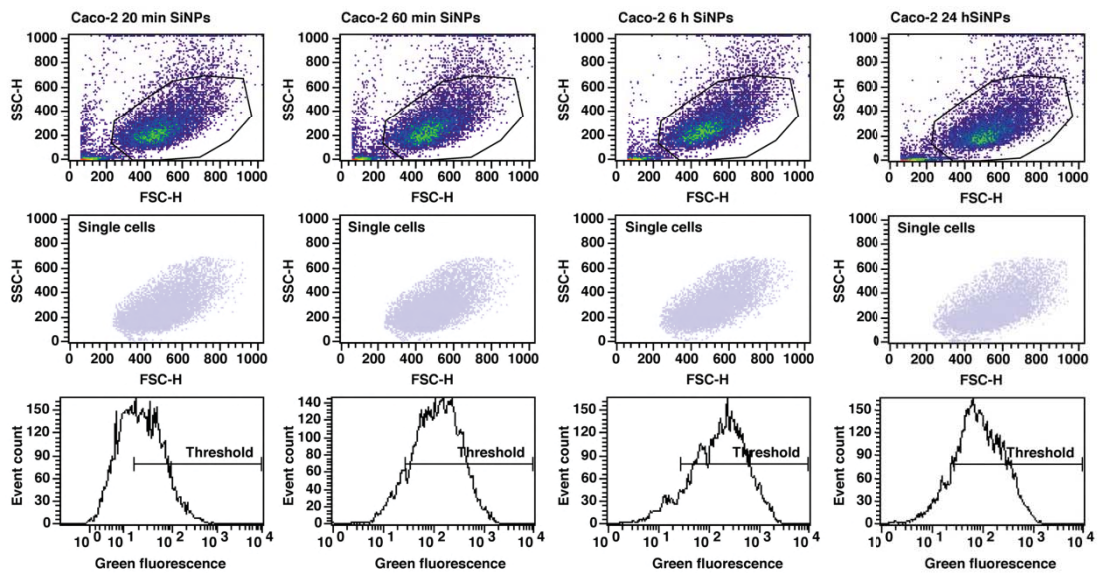


Figure 8. Representative HeLa (A) and Caco-2 (B) cells-SiNPs internalisation cytograms and histograms from flow cytometry analysis. For each cell line (A and B), top row depicts the whole population acquired ($n = +10.000$ events per sample). The delimited area corresponds to that selected by calibration to controls (not shown). Middle row shows the gate population based on the previous selected area and bottom row corresponds to the histogram of counted events according to their green fluorescence intensities. Side scatter height (SSC-H), forward scatter height (FSC-H).

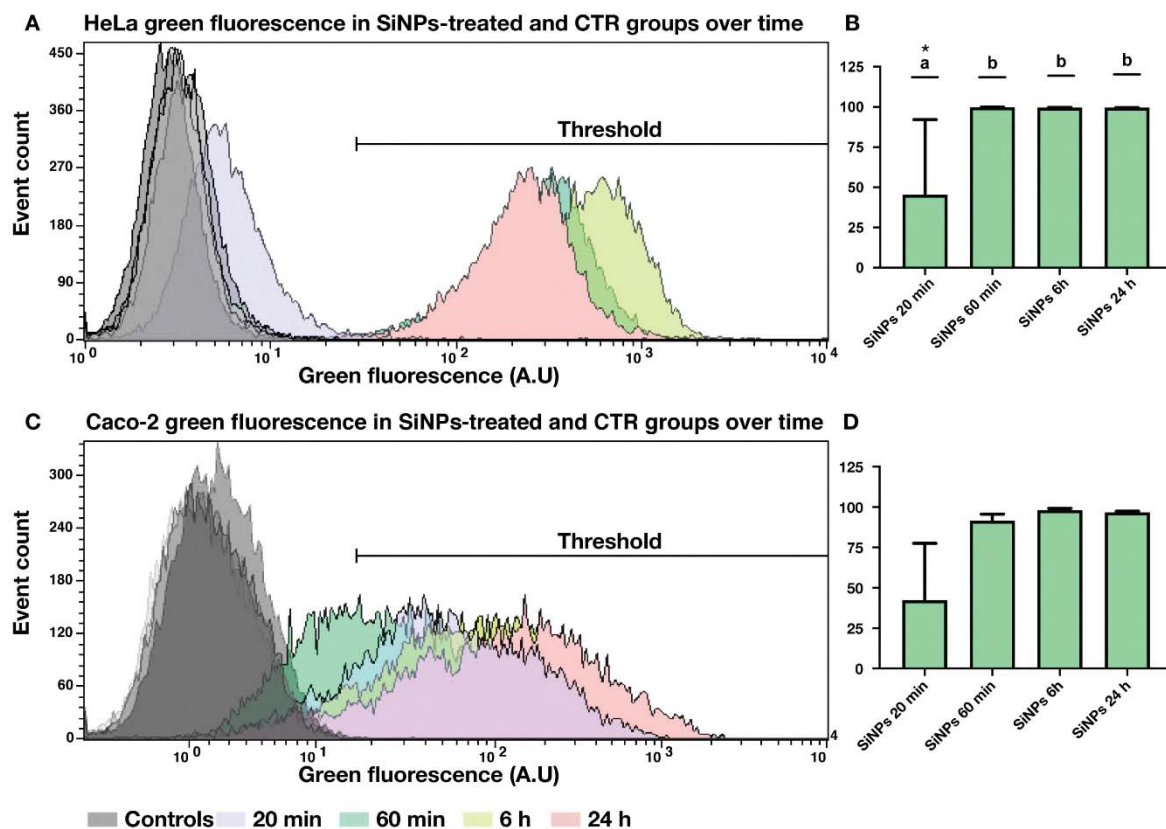


Figure 9. SiNPs internalisation in HeLa and Caco-2 cells over time. **A and C** Representative histogram comparison of the green fluorescence detected in HeLa (A) and Caco-2 (C) cell populations SiNPs-treated vs CTR, analysed through flow cytometry. **B and D** Positive population for internalised SiNPs in HeLa and Caco-2 cell cultures exposed to SiNPs over-time. Depicted as proportions (%) of positive cells within the population + standard deviation. Different superscripts depict statistically significant differences between proportions (%), * depicts $p < 0.05$. Control sample/group (CTR), arbitrary units (A.U.)

This limitation can be overcome using CLSM, because this microscope allows to detect (Fig 11) and, using the appropriate image processing and 3D analysis, quantify the number of NPs inside the cells. After 20 and 60 min of incubation time SiNPs appear to be adhered onto the cell plasma membrane and, apparently, scarce SiNPs are already internalised in HeLa and especially Caco-2 cells (or were not concentrated enough to be detected with CLSM). These results are in accordance with the ones observed in SEM, where SiNPs were still bound to the cell membrane at low incubation time (20 min) and with flow cytometry where only approximately 45% of the cells have positive SiNPs internalisation at low incubation time (20 min). Probably, the effective quantity of SiNPs internalised is only distinguishable when enough time has passed and NPs have been concentrated within the endolysosomal system over time (especially after 6 h of incubation, as shown in figure 10).

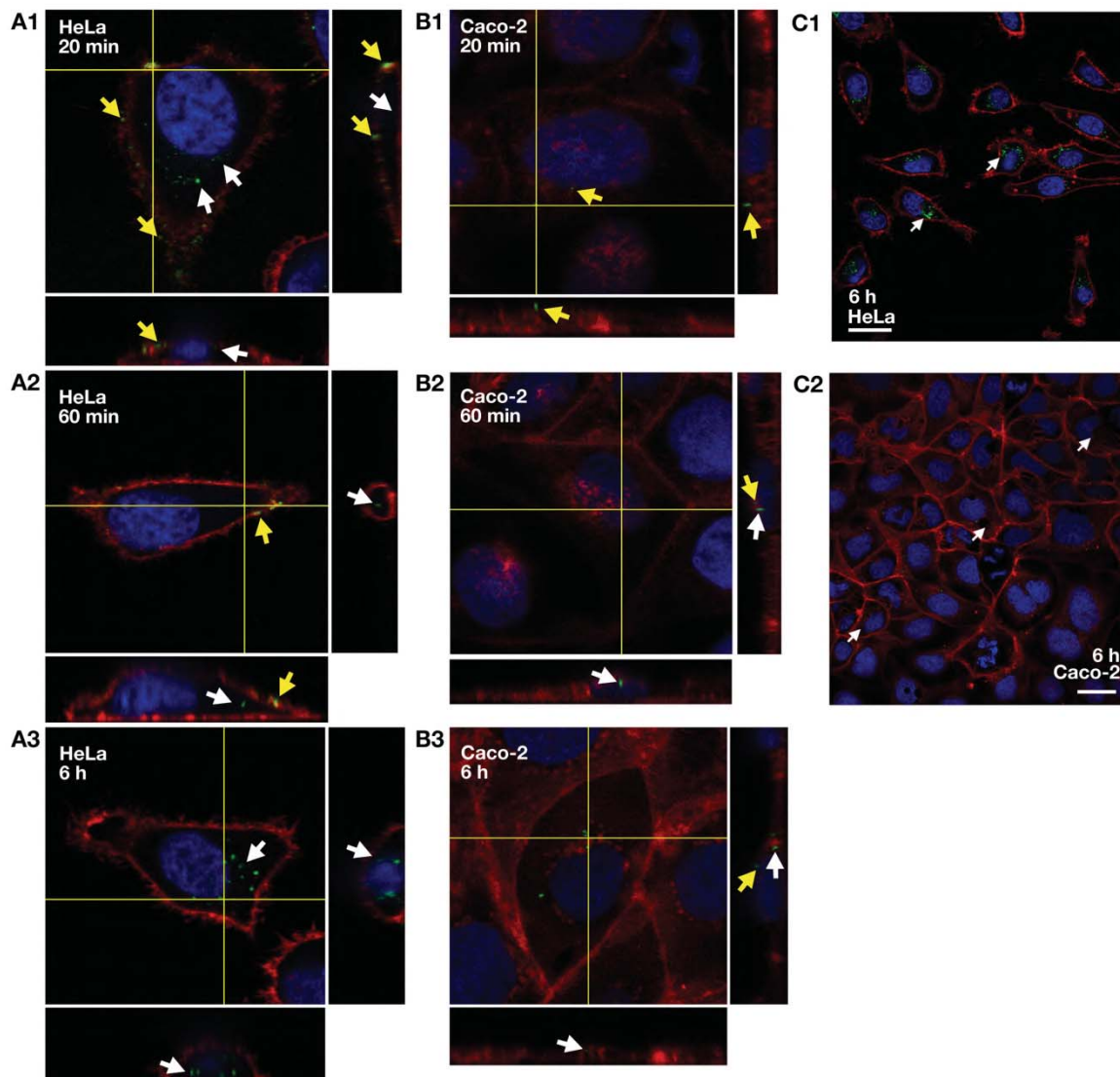


Figure 10. Confocal laser scanning microscope visualisation and orthogonal projections of HeLa and Caco-2 cells incubated with 50 µg/mL of SiNPs in cell medium. A-B Orthogonal projections of cells from 3D CLSM datasets from **A1** 20 min **A2** 60 min and **A3** 6 h SiNPs-incubated HeLa cell cultures and **B1** 20 min **B2** 60 min and **B3** 6 h SiNPs-incubated Caco-2 cell cultures (White arrows= internalised SiNPs, yellow arrows= plasma membrane adsorbed SiNPs). Whole dataset of **C1** HeLa and **C2** Caco-2 cells incubated for 6 h with 50 µg/mL SiNPs in cell medium displaying internalised particles (white arrows) visible through z-slice sectioning of labelled plasma membrane (Cell Mask™ Texas Red stain) and nuclei (Hoechst) after 6 h of incubation. **Scale bar = 30 µm**

SiNPs appear to be scattered in contact with HeLa (Fig 11) and Caco-2 (Fig 12) at short incubation time (20 min), probably as an indicator of their association to the plasma membrane of these cells as revealed by the orthogonal projection analyses in figure 10. After 60 min of incubation the scattered pattern observed begins to form bigger groups of SiNPs, indicating they are still scattered over the whole cell surface but starting to be internalised

inside the cell by its endocytic transport systems (especially in HeLa cells). After 6 and 24 h, almost no SiNPs appear to be scattered over the surface of the cells in HeLa, but some SiNPs remain adsorbed to the plasma membrane in Caco-2 cell cultures, which also showed lower internalisation in figure 10. In HeLa, the detected particles are inside the cell and grouped in big compartments, indicating that probably they are located in the endolysosomal system. The loss of the scattered pattern and progressive formation of SiNPs aggregates shown in figure 11 for HeLa and figure 12 for Caco-2 over time together with the orthogonal projection analysis in figure 10 are a clear sign of internalisation and transportation within the endolysosomal system of internalised SiNPs, since vesicles, endosomes and lysosomes fuse into bigger transitory structures²⁶, as shown in the long incubation times SiNPs data (Fig 11 and Fig 12). Overall, results from CLSM visualisation are in accordance with those observed through SEM and flow cytometry, showing more SiNPs inside over time in both cell lines and especially higher internalisation in HeLa cells.

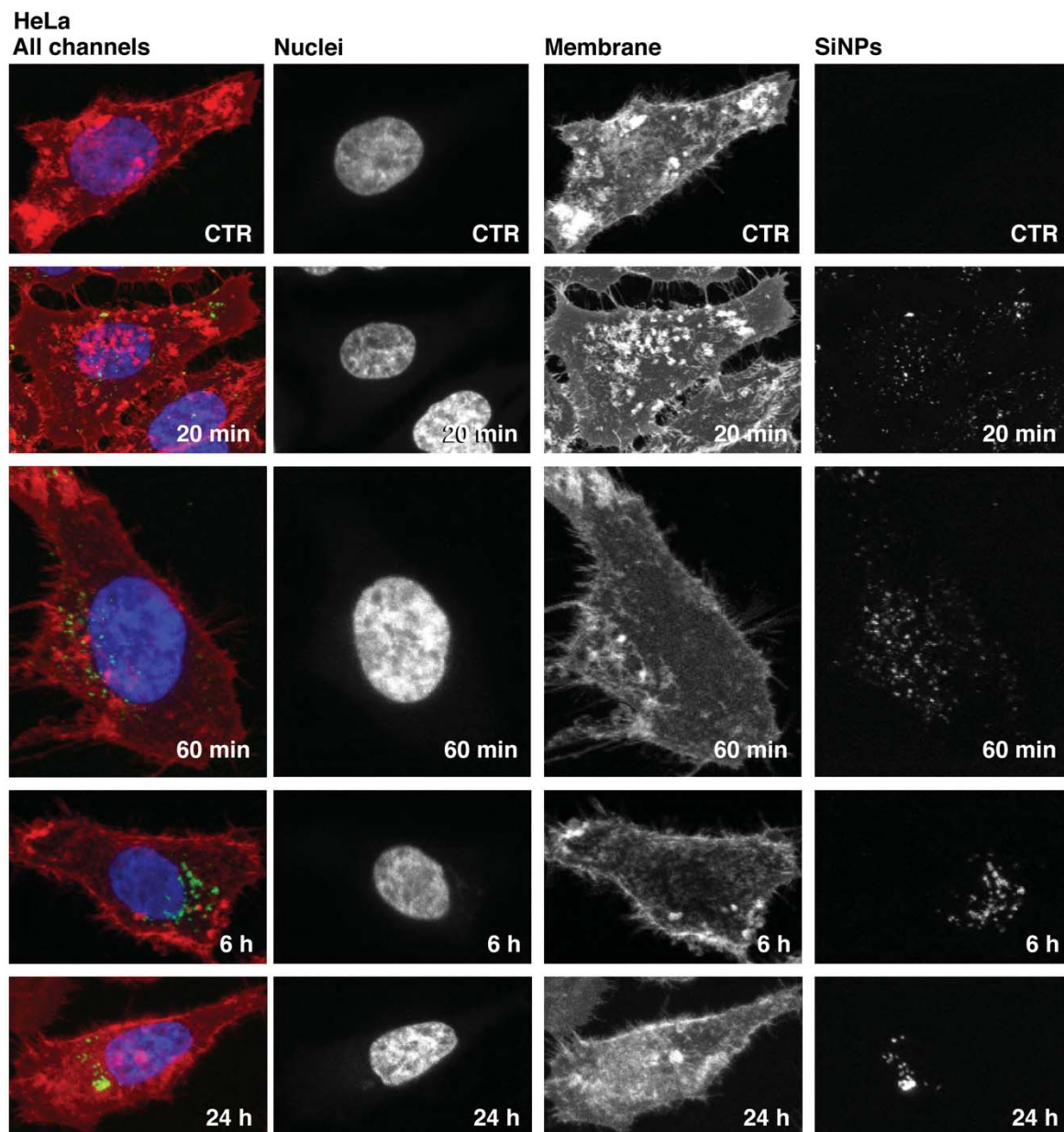


Figure 11. Individual HeLa cell images incubated with 50ug/ml SiNPs at different times. From top to bottom row, first control group followed by 20 min, 60 min, 6 h and 24 h 50 µg/mL SiNPs-incubated samples consecutively. Maximum z-projection of fluorescent signals for each post-incubation time tested. In the first column all channels are displayed with the corresponding fluorescent colours (red=plasma membrane, blue=nucleus and green=SiNPs). In the second column the intensity of the nucleus is showed, while the third and fourth columns correspond to membrane and SiNPs signals, respectively. The aggregation of SiNPs is higher as incubation time increases, especially after 6 h and 24 h incubation indicating the entry of the SiNPs in the endolysosomal system.

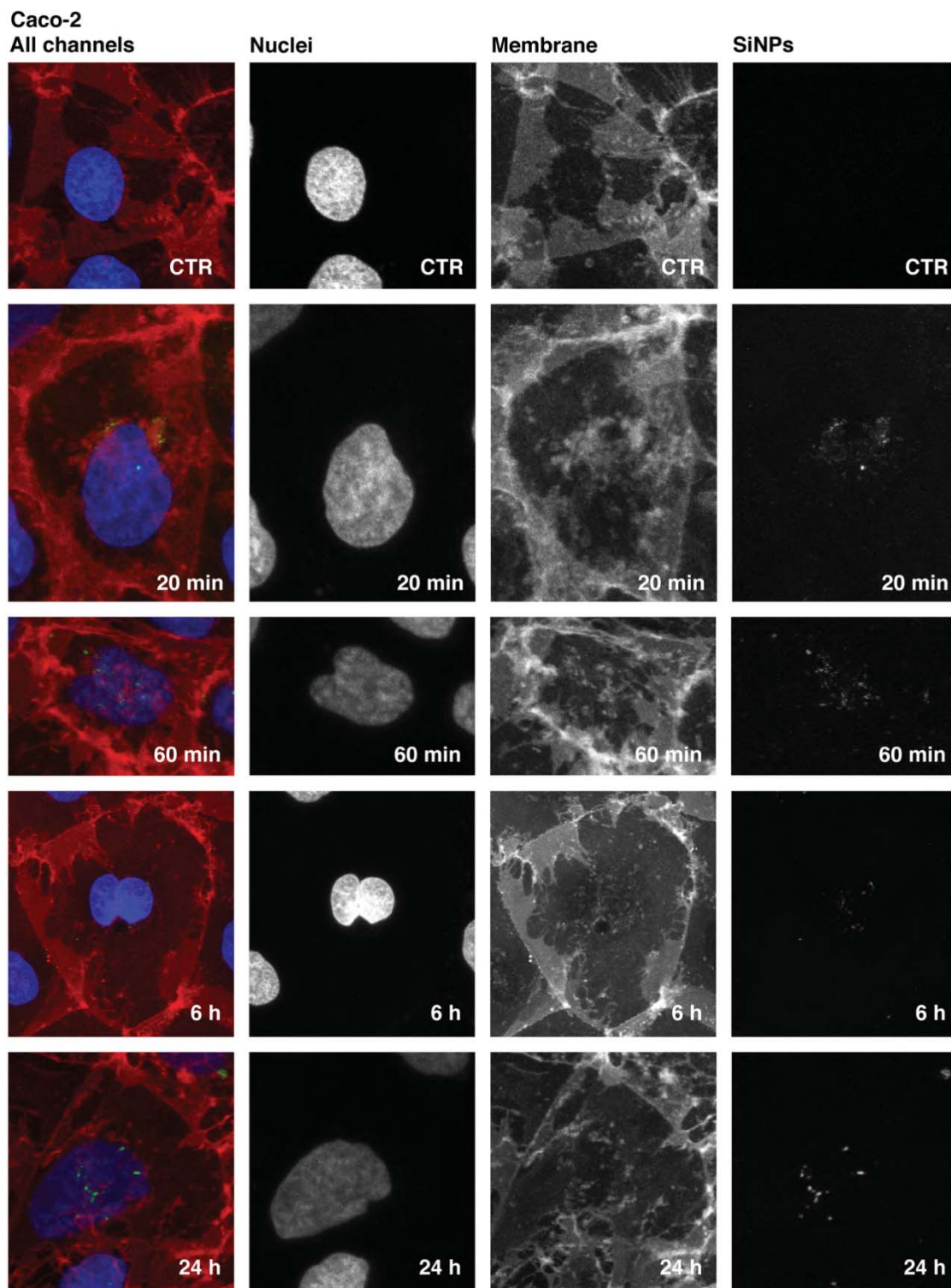


Figure 12. Individual Caco-2 cell images incubated with 50ug/ml SiNPs at different times. From top to bottom row, first control group followed by 20 min, 60 min, 6 h and 24 h 50 µg/mL SiNPs-incubated samples consecutively. Maximum z-projection of fluorescent signals for each post-incubation time tested. In the first column all channels are displayed with the corresponding fluorescent colours (red=plasma membrane, blue=nucleus and green=SiNPs). In the second column the intensity of the nucleus is showed, while in the third and fourth, membrane and SiNPs signals detected are shown. The aggregation of internalised SiNPs seems higher after 24 h incubation.

The confocal microscope was also used to verify the effects of bad handling on SiNPs-exposed HeLa and Caco-2 cell cultures. Big aggregates of SiNPs outside the cells can be observed when SiNPs solutions are not prepared correctly before exposure to cell cultures, as observed in figure 13. Aggregation is a problem when trying to characterise the biointeraction of NPs with cells. As mentioned above it can lead to increased cytotoxic effects due to an uncontrolled uptake and effective dosage of NPs by the cells¹⁹. Aggregation can be caused by the interaction between NPs, their manipulation (synthesis, centrifugation, etc.) prior to the contact with cell cultures, their functionalisation or by the effect of the culture medium, serum or a combination of both, when in contact with cells. As previously discussed in SEM results, when aggregation is detected in biological conditions, especially, in the early contact or exposure with the cell media or cells, the ENMs should be re-characterised in terms of their stability on biologically compatible solutions, their designs re-evaluated (charge, surface modifications, etc) or their handling and colloidal suspension preparation protocol optimised. If upon inspection of these parameters the NPs fail to provide good stability in biological conditions, their application should be re-evaluated, or the lot should be discarded.

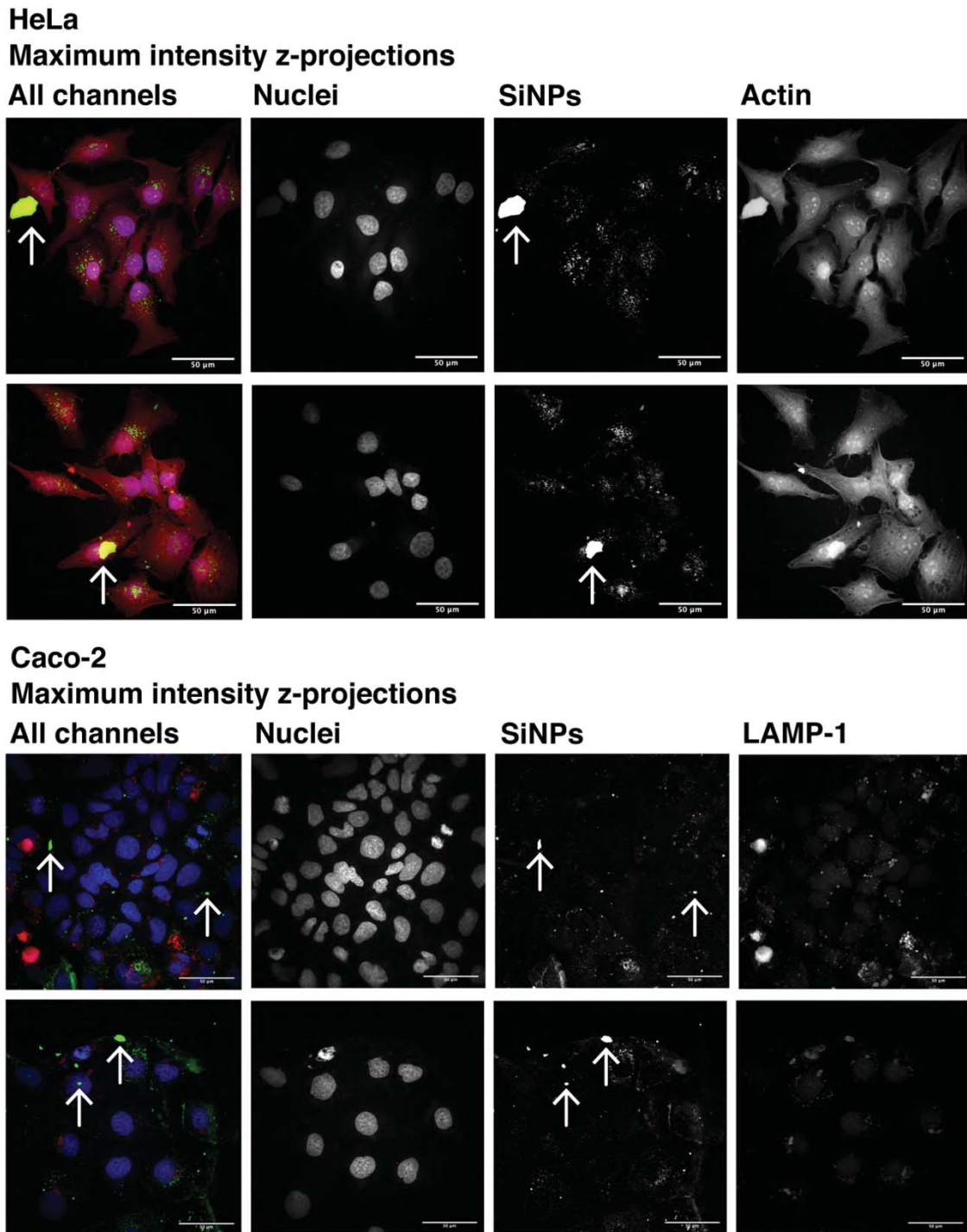


Figure 13. CLSM data from bad handling SiNPs exposed cell cultures. Arrows depict aggregation outside the cells due to bad handling conditions prior to exposure. First row depicts all the channels in the dataset in HeLa (Blue= nuclei, green= SiNPs and red= actin cytoskeleton) and Caco-2 (blue= nuclei, green= SiNPs and red= LAMP-1). **Scale bars = 50 μ m**

Advanced analyses

Quantification of SiNPs internalisation

To accurately quantify SiNPs internalisation and their co-localisation with endolysosomal compartments, deconvolution was applied to restore the degraded signal from optical dispersion when capturing data through CLSM. Deconvolution is a process that uses an algorithm to reverse the effects of convolution in the image formation process. By removing the optical blur, a sharper image is computed based on the knowledge of the blurring (formalized by the so-called point spread function (PSF)). Deconvolution significantly improved the XYZ resolution (Fig 14) and contrast of the datasets (specially the degraded resolution of the Z-axis signal due to its lower axial resolution), leading to an accurate visualisation of small structures like SiNPs, endosomes and lysosomes and their proper segmentation and quantification using the above-mentioned methods. This is critical when facing quantification of NPs inside the cells using resolution limited optical equipments, especially when volumetric analyses are needed, and the Z-resolution is normally lower than that of X and Y axes. It is also fundamental when performing co-localisation analyses^{27,28}, since degraded signals can lead to erroneous results of NPs internalisation (under/over-estimation) and co-localisation (over-estimation) due to diffused fluorescence signal in the z-axis. Moreover, the 3D object detection pipeline applied ensures we use volumetric data to assess not only the internalisation, but also the distribution of SiNPs inside the cells and intracellular organelles, their aggregation, tubeness, intensity or sphericity; values that provide valuable insights when assessing the therapeutic outcome and intracellular fate of these NPs.

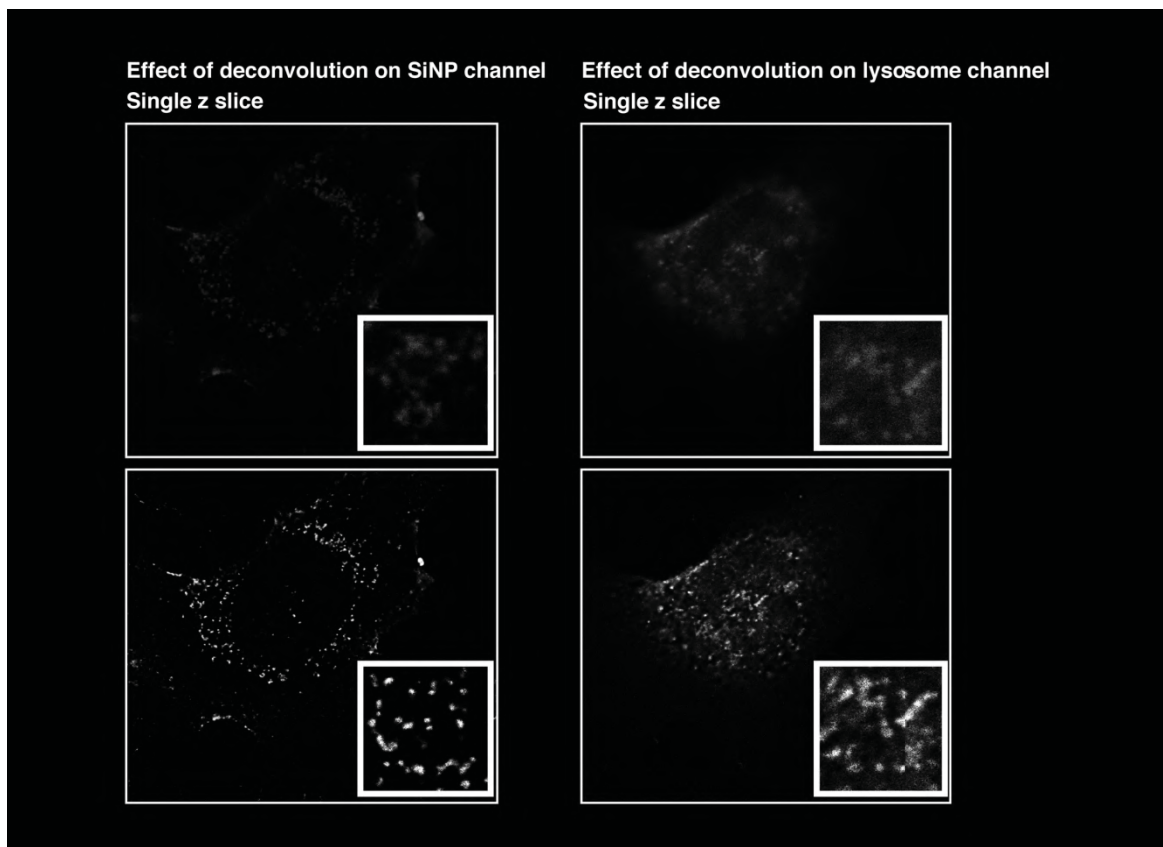


Figure 14. Effect of deconvolution on SiNPs (488 nm) and lysosome (647 nm) channels from HeLa cells exposed to SiNPs for 3 h. An enhancement in resolution, brightness and contrast increases the signal-to-noise ratio of the dataset, allowing for a better segmentation of small structures such as individual SiNPs, SiNPs aggregates, SiNPs in vesicles and intracellular compartments like the lysosome and endosome.

Commonly, quantification of NP uptake is performed through fluorescence-based qualitative or semi-quantitative methods that compare the detected fluorescence by absorbance measurements²⁹, flow cytometry³⁰, fluorescence microscopy³¹ or CLSM³² data relatively between different conditions. This kind of quantification does not allow to extract all-in-one single cell population data and their distributions. The method proposed in this study, merges intensity and accurate volumetric information on the number of NPs per cell based on 3D object detection. It allows direct quantification of NPs at a single-cell level and evaluation of the heterogeneity of the distribution within the population to help in understanding the variability in cell-to-cell NP concentration, and how these variations affect NP–cell interactions and its effects. For example, to identify if cells of a certain morphology or in a particular mitotic stage behave differently, that is, internalise more or less NPs. These are valuable insights that in turn, could provide breakthrough information to improve the ENMs targeting efficiency and allow better NP-based diagnostics and therapeutics.

A similar segmentation at a single-cell method to the one proposed in this study was described by Torrano et al. but it is based on fluorescence determination and calibration, and the extrapolation of the results of this calibration using different instruments on the data obtained. This method could be affected by quenching phenomena within the samples, and in fact, the determination of NPs aggregates of more than 5 NPs is described as limited by this effect³³. Moreover, it is limited to two signals being analysed per experiment which limits the information on the localisation of the NPs with other sub-cellular structures and compartments. The inability to see any quenching effect using trypan blue is only valid to test the quenching efficacy of dyes that can't permeate the cell membrane (like trypan blue on healthy live cells), but won't be applicable on dyes in close contact with the fluorochromes of NPs in protocols such as co-localisation experiments, where structures in close contact with the internalised NPs are stained with other fluorochromes that could interfere with the NPs signal and therefore affect their internalisation and co-localisation quantification²⁰. Fluorescence average methods can also be affected by optical phenomena like quenching (the loss of fluorescence between fluorophore molecules due to excited-state reactions, plasmon-resonance reactions, molecular rearrangements, energy transfer or collisional quenching)³⁴

Other ways to quantify the number of NPs that interacted with cell cultures is the detection through high-performance liquid chromatography (HPLC)³⁵, which gives an estimation of the average number of NPs per cell from whole culture lysates but loses crucial information on what kind of cells internalise more NPs (mitotic cells, interphase attached cells, rounded/detached cells, big or small volume cells, single nucleus/multinuclei cells, dying cells) and their intracellular fate. Other methods commonly used to evaluate the internalisation of NPs is imaging through transmission electron microscopy (TEM)³⁶ or not as commonly used FIB-SEM³⁷. Both of these methods are time-consuming (comparing multiple serial TEM sections simultaneously and the identification of nanoscopic objects is challenging)³⁸ and quantification is often based on extrapolation from very few slices for each analysis and a low volume per cell is analysed. Such analyses are so complex that the sample size is often limited by the technique and resources available. Due to the low number of cells analysed, it does not provide any information of the distributions of NPs in single-cell populations, therefore, its conclusions could be misleading. It provides valuable information on intracellular fate but requires expertise identifying cellular structures. Lastly,

imaging through high-end microscopy techniques such as STED or synchrotron based microscopy³⁹ (synchrotron X-ray fluorescence, soft X-ray tomography, etc.) can accurately provide data regarding internalisation and localisation within single-cell populations, but these resources are very expensive, data extraction is limited to short shifts and equipments are often beyond-reach for most scientists.

The quantification performed in the present study uses CLSM fluorescence data as a reporter, but the fluorescence values are not used as quantification themselves. The volumetric data of the different fluorescence reporters detected is transformed into objects that can be segmented and extracted (covering the whole range of fluorescence they emit) and quantified volumetrically. This information is then used to estimate the number of SiNPs per cell localised inside the cell limits (using the cytoskeleton reported by actin staining as a mask) by using the following equation:

$$\text{SiNPs per volume in } \mu\text{m}^3 = \frac{\text{N}^\circ \text{ SiNPs voxels within cell limits/ Estimated N}^\circ \text{ voxels of a SiNP}}{\text{N}^\circ \text{ voxels of the whole cell}}$$

Using this equation, we detected a +65% increase between the mean number of estimated SiNPs per μm^3 between 1 h and 3 h of 50 $\mu\text{g/mL}$ SiNPs-exposed HeLa cell cultures as observed in figure 15. These results are in accordance with the ones observed through CLSM, where intracellular SiNPs aggregate at longer incubation times, showing a progression within the endolysosomal system and its endosome and lysosome fusing mechanics which led to the further exploration using co-localisation experiments with endolysosomal compartments and its quantification. The violin chart distribution shows how after 3 h post-incubation time more cells display higher estimated number of SiNPs inside than after 1 h post-incubation time.

The approach used in this method, despite taking advantage of fluorescence as the reporter of SiNPs can be applied to other signals detected by CLSM, for example the reflection properties of metallic NPs as shown in Chapter 3 of the present thesis. This is a clear advantage in terms of quantification according to the limitations to add fluorescent probes in certain NPs and ENMs designs.

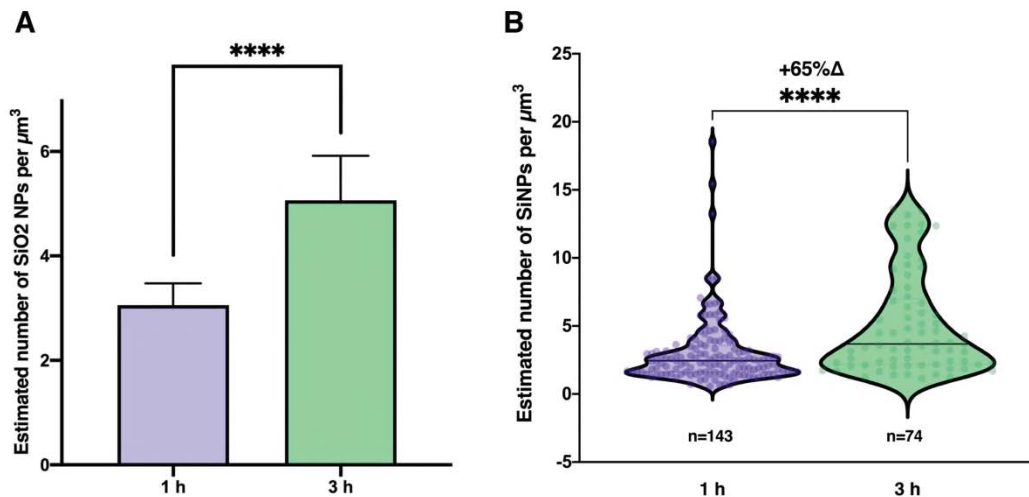


Figure 15. Nanoparticle internalisation over time in HeLa cells **A** Graph bar depicts the mean number of nanoparticles per μm^3 after 1 h and 3 h 50 $\mu\text{g}/\text{mL}$ SiNPs incubation time in HeLa cells and **B** Violin chart depicting the distribution of estimated number of particles per volume (μm^3) per cell quantified through CLSM data analysis after deconvolution and segmentation and the average number of nanoparticles estimated per μm^3 (black line) from the quantified HeLa cell population. Statistically significant differences between conditions are depicted with **** when $p < 0.0001$ and +65% Δ depicts the 65% increase in number of estimated particles per volume (μm^3) between them.

SiNP co-localisation with the endolysosomal system.

Analysing deconvolved data lead to precise co-localisation analysis using 3D object recognition software in Fiji through CLIJ (using GPU-accelerated processing, it accelerates the process of object recognition segmentation and reporting in 3D, especially for big calculations like whole-cell data). Differences were found in the co-localisation between 1 h and 3 h SiNPs-incubated. Data depicted in figure 16 show statistical differences between the intracellular fate of SiNPs after 1 h from exposure. SiNPs co-localise mainly with early endosomes (EEA-1 labelled compartments) (accounting for a mean 2.071% of total SiNPs +/- 2.387%) while at 3 h SiNPs co-localise mainly with late endosomes, endolysosomes or lysosomes (LAMP-1 labelled compartments) (accounting for 6.836 % of total SiNPs quantified +/- 3.360%). These data are proof of the mechanism used by SiNPs to enter the cells. Relatively to the amount of SiNPs internalised, a very low percentage of SiNPs use energetically dependent pathways. Therefore, the vast majority of SiNPs enter through other pathways, either passively through direct diffusion or non-specific mechanisms through the cell membrane or using the macropinocytic or caveolae endocytic pathway (in which they

could be temporarily stored in macropinosomes or caveosomes with low EEA-1/LAMP-1 staining chances). Co-localisation data analysis over-time shows that between 1 h and 3 h there's a progression through the endolysosomal transportation system of the amount of SiNPs that enter the cell through the endovesicular system of HeLa cells, and despite being in 'hostile compartment' because of the organelle's maturation and acidification, it is possible to track their trafficking within the cell as well. Such results are in accordance with the ones observed recently in the literature using a similar approach by Vtyurina et al⁴⁰. Despite using a similar single-cell-level object detection approach, the method proposed by Vtyurina et al. is based on timelapse microscopy, which despite using CLSM technology can lack spatial resolution in favour of short capture times (leading to unprecise NPs detection). It is also worth mentioning that signals used to calculate co-localisation are restored by deconvolution and the mask generated for cell limit segmentation relies on un-specific staining with LysoTracker (specific for lysosome staining). The objects detected as NPs are segmented into homogenous spherical objects instead of relying on the actual signal morphology and volumes to calculate co-localisation and quantify it. Lastly, it relies on commercial software that can be very opaque in how the co-localisation is calculated. In comparison, the method proposed in this study is highly adaptable to experiment conditions and uses fast, optimised and open-source software. All the above-mentioned limitations of the methods compared could lead to the differences observed in the % of co-localisation between the low values obtained in our study and the high values of co-localisation observed in Vtyurina et al study that showed ~10% co-localisation with early endosomes in HeLa Kyoto cells and ~40 % lysosome co-localisation at 3 h of incubation with NPs in HeLa cells.

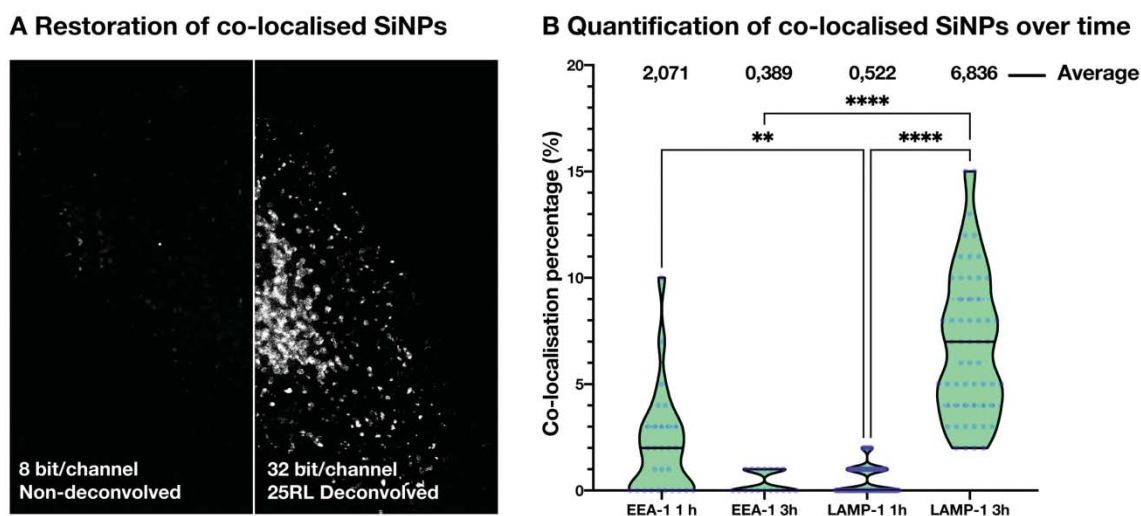


Figure 16. Quantification and SiNP co-localisation with the endolysosomal system. **A** Data deconvolution, increased signal-to-noise ratio leads to a precise information extraction on co-localisation. **B** Violin chart depicts the differences in compartment (endosome/lysosome) co-localisation in HeLa cells in accordance with its post-incubation time (purple line shows the average for the quantified population per condition). Statistically significant differences between conditions are depicted with ** when $p < 0.01$ **** when $p < 0.0001$. Thanks to increased sensitivity of 3D object detection algorithms information is accurately extracted and can be quantified. Deconvolution with Richardson-Lucy for 25 iterations (RL), early endosome antigen-1 (EEA-1), lysosomal-associated membrane protein 1 (LAMP-1)

Conclusions

The visualisation methods introduced within the workflow were useful to evaluate the interaction of ENMs and identify some pitfalls of their manipulation and application. By performing such experiments in the proposed workflow, ENMs can be evaluated from early essential analyses depending on how they perform in biological conditions and after the interaction with the cells. If any problem (aggregation, cytotoxicity, morphology changes, low fluorescence signal detection) is detected, scientists can traceback the material to the previous step in the characterisation and re-evaluate their design or manipulation.

SEM observation has contributed to analyse, the SiNPs status in biological conditions and in contact with cells, or the cell morphology and overall health of cells that have been in contact or associated with SiNPs or that have engulfed and internalised SiNPs over-time.

It was also useful to highlight some pitfalls on SiNPs-solution manipulation prior to cell-exposure as well as to confirm the origin of the flow cytometry fluorescence detected signals. Confocal laser scanning microscopy has been proven to be an optimal method not only for quantitative visualisation and confirmation of the internalisation of SiNPs, but also to quantify it. Accordingly, internalisation, uptake rate, SiNPs progresses through time inside subcellular compartments and their prospective intracellular fate have been successfully investigated and quantified.

Between the visualisation of the data through direct observation in SEM and CLSM we get an overview of the timings and fate of the SiNPs at the biointerface, the plasma membrane (the entry to the cell) and the possible outcomes from their intracellular destiny. The high-brightness of SiNPs allow for an easy to detect target despite their small size. Moreover, the high-surface to volume ratio of the SiNPs tested in this study allow a wide variety of functionalisation possibilities, so they could also be a perfect diagnostic tool for the early diagnosis of diseases.

The development of a single-cell semi-automatic segmentation and deconvolution procedure of CLSM data and their analyses have provided new insights into internalisation and co-localisation over time in HeLa cells. A small portion of the SiNPs that get inside the cell comes from endocytic pathways, while the rest must find their way in through non-specific, macropinocytosis engulfment or caveolae-dependent endocytosis. These analyses provide, single-cell data at a nanoscopic level, and a way to quantify the number, distribution and localisation within the cell in populations solving common ENM-quantification problems.

The results obtained in this study prove that a logical workflow of common cell biology experiments together with material science experiments can be performed to ensure the quality of new ENMs before conducting *in vivo* studies. Such standardisation is especially relevant since the European Union is legislating a shift from *in vivo* testing, towards non-animal approaches based on *in vitro* and computational methods as exposed in recent regulations (EU Directive 2010/63/EU (2010), (EC) No 1907/2006 REACH (2020g)) and the (EC) No 1223/2009 on cosmetic products (2020e))⁴¹. This will allow a better classification of promising materials that can have a beneficial impact in nanomedicine characterisation, by avoiding over-promising materials that could be potentially diagnosed before their application in more complex organisms.

References

1. Moore, C. J. *et al.* Controlling colloidal stability of silica nanoparticles during bioconjugation reactions with proteins and improving their longer-term stability, handling and storage. *J. Mater. Chem. B* **3**, 2043–2055 (2015).
2. Albalawi, F., Hussein, M. Z., Fakurazi, S. & Masarudin, M. J. Engineered Nanomaterials: The Challenges and Opportunities for Nanomedicines. (2021) doi:10.2147/IJN.S288236.
3. REJMAN, J., OBERLE, V., ZUHORN, I. S. & HOEKSTRA, D. Size-dependent internalization of particles via the pathways of clathrin- and caveolae-mediated endocytosis. *Biochem. J.* **377**, 159–169 (2004).
4. Ong, K. J. *et al.* Widespread nanoparticle-assay interference: Implications for nanotoxicity testing. *PLoS One* (2014) doi:10.1371/journal.pone.0090650.
5. Schindelin, J. *et al.* Fiji: An open-source platform for biological-image analysis. *Nat. Methods* **9**, 676–682 (2012).
6. Haase, R. *et al.* CLIJ: GPU-accelerated image processing for everyone. *Nat. Methods* **17**, 5–6 (2020).
7. Riebeling, C. *et al.* A guide to nanosafety testing: Considerations on cytotoxicity testing in different cell models. *NanoImpact* **10**, 1–10 (2018).
8. Kroll, A., Pillukat, M. H., Hahn, D. & Schnekenburger, J. Interference of engineered nanoparticles with in vitro toxicity assays. *Arch. Toxicol.* **86**, 1123–1136 (2012).
9. Bajak, E. *et al.* Changes in Caco-2 cells transcriptome profiles upon exposure to gold nanoparticles. *Toxicol. Lett.* **233**, 187–199 (2015).
10. Krüger, K., Schrader, K. & Klempt, M. Cellular response to titanium dioxide nanoparticles in intestinal epithelial Caco-2 cells is dependent on endocytosis-associated structures and mediated by EGFR. *Nanomaterials* **7**, (2017).
11. Ye, D. *et al.* Low uptake of silica nanoparticles in Caco-2 intestinal epithelial barriers. *Beilstein J. Nanotechnol.* **8**, 1396–1406 (2017).
12. Wörle-Knirsch, J. M., Pulskamp, K. & Krug, H. F. Oops they did it again! Carbon nanotubes hoax scientists in viability assays. *Nano Lett.* **6**, 1261–1268 (2006).
13. Lupu, A. R. & Popescu, T. The noncellular reduction of MTT tetrazolium salt by TiO₂ nanoparticles and its implications for cytotoxicity assays. *Toxicol. Vitro.* **27**, 1445–1450 (2013).
14. Skehan, P. *et al.* New Colorimetric Cytotoxicity Assay for Anticancer-Drug Screening. *JNCI J. Natl. Cancer Inst.* **82**, 1107–1112 (1990).
15. Cortés-Ciriano, I. & Bender, A. How Consistent are Publicly Reported Cytotoxicity Data? Large-Scale Statistical Analysis of the Concordance of Public Independent Cytotoxicity Measurements. *ChemMedChem* **11**, 57–71 (2016).
16. Chaari, M. *et al.* Fluorescent BODIPY-Anionic Boron Cluster Conjugates as Potential Agents for Cell Tracking. *Bioconjug. Chem.* **29**, 1763–1773 (2018).
17. Albanese, A. & Chan, W. C. W. Effect of gold nanoparticle aggregation on cell uptake and toxicity. *ACS Nano* **5**, 5478–5489 (2011).
18. Tripathy, N., Hong, T. K., Ha, K. T., Jeong, H. S. & Hahn, Y. B. Effect of ZnO nanoparticles aggregation on the toxicity in RAW 264.7 murine macrophage. *J. Hazard. Mater.* **270**, 110–117 (2014).
19. Murugadoss, S. *et al.* Agglomeration of titanium dioxide nanoparticles increases toxicological responses in vitro and in vivo. *Part. Fibre Toxicol.* **17**, 1–14 (2020).
20. FitzGerald, L. I. & Johnston, A. P. R. It's what's on the inside that counts: Techniques for investigating the uptake and recycling of nanoparticles and proteins in cells. *J. Colloid Interface Sci.* **587**, 64–78 (2021).
21. Patiño, T., Soriano, J., Barrios, L., Ibáñez, E. & Nogués, C. Surface modification of

- microparticles causes differential uptake responses in normal and tumoral human breast epithelial cells. *Sci. Rep.* **5**, 11371 (2015).
22. Douglas, K. L., Piccirillo, C. A. & Tabrizian, M. Cell line-dependent internalization pathways and intracellular trafficking determine transfection efficiency of nanoparticle vectors. *Eur. J. Pharm. Biopharm.* **68**, 676–687 (2008).
 23. Avelar-Freitas, B. A. *et al.* Trypan blue exclusion assay by flow cytometry. *Brazilian J. Med. Biol. Res.* **47**, 307–315 (2014).
 24. Shin, H. R., Kwak, M., Lee, T. G. & Lee, J. Y. Quantifying the level of nanoparticle uptake in mammalian cells using flow cytometry. *Nanoscale* **12**, 15743–15751 (2020).
 25. Han, J. & Burgess, K. Fluorescent indicators for intracellular pH. *Chem. Rev.* **110**, 2709–2728 (2010).
 26. El-Sayed, A. & Harashima, H. Endocytosis of Gene Delivery Vectors: From Clathrin-dependent to Lipid Raft-mediated Endocytosis. *Mol. Ther.* **21**, 1118–1130 (2013).
 27. Landmann, L. Deconvolution improves colocalization analysis of multiple fluorochromes in 3d confocal data sets more than filtering techniques. *J. Microsc.* **208**, 134–147 (2002).
 28. Villalta, J. I. *et al.* New algorithm to determine true colocalization in combination with image restoration and time-lapse confocal microscopy to map Kinases in mitochondria. *PLoS One* **6**, 1–16 (2011).
 29. Scarpa, E. *et al.* Quantification of intracellular payload release from polymersome nanoparticles. *Sci. Rep.* **6**, 29460 (2016).
 30. Ivask, A. *et al.* Single Cell Level Quantification of Nanoparticle-Cell Interactions Using Mass Cytometry. *Anal. Chem.* **89**, 8228–8232 (2017).
 31. MacDonald, C., Barbee, K. & Polyak, B. Force Dependent Internalization of Magnetic Nanoparticles Results in Highly Loaded Endothelial Cells for Use as Potential Therapy Delivery Vectors. *Pharm. Res.* **29**, 1270–1281 (2012).
 32. Rothen-Rutishauser, B. *et al.* Quantification of gold nanoparticle cell uptake under controlled biological conditions and adequate resolution. *Nanomedicine* **9**, 607–621 (2014).
 33. Torrano, A. A. *et al.* A fast analysis method to quantify nanoparticle uptake on a single cell level. *Nanomedicine* **8**, 1815–1828 (2013).
 34. Kang, K. A., Wang, J., Jasinski, J. B. & Achilefu, S. Fluorescence Manipulation by Gold Nanoparticles: From Complete Quenching to Extensive Enhancement. *J. Nanobiotechnology* **9**, 1–13 (2011).
 35. Panyam, J. & Labhsetwar, V. Dynamics of endocytosis and exocytosis of poly(D,L-lactide-co-glycolide) nanoparticles in vascular smooth muscle cells. *Pharm. Res.* **20**, 212–220 (2003).
 36. Elsaesser, A. *et al.* Quantification of nanoparticle uptake by cells using an unbiased sampling method and electron microscopy. *Nanomedicine* **6**, 1189–1198 (2011).
 37. Guehrs, E. *et al.* Quantification of silver nanoparticle uptake and distribution within individual human macrophages by FIB/SEM slice and view. *J. Nanobiotechnology* **15**, 1–11 (2017).
 38. Drasler, B., Vanhecke, D., Rodriguez-Lorenzo, L., Petri-Fink, A. & Rothen-Rutishauser, B. Quantifying nanoparticle cellular uptake: Which method is best? *Nanomedicine* **12**, 1095–1099 (2017).
 39. Rashkow, J. T., Patel, S. C., Tappero, R. & Sitharaman, B. Quantification of single-cell nanoparticle concentrations and the distribution of these concentrations in cell population. *J. R. Soc. Interface* **11**, 20131152 (2014).
 40. Vtyurina, N., Åberg, C. & Salvati, A. Imaging of nanoparticle uptake and kinetics of intracellular trafficking in individual cells. *Nanoscale* **13**, 10436–10446 (2021).
 41. Pistollato, F. *et al.* Current EU regulatory requirements for the assessment of chemicals and cosmetic products: challenges and opportunities for introducing new approach methodologies. *Archives of Toxicology* vol. 95 (Springer Berlin Heidelberg, 2021).

Keywords for statistical analyses of literature:

Biological interaction, bio-interaction, nanoparticle, nanoparticles, drug delivery, bio-interface, toxicity, characterisation, nano-toxicology

Supplementary material

Image analyses resources

Macro 'ROI splitter'

```
// Set variables
outputdir= getDirectory("SEGMENTED_CELLS");
roiManager("Open", "/path/to/ROI.zip");
open("/path/to/dataset.tif");

// Count number of ROIs
numROIs = roiManager("count");
for(i=0; i<numROIs;i++) // loop through ROIs
    {
        roiManager("Select", i);
        run("Duplicate...");
// Change name of the cropped image
        cropName = getTitle + "_" + i;
        saveAs("tiff", outputdir + cropName);
// Transform: LUT to gray and split channels
        run("Grays");
        run("Split Channels");
// Save splitting results
        title = getTitle();
        saveAs("Tiff", outputdir + title);
        close();
        title = getTitle();
        saveAs("Tiff", outputdir + title);
        close();
        title = getTitle();
        saveAs("Tiff", outputdir + title);
        close();
        title = getTitle();
        saveAs("Tiff", outputdir + title);
        close();
    }
//Close and reset ROI Manager
roiManager("reset");
```

Macro 'ROI extractor and cytoskeleton segmentation'

```
// Set variables
inputdir=getDirectory("CROPS");
list=getFileList(inputdir);
outputdir= getDirectory("SEGMENTED_CELLS");

for(i=0;i<list.length;i++){
    if (endsWith(list[i], ".tif")){
// Open data
        open(inputdir+list[i]);
        image= getTitle();
        setBackgroundColor(0, 0, 0);
        run("Clear Outside");
        run("Duplicate...", "duplicate channels=4");
//GB
// Apply Gaussian blur
        run("CLIJ2 Macro Extensions", "cl_device=[Radeon]");

// gaussian blur
        image1 = getTitle();
        Ext.CLIJ2_push(image1);
        image2 = "C4_GB_10xyz" + getTitle();
        sigma_x = 10.0;
        sigma_y = 10.0;
        sigma_z = 1.0;
        Ext.CLIJ2_gaussianBlur3D(image1,    image2,    sigma_x,    sigma_y,
sigma_z);
        Ext.CLIJ2_pull(image2);

// Save results
//     title2 = getTitle();
//     saveAs("Tiff", outputdir + title2);
//Segmentation
        run("Auto    Threshold",    "method=MinError(I)    white    stack
use_stack_histogram");
        run("Fill Holes", "stack");
        title3= "MASK" + getTitle();
        saveAs("Tiff", outputdir + title3);
run("Close All");
    }
}
//Close and reset ROI Manager
roiManager("reset");
close("*");
```

Macro 'Green AUTO PSF Deconvolution'

```
// Set variables
inputdir= getDirectory("C3");
list=getFileList(inputdir);
outputdir= getDirectory("C3_DECON");

for(i=0;i<list.length;i++){
    if (endsWith(list[i], ".tif")){
// Call CLIJ2
        run("CLIJ2 Macro Extensions", "cl_device=[AMD Radeon Pro 5500M
Compute Engine]");
// Open data
        open(inputdir+list[i]);
        image1= getTitle();
        Ext.CLIJ2_push(image1);
        number= nSlices;
        run("Diffraction PSF 3D", "index=1.520 numerical=1.40 wave-
length=488 longitudinal=0 image=37.30 slice=37.30 width,=100 height,=100
depth,=number normalization=[Peak = 255] title= PSF_ +'number'+_G");
        PSF= getTitle();
        Ext.CLIJ2_push(PSF);
        saveAs("tiff", outputdir + PSF);

// Deconvolve Richardson-Lucy FFT
        num_iterations = 25.0;
        Ext.CLIJx_deconvolveRichardsonLucyFFT(image1, PSF, image3,
num_iterations);
        Ext.CLIJ2_pull(image3);
        image3 = "DECON_25RL_" + image1;
// Save resulting image
        saveAs("tiff", outputdir + image3);
        close("*");
// Cleanup by the end
Ext.CLIJ2_clear();

    }
}
```

Macro 'Far red AUTO PSF Deconvolution'

```
// Set variables
inputdir= getDirectory("C2");
list=getFileList(inputdir);
outputdir= getDirectory("C2_DECONV");

for(i=0;i<list.length;i++){
    if (endsWith(list[i], ".tif")){
// Call CLIJ2
        run("CLIJ2 Macro Extensions", "cl_device=[AMD Radeon Pro 5500M
Compute Engine]");
// Open data
        open(inputdir+list[i]);
        image1= getTitle();
        Ext.CLIJ2_push(image1);
        number= nSlices;
        run("Diffraction PSF 3D", "index=1.520 numerical=1.40 wave-
length=647 longitudinal=0 image=37.30 slice=37.30 width,=100 height,=100
depth,=number normalization=[Peak = 255] title= PSF_ +'number'+_G");
        PSF= getTitle();
        Ext.CLIJ2_push(PSF);
        saveAs("tiff", outputdir + PSF);

// Deconvolve Richardson-Lucy FFT
        num_iterations = 25.0;
        Ext.CLIJx_deconvolveRichardsonLucyFFT(image1, PSF, image3,
num_iterations);
        Ext.CLIJ2_pull(image3);
        image3 = "DECON_25RL_" + image1;
// Save resulting image
        saveAs("tiff", outputdir + image3);
        close("*");
// Cleanup by the end
Ext.CLIJ2_clear();

    }
}
```



```
run("Analyze Particles...", "display clear include summarize
in_situ");
//Saving Results
selectWindow("Results");
saveAs("Results_area"+mask, outputdir);
run("Close" );
// Closing
close("*");
}
```


Macros 'Complete quantification' for internalisation and co-localisation quantification

```
// Set variables
inputC2=getDirectory("C2_DECONV");
listC2=getFileList(inputC2);

inputC3=getDirectory("C3_DECONV");
listC3=getFileList(inputC3);

inputmask=getDirectory("CYTO_MASKS");
listmask=getFileList(inputmask);

outputdir= getDirectory("OUTPUT");

// Call CLIJ2
run("CLIJ2 Macro Extensions", "cl_device=[AMD Radeon Pro 5500M
Compute Engine]");

for(i=0;i<listC2.length;i++){
    if (endsWith(listC2[i], ".tif")){
// Open data
        open(inputC2+listC2[i]);
        c2= getTitle();

        open(inputmask+listmask[i]);
        mask= getTitle();

        open(inputC3+listC3[i]);
        c3= getTitle();

//AND operator for C2_INS
        imageCalculator("AND create stack", c2 , mask);

        c2ins= "INS_" + getTitle();
        saveAs("Tiff", outputdir + c2ins);

//AND operator for C3_INS
        imageCalculator("AND create stack", c3 , mask);

        c3ins= "INS_" + getTitle();
        saveAs("Tiff", outputdir + c3ins);

//AND operator for COLOC
        imageCalculator("AND create stack", c2ins , c3ins);

        coloc= "COLOC" + getTitle();
        saveAs("Tiff", outputdir + coloc);

// 3D object detection
        Ext.CLIJ2_clear();

// C2_INSIDE
// Load image to CLIJ
        Ext.CLIJ2_push(c2ins);

// Segmentation
        threshold = 25.0;
        Ext.CLIJ2_greaterConstant(c2ins, binary_image, threshold);
        Ext.CLIJ2_connectedComponentsLabelingDiamond(binary_image, la-
bel_image);

// Exclude Labels Outside Size Range
```

```

        minimum_size = 16.0;
        maximum_size = 999999.0;
        Ext.CLIJ2_excludeLabelsOutsideSizeRange(label_image,    large_la-
bel_image, minimum_size, maximum_size);

// show result
        Ext.CLIJ2_pull(large_label_image);
        run("glasbey_on_dark");

// measure
        Ext.CLIJ2_statisticsOfLabelledPixels(c2ins, large_label_image);
        image4= getTitle();
        saveAs("3DOC_"+c2ins+".tiff", outputdir);

//Saving Results
        selectWindow("Results");
        saveAs("Results", outputdir+"3DOC_"+c2ins+".csv");
        Ext.CLIJ2_clear();
        run("Close" );

// C3_INSIDE
// Load image to CLIJ
        Ext.CLIJ2_push(c3ins);

// Segmentation
        threshold = 25.0;
        Ext.CLIJ2_greaterConstant(c3ins, binary_image, threshold);
        Ext.CLIJ2_connectedComponentsLabelingDiamond(binary_image,    la-
bel_image);

// Exclude Labels Outside Size Range
        minimum_size = 16.0;
        maximum_size = 999999.0;
        Ext.CLIJ2_excludeLabelsOutsideSizeRange(label_image,    large_la-
bel_image, minimum_size, maximum_size);

// show result
        Ext.CLIJ2_pull(large_label_image);
        run("glasbey_on_dark");

// measure
        Ext.CLIJ2_statisticsOfLabelledPixels(c3ins, large_label_image);
        image4= getTitle();
        saveAs("3DOC_"+c3ins+".tiff", outputdir);

//Saving Results
        selectWindow("Results");
        saveAs("Results", outputdir+"3DOC_"+c3ins+".csv");
        Ext.CLIJ2_clear();
        run("Close" );

// COLOC_INSIDE
// Load image to CLIJ
        Ext.CLIJ2_push(coloc);

// Segmentation
        threshold = 25.0;
        Ext.CLIJ2_greaterConstant(coloc, binary_image, threshold);
        Ext.CLIJ2_connectedComponentsLabelingDiamond(binary_image,    la-
bel_image);

// Exclude Labels Outside Size Range
        minimum_size = 16.0;

```

```

        maximum_size = 999999.0;
        Ext.CLIJ2_excludeLabelsOutsideSizeRange(label_image,    large_la-
bel_image, minimum_size, maximum_size);

// show result
        Ext.CLIJ2_pull(large_label_image);
        run("glasbey_on_dark");

// measure
        Ext.CLIJ2_statisticsOfLabelledPixels(coloc, large_label_image);
        image4= getTitle();
        saveAs("3DOC_"+coloc+".tiff", outputdir);

//Saving Results
        selectWindow("Results");
        saveAs("Results", outputdir+"3DOC_"+coloc+".csv");
        Ext.CLIJ2_clear();
        run("Close" );

// Closing
        close("*");
    }
}

// -FIN-

```


3.3 Chapter 3: Biointeraction and hyperthermia effects of magnetoplasmonic nanodomes on cancer cells.

Biointeraction and hyperthermia effects of magnetoplasmonic nanodomains on cancer cells.

A. Aranda-Ramos^a, Z. Li^b, N. Bast^b, L. Pou-Macayo^a, M. Royo-Llonch^c, B. Sepúlveda^b, and C. Nogués^{a,*}.

Affiliations:

^a Departament Biologia Cel·lular, Fisiologia i Immunologia. Unitat Biologia Cel·lular. Facultat Biociències. Campus de la UAB, 08193, Bellaterra (Cerdanyola del Vallès) Barcelona, Spain.

^b Catalan Institute of Nanoscience and Nanotechnology (ICN2). Consejo Superior de Investigaciones Científicas (CSIC) and Barcelona Institute of Science and Technology (BIST) Campus UAB, Bellaterra 08193, Barcelona, Spain

^c Department of Marine Biology and Oceanography, Institut de Ciències del Mar, Barcelona, Spain.

* Corresponding author carne.nogues@uab.cat

Introduction.

Gold and iron oxide magnetoplasmonic nanodomains (MPNDs) are one of the most promising systems within the field of biomedicine and biotechnology¹. Their unique physico-chemical properties and their magnetoplasmonic characteristics offer a great opportunity for the development of a wide range of applications that will impact health sciences, improving areas like diagnostics by enhancing the efficiency of biosensors² and contrast agents for Magnetic Resonance Imaging (MRI) or therapy providing new strategies for controlled drug delivery-systems and cancer therapies³. In fact, one of the magnetoplasmonic properties of MPNDs is their application for magnetic and magnetoplasmonic hyperthermia⁴. Hyperthermia has been used to treat diseases from ancient times, but the precise control of this kind of treatment wasn't achieved until recently as a result of the application of nanomedicine research in tumour ablation therapies such as optical coherence tomography ablation. It is thanks to the application of the advances of material sciences in the nanoscale that hyperthermia, as a cancer therapy against malignant tumours, has been particularly explored and studied in the last two decades as a form of applied precision medicine⁵. It is widely known that cancer cells are more sensitive to heat than non-tumoral ones⁶. MPNDs act as localised heating sources in the region where they are situated when exposed to triggers like an alternating magnetic field (AMF) or a laser at a specific wavelength due to their plasmon resonance properties⁷. A local temperature increase in the targeted area activated by the trigger induces cell death or alters the growth of tumoral cells⁸. Moreover, magnetic and magnetoplasmonic hyperthermia have been used to promote synergistic effects by sensitising tumoral cells when combined with other conventional treatments such as radiation or chemotherapy⁵. Hyperthermia causes changes in the metabolic and structural repair mechanisms within the cell, as proved by Krawczyk et al, which described that hyperthermia caused cells to become deficient in a DNA repair mechanism (inactivating BRCA2) becoming more sensitive to drugs that induce DNA damage⁹. Despite this clear evidence, the cell death mechanisms activated by the magnetic and magnetoplasmonic hyperthermia treatment of cells and the relevant parameters that control the triggering of each mechanism are not yet completely identified. If there are differences between tumoral and non-tumoral cells in terms of this activation is also unknown. This information is crucial to be able to control the activation of regulated cell death mechanisms¹⁰ and to try to control the pro-inflammatory immune response that could be sometimes negative for tumour treatments, as it involves non-desirable processes such as the tumour

invasion or metastasis, and contribute to their side-effects¹¹. Currently, most of the in vitro studies that analyse the efficacy of the hyperthermia treatment are being performed in monolayer cell cultures and focused on static conditions, and most of them lack specific quantification at the nanoscale when analysing their biointeraction with cells. In this study, we analysed the effect of magnetic actuation on static and dynamic conditions in 2D cell cultures to replicate blood circulation conditions closer to what happens within the tumour. The present study also explores the differential pathways of regulated cell death induced in tumoral versus non-tumoral cells under different hyperthermia conditions.

Materials and methods.

Magnetoplasmonic nanodomes.

MPNDs were synthesised following the method described in Li et al, 2018. MPND are made from polystyrene and modified by electron beam evaporation to form a 40 nm semishell of gold and iron on top of the core. Their hydrodynamic diameter is around 114 nm as determined by dynamic light scattering and remains stable in MilliQ water as a colloidal suspension for months¹.

MPNDs solutions were freshly prepared before exposure to cell cultures by centrifugation in water for 15 min at 5000 rpm and were finally resuspended and sonicated for 1 min at room temperature (RT) using an ultrasonication bath (FisherBrand) in 500 µL of cell culture medium. Finally, the MPNDs solutions was further diluted to fit the desired concentration.

Cell Culture.

Human epithelial cervical adenocarcinoma Cells (HeLa, ATCC) were cultured in Minimal Essential Medium (Gibco, Life Technologies) supplemented with 10% foetal bovine serum (Gibco) and 2 mM L-Glutamine (Life Technologies). Human epithelial breast adenocarcinoma cells (SKBR-3, ATCC) were used as tumoral cell/metastatic line and cultured in McCoy's 5A modified medium (Gibco) supplemented with 10% foetal bovine serum (Gibco). Human epithelial breast cells (MCF10a, ATCC) were used as non-tumorigenic cell line and were cultured in DMEM/F:12 (Gibco) supplemented with 5% horse serum (Gibco), 20 ng/ml epidermal growth factor (Gibco), 0.5 mg/ml hydrocortisone (Sigma-Aldrich), 100

ng/ml cholera toxin (Sigma) and 10 μ g/ml human recombinant insulin (Gibco). All cell lines were maintained at 37 °C in a 5% CO₂ humidified atmosphere (standard conditions).

Cytotoxicity evaluation.

For cytotoxicity experiments SKBR-3 and MCF10a cells were seeded in 24-well plates (Nunc, Thermo Scientific) at a density of 3×10^4 cells per well and incubated in standard conditions for 24 h. Three concentrations of MPNDs were tested: 5, 10 and 50 μ g/mL diluted in the cell line's corresponding cell culture media. MPNDs solutions were added to the cell cultures and incubated in standard conditions for 3 h. After incubation time and to remove non-internalised MPNDs, cell media was replaced with fresh medium and cells were incubated an additional 24 h before evaluating the effect of MPNDs on cell viability. After 24 h post-exposure to MPNDs, cell cultures were incubated with 0.1 mg/mL solution of 3-(4,5-Dimethylthiazol-2-yl)-2,5-Diphenyltetrazolium Bromide (MTT) (Sigma-Aldrich) in medium for 3 h to allow formazan crystals formation by viable cells' reduction activity. After 3 h of incubation, the crystals obtained were dissolved in dimethyl sulfoxide (DMSO) (Sigma-Aldrich) and the supernatant obtained transferred to a new 24-well plate. Absorbance was quantified at 550 nm using a Multilabel plate reader (Victor™ X3 Multilabel Plate Reader, Perkin Elmer). Three independent experiments were performed, wells containing only DMSO were used as blank and non-exposed to MPNDs cell cultures were used as control for each corresponding replicate.

Alternatively, cytotoxicity was also analysed using the sulforhodamine B (SRB) cytotoxicity assay (Canvax Biotech). In this case, cells were seeded on 6-well plates at a density of 1.5×10^5 cells per well. After 24 h of incubation with 5, 10, 25 and 50 μ g/mL MPNDs solutions (keeping the MPNDs-cell ratio), cell cultures were washed twice with PBS and 1.25 mL of cold SRB Fixative Reagent was added to each well and was incubated for 1 h at 4°C. After that, wells were washed four times with 2.5 mL/well distilled water (removing excess fixative and serum proteins). Plates were further incubated at 37°C for 15 min to remove excess liquid from the wash. Next, 1.25 mL SRB Solution was added to each well and the plates were incubated at room temperature (RT) for 30 min in the dark. Subsequently, SRB Solution was washed with the kit's Wash Solution, four times (to remove unbound dye). The washed plates were air dried overnight in the dark. Finally, the bound SRB was solubilised by adding 2.5 mL of SRB Solubilisation Buffer to each well and shaking for 5 min on a

shaker platform at low speed. The contents of each well were transferred to a 2 mL Eppendorf and centrifuged for 5 min at 14,000 rpms in order to remove cell debris. A volume of 500 μ L of the supernatant of each well was transferred to a 24-well plate and the absorbance was read at 565 nm with a VictorTMX3 Multilabel Plate Reader (Perkin Elmer). The background absorbance was read with a reference filter at 690 nm and the SRB Solubilisation Buffer signal was subtracted. The OD of SRB in each well is directly proportional to the cell number in culture.

Scanning electron microscopy association evaluation.

An evaluation of the association of MPNDs at different concentrations (5, 10, 50, 200 μ g/mL) was performed using HeLa cell cultures. Cells were seeded in 24-well plates (Nunc, Thermo Scientific) at a density of 3×10^4 cells per well and incubated in standard conditions for 24 h. After 24 h of MPNDs solution incubation, cells were rinsed twice in 0.1 M Sodium Cacodylate Buffer at pH 7.3 (TAAB), fixed using a 2.5 % Microscopy Glutaraldehyde solution for electron microscopy (Merck) in 0.1 M Sodium Cacodylate Buffer (TAAB) for 45 min at RT and rinsed again twice in 0.1 M Sodium Cacodylate Buffer. Cell dehydration was done in a series of ethanol washes (50, 70, 90 and twice 100 %), for 7 min each. Finally, cells were dried in hexamethyldisilazane (HMDS; Electron Microscope Science) for 15 min after which HMDS was withdrawn, and samples were let to dry overnight. Samples were mounted on special stubs, metallised in Au/Pd scatterer for 5 min and observed using the secondary electron detector of a SEM (Zeiss Merlin).

Flow cytometry.

Internalisation was firstly evaluated by flow cytometry using orange fluorescent-core MPNDs. SKBR-3 and MCF10a cells were seeded on 6-well plates at a density of 1.5×10^5 cells per well and let to attach for 24 h. Then, cell cultures were exposed to 5, 10 and 50 μ g/mL MPNDs solutions for 3 h. After incubation time the solutions were removed and cell cultures were washed twice with HBSS. Cultures were further trypsinised with 1x Trypsin-EDTA (Biowest) diluted in HBBS and neutralised after 5 min with cell medium. The cellular suspensions were analysed using the cytometer FACSCanto (BD Biosciences) equipment and FACSDiva[®] Software (BD Biosciences). At least 10^4 cells (events) were included (when

possible) in each measurement and analysis. Control cell cultures were used to establish the negative and positive association gates and thus to delimit the MPNDs-cell positive association area. Data obtained were processed using FACSDiva® 7.0 Software (Becton Dickinson) and FACSAnalyzer (Version 0.9.22-alpha). The experiment was done in triplicate.

Magnetic actuation.

To test the magnetically-induced targeting capabilities of MPNDs under magnetic actuation against tumoral SKBR-3 cell cultures, magnetic actuation experiments were performed. Magnetic actuation consisted on placing a spherical neodymium magnet at the bottom of the cell culture growth support, either a 35 mm glass-bottom microscopy dish (Ibidi) for static cultures or a fluidic chamber (μ -Slide I 0.8mm Luer ibiTreat: #1.5 polymer coverslip, Ibidi) in dynamic cultures, during the MPNDs incubation time tested. The magnet was placed using a special support that kept the magnet in a fixed place approximately 0.5 mm from the bottom of the cell culture support while the incubation was performed. For static conditions the magnetic actuation was tested on SKBR-3 cells incubated for 30 min with 10 μ g/mL MPNDs in medium. For dynamic conditions, the magnetic actuation was tested in SKBR-3 and MCF10a cell cultures exposed to 0.333 μ g/mL MPNDs solution in media (respecting the MPNDs amount per cell used in static conditions) for 24 h.

Confocal Laser Scanning Microscopy (CLSM).

As a first approach to the visualisation of MPNDs internalisation in cell cultures, HeLa cells were used as a model. HeLa cells were seeded in glass bottom dishes (MatTek Corporation) at a density of 3×10^4 cells per dish and incubated in standard conditions for 24 h. Then, 10 μ g/mL of fluorescent MPNDs ($\lambda_{\text{excitation}} = 575$, $\lambda_{\text{emission}} = 610$ nm) solutions were added to cell cultures and incubated for 3 h in standard conditions. After incubation, cells were washed twice with HBSS and 1 mL of fresh medium was added to the sample. Finally, cells were stained with 1 μ l of Cell Mask™ Deep Red plasma membrane stain (Life Technologies), to reveal the plasma membrane and 0.5 μ l of Hoechst 33342 (Life Technologies) to expose the nucleus. Images were captured sequentially using an Olympus CLSM (Olympus FV1000). Three different lasers were used: 405, 559 and 635 nm, to visualise nucleus, MPNDs and plasma membrane, respectively. Stacks of images along the z-axis

were obtained for a selected area using the xyz mode of the CLSM, and the 3D analysis was done in Fiji¹² which was used to obtain overlapped images of all channels (nuclei, plasma membranes and MPNDs), as well as maximum and orthogonal projections. 3D reconstructions and cross-section projections were used to confirm MPNDs' internalisation. To test the magnetically-actuated targeting efficiency, the effects of magnetic concentration on internalisation and co-localisation of MPNDs in SKBR-3 cell cultures were analysed quantitatively. For the internalisation and co-localisation quantification experiments of the targeting efficiency through magnetic actuation, targeted tumoral SKBR-3 cell cultures were exposed to 10 µg/mL MPNDs in static conditions for either 30 min under magnetic actuation or 3 h without magnetic actuation. After treatment, cell cultures were fixed with 4% PFA in PBS for 15 min, followed by a permeabilisation with 0.1 % Triton X-100 in PBS for 15 min at RT and blocking with 5% PBS-BSA (Sigma-Aldrich) for 40 min at RT. Cell cultures were then incubated for 1 h at RT with mouse anti-EEA-1 monoclonal antibody (1:50 BD Biosciences 610457). Samples were sealed using parafilm (avoiding bubble formation) and kept at 4°C overnight in a humid chamber. Next day, samples were washed 3x with PBS, incubate for 1 h at RT with goat anti-mouse IgG antibody 647 (1:500; Life Technologies) while sealed with parafilm if needed (avoiding bubble formation). Lastly, cell cultures were washed twice with PBS before being labelled with 2 drops of ActinRed™ 555 (ReadyProbes™) Reagent (Rhodamine phalloidin) to reveal the actin cytoskeleton of the cell and 0.5 µL of Hoechst 33342 (Life Technologies) to visualise nuclei, according to manufacturers' instructions. Samples were finally mounted in Prolong Glass® antifade mounting media and let to cure at RT according to manufacturer's instruction at least 48 h before observation. Internalisation and co-localisation experiments were done in triplicate.

Images were captured with a confocal laser scanning microscope (Leica TCS-SP5 AOBS spectral; Leica Microsystems) using a Plan-Apochromatic 63x Oil objective (NA 1.4). Image acquisition of the cells was carried out sequentially with a 405 nm blue diode for the cell nucleus, a 488 nm Argon laser for the reflection of MPNDs, a 594 nm HeNe laser for the cytoskeleton and a 633 nm HeNe laser for EEA-1 labelled compartments. Stacks of images along the z-axis were obtained for a selected area using the xyz mode of the microscope at the highest resolution level available. Pinhole was set to 1 Airy disk units. Image size was set at 3296x3296, resulting in 37,3 nm/pixel size. Z-Depth size was set at 125 nm. ImageJ (Fiji)¹² was used to obtain overlapped images including all channels (nuclei, cell limit and

MPNDs) and to evaluate internalisation and localisation of MPNDs within the cells datasets that were post-processed through semi-automatic segmentation and macro processing.

Fluidic cultures.

To test the efficacy of magnetically targeting MPNDs to targeted cells (SKBR-3) under magnetic actuation in dynamic culture conditions a fluidic experiment was set. SKBR-3 and MCF10a cell cultures were seeded in a fluidic chamber (Ibidi) at a density of 36,000 cells/channel. Once allowed to attach overnight, cell cultures were exposed for 24 h to a 0,333 µg/mL MPNDs solution (respecting the amount of MPNDs per cell used in above-mentioned magnetic actuation static characterisations) using a fluidic pump system (Ibidi) at x30 the pressure to simulate the pressure of the blood that circulates within a breast tumour (due to the interstitial and oncotic pressure of the tumour)¹³ in the presence or absence of magnetic actuation at the bottom of the channel where cells were seeded.

For quantification, targeted tumoral SKBR-3 and non-tumoral MCF10a cell cultures exposed to MPNDs for 24 h in fluidic conditions were fixed with 4% paraformaldehyde (PFA) in PBS for 15 min, washed twice with PBS and then labelled with 2 drops of ActinRed™ 555 (ReadyProbes™) Reagent (Rhodamine phalloidin) according to manufacturer's instructions to reveal the actin cytoskeleton of the cell and 0.5 µL of Hoechst 33342 (Life Technologies) to visualise nuclei (according to manufacturers' instructions). Samples were finally immersed in immersion oil and kept at RT before observation. Fluidics experiments were done in triplicate.

Images were captured with a confocal laser scanning microscope (Leica TCS-SP5 AOBS spectral; Leica Microsystems) using a Plan-Apochromatic 63x Oil objective (NA 1.4). Image acquisition of the cells was carried out sequentially with a 405 nm blue diode for the cell nucleus, a 488 nm Argon laser for the reflection of MPNDs and a 594 nm HeNe laser for the cytoskeleton. Stacks of images along the z-axis were obtained for a selected area using the xyz mode of the microscope at the highest resolution level available. Pinhole was set to 1 Airy disk units. Image size was set at 3296x3296, resulting in 37,3 nm/pixel size. Z-Depth size was set at 125 nm. ImageJ (Fiji) was used to obtain overlapped images including all channels (nuclei, cell limit and MPNDs) and to evaluate localisation of MPNDs within the

cells datasets were post-processed through semi-automatic segmentation and macro processing.

Photo-thermal treatment.

SKBR-3 and MCF10a cells were seeded in cover glass-bottom dishes (Ibidi) at a density of 3×10^4 cells per dish (just in the area of the glass coverslip) and kept in standard conditions for 24 h. Next, the cell cultures were incubated in the presence or absence (control cultures) of 10 $\mu\text{g/mL}$ of MPNDs for 3 h. After incubation, the MPNDs solution was withdrawn and replaced with fresh medium and let inside the incubator to recover temperature before laser treatments.

The in-vitro photo-thermal treatments were carried out inside the incubator with controlled temperature of 37°C . The glass bottom dishes containing the cell cultures were placed on top of a support to allow the laser hitting the glass bottom dish from below. Photo-thermal treatment started once the temperature of the sample was stable at 37°C . The photothermal treatment was performed using the light from a collimated fibre-coupled laser diode with emission wavelength at 1064 nm (Laser Components). The incident intensity in the sample was approximately 3 W/cm^2 and the treated area was a circle of $\sim 150 \text{ mm}$ in diameter. Hyperthermia treatments were carried out for either 5 or 15 min by laser irradiation.

Cell death evaluation.

To evaluate the cytotoxicity of the photo-thermal treatment, after irradiation, cells were incubated again in standard conditions for 24 h and then incubated with the LIVE/DEAD[®] Viability and Cytotoxicity (Life Technologies) assay following manufacturer's guidelines. This kit is provided with two probes, calcein and propidium iodide that measure recognised parameters of cell viability (intracellular esterase activity) and plasma membrane integrity. Images were acquired using the inverted fluorescence microscope Olympus IX71 (Olympus) and processed through ImageJ (Fiji). Three independent experiments were performed for each condition.

For caspase-3 activation evaluation, after irradiation cell cultures exposed to hyperthermia treatments were incubated again in standard conditions for 24 h and then washed with

phosphate buffer saline solution (PBS) gently, fixed with 4% PFA in PBS and permeabilised with 0.1% Triton X-100 in PBS for 15 min at RT. Next, cell cultures were washed once with PBS and blocked using a 5% PBS-BSA (Sigma-Aldrich) for 30 min at RT. After blocking, cultures were incubated for 1 h at RT with rabbit anti-active caspase 3 polyclonal antibody (1:1000; Sigma-Aldrich. Ref: C8487), washed 3 times with PBS and then incubated 1 h at 37 °C with Alexa 594-conjugated goat anti-rabbit IgG antibody (1:2000; Life Technologies. Ref: A-11012). Finally, cells were washed thrice with PBS, counterstained with 0.5 µl of Hoechst 33342 (Life Technologies) for 3 min and let to air dry for 1 min at RT and mounted with Prolong Glass antifade mounting medium.

Images were acquired using the inverted fluorescence microscope Olympus IX71 (Olympus) and processed through ImageJ (Fiji) macros to extract information of each channel. Three independent experiments were performed for each condition.

Data analyses.

Data obtained from images through segmentation and quantification macros from CLSM and cell death pathway determination experiments were collected, concatenated, summarised and analysed through R and RStudio¹⁴. Once prepared for statistical analyses, MPNDs cytotoxicity, internalisation in static and dynamic conditions, co-localisation, hyperthermia and caspase-3 activation experimental data were statistically tested for differences using Kruskal–Wallis test in Prism® 9.0 software (Graphpad). Alpha was set at 0,05 and therefore significance levels were reported as follows: * when $p < 0.05$, ** when $p < 0.01$, *** when $p < 0.001$ and **** when $p < 0.0001$ unless stated otherwise on the figure footer

Results and discussion.

Cytotoxicity evaluation in, SKBR-3 and MCF10a cells.

The cytotoxicity in SKBR-3 and MCF10a was evaluated. No statistical differences were found in SKBR-3 and MCF10a between 5, 10, 25 and 50 µg/mL MPNDs-exposed cell cultures and their control groups, either using MTT or SRB assay (Fig 1). The only statistical difference observed was between 10 and 25 µg/mL MPNDs-treated samples in SKBR-3 cells analysed by MTT were 10 µg/mL led to a higher viability. These results were expected

because the cytotoxic effect of MPNDs at the same concentration was tested in Hela cells in a previous work¹.

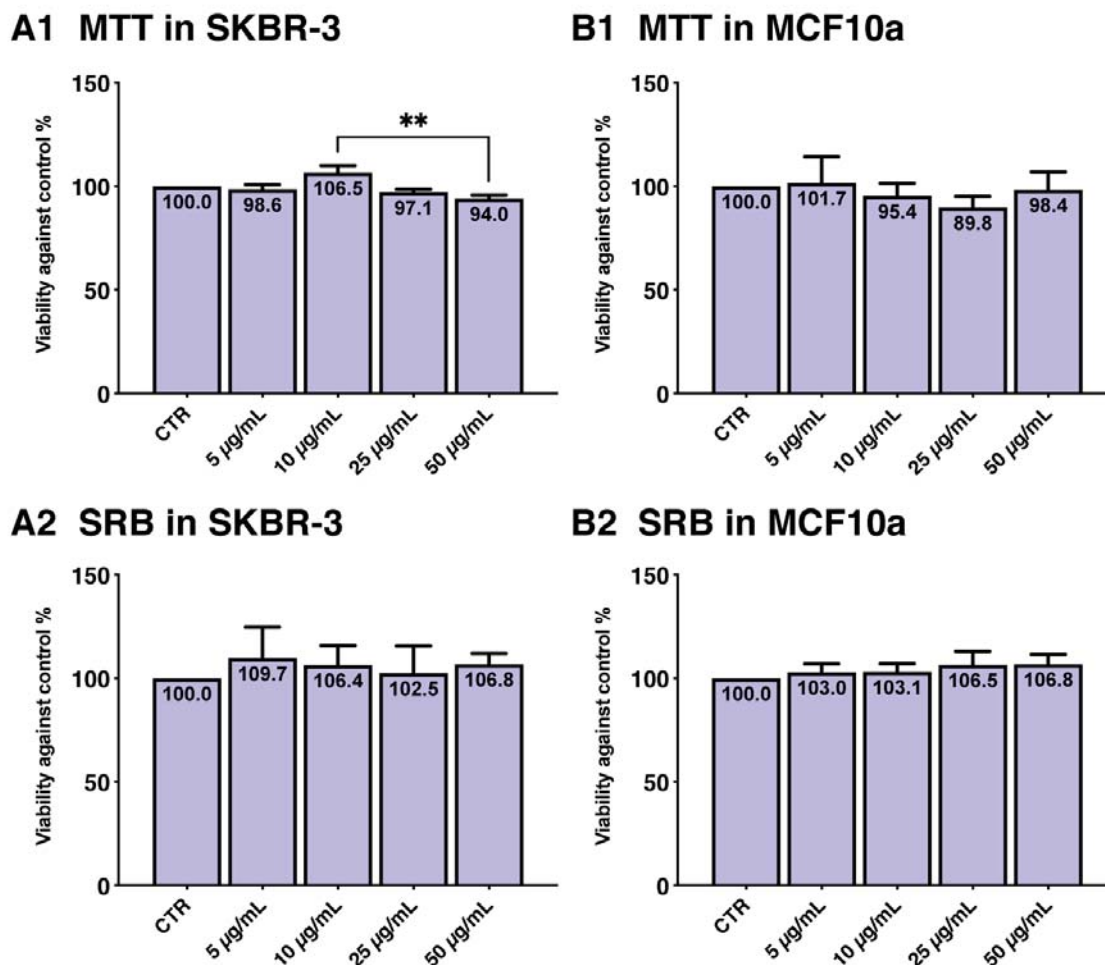


Figure 1 Viability of SKBR-3 and MCF10A cells after exposure to 5, 10, 25 and 50 µg/mL of MPNDs in complete media for 3 h + 24 h post-incubation. A1 SKBR-3 cells and **B1** MCF10A cells show plotted bars depicting viability by Methylthiazolyldiphenyl-tetrazolium-bromide (MTT) absorbance analysis, while **A2** SKBR-3 cells and **B2** MCF10A cells depict the viability by sulforhodamine B (SRB) absorbance analysis. All values depicted as the % viability +/- standard deviation, after normalisation against the absorbance values of the control group (0 µg/mL). Statistical differences were found between viability of 10 µg/mL and 50 µg/mL MPNDs-treated groups (**, $p < 0.01$) concentrations. Experiment done in triplicate.

All the viability values obtained in SKBR-3 and MCF10a cell lines are above the common cytotoxicity threshold set at 80% viability according to UNE-EN ISO 10993-5:2009¹⁵. No interferences were found using either MTT or SRB assays, contrary to what has been described that can happen using metal-containing ENMs¹⁶. No apparent effect on viability was found contrary to previously published data on iron-containing ENMs, that can induce ferroptosis¹⁷.

MPNDs association to cells.

Scanning electron microscopy images were obtained of MPNDs after their synthesis by electron beam evaporation with gold and iron to form the semi-shell covering the original polystyrene nanoparticle (Fig 2A). This visualisation led to the conclusion that MPNDs stay mono-dispersed in majority and allowed for MPNDs quantification while on the silicon wafer before their re-dispersion to estimate the quantity of MPNDs and generate a 500 µg/mL MPNDs stock solution. As an initial exploration of the association of MPNDs with cell cultures we chose HeLa cell as a model, which was previously used in our earlier work using MPNDs¹. Images of the interaction with HeLa cells were also analysed to evaluate how MPNDs behave in biological conditions and interact with human tumoral cells after 24 h of exposure. The images (Fig 2B-2F) show that when cells were incubated with 5 and 10 µg/mL MPNDs, the membrane showed some protrusions (bumps, depicted by white arrows) despite the cells were perfectly attached, probably because of MPNDs internalisation and storage within the cell. An increasing level of adsorption to the plasma membrane was observed along the increasing concentrations of MPNDs solutions. Higher concentrations (50 and 200 µg/mL of MPNDs) lead to big clumps of particles outside the cells (yellow arrows) probably too big to be internalised, some protrusions and increased membrane bulging were also visible in these cells indicating endocytic activity and MPNDs engulfment. Cell-MPNDs interactions and membrane morphology modifications revealed by SEM and described above are in accordance to previously described adsorption, engulfment and internalisation morphologies observed through SEM using other kinds of magnetic and metal oxide NPs. Cell morphology modifications and the evidence of internalisation and protrusions formation on the cell plasma membrane corresponding to F-actin in specific areas of the cell membrane in contact with NPs was observed in human fibroblasts^{18,19} and macrophages²⁰. Clumping of NPs on top of the cell membrane and the increased difficulty to enter the cell when forming big aggregates has been previously described in macrophages^{21,22}

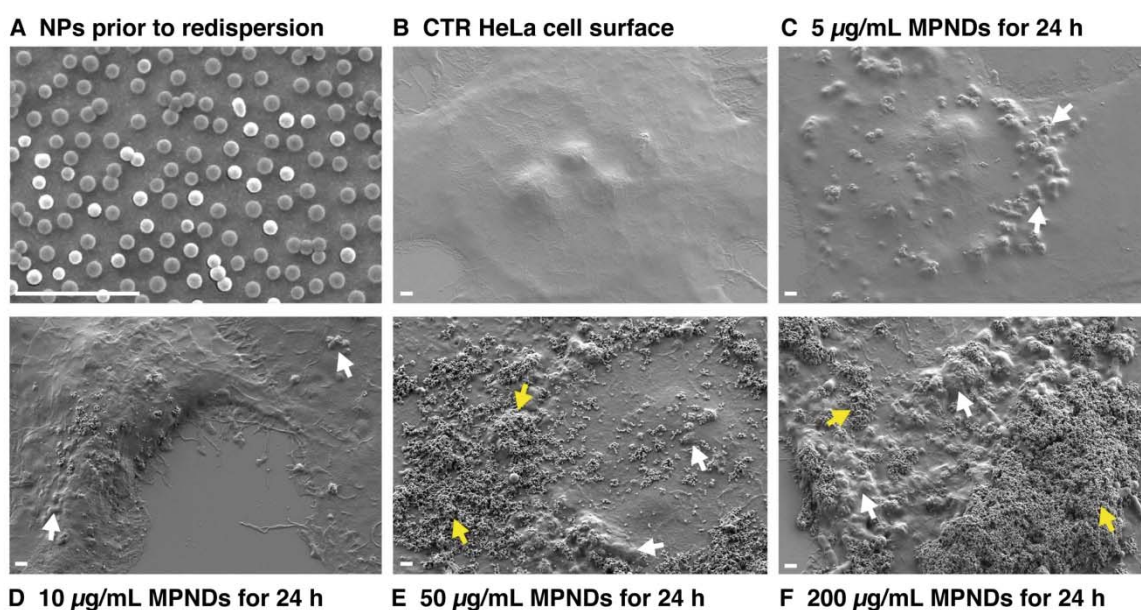


Figure 2. SEM images analysis. **A** MPNDs on a silicon wafer after their synthesis by electron beam evaporation of Au and Fe atoms on the surface of immobilised and dispersed latex nanoparticles. **B** HeLa cells non-exposed to MPNDs **C, D, E and F** SEM images of HeLa cells exposed for 24 h to 5, 10, 50 and 200 $\mu\text{g}/\text{mL}$ MPNDs. Differences in MPNDs interactions with the cells can be observed as concentration increases, membrane bulging (white arrows) and protrusions are visible in 5 and 10 $\mu\text{g}/\text{mL}$ MPNDs-exposed cultures as an indication of engulfment and internalisation in HeLa cells, while large aggregates are observed on the plasma membrane (yellow arrows) and inside the cells for higher concentrations. Control (CTR)

This imaging technique can yield important information to visualise and analyse changes in 3D cell morphology and therefore their health status, and details of cellular interactions with MPNDs tested, elucidating mechanisms of adsorption and uptake of nanomaterials on human tumoral cells. Based on the obtained results, and in accordance with the cytotoxicity and visualisation internalisation data an optimal MPNDs concentration of 10 $\mu\text{g}/\text{mL}$ was set for the rest of the experimental setup using SKBR-3 and MCF10a cells.

MPNDs Internalisation in static conditions.

MPNDs internalisation was evaluated by flow cytometry using orange fluorescent-core MPNDs. Due to the high-throughput nature of the technique, flow cytometry is one of the most common methods used to elucidate ENM internalisation in mammalian cells. It is based on the analysis of the fluorescence signals coming from individual cells as they cross the cytometry channel at different excitation wavelengths. Increasing concentrations (5, 10

and 50 µg/mL) of MPNDs were incubated for 24 h with HeLa cells. An example of the outputs produced by the data analyses from flow cytometry experiments can be observed in figure 3.

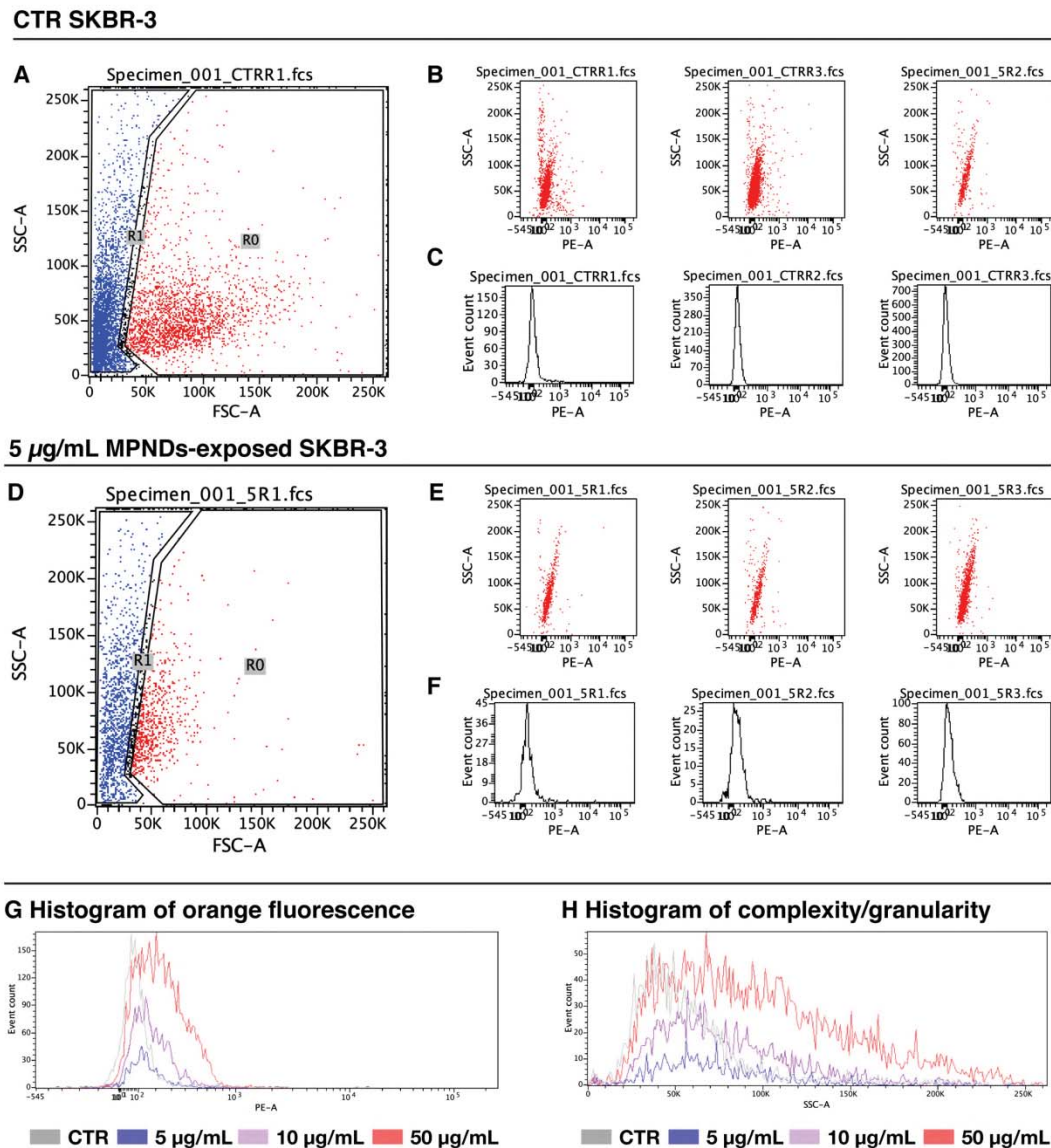


Figure 3 Flow cytometry analyses from CTR SKBR-3 cells and MPNDs-exposed SKBR-3 cells after 24 h incubation. **A** CTR cells and **D** 5 µg/mL MPNDs-exposed SKBR-3 cells' cytogram showing the whole population with the gates corresponding to the debris (R1) and the region corresponding to individual cells (R0). **B** CTR and **E** 5 µg/mL MPNDs-exposed individual SKBR-3 cells orange fluorescence cytogram, respectively. **C** CTR and **F** 5 µg/mL MPNDs-exposed cells their histogram of event counts vs orange fluorescence detected. Side scattering area (SSC-A), Orange fluorescence area (PE-A). **G** Overlapped histograms from one replicate of individual SKBR-3 cells and their detected orange fluorescence signal in CTR (gray) and MPNDs-exposed (purple= 5 µg/mL, pink= 10 µg/mL and red= 50 µg/mL) samples **H** Overlapped histograms from one replicate of individual SKBR-3 cells and their complexity/granularity signal in CTR (gray) and MPNDs-exposed (purple= 5 µg/mL, pink= 10 µg/mL and red= 50 µg/mL) samples. Control (CTR)

Despite being able to visualise the cell events in data cytograms, fluorescence-based separation was difficult to achieve due to overlapping population with control cells, possibly due to a combination of the autofluorescence detected (even if signal detection was compensated) and the quenching activity on fluorescent markers of MPNDs. This quenching effect due to the metals present on the MPNDs design, can be observed when analysing the histograms (Fig 3G), where 5 $\mu\text{g}/\text{mL}$ MPNDs-exposed SKBR-3 cells' "orange fluorescent" signal is completely overlapped with the fluorescent signal of the control group. This phenomenon is based on a transference of energy from the excited fluorochrome molecules to the metal semi-shell formed of iron and gold atoms that quench their fluorescence emission as described in literature²³⁻²⁷. An increasing number of cells were detected as MPNDs-positive as the concentration increases after 3 h incubation time. This increase is observable both by "orange fluorescence" signal detection and "complexity/granularity" analysis, proving the relationship between MPNDs uptake and the increased fluorescence and complexity/granularity of cells exposed to MPNDs. This is in accordance to observed dose-dependent increases in cellular granularity indicating active cellular uptake mechanisms^{28,29}. The overlapping signals at low concentrations, due to the quenching effect of the metallic bilayer of MPNDs, and the difficulty to quantify the actual number of NPs based on fluorescence signal and complexity/granularity, as previously described in literature³⁰, it was decided to turn to CLSM visualisation and 3D data analysis techniques moving forward in the internalisation characterisation.

Thus, CLSM was used to test the internalisation on HeLa cell cultures exposed to MPNDs at 10 $\mu\text{g}/\text{mL}$ for 24 h (Fig 4). Since the Fe/Au bilayer induces a 5-fold reduction of the fluorescence of MPNDs compared to the fluorescent core bare NPs used for MPNDs synthesis¹, we used the CLSM mode to detect the reflected signal of the metallic compounds of the bilayer. Moreover, this kind of detection allows for precise MPNDs detection due to its different properties compared to fluorescence signal. Reflected signal does not need to be deconvolved to restore the optical degradation across the axes, especially the z-axis, due to light diffraction and mounting media of choice. Thanks to the observation using the reflected light, MPNDs are visible inside the cell limits, forming small aggregates that indicates a possible transportation within the endolysosomal system after 24 h of MPNDs exposure. It was proved that 24 h are enough for MPNDs to enter HeLa cells in static conditions and the cells show overall a good health based on their morphology. Internalisation of magnetoplasmonic NPs like gold nanorods³¹ and $\text{Fe}_3\text{O}_4/\text{Au}$ nanocomposites³² in HeLa

cells has been previously described, with and without magnetic field manipulation to enhance the interaction between NPs and cells.

However, in the present study, HeLa cells display a higher MPNDs uptake than that of the above-mentioned studies, despite no magnetic field concentration was applied in this experiment. Although the NPs and goals of the above-mentioned studies are similar to the present study, the concentrations, experimental conditions and techniques are different or are not stated. Both publications fail to differentiate by cell segmentation the NPs within the cell limits and the ones attached or outside the cell. Since the uptake efficiency was not quantified, only the qualitative comparison between the images provided is possible.

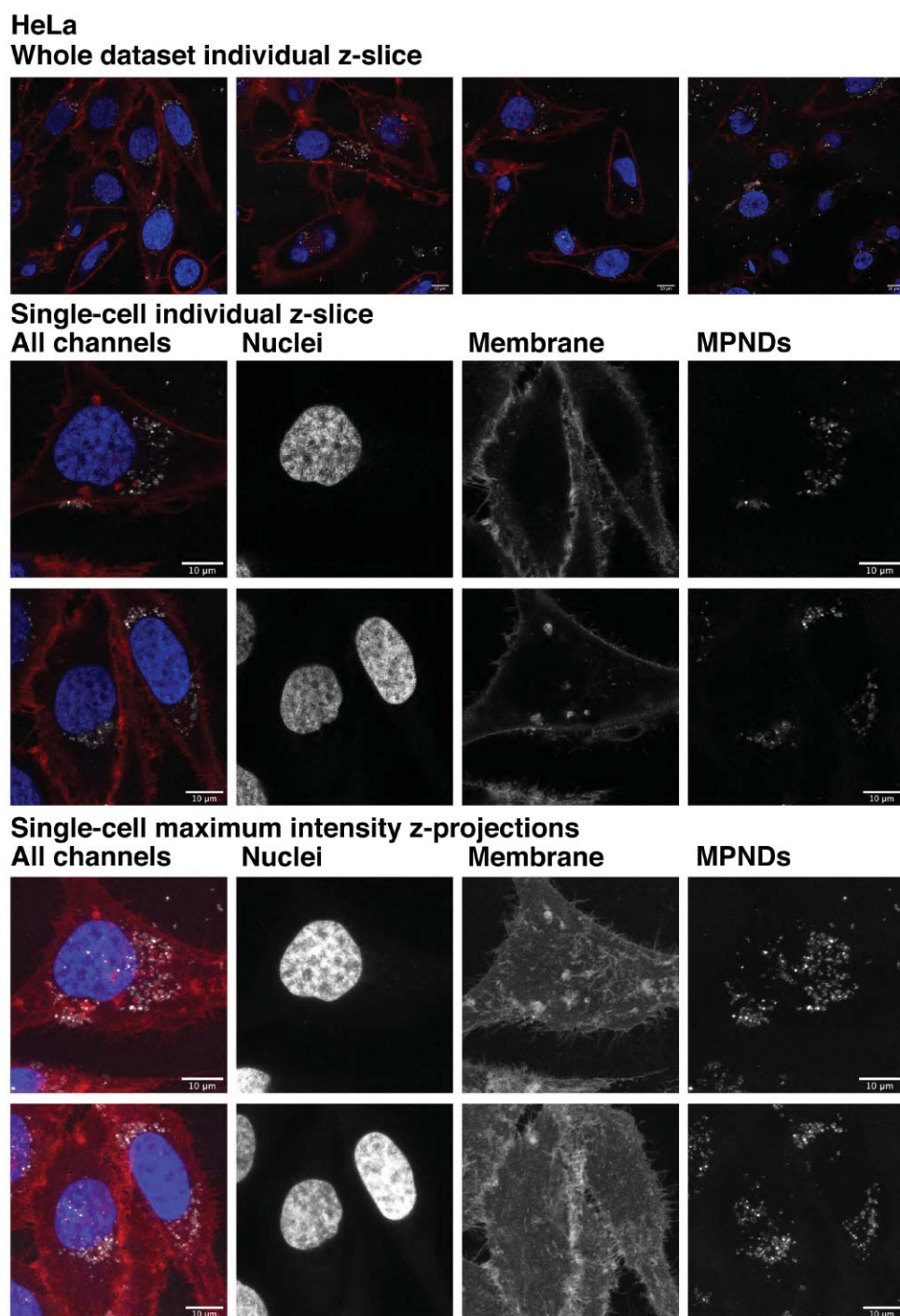


Figure 4 CLSM images of 3D stacked datasets of HeLa cells exposed to 10 $\mu\text{g}/\text{mL}$ MPNDs solutions for 24 h. Top row are snapshots of a single z-slice of the whole dataset (multiple cells per field). The rest of rows are detailed views of 1 or 2 cells in single z-slice or maximum intensity z-projections with composites of 3 channels in fake colour and each individual channel split.

Effect of magnetic actuation on MPNDs internalisation and co-localisation under static conditions.

Due to the nature of the MPNDs, that is, their semi-shell Fe composition, a neodymium magnet was used to concentrate the MPNDs in the center of the glass-bottom dish used as cell culture growth area. To compare the effect of the magnetic actuation on the internalisation in SKBR-3 targeted cell cultures, incubation of MPNDs (10 $\mu\text{g}/\text{mL}$) was reduced to 30 min in cell cultures exposed to the magnet compared to the 3h incubation in the cell cultures not exposed to the magnet.

The internalisation efficiency was almost thrice (193%) of that without magnetic actuation using 6 times less time for MPNDs incubation (Fig 5). Magnetic targeting of magnetic and magnetoplasmonic NPs have previously been described in literature³³ as observed by TEM in colon carcinoma cells.

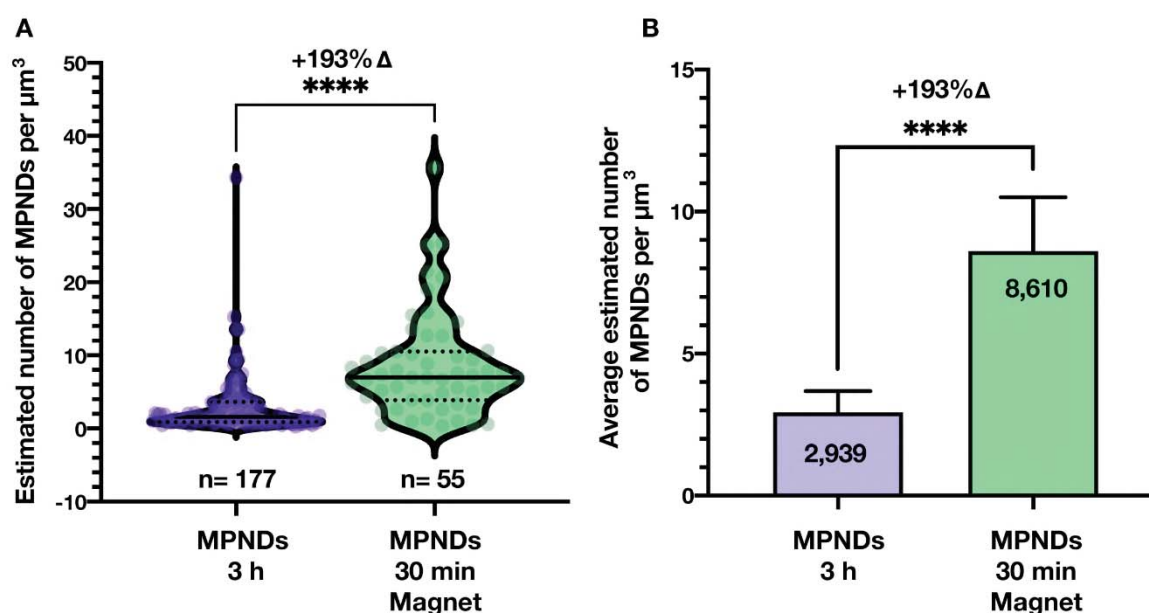


Figure 5. CLSM analyses of SKBR-3 cells exposed to 10 $\mu\text{g}/\text{mL}$ MPNDs solutions for 3 h in absence of magnet and 30 min in presence of magnet and. **A** Violin plots depict the distribution of estimated number of MPNDs per cell, the average (black line) and the quartiles (discontinued black line) for each condition and **B** bar plot shows the average (number inside the bar) of the estimated number of MPNDs per μm^3 per cell in each condition. A statistically significant effect (193% increase) was found between 3 h MPNDs-exposed cultures and 30 min MPNDs-exposed cultures with magnetic actuation.

Despite the increase in MPNDs within the cells, magnetic actuation did not affect the co-localisation of MPNDs with early endosomes (Fig 6). This probably means that the way MPNDs get into the cells when performing magnetic concentration (which increases the MPNDs aggregation due to the interaction with the magnetic field) does not follow classical

endocytic pathways like clathrin-mediated endocytosis or caveolae-dependent endocytosis. Probably macropinocytosis is the selected pathway to enter the cells, since the aggregated MPNDs are bigger than 200 nm in size.

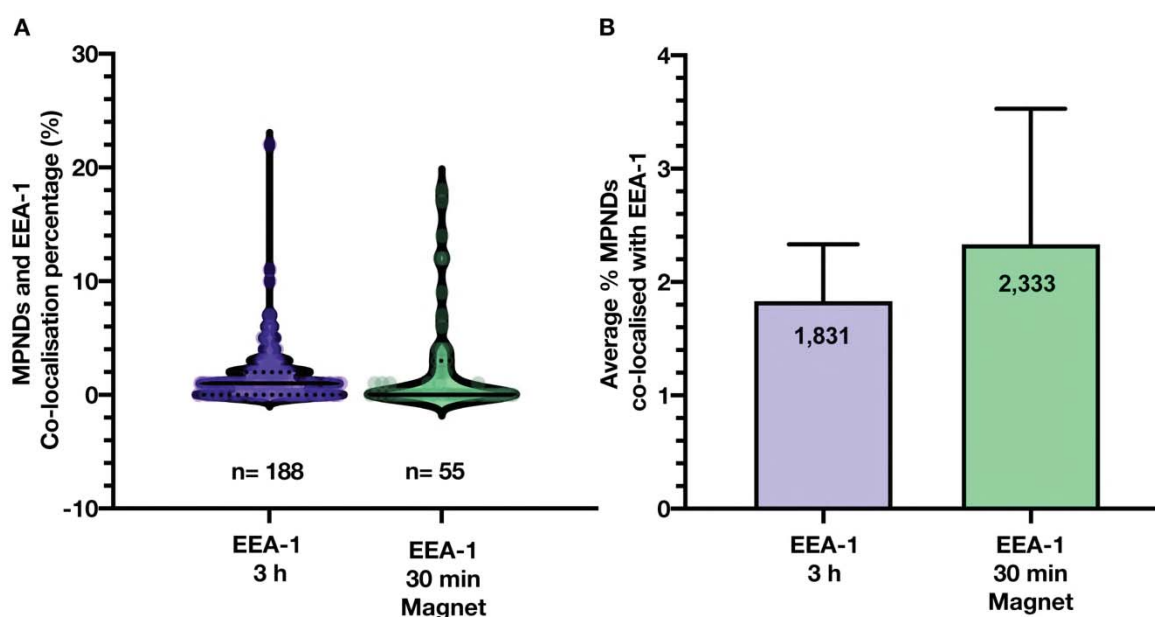


Figure 6. Co-localisation of MPNDs with early endosomes within SKBR-3 cells. No significant effect was found between 3 h MPNDs-exposed cultures and 30 min MPNDs-exposed cultures with magnetic actuation. Violin plots depict the distribution of the percentage of the estimated number of MPNDs that co-localise with early endosomes for each cell analysed.

Once demonstrated the efficiency of the magnetic actuation in MPND internalisation under static conditions, we decided to perform the same study under fluidic conditions. In this case, a tumoral (SKBR-3) and a non-tumoral (MCF10a) cell lines were compared.

Effect of magnetic actuation on internalisation in dynamic conditions.

Static MPNDs incubation conditions do not mimic what happens in a real condition inside organisms, in which the blood circulation makes it difficult for NPs to adsorb, interact and internalise in cells. For this reason, fluidics experiments were set to mimic the circulation of MPNDs through the vascular system and test the levels of MPNDs arrest and internalisation in SKBR-3 and MCF10a cells by magnetic actuation as a targeting strategy within the tumour. To test the efficacy of internalisation in dynamic culture conditions and the ability to retain and enhance internalisation in such conditions using a magnet, cell cultures were exposed to a MPNDs (10 $\mu\text{g}/\text{mL}$) for 24 h using a microfluidic pump system at 30 times more pressure than that described for the blood circulating nearby a tumoral breast area¹³.

Experiments were done in the presence or absence of a fixed neodymium magnet at the bottom of the channel where cells were seeded (Fig 7). Internalisation was quantified by semi-automated cell segmentation and quantified as the number of MPNDs per μm^3 for each detected cell. Internalisation was critically affected by magnetic actuation in fluidic conditions, being close to 0 on cell cultures in fluidic systems without the magnetic actuation and significant differences were found in both cell lines thanks to magnetic actuation. Moreover, SKBR-3 cells internalise more MPNDs per cell than MCF10a, showing that a preferential targeting towards the tumoral cell line³⁴ using magnetic actuation within tumour is possible. Magnetic actuation in vivo could be applied by directly placing a magnet or magnetic field device on top of a superficial tumour (like common breast cancer or skin tumours) or by intra-tissue insertion if the tumour is in a deeper tissue. Then, delivered MPNDs could be concentrated after administration on the targeted site thanks to the magnetic field and the preferential uptake by targeted cells and develop their therapeutic strategy.

Uptake of magnetoplasmonic NPs by SKBR-3 breast cancer cells has been previously described by Wu et al under mild shaking conditions using specific targeting (HER2-conjugated) magnetoplasmonic nanoclusters³⁵. Despite their experiments were also dynamic in nature they were not under flow conditions, which are closer to what happens in reality within tumour blood circulation systems. The ability to concentrate magnetic NPs in flow conditions³⁶⁻³⁹ was previously described in the literature, specially using in vitro phantoms^{40,41} but its effect on the internalisation and localisation in cells have not been previously described nor quantified at a single-cell level. Therefore, magnetic arrest in fluidic conditions and its effects on internalisation and localisation on cell cultures remains vaguely explored. Matuszak et al³⁶ tested SPIONs internalisation in endothelial cells by optical microscopy, but didn't perform a quantification of their internalisation. Tapeinos et al tried replicating the blood-brain barrier conditions using two different cell lines and testing the magnetic arrest, internalisation and crossing efficiency of magnetic nanocubes under flow conditions and static magnetic field actuation.³⁷ Similarly to our obtained results, their magnetic actuation produced an arrest of the NPS that led to a higher presence of magnetic NPs within the cells after short incubation times, however the internalisation was qualitatively shown only in images.

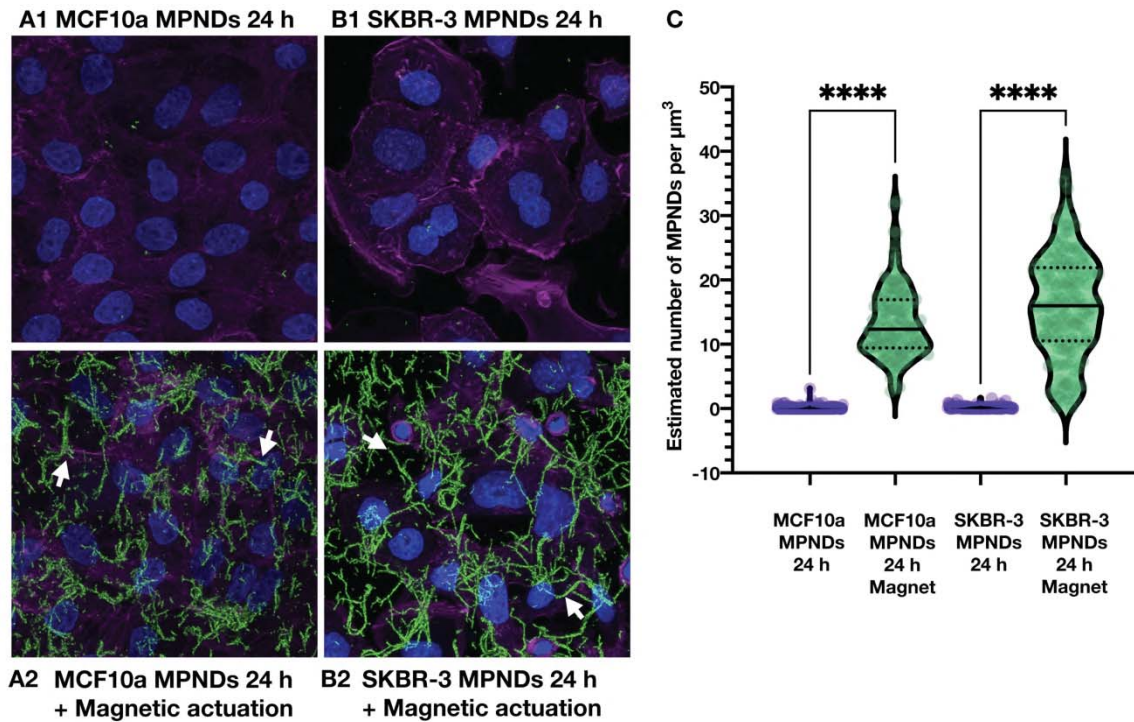


Figure 7. CLSM images and quantification of MPNDs internalisation in MCF10a and SKBR-3 in fluidic culture conditions. Maximum z-projection of all channels (blue= nuclei, green= MPNDs and magenta= actin cytoskeleton). **A1-B2** Images show the effect of magnetic actuation on MPNDs concentration in flow conditions. Big chain like structures (arrows) on magnetically concentrated MPNDs (**A2**, **B2**) appear on top and inside the cells in both cell lines. Very few MPNDs are found in cell cultures where no magnetic actuation was applied (**A1**, **B1**). **C** MPNDs within the cell limits (by semi-automated cell segmentation and calculation) were quantified and the number of MPNDs per μm^3 for each detected cell are plotted in the violin graphs (Black line= average; discontinued black line= quartiles). Statistically significant different values against groups are depicted with **** (when $p < 0.0001$). Magnetic actuation for MPNDs concentration (M).

Hyperthermia cell death induction.

In order to test the efficacy of these MPNDs against tumoral cells the $10 \mu\text{g}/\text{mL}$ concentration was selected as the best one to test the magnetoplasmonic hyperthermia effect on SKBR-3 and MCF10a.

The effect of the hyperthermia using the same MPNDs was tested and reported in a previous article using the same concentration ($10 \mu\text{g}/\text{mL}$) and incubation conditions in HeLa cells¹ but irradiating (30 min) with a 808 nm laser. Under these conditions, MPNDs proved

to be successful at triggering necrotic cell death in HeLa cells. After testing such long treatment conditions with the 808 nm laser, the laser wavelength of choice was re-evaluated to reach deeper tissues and have more excitation power to optimise the treatments. The 1064 nm wavelength laser was chosen because it belongs to the second NIR window of the UV-Visible spectrum, where light is able to penetrate deeper into biologic tissues⁴² and produce heat locally by the plasmonic excitation of gold on the MPNDs semi-shell^{1,7}. The laser irradiation time was also changed and was reduced from 30 min to 15 min and 5 min, respectively. The MPND concentration was maintained 10 µg/mL in both cell lines (Fig 8).

Viability after hyperthermia treatments was analysed by calcein and propidium iodide fluorescence staining. This staining allows discerning viable vs non-viable cells by the detection of necrotic or late necroptotic cells with damaged plasma membrane and therefore propidium iodide cell permeability. According to the obtained results, 5 min laser hyperthermia treatments induce necrotic or necroptotic cell death in SKBR-3 cells but not in MCF10a when MPNDs are not concentrated with a magnet. According to LIVE/DEAD[®] analysis, when magnetic actuation is used to concentrate the MPNDs on the irradiation spot during incubation (increasing the chances of MPNDs internalisation on local cells) and after 5 min of laser irradiation, an increase in both cell lines in terms of necrotic/late necroptotic cell death can be observed. This increase is higher (approximately twice) in SKBR-3 tumoral cells. When 15 min laser irradiation hyperthermia treatments are applied after MPNDs exposure, MCF10a control group is also heavily affected compared to the same conditions in SKBR-3. Exploring the effect of 15 min irradiation an effect on Calcein-AM staining was observed (data not shown). The fluorescence was highly diminished in MCF10a cells, and unaffected in SKBR-3 cells. For that reason, it was decided to compare the results in both cell lines using a double nuclear staining (Propidium iodide and Hoechst) to quantify the number of cells accurately. The analysis revealed a much lower mortality, around 8% in MCF10a and ~3% in SKBR-3 than that detected using the Calcein-AM staining. This is due to the fact that more cells were revealed by Hoechst staining especially in the case of MCF10a compared to the identified by Calcein-AM staining. SKBR-3 cell line mortality remained very low in the above-mentioned conditions, corroborating the results obtained by LIVE/DEAD[®] analysis. Despite these results, MCF10a nuclei appeared reduced in size and with chromatin condensation modifications compared to control cells (data not shown). The low staining efficiency with propidium iodide indicates that despite the nuclei

modifications, the plasma membrane is not compromised, which could be an indication of the induction of a preferential regulated pathway to cell death.

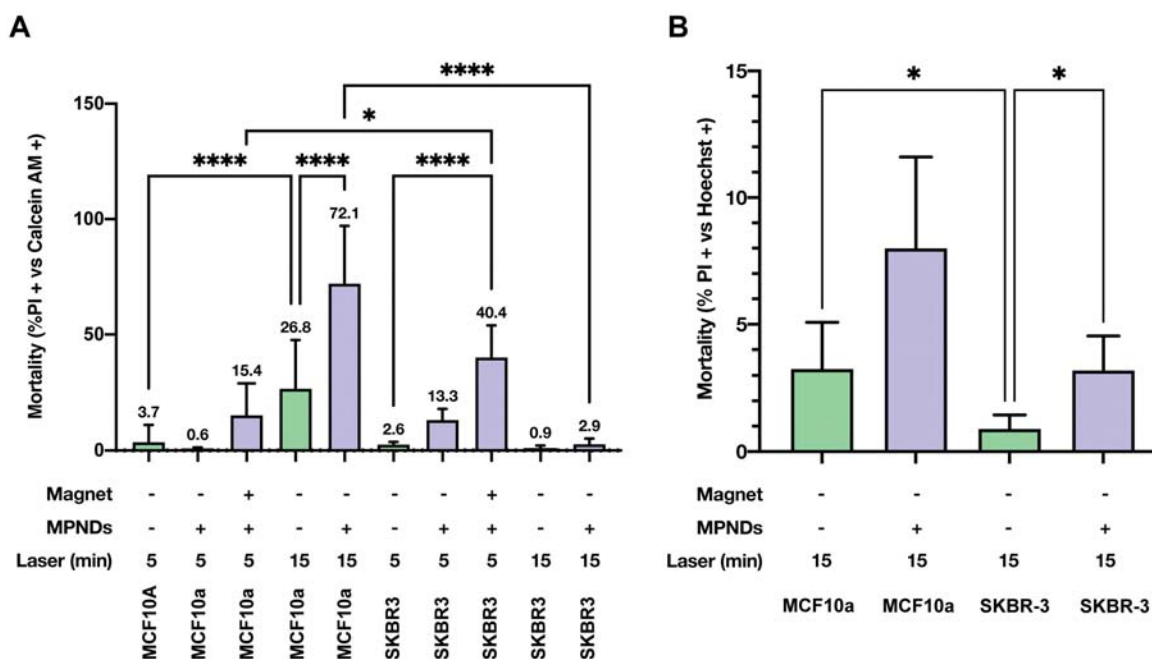


Figure 8 Analysis of hyperthermia results on SKBR-3 and MCF10a cell lines. Hyperthermia effectivity is analysed by **A** LIVE/DEAD® viability staining and depicted as percentage of dead cells detected for each condition (average value on top of the bar) or **B** Propidium iodide positive cells versus Hoechst-stained nuclei in 15 min laser-treated samples. X axes depict the cell line and conditions tested for each experiment: magnetic actuation performed (+) or not (-), MPNDs present (+) or not (-) and laser irradiation time (5 or 15 min), Statistically significant different values between groups are depicted with * (for $p < 0.05$), ** (for $p < 0.01$), *** (for $p < 0.001$) and **** (when $p < 0.0001$). Controls (CTR), Propidium iodide (PI)

Evaluation of the nuclear morphology and condensation status has widely been used in cell biology as an indicator of cellular health status. For example, nuclear degradation (karyolysis) is an indicator of ongoing cellular problems or cell death¹⁰. Nuclear morphology modifications can be an evidence of abnormal nuclear lamina organisation which can lead to apoptosis as lamins are targets for proteolytic degradation by caspases⁴³. MCF10a cells present a typical rounded and oval nuclei structure, showing chromatin condensation, with up to three distinct nucleoli, a classic sign of cell health. SKBR-3, as a tumoral cell line, present what seems two different populations with slightly different cell morphologies and nuclei structures. The first and more predominant population, are the cells that grow completely attached to the growth surface and are overall flatter in their 3D structure, commonly present oval shaped nuclei (sometimes more than one per cell). A second population of cells, based on their morphology, appear more rounded and slightly detached from the

growth surface. These kinds of cells often show an aberrant nuclei morphology, as their nuclei are slightly polygonal and their condensation status is higher.

In general, nuclei changes indicating a progressive cell death mechanism are defined by their nuclear characteristics as follows: shrinkage of nuclei is defined as karyopyknosis, the loss of oval-shaped structure and increased DNA condensation is defined as karyorrhexis and the complete loss of nuclear outlines and DNA fragmentation within the cell is defined as karyolysis⁴⁴.

After MPNDs and 5 min hyperthermia treatments with a 1064 nm laser, nuclear morphology is distinctly changed between cell lines, as shown in figure 9. In SKBR-3 hyperthermia treated cells with and without magnetic actuation, show higher DNA condensation levels than control cells. Their nuclear shape is drastically changed and present aberrant polygonal shaped structures compatible with karyopyknosis and karyorrhexis characteristics. This is in accordance to what Sanz et al described in human neuroblastoma cells when triggering magnetic hyperthermia using an alternating magnetic field⁴⁵. The authors described that despite the aberrant formations of the nuclei after heat-inducing treatments the nuclear membrane remained undisrupted due to the resistant nuclear membrane cytoskeleton and their nuclear laminas. These protein networks further support and might preserve temporarily the lipid bilayer of the nuclear membrane from disorganizing after the heat shock treatments, resulting in the angular structure of the affected nuclei. Once the cell death mechanisms, induced by the heat treatments progress, the cell nucleus morphology is consecutively changed into karyorrhexis, first as chromatin condensation is affected, and finally karyolysis, that leads to nuclear fragmentation. Both processes are described in necroptosis progression⁴⁴.

In contrast, MCF10a cells show no differences in nuclear morphology between control conditions and 5 min laser hyperthermia treated cells when MPNDs are not magnetically concentrated within laser treatment spot, while karyopyknosis and slight karyorrhexis can be observed in magnetically concentrated MPNDs-samples. When hyperthermia treatments are extended to 15 min karyopyknosis occurs in this cell line too, proving that 15 min laser irradiation is a high dose that doesn't help to achieve a differential therapeutic between tumoral and non-tumoral cell lines.

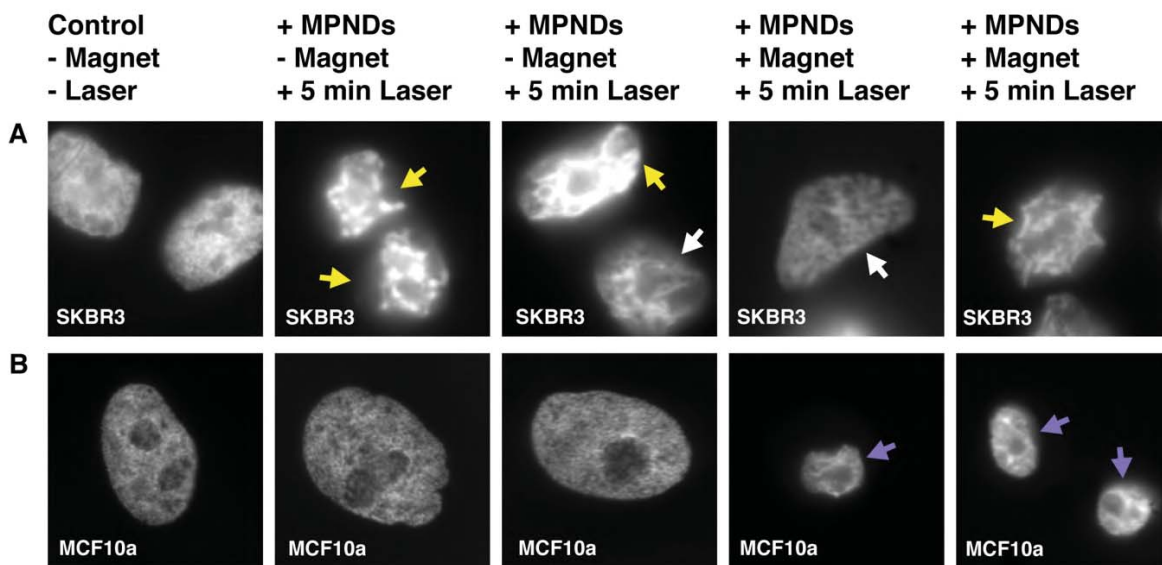


Figure 9. Nuclear morphology of CTR and MPNDs + 5 min Laser-treated SKBR-3 and MCF10a cell lines 24 h post-treatment. Detailed image of the nuclei 24 h after hyperthermia treatments with the laser for 5 min with and without magnetic actuation for MPNDs concentration. Karyorrhexis (white arrows), kharyolysis (yellow arrows) and karyopyknosis (purple arrows), depicted in each condition. All images shown at the same magnification.

The differential nuclear morphologies between cell lines prove that MCF10a and SKBR-3 5 min laser hyperthermia-treated cells have very distinct sensitivities to the laser treatment when MPNDs are not concentrated with the laser on the irradiation spot. SKBR-3 presenting aberrant nuclear morphologies when treated with MPNDs, not concentrated with magnetic actuation, and the laser prove the treatment is effectively inducing cell death mechanisms in tumoral cell lines, while the same conditions are not causing an effect on the MCF10a non-tumoral cell line.

To distinguish the cell death pathway induced in SKBR-3 and MCF10a MPNDs-exposed cultures by hyperthermia treatments triggered by the irradiation with a 1064 nm laser for 5 min or 15 min Caspase 3 immunofluorescence detection was performed. Caspase 3 is an effector caspase that once activated promotes apoptotic cell death in cells¹⁰. The differential activation after MPNDs incubation and 5 min laser treatment in SKBR-3 cell line can be observed in figure 10 (C1), where a 2.4 fold change increase in detected fluorescence is shown in SKBR-3 compared to the 5 min laser irradiated control group. A 3.64 fold change increase is detected in caspase-3 activation of MPNDs-exposed SKBR-3 under magnetic actuation conditions, compared to the 5 min laser irradiated control group.

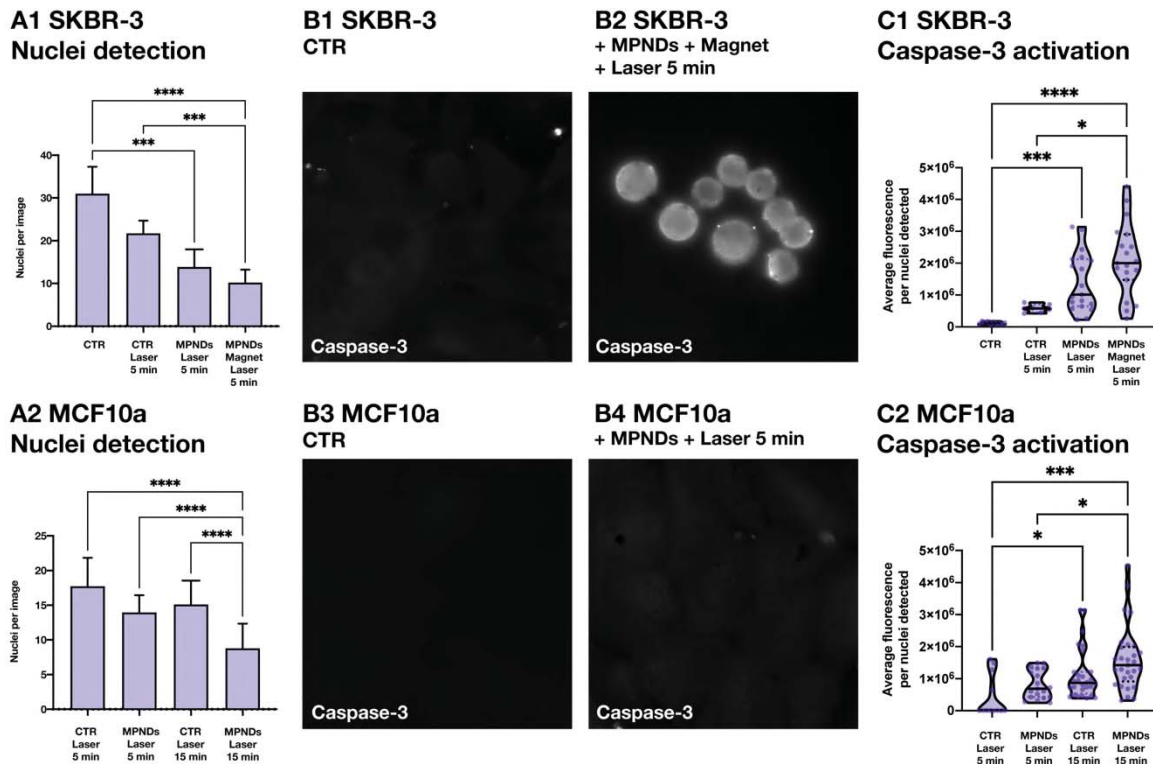


Figure 10. Caspase 3 activation analyses in SKBR-3 and MCF10a cells by fluorescence immunodetection and nuclei detection per image. A1-A2 Bar plots depicting the decrease in nuclei detection after treatments in SKBR-3 and MCF10a cells. The data reflects the differences in remaining cells in culture 24 h post-treatment between conditions **B1-B4** Images show immunofluorescence detection of active caspase-3 in SKBR-3 (**B1** CTR and **B2** MPNDs-exposed under magnetic actuation and posterior 5 min laser treatment) and MCF10a (**B3** CTR and **B4** MPNDs-exposed without magnetic actuation and posterior 5 min laser treatment) cell cultures. **C1-C2** Violin plots show the average (black line) fluorescence intensity per number of nuclei detected. Statistically significant different values between groups are depicted with * (for $p < 0.05$), ** (for $p < 0.01$), *** (for $p < 0.001$) and **** (when $p < 0.0001$).

Caspase-3 was significantly increased 24 h post-treatment with MPNDs under magnetic actuation and 5 min laser irradiation in SKBR-3. Caspase-3 activation was not significantly increased in MPNDs-exposed MCF10a after 24 h post-treatment with 5 min laser irradiation. The activation happened when the laser irradiation was increased to 15 min in this cell line. There is a higher activation of the caspase-3 activity in 15 min laser-treated samples than 5 min in MCF10a. The differential activation of caspase-3 in 5 min laser-treated samples indicates a differential pathway induction between tumoral SKBR-3 and non-tumoral MCF10a cells. That is, at 5 min laser treated hyperthermia conditions, tumoral SKBR-3 enter the apoptotic pathway of regulated cell death, especially after magnetic actuation of

MPNDs concentration within irradiation spot. This activation is not observed when comparing the MPNDs-exposed and control groups after 5 min laser irradiation hyperthermia in MCF10a without magnetic actuation.

Hyperthermia effect can also be evaluated by nuclei counts per image. This analysis confirms that SKBR-3 die after 5 min laser-induced hyperthermia (especially after magnetic actuation to concentrate the particles within the laser irradiation spot), while MCF10a show no differences compared to the controls. It also proved that 15 min irradiation was enough to trigger caspase 3 activation both in control laser-irradiated cultures and MPNDs-exposed and laser-irradiated cultures in MCF10a non-tumoral cells. No effect in nuclei count was observed in 15 min laser-irradiated control group but a significant drop in nuclei count was found in MPNDs-exposed and 15 min laser-irradiated cell cultures.

The hyperthermia effects on cell death induction are different to those described by magnetic intra-lysosomal hyperthermia by Clerc et al⁴⁶. According to their study, iron oxide magnetic nanoparticles can produce hyperthermia by alternating magnetic field and induces cell death through reactive oxygen species production within lysosomes which subsequently causes lipid peroxidation, followed by lysosome membrane permeabilisation and the leakage of lysosomal content into the cytosol. According with these authors, once in the cytosol, Cathepsin-B plays a critical role in cell death activation by activation of Caspase-1 which can be related to pyroptosis. In their study, cells present AnnV and/or PI positive labelling and irregular DNA fragmentation after hyperthermia treatment, hallmarks that could be related to apoptotic cell death. Contrary to our findings, in Clerc et al study apoptosis was not induced, since magnetic intra-lysosomal hyperthermia did not activate Caspase-3 activity.

According to the changes in nuclear morphology compatible with necroptosis induced in SKBR-3 cells (aberrant shape, karyorrhexis and karyolysis) and the caspase-3 activation, a regulated cell death pathway (apoptosis) must be active 24 h post-treatment with 5 min laser hyperthermia-induced treatments in MPNDs-exposed tumoral cells. These data shows a higher regulated cell death induction efficiency than that described previously in literature for similar NPs with higher NP concentration and longer treatments^{1,45,46}.

Conclusions.

The present study provides essential new data on MPNDs interaction with SKBR-3 and MCF10a breast epithelial cells. SEM allowed us to fix the optimal MPNDs concentration, in terms of aggregation and internalisation, to be used in the following experiments, and their magnetic manipulation to concentrate or arrest and enhance internalisation in static and dynamic conditions. It also describes the mechanism whereby magnetically targeted MPNDs induce the death of tumour cells when exposed to a NIR laser. The central role and differential behaviour of Caspase-3 activation and nuclear morphology modifications after hyperthermia treatments between tumoral and non-tumoral epithelial breast cells is also defined. The precise quantification of internalisation and localisation under static, the arrest and internalisation in flow and magnetic actuation conditions performed brings novel information towards the optimisation of MPNDs treatments and their tumour targeting capabilities. Moreover, the definition of the cell death mechanisms induced by NIR-laser hyperthermia to kill cancer cells contributes to future developments of selective magnetoplasmonic-based nanotherapies as alternative anti-tumoral therapies.

References.

1. Li, Z. *et al.* Magnetically amplified photothermal therapies and multimodal imaging with magneto-plasmonic nanodomains. *Appl. Mater. Today* **12**, 430–440 (2018).
2. Donolato, M. *et al.* Novel readout method for molecular diagnostic assays based on optical measurements of magnetic nanobead dynamics. *Anal. Chem.* **87**, 1622–1629 (2015).
3. Urries, I. *et al.* Magneto-plasmonic nanoparticles as theranostic platforms for magnetic resonance imaging, drug delivery and NIR hyperthermia applications. *Nanoscale* **6**, 9230–9240 (2014).
4. Zhou, H., Zou, F., Koh, K. & Lee, J. Multifunctional magnetoplasmonic nanomaterials and their biomedical applications. *J. Biomed. Nanotechnol.* **10**, 2921–2949 (2014).
5. Cheng, Y. *et al.* The Role of Hyperthermia in the Multidisciplinary Treatment of Malignant Tumors. *Integr. Cancer Ther.* **18**, (2019).
6. Kobayashi, T. Cancer hyperthermia using magnetic nanoparticles. *Biotechnol. J.* **6**, 1342–1347 (2011).
7. Li, Z. *et al.* Simultaneous Local Heating/Thermometry Based on Plasmonic Magneto-chromic Nanoheaters. *Small* **14**, 1800868 (2018).
8. Roti, J. L. Cellular responses to hyperthermia (40–46°C): Cell killing and molecular events. *Int. J. Hyperth.* **24**, 3–15 (2008).
9. Oei, A. L., Vriend, L. E. M., Crezee, J., Franken, N. A. P. & Krawczyk, P. M. Effects of hyperthermia on DNA repair pathways: One treatment to inhibit them all. *Radiat. Oncol.* **10**, 1–13 (2015).
10. Galluzzi, L. *et al.* Molecular mechanisms of cell death: recommendations of the Nomenclature Committee on Cell Death 2018. *Cell Death Differ.* **25**, 486–541 (2018).
11. Grivennikov, S. I., Greten, F. R. & Karin, M. Immunity, Inflammation, and Cancer. *Cell* **140**, 883–899 (2010).
12. Schindelin, J. *et al.* Fiji: An open-source platform for biological-image analysis. *Nat. Methods* **9**, 676–682 (2012).
13. Pratt, S. J. P., Lee, R. M. & Martin, S. S. The mechanical microenvironment in breast cancer. *Cancers (Basel)*. **12**, 1–25 (2020).
14. R Core Team. R: A language and environment for statistical computing. (2020).
15. International Organization for Standardization. ISO 10993-5:2009(E) Biological evaluation of medical devices - Part 5: Tests for in vitro cytotoxicity. vol. Third edit (2009).
16. Kroll, A., Pillukat, M. H., Hahn, D. & Schneckeburger, J. Interference of engineered nanoparticles with in vitro toxicity assays. *Arch. Toxicol.* **86**, 1123–1136 (2012).
17. Sung Eun Kim^{1,2}, Li Zhang³, Kai Ma⁴, M. R. *et al.* Ultrasmall nanoparticles induce ferroptosis in nutrient-deprived cancer cells and suppress tumour growth. *Nat. Nanotechnol.* (2016) doi:10.1038/NNANO.2016.164.
18. Berry, C. C. Possible exploitation of magnetic nanoparticle-cell interaction for biomedical applications. *J. Mater. Chem.* **15**, 543–547 (2005).
19. Gupta, A. K., Berry, C., Gupta, M. & Curtis, A. Receptor-mediated targeting of magnetic nanoparticles using insulin as a surface ligand to prevent endocytosis. *IEEE Trans. Nanobioscience* **2**, 255–261 (2003).
20. Hill, C. *et al.* Imaging interactions of metal oxide nanoparticles with macrophage cells by ultra-high resolution scanning electron microscopy techniques. *Proc. SPIE--the Int. Soc. Opt. Eng.* **73**, 389–400 (2015).
21. Goldstein, A., Soroka, Y., Frušić-Zlotkin, M., Popov, I. & Kohen, R. High resolution

- SEM imaging of gold nanoparticles in cells and tissues. *J. Microsc.* **256**, 237–247 (2014).
22. Pelka, J. *et al.* Cellular uptake of platinum nanoparticles in human colon carcinoma cells and their impact on cellular redox systems and DNA integrity. *Chem. Res. Toxicol.* **22**, 649–659 (2009).
 23. Pons, T. *et al.* On the quenching of semiconductor quantum dot photoluminescence by proximal gold nanoparticles. *Nano Lett.* **7**, 3157–3164 (2007).
 24. Li, X., Qian, J., Jiang, L. & He, S. Fluorescence quenching of quantum dots by gold nanorods and its application to DNA detection. *Appl. Phys. Lett.* **94**, 94–97 (2009).
 25. Pustovit, V. N. & Shahbazyan, T. V. Fluorescence quenching near small metal nanoparticles. *J. Chem. Phys.* **136**, 0–6 (2012).
 26. Reineck, P. *et al.* Distance and wavelength dependent quenching of molecular fluorescence by Au@SiO₂ core-shell nanoparticles. *ACS Nano* **7**, 6636–6648 (2013).
 27. Ribeiro, T., Baleizão, C. & Farinha, J. P. S. Artefact-free evaluation of metal enhanced fluorescence in silica coated gold nanoparticles. *Sci. Rep.* **7**, 1–12 (2017).
 28. Bohmer, N. *et al.* Interference of engineered nanomaterials in flow cytometry: A case study. *Colloids Surfaces B Biointerfaces* **172**, 635–645 (2018).
 29. Vassie, J. A., Whitelock, J. M. & Lord, M. S. Endocytosis of cerium oxide nanoparticles and modulation of reactive oxygen species in human ovarian and colon cancer cells. *Acta Biomater.* **50**, 127–141 (2017).
 30. FitzGerald, L. I. & Johnston, A. P. R. It's what's on the inside that counts: Techniques for investigating the uptake and recycling of nanoparticles and proteins in cells. *J. Colloid Interface Sci.* **587**, 64–78 (2021).
 31. Kopwiththaya, A. *et al.* Magnetoplasmonic nanoplatforms for enhanced bioimaging and photothermal cancer therapy. *Tech. Proc. 2012 NSTI Nanotechnol. Conf. Expo, NSTI-Nanotech 2012* **3**, 32–35 (2012).
 32. Mukha, I. *et al.* Multifunctional magneto-plasmonic fe₃o₄/au nanocomposites: Approaching magnetophoretically-enhanced photothermal therapy. *Nanomaterials* **11**, (2021).
 33. Espinosa, A. *et al.* Janus Magnetic-Plasmonic Nanoparticles for Magnetically Guided and Thermally Activated Cancer Therapy. *Small* **16**, 1–14 (2020).
 34. Patiño, T., Soriano, J., Barrios, L., Ibáñez, E. & Nogués, C. Surface modification of microparticles causes differential uptake responses in normal and tumoral human breast epithelial cells. *Sci. Rep.* **5**, 11371 (2015).
 35. Wu, C. H., Cook, J., Emelianov, S. & Sokolov, K. Multimodal magneto-plasmonic nanoclusters for biomedical applications. *Adv. Funct. Mater.* **24**, 6862–6871 (2014).
 36. Matuszak, J. *et al.* Endothelial biocompatibility and accumulation of SPION under flow conditions. *J. Magn. Magn. Mater.* **380**, 20–26 (2015).
 37. Tapeinos, C. *et al.* Cell Membrane-Coated Magnetic Nanocubes with a Homotypic Targeting Ability Increase Intracellular Temperature due to ROS Scavenging and Act as a Versatile Theranostic System for Glioblastoma Multiforme. *Adv. Healthc. Mater.* **8**, (2019).
 38. Sanz-Ortega, L., Rojas, J. M., Portilla, Y., Pérez-Yagüe, S. & Barber, D. F. Magnetic nanoparticles attached to the NK cell surface for tumor targeting in adoptive transfer therapies does not affect cellular effector functions. *Front. Immunol.* **10**, 1–17 (2019).
 39. Nguyen, K. *et al.* Superparamagnetic iron oxide nanoparticles carrying chemotherapeutics improve drug efficacy in monolayer and spheroid cell culture by enabling active accumulation. *Nanomaterials* **10**, 1–21 (2020).
 40. Radon, P. *et al.* Magnetic Particle Spectroscopy to Determine the Magnetic Drug Targeting Efficiency of Different Magnetic Nanoparticles in a Flow Phantom. *IEEE*

- Trans. Magn.* **51**, 6000104 (2015).
41. Cao, Q., Han, X. & Li, L. Numerical analysis of magnetic nanoparticle transport in microfluidic systems under the influence of permanent magnets. *J. Phys. D. Appl. Phys.* **45**, (2012).
 42. Guo, C. *et al.* Highly efficient ablation of metastatic breast cancer using ammonium-tungsten-bronze nanocube as a novel 1064nm-laser-driven photothermal agent. *Biomaterials* **52**, 407–416 (2015).
 43. Fischer, E. G. Nuclear Morphology and the Biology of Cancer Cells. *Acta Cytol.* **64**, 511–519 (2020).
 44. Hu, X. M. *et al.* Guidelines for Regulated Cell Death Assays: A Systematic Summary, A Categorical Comparison, A Prospective. *Front. Cell Dev. Biol.* **9**, 1–28 (2021).
 45. Sanz, B. *et al.* Magnetic hyperthermia enhances cell toxicity with respect to exogenous heating. *Biomaterials* **114**, 62–70 (2017).
 46. Clerc, P. *et al.* Targeted Magnetic Intra-Lysosomal Hyperthermia produces lysosomal reactive oxygen species and causes Caspase-1 dependent cell death. *J. Control. Release* **270**, 120–134 (2018).

4 General discussion

Nanomedicine, has been explored as a promising application of nanosciences to health sciences for the last three decades (Anselmo & Mitragotri, 2019). Despite that, nowadays, it remains a field with a vast potential of application but a low translation to real strategies to treat and diagnose diseases. In fact, the high ability to change the physicochemical properties of ENMs (Conde et al., 2014) and generate new materials, which is perceived as an advantage to fine-tune their application, could be the reason for the slowdown of their biological application. The lack of a standard biological characterisation difficults the application of the large amounts of ENMs generated. Characterisation at the biointerface is lacking a profound analysis, the interactions between ENMs-cells are often overlooked or superficially explored.

Often, the properties of certain kind of materials are reported in the literature after proving the application based on their physicochemical characteristics but not in *in vitro* cell cultures conditions. That is, ENMs are reported to have an activity that could potentially be translated to fighting a disease but in conditions that are very different from the ones that happen in biological conditions in some cases. When reporting the potential application of ENMs to nanomedicine, essential experiments of the biointeraction should be performed in *in vitro* cell culture conditions and cover at least their cytotoxicity, association, uptake, and evaluation of their therapeutic strategy in such conditions. Here, we present three different works based on the evaluation of the ENMs biointeraction *in vitro* and the proposed workflows is expected to set an example on how to investigate them from a biological perspective. *In vitro* characterisation workflows when interrogating ENMs biologically and their standardisation, are especially relevant now that the European Union is making efforts on legislations proposing a shift from *in vivo* testing, towards non-animal approaches based on *in vitro* and computational methods. The results of such regulations are exposed on the EU Directive 2010/63/EU (2010) on the protection of animals used for scientific purposes, the regulation (EC) No 1907/2006 concerning the Registration, Evaluation, Authorisation and Restriction of Chemicals (REACH (2020g)) and the regulation (EC) No 1223/2009 on cosmetic products (2020e) (Pistollato et al., 2021).

The *in vitro* investigation approach is especially crucial when reporting the biological effects of ENMs that were not first conceived for biological applications. That is the case of the first kind of ENMs used in this thesis (Chapter 1), cerium oxide NPs. They were first designed as NPs that would allow for superconductor materials to be developed and their industrial and ecological applications in products such as the development of better catalytic materials or fuels and efficient solar panels

that harvest and store energy more efficiently. Due to their composition and elemental properties, cerium nanocrystals were proposed as a good alternative to quench the ROS produced in organisms under oxidative stress conditions and their possible use as nanomedicine for the treatment of diseases that cause or are triggered by high production levels of such species (Xu & Qu, 2014), like cancer (Vassie et al., 2017a), Alzheimer's disease (Kwon et al., 2016) or heart attack injury (Pagliari et al., 2012). First, we tried to characterise their biointeraction with SKBR3 cells, but their small size (around 2,5 nm) and the lack of fluorescent properties made impossible to use fluorescent microscopy, flow cytometry and spectroscopy techniques. Only large cerium NPs or presenting fluorescence-probes in their surface can be observed by SEM or CLSM thanks to the reflection properties of the cerium metal atoms or their fluorescence as observed in Vassie et al. study of nanoceria on human ovarian and colon cancer cells (Vassie et al., 2017b). These would allow for semi-quantitative or quantitative internalisation analysis. In our case, internalisation was confirmed through absorption determination of cell lysates after exposure to cerium oxide NPs at 210, 250, 280 and 298 nm wavelengths as proposed in previous studies (Inerbaev et al., 2015; Pulido-Reyes et al., 2015). We tested their cytotoxicity using two different assays, in order to discard any interference with the tests used due to the nanoparticles' redox properties and absorption. In terms of cytotoxicity, we have demonstrated that cerium oxide NPs are safe at low concentration (5 µg/mL) and have a cytotoxic effect in higher concentrations in tumoral cells. Previous studies have highlighted the importance of investigating the cell viability after interaction of ENMs with mammalian cells in different ways (Kroll et al., 2012; Ong et al., 2014; Wörle-Knirsch et al., 2006) because overestimation or underestimation of cell viability has been reported after different NPs treatments, especially at high NP concentrations (Ong et al., 2014). For example, the interference of carbon nanotubes in an MTT assay has been described by Wörle-Knirsch et al. (Wörle-Knirsch et al., 2006), where carbon nanotubes were bound to formazan crystals during the assay and stabilised their structures, preventing their posterior solubilisation and absorbance detection. This phenomenon led to lower absorbance results that could be misinterpreted as a high cytotoxicity effect of carbon nanotubes on cell cultures compared to the control group. On the other hand, Kroll et al. (Kroll et al., 2012) found that higher concentrations of NPs lead to higher absorbance levels in MTT results, leading to the misinterpretation of a higher viability in such conditions, similarly to what we found on cerium oxide NPs results. These researchers also detected interferences when evaluating oxidative stress using the H2DCF-DA assay (both in cell cultures and in a cell-free assay), or the NPs effect on cell culture using enzymatic activity methods (measured by a slight decrease in LDH activity) or interference in immunoassays, measured by ELISA IL-8 assays, where NPs bound to proteins and cytokines led to underestimation of their possible pro-inflammatory effect. In our study, we highlight the importance of carefully analysing the viability and how the ENMs characteristics (composition, redox activity, absorbance, plasmonic and quenching properties) can greatly influence such results. Dis-

crepancies between the values obtained using direct and indirect methods for cell viability determination have been described before (Chan et al., 2013) especially involving metal-based ENMs or ENMs containing redox-active molecules. In this sense, we used two different assays to check the cytotoxicity of cerium oxide NPs. The first one based on indirect viability examination is the MTT, which provides information on the MTT reduction activity of live cells within a culture. Accordingly to the manufacturer, MTT reduction activity is directly related to the number of cells in culture. However, this test can be sensitive to temporary increases of metabolic activity (not related to proliferation) or MTT could be reduced by direct ENM activity due to their redox properties, surface modifications or composition (Sadik et al., 2009). In both cases these activities would interfere with the viability results. According to the data obtained by MTT assay analysis, no cytotoxic effect was found in any of the tested concentrations (ranging from 0 to 100 $\mu\text{g/mL}$). This is in accordance to previously described viability of cerium oxide NPs in literature (Lyu et al., 2016; Vassie et al., 2017b; Zholobak et al., 2014). Despite this, we observed an increase of formazan crystal formation in cell cultures exposed to cerium oxide NPs but no increase in cell confluence and proliferation (under contrast phase microscope), so the interference effect was reverse to that described by Wörle-Knirsch et al. and was similar to the direct interference with the MTT assay described by Sadik et al. (Sadik et al., 2009). In order to properly evaluate the possible interference of the indirect method and quantify the cytotoxicity using a direct method, the SRB assay was used. This is a stoichiometrically method, based on protein detection (and therefore, directly related to the cell number in culture). An additional centrifugation step prior to absorbance readings was introduced, to avoid a possible interference of the remaining cerium oxide NPs on the supernatant or bound to cell remnants. The centrifugation step should be evaluated depending on the ENMs type, since carbon nanotubes interaction with several dyes showed that centrifugation can lead to misinterpretation of reduced absorbance causing a false toxic response (Sadik et al., 2009). This method proved to be essential to analyse cerium oxide NPs toxicity, when relevant differences in viability were identified: the indirect MTT assay showed no cytotoxic effect while the direct stoichiometric SRB assay revealed the real cytotoxic effect at high concentrations. Therefore, the effect on viability was masked by the possible direct redox activity of the NPs on MTT reduction to formazan crystals. Accordingly, an assessment workflow that combines complementary direct and indirect methods to evaluate the same biological questions is recommended, in order to make sure that the conclusions the data led are correct and discard possible interferences with the method used.

The investigation of toxicity and antioxidant properties of rare earth oxides is very limited. Specifically only cerium oxide nanoparticles have been studied and the results in literature are conflicting, likely due to the differences in the procedures to synthesise them (Karakoti et al., 2010). In order to prove the therapeutic efficiency of the cerium oxide NPs used in this thesis, we tested their therapeutic potential as an antioxidant to revert the effects of a commonly used ROS induction protocol that uses TBHP as an inductor of oxidative stress.

Regarding its antioxidant properties, it has been previously described that nanocerium can act both producing and reverting ROS production within cells (Karakoti et al., 2010), depending on the valence status of cerium in their composition (Leung et al., 2015). In our case, we were able to prove that the valence status of cerium within the tested NPs in biological conditions, enabled electron scavenging and lowered ROS production, having a protective behaviour on TBHP-ROS-induced cultures comparable to that achieved by commercially available N-acetylcysteine. Using free antioxidant compounds like N-acetylcysteine, glutathione based formulations, or vitamin C, it is possible to have several drawbacks compared to the delivery of antioxidant therapeutics in nanoformulations. Free antioxidant molecules show low permeability and are poorly soluble in hydrophilic solutions, which leads to low bioavailability due to instability during storage and gastrointestinal degradation (Hu et al., 2017). Delivery of antioxidants through nanoformulations like the cerium oxide nanoparticles used in our study provides an alternative as antioxidant compounds that can be delivered in colloidal suspension with high stability. Moreover, the auto-regenerative redox cycle of cerium oxide NPs, with its ability to reversibly switch between both oxidation states and the reduction potential of available cerium, allows them to modulate the oxidative stress rapidly and reversibly, ensuring a stable and long-lasting antioxidant function compared to free antioxidant molecules (Kumar et al., 2020). The antioxidant in vitro effect of cerium oxide NPs is comparable to that observed by Vassie et al. (Vassie et al., 2017b), where a size-dependency effect was observed in human ovarian and colon cancer cells. In Vassie et al. study, 7 nm sized cerium NPs showed less efficiency than 94 nm sized cerium NPs, as they report that the smaller size of the NPs increased their aggregation potential in aqueous solutions and in contact with the cell media, limiting ROS from accessing the oxygen vacancies on the surfaces of nanocerium that impart their antioxidant properties (Vassie et al., 2017b). However, their results are based on the basal ROS level characterisation of the cell and not the induction of oxidative stress. The results were highly variable in terms of cerium oxide NPs time-exposure, as 7 nm-sized cerium oxide NPs were found to increase the intracellular ROS levels 24 h after treatment, reduce those levels after 48 h of exposure and had no significant effect after 72 h. The direct protective antioxidant effect of our cerium oxide NPs on ROS-induced cell cultures was more effective (leading to higher significant ROS-level fold change decrease after oxidative stress induction) and in shorter times (3 h vs 24 h NPs exposure pre-induction treatment) at the same concentration than that of 5-8 nm size cerium oxide nanoparticles tested on cardiac progenitor cells (Pagliari et al., 2012). In addition to their direct therapeutic antioxidant effect, the co-adjuvant use of antioxidant cerium nanoparticles can be beneficial to control the secondary effects of chemotherapy, as they protect normal cells indirectly by priming cells to respond to ROS insult or directly by scavenging cellular ROS. Meanwhile, they can be detrimental to cancer cells by inhibiting their ROS-induced-invasion ability and sensitising them for radiotherapy (Häfeli, 2004) as described by Madero-Visbal et al. in mice (Madero-Visbal et al., 2012).

When bigger sizes, metallic composition and fluorescent properties are incorporated into the ENMs design, like the SiNPs or MPNDs used in chapter 2 and 3, the investigation of their interaction with cells was inevitably linked to visualisation techniques. This, was the main point to develop in the second chapter's workflow, based on the 'seeing is believing' principle when investigating SiNPs-cell interactions. These properties (presence of metals or fluorescence) allow direct inspection through microscopy techniques and quantification based on the optical properties of the signal detected by fluorescence and reflection imaging.

Commonly used techniques to assess NPs internalisation are CLSM and flow cytometry, the later allowing for big population analysis. Despite the advantages of having reporter fluorescent probes within the NPs design, several limitations arise when experimenting with this kind of NPs and the quantification of their analysis. First, the size of the NPs can be a limitation when visualising and quantifying their interaction with cells. Most commonly available microscopes at the cell culture laboratories (epifluorescence) lack enough resolution to resolve small sized NPs within the nanoscale. Second, in internalisation and localisation experiments, the kind of signal detected and reported through microscopy techniques like CLSM must be corrected and restored considering the diffraction within the sample, mounting media, the microscope's optical components and the imaging properties. Failing to restore the signal will draw estimation errors as reported by Landmann et al. (Landmann, 2002). Moreover, the segmentation of single cells by staining of structures like the plasma membrane or the actin cytoskeleton is vital for the correct identification of the NPs within the cell limits and accurate uptake determination. Lastly, fluorescence can be easily quenched by other materials and probes around the embedded fluorescent molecules within the NPs design. That is, if the ENMs are functionalised with surface modifications such as the addition of additional fluorescent reporters, covalent attachment of macromolecules or sputtering of metals over their fluorescent cores, the photons emitted by the fluorescent reporters when excited could trigger an excitation of other compounds and molecules within the design, leading to a decreased fluorescent signal in the donor's fluorescent reporter (Gubala et al., 2020). This can be critical in quantification experiments that depend solely on fluorescence signal determination and should be taken in consideration when discussing the obtained results. Flow cytometry data analysis, despite providing the ability to extract information from large populations to evaluate internalisation, has been pointed to have several drawbacks. The first one is differentiating if the detected signal comes from inside the cell or from NPs bound to the plasma membrane. The following is the data that can be extracted from these analyses, as the percentage of positive cells for internalisation calculated by setting up a threshold gives no indication about the actual number of particles that are inside of the cells. Their mean fluorescence intensity information calculates these parameters for the whole population, and despite the single-cell nature of the technique does not accurately distinguish between cells that have a high number of NPs internalised or the ones that have very few. It also assumes that the intensity values of NPs will not change depending on intracellular parameters like

the local environment, especially the pH (Han & Burgess, 2010), granularity and intracellular compounds or the presence of other markers that could diminish the detection or quench the signal (FitzGerald & Johnston, 2021). Moreover, it lacks precise localisation information. We propose this method as an essential analysis for determining how cells internalise NPs in a semi-quantitative manner as long as it has been previously demonstrated by SEM that no NPs remain bound to the cell membrane once cells have been trypsinised before their analysis. This provides complementary data on internalisation that can be later expanded using precise quantitative internalisation, co-localisation and intracellular fate methods by CLSM analyses as proposed in chapters 2 and 3.

Regarding the conclusions that can be extracted from NPs visualisation in CLSM and other microscopy techniques, it is usually observed in literature that the data obtained from this kind of analyses are often used as proof of internalisation and interaction with cells but are often reported as merely informative in a qualitative or semi-quantitative manner (Cheng et al., 2015; Hesler et al., 2019; Hill et al., 2015; Hou et al., 2014; Rothen-Rutishauser et al., 2014; Y. Wang et al., 2016). This leads to a superficial analysis and results in conclusions by mere extrapolation that could be biased or inaccurate. It was our goal to provide a new way to process and analyse CLSM-obtained data, using precise data interpretation to provide a quantitative approach by single cell volumetric analysis within the nanoscale. Taking advantage of the volumetric information of the obtained datasets we were able to extract precise quantifiable single-cell internalisation information at a high resolution and provide localisation analyses within a single experiment. This level of detail when analysing internalisation and co-localisation in mammalian cell cultures at single-cell level and precise nanometric resolution has unprecedented records in literature. A previous article (Torrano et al., 2013) that used a similar method when quantifying nanoparticles (silica and cerium) at the nanoscale used a similar approach in terms of single-cell segmentation. Despite that, Torrano et al. method is based on fluorescence determination and calibration, and the extrapolation of the results of this calibration using different instruments on the data obtained. This procedure, despite having a similar resolution (lower in the z-axis) and procedure for the segmentation of single cells, could be affected by quenching happening within the samples, and therefore the determination of NPs aggregates of more than 5 NPs is described as limited by this effect (Torrano et al., 2013). Moreover, it is a method limited to two signals analyses and this is a limitation when trying to add more information on the localisation of the NPs with other sub-cellular structures and compartments. The quenching of the intensity of the NPs used in their work, and the inability to see any quenching effect when they performed a test on the quenching phenomenon using trypan blue is only valid to test the quenching efficacy of dyes that can't permeate the cell membrane (like trypan blue on healthy live cells), but won't be applicable on dyes in close contact with the fluorochromes of NPs in protocols such as co-localisation experiments, where structures in close contact with the internalised NPs are stained with other fluorochromes that could interfere with the NPs signal (FitzGerald & Johnston, 2021). Our method brings spatial resolution that allows for intracellular distribution and localisation

determination at a high level of resolution. The signal detected and quantified is accurate as the datasets are deconvolved prior to quantification. This deconvolution uses GPU power making it faster than other methods reported (Haase et al., 2020). It is also based on 3D object detection using GPU powered algorithms (that make analyses faster than CPU methods) and provides the possibility to analyse sub-cellular localisation of the data thanks to the addition of more immunofluorescence detection channels. The sample size for the presented study for the determination of internalisation and co-localisation of SiNPs within the nanoscale in cells is also bigger than those observed in literature using CLSM (Johnston et al., 2010; Schweiger et al., 2012). Moreover, our method doesn't require a calibration based on fluorescence. This is an advantage taking in consideration that fluorescence detection could fluctuate between instruments, the self-quenching of dyes or the quenching depending on contact with other intracellular fluorescent probes, degradative intracellular compounds, with metals from the ENMs functionalisation or because of aggregation, as explained above.

In this sense, SiNPs proved to be excellent in providing information through the several methods used for their investigation in characterising how distinct cell types behave under their exposure. Their stability in storage and in biologically compatible conditions was excellent. Their fluorescent cores provide a high-brightness signal that can be easily detected both through flow cytometry and in common microscopy instruments, from the live cell epifluorescence microscope to the more advanced CLSM microscopes once samples have been fixed, immunostained and processed for CLSM investigation. They were also observable in SEM in contact to the cell plasma membrane at the very first contact between SiNPs and the cells and proved to be non-toxic after compatible cytotoxicity assays investigation. This leads to the conclusion that they are a good alternative to investigate ENM-cell interaction and common biological processes such as the internalisation of drugs and other molecules and their intracellular fate. The development of ENMs such as the SiNPs we used, that are easily internalised into cancer cell lines and make them easily detected through fluorescence and spectroscopic data, is contributing to new diagnostic and theranostic technologies that help to improve the accuracy of detection of cancer cells. Moreover, their use as a model for the biological investigation of ENMs in mammalian cells, provides data identifying the mechanisms responsible for the biological responses observed after NPs exposure related to their physicochemical characteristics and therapeutic effect. Through the analyses from a cellular perspective, scientists are able to understand their interaction with low complexity biological systems and predict their in vivo behaviour, getting closer to optimise their design towards low-toxic and safe nanomaterials for human use. The single-cell evaluation of NP internalisation, localisation and intracellular fate over-time expands the knowledgebase of the mechanistic effects of inorganic nanoparticles in vitro and their effective cellular dosage and effects.

For the last chapter of the thesis, we evaluated the therapeutic potential of MPNDs to kill cancer cells. We tested the biointeraction of MPNDs with a human cervical adenocarcinoma (HeLa cell

line) and breast epithelial cell lines, the tumoral SKBR3 and the non-tumoral MCF10a. To harvest the potential therapeutic effect of these NPs, cell cultures were treated with a 1064 nm wavelength laser that triggers hyperthermia due to the plasmonic properties of MPNDs. MPNDs present two different layers on the semi-shell structure, the gold that confers de plasmonic properties and the iron oxide layer that allows their concentration using neodymium magnets and their hyperthermia effect that can be triggered when an alternating magnetic field is applied (Li et al., 2018). The results obtained prove that the magnetically-driven internalisation of MPNDs results in specific intracellular fate within the endosomes after magnetic actuation, a proof of the active endocytic mechanisms involved in their internalisation and are in accordance with other studies. That is, magnetically driven local delivery of drug-loaded nanoparticles to tumours has been reported both experimentally (Alexiou et al., 2000) and clinically (Lemke et al., 2004; Lübbe et al., 1996) using direct positioning of a fixed magnet over the targeting site for localisation. In most cases, the magnetic drug targeting/delivery is accomplished upon the application of an external magnetic field from electromagnetic coils (Hoshiar et al., 2017) or various types of permanent magnets (Carenza et al., 2014; Li et al., 2018). The magnet geometry and tumour-magnet distance can be of crucial importance for the effective magnetic drug delivery (Shamsi et al., 2018), by generating a magnetic field strong enough and with a field gradient deep enough to magnetise the magnetic NPs as deep as possible inside the tissue to treat. Thus, the importance of proving that ENMs have a strong magnetic moment (both for MRI qualities and targeting purposes) and the application of targeting actuators within the tumour by locating the magnetic field in the tumour region (for superficial tumours) or the installation of magnetic implants within deep-tissue tumours (Price et al., 2018). The ability to concentrate magnetic NPs in flow conditions (Matuszak et al., 2015; Nguyen et al., 2020; Sanz-Ortega et al., 2019; Tapeinos et al., 2019) was previously described in literature, specially using in vitro phantoms (Cao et al., 2012; Radon et al., 2015) but its effect on the internalisation and localisation have not been previously quantified at a single-cell level. The effects of magnetic field actuation on internalisation in mammalian cells have been previously reported by means of 2D whole-field fluorescence intensity analysis (MacDonald et al., 2012) or by evaluation of the iron content by direct analyte detection an spectroscopy methods (ICP-MS, ICP-AES or H-NMR spectroscopy) by quantification of whole population lysates (Gunn et al., 2009). The investigation of whether this internalisation process is a result of force-driven processes due to magnetic forces applied to the magnetic NPs solely or in combination with the active uptake processes involved in endocytic pathways to enter the cell was tested by MacDonald et al. (Sensenig et al., 2012). In their work, after treating bovine aortic endothelial cells with cytochalasin-D (a cell permeable inhibitor of actin polymerisation resulting in phagocytosis inhibition), magnetic nanoparticle uptake was significantly decreased in cultures with (up to 3.6 times less) and without magnetic actuation (up to 10 times less) when compared to cytochalasin-D-free cell cultures (MacDonald et al., 2012). The results described after affecting a com-

mon endocytic pathway depending on cytoskeletal reorganisation and actin polymerisation, highlight the importance of the active role of the cell in the internalisation and transportation systems for the uptake of magnetic NPs by the cell despite magnetic actuation forces.

It is also worth mentioning, that the magnetic arrest in fluidic conditions and its effects on internalisation and localisation on cell cultures is vaguely described in literature and is rarely quantified. For example, Matuszak et al. (Matuszak et al., 2015) tested SPIONs internalisation in endothelial cells by optical microscopy, but didn't perform a quantification of the number of NPs internalised. According to our results, magnetic actuation affects drastically the uptake and internalisation in epithelial breast cells, being almost zero when there was no magnetic concentration. Tapeinos et al. performed a similar study replicating the blood-brain barrier conditions using two different cell lines and testing the magnetic arrest, internalisation and crossing efficiency of magnetic nanocubes under flow conditions and static magnetic field actuation (Tapeinos et al., 2019). Similarly to our obtained results, magnetic actuation produced an arrest that led to a higher presence of magnetic NPs within the cells after short incubation times. This increase in internalisation was qualitatively shown in images, and the localisation within the endolysosomal system was not analysed, contrary to our study. Moreover, the data obtained was not quantified at a single cell-level as it was done with the MPNDs we tested in chapter 3. This leads to the conclusion that the magnetically-targeted administration of MPNDs to tumours is effective and lead to great internalisation and effective therapeutic results. Despite the internalisation was greatly affected by the magnetic concentration of MPNDs in fluidic conditions, a lot of the MPNDs remain outside the cells forming chain-like structures in close contact with the plasma membrane and their surrounding ECM. These structures, could be beneficial when targeting the tumour microenvironment rich in proteins and glycoproteins and collagen fibres that prevent the specific interaction of MPNDs or other synergistic treatments with the tumoral cells. Their presence within the tumour ECM could lead to a hyperthermia-triggered 'solubilisation' of dense protein and collagen fibres that contribute to the tumours self-protective environment (Kolosnjaj-Tabi et al., 2017; Piehler et al., 2020), helping targeted therapeutics reach their destination.

In terms of hyperthermia efficiency, MPNDs showed good hyperthermia inducing properties once exposed to the 1064 nm wavelength laser for 15 min or 5 min, at a low concentration 10 µg/mL and short MPNDs incubation times (3 h) even after rinsing, especially in the more sensitive SKBR-3 cell line. Other magnetic NPs based on iron oxides showed good hyperthermia efficiency when magnetic hyperthermia was triggered using an alternating magnetic field, but only when no rinsing was performed in human osteosarcoma cells (R. Wang et al., 2020), proving the effect of locally-induced heat production and the effects on cell membrane of bound and extracellular but close NPs in generating heat damage. Apart from the differential sensitivity of SKBR-3 at low hyperthermia conditions (5 min exposure to laser), we described that the cell death induced in this tumoral cell line

is apoptosis, a regulated cell death pathway dependant on caspase-3 activity activation, as previously described in literature by other magnetic NPs and triggers (Beola et al., 2020; Prasad et al., 2007; Shetake et al., 2015; Yoo et al., 2012). The activation of regulated cell death mechanisms is beneficial for the therapeutic outcome of the therapy per se, but also because it lowers side-effects related to uncontrolled cell death induction within the tumour and surrounding areas.

Moreover, the ability to manipulate and target tumours and cells with magnetic NPs by applying an external magnetic field has been explored for the last three decades, but the precise nanoscopic volumetric analysis of how this manipulation affects the retention and intracellular fate of MPNDs in human cells at a single-cell level has never been described before. The precise visualisation and quantification of these data allows for better interpretation on the behaviour of MPNDs in biological conditions, under magnetic actuation and their effects on extracellular and intracellular potential targets. This will allow for a better identification of the mechanisms involved in hyperthermia-derived damage and the mechanisms by which the treatment is effective at impairing tumour progression.

Overall, the advances presented in this thesis will help future generations of scientist to navigate the questions that arise from the interrogation of how ENMs and cells interact. It will lead to better interpretation of results obtained in terms of viability and internalisation experiments in the biological characterisation workflow. The results obtained using cerium oxide NPs showed that NPs can be a great therapeutic alternative to revert oxidative stress in cell cultures solving common antioxidant drawbacks like their low solubility and bioavailability of potential reactive sites when delivered to the cells. Cerium oxide NPs provide a colloidal suspension solution that delivers efficiently stable and reversible redox capabilities to modulate the oxidative stress rapidly and reversibly, ensuring a long-lasting antioxidant function compared to free antioxidant molecules. The evaluation of NP internalisation, localisation and intracellular fate at the nanoscale using SiNPs and MPNDs expands our knowledgebase of the mechanistic effects of inorganic nanoparticles in vitro and the effects of dosage in terms of concentration and exposure time at a single-cell level. It also allows us to identify the potential differences between cell lines and how treatments can have very different potential effects depending on the cell line used to analyse the therapeutic effect of ENMs. We believe our results can contribute from a methodological perspective to guide further experiments in the direction of highly quantitative and reproducible in vitro data analysis. It also highlights the hyperthermia sensitivity of two different cell lines, SKBR3 and MCF10a and how differences in hyperthermia-triggered treatment can lead to differential regulated cell death activation in tumoral cells. The present study highlighted the importance to precisely adapt the NPs and hyperthermia trigger treatment to induce a regulated cell-death to effectively treat cancer cells, without compromising normal ones. Thanks to the calibration between effective NP/cell ratio, exposure time, internalisation enhancements by magnetic concentration and duration of the laser irradiation treatment we have been

able to modulate the hyperthermia effect of MPNDs in order to reduce the uncontrolled cell death induction that would lead to strong side-effects in their potential use for tumour ablation.

5 Conclusions

1. Cerium oxide NPs (CeO_2 NPs) were non-toxic at low concentrations (5 and 10 $\mu\text{g}/\text{mL}$). Their bioapplication and efficiency as antioxidants was demonstrated, as they were able to revert up to a 23% the oxidative stress level in ROS-induced human cervical adenocarcinoma cells at 25 $\mu\text{g}/\text{mL}$ CeO_2 NPs at a similar efficiency than commercial products.
2. Internalisation of silicon dioxide NPs (SiNPs) is detected after 20 min of incubation reaching a plateau after 1 h of incubation, in HeLa and Caco-2 cells, according to flow cytometry results. They were non-toxic at 50 $\mu\text{g}/\text{mL}$ after 1 h exposure with no effects on viability and progression up to 7 days post-incubation time.
3. The development of a single-cell semi-automatic segmentation and deconvolution procedure of CLSM data and their analysis allows to accurately quantify differences in the number of NP per cell due to time exposure (1 or 3 h) as well as to differentiate the intracellular fate in HeLa cells incubated with 50 $\mu\text{g}/\text{mL}$ SiNPs.
4. Gold and Iron magnetoplasmonic nanodomains (MPNDs) were non-toxic to SKBR3 and MCF10a cell lines. Magnetic actuation proved to concentrate MPNDs and increased their cell internalisation using short incubation times (30 min).
5. The efficiency to arrest MPNDs using a magnetic field and enhance their internalisation in dynamic conditions was demonstrated both in MCF10a and SKBR3 cells, especially in the later as they internalise MPNDs more efficiently in such conditions.
6. Hyperthermia was achieved in MPNDs-incubated cell cultures using a 1064 nm NIR laser at 10 $\mu\text{g}/\text{mL}$ concentration. SKBR3 showed higher mortality and therefore differential sensitivity to 5 min laser irradiation compared to the MCF10a non-tumoral cell line. Differential activation of the caspase 3 by 5 min laser irradiation proved that SKBR3 cells are progressing into apoptosis while MCF10a are not affected by the treatment. Longer exposure to the laser increased the effects in cell viability in MCF10a, the non-tumoral cell line.

6 References

A

- Abe, M., Hiraoka, M., Takahashi, M., Egawa, S., Matsuda, C., Onoyama, Y., Morita, K., Kakehi, M., & Sugahara, T. (1986). Multi-institutional studies on hyperthermia using an 8-MHz radiofrequency capacitive heating device (thermotron RF-8) in combination with radiation for cancer therapy. *Cancer*, 58(8), 1589–1595. [https://doi.org/10.1002/1097-0142\(19861015\)58:8<1589::AID-CNCR2820580802>3.0.CO;2-B](https://doi.org/10.1002/1097-0142(19861015)58:8<1589::AID-CNCR2820580802>3.0.CO;2-B)
- Administration, F. and D. (2014). Considering whether an FDA-regulated product involves the application of nanotechnology. U.S. Food and Drug Administration.
- Albalawi, F., Hussein, M. Z., Fakurazi, S., & Masarudin, M. J. (2021a). Engineered nanomaterials: The challenges and opportunities for nanomedicines. *International Journal of Nanomedicine*, 16, 161–184. <https://doi.org/10.2147/IJN.S288236>
- Albalawi, F., Hussein, M. Z., Fakurazi, S., & Masarudin, M. J. (2021b). Engineered Nanomaterials: The Challenges and Opportunities for Nanomedicines. <https://doi.org/10.2147/IJN.S288236>
- Albanese, A., & Chan, W. C. W. (2011). Effect of gold nanoparticle aggregation on cell uptake and toxicity. *ACS Nano*, 5(7), 5478–5489. <https://doi.org/10.1021/nn2007496>
- Alexiou, C., Arnold, W., Klein, R. J., Parak, F. G., Hulin, P., Bergemann, C., Erhardt, W., Wagenpfeil, S., & Lubbe, A. S. (2000). Locoregional cancer treatment with magnetic drug targeting. *Cancer Research*, 60(23), 6641–6648.
- Allothman, Z. A. (2012). A review: Fundamental aspects of silicate mesoporous materials. *Materials*, 5(12), 2874–2902. <https://doi.org/10.3390/ma5122874>
- Anchordoquy, T. J., Barenholz, Y., Boraschi, D., Chorny, M., Decuzzi, P., Dobrovolskaia, M. A., Farhangrazi, Z. S., Farrell, D., Gabizon, A., Ghandehari, H., Godin, B., La-Beck, N. M., Ljubimova, J., Moghimi, S. M., Pagliaro, L., Park, J. H., Peer, D., Ruoslahti, E., Serkova, N. J., & Simberg, D. (2017). Mechanisms and Barriers in Cancer Nanomedicine: Addressing Challenges, Looking for Solutions. *ACS Nano*, 11(1), 12–

18. <https://doi.org/10.1021/acsnano.6b08244>

Anselmo, A. C., & Mitragotri, S. (2019). Nanoparticles in the clinic: An update. *Bioengineering & Translational Medicine*, 4(3), 1–16. <https://doi.org/10.1002/btm2.10143>

Aurelia Chis, A., Dobrea, C., Morgovan, C., Arseniu, A. M., Rus, L. L., Butuca, A., Juncan, A. M., Totan, M., Vonica-Tincu, A. L., Cormos, G., Muntean, A. C., Muresan, M. L., Gligor, F. G., & Frum, A. (2020). Applications and Limitations of Dendrimers in Biomedicine. *Molecules*, 25(17). <https://doi.org/10.3390/molecules25173982>

Avelar-Freitas, B. A., Almeida, V. G., Pinto, M. C. X., Mourão, F. A. G., Massensini, A. R., Martins-Filho, O. A., Rocha-Vieira, E., & Brito-Melo, G. E. A. (2014). Trypan blue exclusion assay by flow cytometry. *Brazilian Journal of Medical and Biological Research*, 47(4), 307–315. <https://doi.org/10.1590/1414-431X20143437>

B

Babitha, K. K., Sreedevi, A., Priyanka, K. P., Sabu, B., & Varguese, T. (2015). Structural characterization and optical studies of CeO₂ nanoparticles synthesized by chemical precipitation. *Indian. J. Appl. Phys.*, 53, 596–603.

Bae, Y. H., & Park, K. (2011). Targeted drug delivery to tumors: Myths, reality and possibility. *Journal of Controlled Release*, 153(3), 198–205. <https://doi.org/10.1016/j.jconrel.2011.06.001>

Bajak, E., Fabbri, M., Ponti, J., Gioria, S., Ojea-Jiménez, I., Collotta, A., Mariani, V., Gilliland, D., Rossi, F., & Gribaldo, L. (2015). Changes in Caco-2 cells transcriptome profiles upon exposure to gold nanoparticles. *Toxicology Letters*, 233(2), 187–199. <https://doi.org/10.1016/j.toxlet.2014.12.008>

Barenholz, Y. (Chezy). (2012). Doxil® — The first FDA-approved nano-drug: Lessons learned. *Journal of Controlled Release*, 160(2), 117–134. <https://doi.org/10.1016/j.jconrel.2012.03.020>

Benachour, H., Sève, A., Bastogne, T., Frochot, C., Vanderesse, R., Jasniewski, J. D., Miladi, I., Billotey, C., Tillement, O., Lux, F., & Barberi-Heyob, M. (2012). Multifunctional peptide-conjugated hybrid silica nanoparticles for photo-dynamic therapy and MRI.

Theranostics, 2(9), 889–904. <https://doi.org/10.7150/thno.4754>

- Beola, L., Asín, L., Roma-Rodrigues, C., Fernandez-Afonso, Y., Fratila, R. M., Serantes, D., Ruta, S., Chantrell, R. W., Fernandes, A. R., Baptista, P. V., de la Fuente, J. M., Grazu, V., & Gutierrez, L. (2020). The intracellular number of magnetic nanoparticles modulates the apoptotic death pathway after magnetic hyperthermia treatment. *ACS Applied Materials and Interfaces*, 12(39), 43474–43487. <https://doi.org/10.1021/acsami.0c12900>
- Berry, C. C. (2005). Possible exploitation of magnetic nanoparticle–cell interaction for biomedical applications. *Journal of Materials Chemistry*, 15(5), 543–547. <https://doi.org/10.1039/b409715g>
- Bhushan, B., Nandhagopal, S., Rajesh Kannan, R., & Gopinath, P. (2016). Biomimetic nanomaterials: Development of protein coated nanoceria as a potential antioxidative nano-agent for the effective scavenging of reactive oxygen species in vitro and in zebrafish model. *Colloids and Surfaces B: Biointerfaces*, 146, 375–386. <https://doi.org/10.1016/j.colsurfb.2016.06.035>
- Bohmer, N., Rippl, A., May, S., Walter, A., Heo, M. B., Kwak, M., Roeslein, M., Song, N. W., Wick, P., & Hirsch, C. (2018). Interference of engineered nanomaterials in flow cytometry: A case study. *Colloids and Surfaces B: Biointerfaces*, 172(August), 635–645. <https://doi.org/10.1016/j.colsurfb.2018.09.021>
- Boilard, S. P., Amyotte, P. R., Khan, F. I., Dastidar, A. G., & Eckhoff, R. K. (2013). Explosibility of micron- and nano-size titanium powders. *Journal of Loss Prevention in the Process Industries*, 26(6), 1646–1654. <https://doi.org/10.1016/j.jlp.2013.06.003>
- Borkowska, M., Siek, M., Kolygina, D. V., Sobolev, Y. I., Lach, S., Kumar, S., Cho, Y. K., Kandere-Grzybowska, K., & Grzybowski, B. A. (2020). Targeted crystallization of mixed-charge nanoparticles in lysosomes induces selective death of cancer cells. *Nature Nanotechnology*, 15(4), 331–341. <https://doi.org/10.1038/s41565-020-0643-3>
- Buschmann, M. D., Carrasco, M. J., Alishetty, S., Paige, M., Alameh, M. G., & Weissman, D. (2021). Nanomaterial Delivery Systems for mRNA Vaccines. *Vaccines*, 9(1), 65. <https://doi.org/10.3390/vaccines9010065>

C

- Calvo, F., Ege, N., Grande-Garcia, A., Hooper, S., Jenkins, R. P., Chaudhry, S. I., Harrington, K., Williamson, P., Moeendarbary, E., Charras, G., & Sahai, E. (2013). Mechanotransduction and YAP-dependent matrix remodelling is required for the generation and maintenance of cancer-associated fibroblasts. *Nature Cell Biology*, 15(6), 637–646. <https://doi.org/10.1038/ncb2756>
- Canton, J. (2018). Macropinocytosis: New insights into its underappreciated role in innate immune cell surveillance. *Frontiers in Immunology*, 9(OCT), 1–8. <https://doi.org/10.3389/fimmu.2018.02286>
- Cao, Q., Han, X., & Li, L. (2012). Numerical analysis of magnetic nanoparticle transport in microfluidic systems under the influence of permanent magnets. *Journal of Physics D: Applied Physics*, 45(46). <https://doi.org/10.1088/0022-3727/45/46/465001>
- Carenza, E., Barceló, V., Morancho, A., Levander, L., Boada, C., Laromaine, A., Roig, A., Montaner, J., & Rosell, A. (2014). In vitro angiogenic performance and in vivo brain targeting of magnetized endothelial progenitor cells for neurorepair therapies. *Nanomedicine: Nanotechnology, Biology, and Medicine*, 10(1), 225–234. <https://doi.org/10.1016/j.nano.2013.06.005>
- Cayado, P., De Keukeleere, K., Garzón, A., Perez-Mirabet, L., Meledin, A., De Roo, J., Vallés, F., Mundet, B., Rijckaert, H., Pollefeyt, G., Coll, M., Ricart, S., Palau, A., Gázquez, J., Ros, J., Van Tendeloo, G., Van Driessche, I., Puig, T., & Obradors, X. (2015). Epitaxial YBa₂Cu₃O_{7-x} nanocomposite thin films from colloidal solutions. *Superconductor Science and Technology*, 28(12), 124007. <https://doi.org/10.1088/0953-2048/28/12/124007>
- Celardo, I., Pedersen, J. Z., Traversa, E., & Ghibelli, L. (2011). Pharmacological potential of cerium oxide nanoparticles. *Nanoscale*, 3(4), 1411–1420. <https://doi.org/10.1039/c0nr00875c>
- Chaari, M., Gaztelumendi, N., Cabrera-González, J., Peixoto-Moledo, P., Viñas, C., Xochitiotzi-Flores, E., Farfán, N., Ben Salah, A., Nogués, C., & Núñez, R. (2018). Fluorescent BODIPY-Anionic Boron Cluster Conjugates as Potential Agents for Cell Tracking. *Bioconjugate Chemistry*, 29(5), 1763–1773.

<https://doi.org/10.1021/acs.bioconjchem.8b00204>

Chan, G. K. Y., Kleinheinz, T. L., Peterson, D., & Moffat, J. G. (2013). A Simple High-Content Cell Cycle Assay Reveals Frequent Discrepancies between Cell Number and ATP and MTS Proliferation Assays. *PLoS ONE*, 8(5). <https://doi.org/10.1371/journal.pone.0063583>

Channei, D., Inceesungvorn, B., Wetchakun, N., & Phanichphant, S. (2013). Kinetics Study of Photocatalytic Activity of Flame-Made Unloaded and Fe-Loaded CeO₂ Nanoparticles. *International Journal of Photoenergy*, 2013, 1–9. <https://doi.org/10.1155/2013/484831>

Cheng, S. H., Lee, C. H., Chen, M. C., Souris, J. S., Tseng, F. G., Yang, C. S., Mou, C. Y., Chen, C. T., & Lo, L. W. (2010). Tri-functionalization of mesoporous silica nanoparticles for comprehensive cancer theranostics - The trio of imaging, targeting and therapy. *Journal of Materials Chemistry*, 20(29), 6149–6157. <https://doi.org/10.1039/c0jm00645a>

Cheng, Y.-J., Luo, G.-F., Zhu, J.-Y., Xu, X.-D., Zeng, X., Cheng, D.-B., Li, Y.-M., Wu, Y., Zhang, X.-Z., Zhuo, R.-X., & He, F. (2015). Enzyme-Induced and Tumor-Targeted Drug Delivery System Based on Multifunctional Mesoporous Silica Nanoparticles. *ACS Applied Materials & Interfaces*, 150424082723008. <https://doi.org/10.1021/acsami.5b00752>

Cheng, Y., Weng, S., Yu, L., Zhu, N., Yang, M., & Yuan, Y. (2019). The Role of Hyperthermia in the Multidisciplinary Treatment of Malignant Tumors. *Integrative Cancer Therapies*, 18. <https://doi.org/10.1177/1534735419876345>

Clerc, P., Jeanjean, P., Hallalli, N., Gougeon, M., Pipy, B., Carrey, J., Fourmy, D., & Gigoux, V. (2018). Targeted Magnetic Intra-Lysosomal Hyperthermia produces lysosomal reactive oxygen species and causes Caspase-1 dependent cell death. *Journal of Controlled Release*, 270, 120–134. <https://doi.org/10.1016/j.jconrel.2017.11.050>

Cocucci, E., Aguet, F., Boulant, S., & Kirchhausen, T. (2012). The First Five Seconds in the Life of a Clathrin-Coated Pit. *Cell*, 150(3), 495–507. <https://doi.org/10.1016/j.cell.2012.05.047>

Coey, M., Ackland, K., Venkatesan, M., & Sen, S. (2016). Collective magnetic response of CeO₂ nanoparticles. *Nature Physics*, 12(7), 694–699.

<https://doi.org/10.1038/nphys3676>

Conde, J., Dias, J. T., Grazú, V., Moros, M., Baptista, P. V., & de la Fuente, J. M. (2014). Revisiting 30 years of biofunctionalization and surface chemistry of inorganic nanoparticles for nanomedicine. *Frontiers in Chemistry*, 2, 48. <https://doi.org/10.3389/fchem.2014.00048>

Corma, A., Atienzar, P., García, H., & Chane-Ching, J. Y. (2004). Hierarchically mesostructured doped CeO₂ with potential for solar-cell use. *Nature Materials*, 3(6), 394–397. <https://doi.org/10.1038/nmat1129>

Cortés-Ciriano, I., & Bender, A. (2016). How Consistent are Publicly Reported Cytotoxicity Data? Large-Scale Statistical Analysis of the Concordance of Public Independent Cytotoxicity Measurements. *ChemMedChem*, 11(1), 57–71. <https://doi.org/10.1002/cmdc.201500424>

Coty, J. B., Eleamen Oliveira, E., & Vauthier, C. (2017). Tuning complement activation and pathway through controlled molecular architecture of dextran chains in nanoparticle corona. *International Journal of Pharmaceutics*, 532(2), 769–778. <https://doi.org/10.1016/j.ijpharm.2017.04.048>

D

Donolato, M., Antunes, P., Bejhed, R. S., Zardán Gómez De La Torre, T., Østerberg, F. W., Strömberg, M., Nilsson, M., Strømme, M., Svedlindh, P., Hansen, M. F., & Vavassori, P. (2015). Novel readout method for molecular diagnostic assays based on optical measurements of magnetic nanobead dynamics. *Analytical Chemistry*, 87(3), 1622–1629. <https://doi.org/10.1021/ac503191v>

Douglas, K. L., Piccirillo, C. A., & Tabrizian, M. (2008). Cell line-dependent internalization pathways and intracellular trafficking determine transfection efficiency of nanoparticle vectors. *European Journal of Pharmaceutics and Biopharmaceutics*, 68(3), 676–687. <https://doi.org/10.1016/j.ejpb.2007.09.002>

Drasler, B., Vanhecke, D., Rodriguez-Lorenzo, L., Petri-Fink, A., & Rothen-Rutishauser, B. (2017). Quantifying nanoparticle cellular uptake: Which method is best? *Nanomedicine*, 12(10), 1095–1099. <https://doi.org/10.2217/nnm-2017-0071>

Duan, F., Kwek, D., & Crivoi, A. (2011). Viscosity affected by nanoparticle aggregation in Al₂O₃-water nanofluids. *Nanoscale Research Letters*, 6(1), 248. <https://doi.org/10.1186/1556-276X-6-248>

E

El-Sayed, A., & Harashima, H. (2013). Endocytosis of Gene Delivery Vectors: From Clathrin-dependent to Lipid Raft-mediated Endocytosis. *Molecular Therapy*, 21(6), 1118–1130. <https://doi.org/10.1038/mt.2013.54>

Elsaesser, A., Barnes, C. A., McKerr, G., Salvati, A., Lynch, I., Dawson, K. A., & Howard, C. V. (2011). Quantification of nanoparticle uptake by cells using an unbiased sampling method and electron microscopy. *Nanomedicine*, 6(7), 1189–1198. <https://doi.org/10.2217/nnm.11.70>

Espinosa, A., Reguera, J., Curcio, A., Muñoz-Noval, Á., Kuttner, C., Van de Walle, A., Liz-Marzán, L. M., & Wilhelm, C. (2020). Janus Magnetic-Plasmonic Nanoparticles for Magnetically Guided and Thermally Activated Cancer Therapy. *Small*, 16(11), 1–14. <https://doi.org/10.1002/sml.201904960>

EU Regulation (EC) No. 1272/2008 of the European Parliament and of the Council on classification, labelling and packaging of substances and mixtures, (2008) (testimony of EU Regulation (EC) No. 1272/2008 - European Parliament).

Eustis, S., & El-Sayed, M. A. (2006). Why gold nanoparticles are more precious than pretty gold: Noble metal surface plasmon resonance and its enhancement of the radiative and nonradiative properties of nanocrystals of different shapes. *Chem. Soc. Rev.*, 35(3), 209–217. <https://doi.org/10.1039/B514191E>

F

Farjadian, F., Ghasemi, A., Gohari, O., Roointan, A., Karimi, M., & Hamblin, M. R. (2019). Nanopharmaceuticals and nanomedicines currently on the market: challenges and opportunities. *Nanomedicine*, 14(1), 93–126. <https://doi.org/10.2217/nnm-2018-0120>

Ferlay, J., Soerjomataram, I., Dikshit, R., Eser, S., Mathers, C., Rebelo, M., Parkin, D. M.,

Forman, D., & Bray, F. (2015). Cancer incidence and mortality worldwide: Sources, methods and major patterns in GLOBOCAN 2012. *International Journal of Cancer*, 136(5), E359–E386. <https://doi.org/10.1002/ijc.29210>

Fischer, E. G. (2020). Nuclear Morphology and the Biology of Cancer Cells. *Acta Cytologica*, 64(6), 511–519. <https://doi.org/10.1159/000508780>

FitzGerald, L. I., & Johnston, A. P. R. (2021). It's what's on the inside that counts: Techniques for investigating the uptake and recycling of nanoparticles and proteins in cells. *Journal of Colloid and Interface Science*, 587, 64–78. <https://doi.org/10.1016/j.jcis.2020.11.076>

Fluegen, G., Avivar-Valderas, A., Wang, Y., Padgen, M. R., Williams, J. K., Nobre, A. R., Calvo, V., Cheung, J. F., Bravo-Cordero, J. J., Entenberg, D., Castracane, J., Verkhusha, V., Keely, P. J., Condeelis, J., & Aguirre-Ghiso, J. A. (2017). Phenotypic heterogeneity of disseminated tumour cells is preset by primary tumour hypoxic microenvironments. *Nature Cell Biology*, December 2016. <https://doi.org/10.1038/ncb3465>

Fu, P. P., Xia, Q., Hwang, H.-M., Ray, P. C., & Yu, H. (2014). Mechanisms of nanotoxicity: Generation of reactive oxygen species. *Journal of Food and Drug Analysis*, 22(1), 64–75. <https://doi.org/10.1016/j.jfda.2014.01.005>

G

Galluzzi, L., Vitale, I., Aaronson, S. A., Abrams, J. M., Adam, D., Agostinis, P., Alnemri, E. S., Altucci, L., Amelio, I., Andrews, D. W., Annicchiarico-Petruzzelli, M., Antonov, A. V., Arama, E., Baehrecke, E. H., Barlev, N. A., Bazan, N. G., Bernassola, F., Bertrand, M. J. M., Bianchi, K., ... Kroemer, G. (2018). Molecular mechanisms of cell death: recommendations of the Nomenclature Committee on Cell Death 2018. *Cell Death & Differentiation*, 25(3), 486–541. <https://doi.org/10.1038/s41418-017-0012-4>

Gao, Y., Gao, F., Chen, K., & Ma, J. (2014). Cerium oxide nanoparticles in cancer. *OncoTargets and Therapy*, 835. <https://doi.org/10.2147/OTT.S62057>

Garzón-Manjón, A., Solano, E., de la Mata, M., Guzmán, R., Arbiol, J., Puig, T., Obradors, X., Yáñez, R., Ricart, S., & Ros, J. (2015). Induced shape controllability by tailored

precursor design in thermal and microwave-assisted synthesis of Fe_3O_4 nanoparticles. *Journal of Nanoparticle Research*, 17(7), 291. <https://doi.org/10.1007/s11051-015-3070-x>

Ghezzi, M., Pescina, S., Padula, C., Santi, P., Del Favero, E., Cantù, L., & Nicoli, S. (2021). Polymeric micelles in drug delivery: An insight of the techniques for their characterization and assessment in biorelevant conditions. *Journal of Controlled Release*, 332(February), 312–336. <https://doi.org/10.1016/j.jconrel.2021.02.031>

Ginader Timothy, et al B. M. (2016). PEGylation as a strategy for improving nanoparticle-based drug and gene delivery. *Advanced Drug Delivery Reviews*, 99(3), 28–51. <https://doi.org/10.1016/j.addr.2015.09.012>

Goldstein, A., Soroka, Y., Frušić-Zlotkin, M., Popov, I., & Kohen, R. (2014). High resolution SEM imaging of gold nanoparticles in cells and tissues. *Journal of Microscopy*, 256(3), 237–247. <https://doi.org/10.1111/jmi.12179>

Gradishar, W. J., Tjulandin, S., Davidson, N., Shaw, H., Desai, N., Bhar, P., Hawkins, M., & O'Shaughnessy, J. (2005). Phase III trial of nanoparticle albumin-bound paclitaxel compared with polyethylated castor oil-based paclitaxel in women with breast cancer. *Journal of Clinical Oncology*, 23(31), 7794–7803. <https://doi.org/10.1200/JCO.2005.04.937>

Grivennikov, S. I., Greten, F. R., & Karin, M. (2010). Immunity, Inflammation, and Cancer. *Cell*, 140(6), 883–899. <https://doi.org/10.1016/j.cell.2010.01.025>

Gu, H., & Soucek, M. D. (2007). Preparation and Characterization of Monodisperse Cerium Oxide Nanoparticles in Hydrocarbon Solvents. *Chemistry of Materials*, 19(5), 1103–1110. <https://doi.org/10.1021/cm061332r>

Gubala, V., Giovannini, G., Kunc, F., Monopoli, M. P., & Moore, C. J. (2020). Dye-doped silica nanoparticles: synthesis, surface chemistry and bioapplications. *Cancer Nanotechnology*, 11(1), 1. <https://doi.org/10.1186/s12645-019-0056-x>

Guehrs, E., Schneider, M., Günther, C. M., Hessing, P., Heitz, K., Wittke, D., López-Serrano Oliver, A., Jakubowski, N., Plendl, J., Eisebitt, S., & Haase, A. (2017). Quantification of silver nanoparticle uptake and distribution within individual human macrophages by FIB/SEM slice and view. *Journal of Nanobiotechnology*, 15(1), 1–11. <https://doi.org/10.1186/s12951-017-0255-8>

- Gunn, J., Paranj, R. K., & Zhang, M. (2009). A simple and highly sensitive method for magnetic nanoparticle quantitation using ^1H -NMR spectroscopy. *Biophysical Journal*, 97(9), 2640–2647. <https://doi.org/10.1016/j.bpj.2009.08.013>
- Guo, C., Yu, H., Feng, B., Gao, W., Yan, M., Zhang, Z., Li, Y., & Liu, S. (2015). Highly efficient ablation of metastatic breast cancer using ammonium-tungsten-bronze nanocube as a novel 1064nm-laser-driven photothermal agent. *Biomaterials*, 52(1), 407–416. <https://doi.org/10.1016/j.biomaterials.2015.02.054>
- Gupta, A. K., Berry, C., Gupta, M., & Curtis, A. (2003). Receptor-mediated targeting of magnetic nanoparticles using insulin as a surface ligand to prevent endocytosis. *IEEE Transactions on Nanobioscience*, 2(4), 255–261. <https://doi.org/10.1109/TNB.2003.820279>
- Gupta, A. K., Naregalkar, R. R., Vaidya, V. D., & Gupta, M. (2007). Recent advances on surface engineering of magnetic iron oxide nanoparticles and their biomedical applications. *Nanomedicine*, 2(1), 23–39. <https://doi.org/10.2217/17435889.2.1.23>

H

- Haase, R., Royer, L. A., Steinbach, P., Schmidt, D., Dibrov, A., Schmidt, U., Weigert, M., Maghelli, N., Tomancak, P., Jug, F., & Myers, E. W. (2020). CLIJ: GPU-accelerated image processing for everyone. *Nature Methods*, 17(1), 5–6. <https://doi.org/10.1038/s41592-019-0650-1>
- Häfeli, U. O. (2004). Magnetically modulated therapeutic systems. *International Journal of Pharmaceutics*, 277(1–2), 19–24. <https://doi.org/10.1016/j.ijpharm.2003.03.002>
- Halamoda-Kenzaoui, B., & Bremer-Hoffmann, S. (2018). Main trends of immune effects triggered by nanomedicines in preclinical studies. *International Journal of Nanomedicine*, 13, 5419–5431. <https://doi.org/10.2147/IJN.S168808>
- Han, J., & Burgess, K. (2010). Fluorescent indicators for intracellular pH. *Chemical Reviews*, 110(5), 2709–2728. <https://doi.org/10.1021/cr900249z>
- Haneda, M., Kaneko, T., Kamiuchi, N., & Ozawa, M. (2015). Improved three-way catalytic activity of bimetallic Ir-Rh catalysts supported on CeO₂-ZrO₂. *Catalysis Science and Technology*, 5(3), 1792–1800. <https://doi.org/10.1039/c4cy01502a>

- Harthøj, A., Holt, T., & Møller, P. (2015). Oxidation behaviour and electrical properties of cobalt/cerium oxide composite coatings for solid oxide fuel cell interconnects. *Journal of Power Sources*, 281, 227–237. <https://doi.org/10.1016/j.jpowsour.2015.01.128>
- Hesler, M., Aengenheister, L., Ellinger, B., Drexel, R., Straskraba, S., Jost, C., Wagner, S., Meier, F., von Briesen, H., Büchel, C., Wick, P., Buerki-Thurnherr, T., & Kohl, Y. (2019). Multi-endpoint toxicological assessment of polystyrene nano- and microparticles in different biological models in vitro. *Toxicology in Vitro*, 61(July), 104610. <https://doi.org/10.1016/j.tiv.2019.104610>
- Hill, C., Jain, a, Takemoto, H., Silver, M. D., Nagesh, S. V. S., Ionita, C. N., Bednarek, D. R., & Rudin, S. (2015). Imaging interactions of metal oxide nanoparticles with macrophage cells by ultra-high resolution scanning electron microscopy techniques. *Proceedings of SPIE--the International Society for Optical Engineering*, 73(4), 389–400. <https://doi.org/10.1530/ERC-14-0411.Persistent>
- Hirst, S. M., Karakoti, A. S., Tyler, R. D., Sriranganathan, N., Seal, S., & Reilly, C. M. (2009). Anti-inflammatory Properties of Cerium Oxide Nanoparticles. *Small*, 5(24), 2848–2856. <https://doi.org/10.1002/sml.200901048>
- Hortelao, A. C., Simó, C., Guix, M., Guallar-Garrido, S., Julián, E., Vilela, D., Rejc, L., Ramos-Cabrer, P., Cossío, U., Gómez-Vallejo, V., Patiño, T., Llop, J., & Sánchez, S. (2021). Swarming behavior and in vivo monitoring of enzymatic nanomotors within the bladder. *Science Robotics*, 6(52), eabd2823. <https://doi.org/10.1126/scirobotics.abd2823>
- Hoshlar, A. K., Le, T. A., Amin, F. U., Kim, M. O., & Yoon, J. (2017). Studies of aggregated nanoparticles steering during magnetic-guided drug delivery in the blood vessels. *Journal of Magnetism and Magnetic Materials*, 427(November), 181–187. <https://doi.org/10.1016/j.jmmm.2016.11.016>
- Hou, Y., Lai, M., Chen, X., Li, J., Hu, Y., Luo, Z., Ding, X., & Cai, K. (2014). Effects of mesoporous SiO₂, Fe₃O₄, and TiO₂ nanoparticles on the biological functions of endothelial cells in vitro. *Journal of Biomedical Materials Research. Part A*, 102(6), 1726–1736. <https://doi.org/10.1002/jbm.a.34839>
- Hu, B., Liu, X., Zhang, C., & Zeng, X. (2017). Food macromolecule based nanodelivery systems for enhancing the bioavailability of polyphenols. *Journal of Food and Drug*

Analysis, 25(1), 3–15. <https://doi.org/10.1016/j.jfda.2016.11.004>

Hu, X. M., Li, Z. X., Lin, R. H., Shan, J. Q., Yu, Q. W., Wang, R. X., Liao, L. S., Yan, W. T., Wang, Z., Shang, L., Huang, Y., Zhang, Q., & Xiong, K. (2021). Guidelines for Regulated Cell Death Assays: A Systematic Summary, A Categorical Comparison, A Prospective. *Frontiers in Cell and Developmental Biology*, 9(March), 1–28. <https://doi.org/10.3389/fcell.2021.634690>

Huang, L., & Guo, S. (2011). Nanoparticles escaping RES and endosome: Challenges for siRNA delivery for cancer therapy. *Journal of Nanomaterials*, 2011. <https://doi.org/10.1155/2011/742895>

I

Inerbaev, T. M., Karakoti, A. S., Kuchibhatla, S. V. N. T., Kumar, A., Masunov, A. E., & Seal, S. (2015). Aqueous medium induced optical transitions in cerium oxide nanoparticles. *Physical Chemistry Chemical Physics*, 17(9), 6217–6221. <https://doi.org/10.1039/c4cp04961f>

International Organization for Standardization. (2009). ISO 10993-5:2009(E) Biological evaluation of medical devices - Part 5: Tests for in vitro cytotoxicity: Vol. Third edit. IHS under license with ISO.

Ishida, O., Maruyama, K., Tanahashi, H., Iwatsuru, M., Sasaki, K., Eriguchi, M., & Yanagie, H. (2001). Liposomes bearing polyethyleneglycol-coupled transferrin with intracellular targeting property to the solid tumors in vivo. *Pharmaceutical Research*, 18(7), 1042–1048. <https://doi.org/10.1023/a:1010960900254>

Ivask, A., Mitchell, A. J., Hope, C. M., Barry, S. C., Lombi, E., & Voelcker, N. H. (2017). Single Cell Level Quantification of Nanoparticle-Cell Interactions Using Mass Cytometry. *Analytical Chemistry*, 89(16), 8228–8232. <https://doi.org/10.1021/acs.analchem.7b01006>

J

- Johnston, H. J., Semmler-Behnke, M., Brown, D. M., Kreyling, W., Tran, L., & Stone, V. (2010). Evaluating the uptake and intracellular fate of polystyrene nanoparticles by primary and hepatocyte cell lines in vitro. *Toxicology and Applied Pharmacology*, 242(1), 66–78. <https://doi.org/10.1016/j.taap.2009.09.015>
- Jordan, A., Scholz, R., Wust, P., Fähling, H., & Felix, R. (1999). Magnetic fluid hyperthermia (MFH): Cancer treatment with AC magnetic field induced excitation of biocompatible superparamagnetic nanoparticles. *Journal of Magnetism and Magnetic Materials*, 201(1–3), 413–419. [https://doi.org/10.1016/S0304-8853\(99\)00088-8](https://doi.org/10.1016/S0304-8853(99)00088-8)

K

- Kamińska, K., Szczylik, C., Bielecka, Z. F., Bartnik, E., Porta, C., Lian, F., & Czarnecka, A. M. (2015). The role of the cell-cell interactions in cancer progression. *Journal of Cellular and Molecular Medicine*, 19(2), 283–296. <https://doi.org/10.1111/jcmm.12408>
- Kang, K. A., Wang, J., Jasinski, J. B., & Achilefu, S. (2011). Fluorescence Manipulation by Gold Nanoparticles: From Complete Quenching to Extensive Enhancement. *Journal of Nanobiotechnology*, 9, 1–13. <https://doi.org/10.1186/1477-3155-9-16>
- Karakoti, A. S., Singh, S., Kumar, A., Malinska, M., Kuchibhatla, S. V. N. T., Wozniak, K., Self, W. T., & Seal, S. (2009). PEGylated Nanoceria as Radical Scavenger with Tunable Redox Chemistry. *Journal of the American Chemical Society*, 131(40), 14144–14145. <https://doi.org/10.1021/ja9051087>
- Karakoti, A., Singh, S., Dowding, J. M., Seal, S., & Self, W. T. (2010). Redox-active radical scavenging nanomaterials. *Chemical Society Reviews*, 39(11), 4422–4432. <https://doi.org/10.1039/b919677n>
- Kim, D. W., Kim, S. Y., Kim, H. K., Kim, S. W., Shin, S. W., Kim, J. S., Park, K., Lee, M. Y., & Heo, D. S. (2007). Multicenter phase II trial of Genexol-PM, a novel Cremophor-free, polymeric micelle formulation of paclitaxel, with cisplatin in patients with advanced

non-small-cell lung cancer. *Annals of Oncology*, 18(12), 2009–2014.
<https://doi.org/10.1093/annonc/mdm374>

Kim, T.-Y., Kim, D.-W., Chung, J.-Y., Shin, S. G., Kim, S.-C., Heo, D. S., Kim, N. K., & Bang, Y.-J. (2004). Phase I and Pharmacokinetic Study of Genexol-PM, a Cremophor-Free, Polymeric Micelle-Formulated Paclitaxel, in Patients with Advanced Malignancies. *Clinical Cancer Research*, 10(11), 3708–3716. <https://doi.org/10.1158/1078-0432.CCR-03-0655>

Kirpotin, D. B., Drummond, D. C., Shao, Y., Shalaby, M. R., Hong, K., Nielsen, U. B., Marks, J. D., Benz, C. C., & Park, J. W. (2006). Antibody targeting of long-circulating lipidic nanoparticles does not increase tumor localization but does increase internalization in animal models. *Cancer Research*, 66(13), 6732–6740. <https://doi.org/10.1158/0008-5472.CAN-05-4199>

Kobayashi, T. (2011). Cancer hyperthermia using magnetic nanoparticles. *Biotechnology Journal*, 6(11), 1342–1347. <https://doi.org/10.1002/biot.201100045>

Kolosnjaj-Tabi, J., Marangon, I., Nicolas-Boluda, A., Silva, A. K. A., & Gazeau, F. (2017). Nanoparticle-based hyperthermia, a local treatment modulating the tumor extracellular matrix. *Pharmacological Research*, 126, 123–137. <https://doi.org/10.1016/j.phrs.2017.07.010>

Kopwiththaya, A., Ohulchansky, T. Y., Jeon, M., Law, W. C., Xue, X., Xie, Q., Chada, R. R., Furlani, E. P., Kim, C., & Prasad, P. N. (2012). Magnetoplasmonic nanoplatforms for enhanced bioimaging and photothermal cancer therapy. *Technical Proceedings of the 2012 NSTI Nanotechnology Conference and Expo, NSTI-Nanotech 2012*, 3, 32–35.

Kroll, A., Pillukat, M. H., Hahn, D., & Schnekenburger, J. (2012). Interference of engineered nanoparticles with in vitro toxicity assays. *Archives of Toxicology*, 86(7), 1123–1136. <https://doi.org/10.1007/s00204-012-0837-z>

Krüger, K., Schrader, K., & Klempt, M. (2017). Cellular response to titanium dioxide nanoparticles in intestinal epithelial Caco-2 cells is dependent on endocytosis-associated structures and mediated by EGFR. *Nanomaterials*, 7(4). <https://doi.org/10.3390/nano7040079>

Kumar, A., Das, S., Munusamy, P., Self, W., Baer, D. R., Sayle, D. C., & Seal, S. (2014). Behavior of nanoceria in biologically-relevant environments. *Environ. Sci.: Nano*, 1(6),

516–532. <https://doi.org/10.1039/C4EN00052H>

Kumar, H., Bhardwaj, K., Nepovimova, E., Kuča, K., Dhanjal, D. S., Bhardwaj, S., Bhatia, S. K., Verma, R., & Kumar, D. (2020). Antioxidant functionalized nanoparticles: A combat against oxidative stress. *Nanomaterials*, 10(7), 1–31. <https://doi.org/10.3390/nano10071334>

Kwon, H. J., Cha, M. Y., Kim, D., Kim, D. K., Soh, M., Shin, K., Hyeon, T., & Mook-Jung, I. (2016). Mitochondria-Targeting Ceria Nanoparticles as Antioxidants for Alzheimer's Disease. *ACS Nano*, 10(2), 2860–2870. <https://doi.org/10.1021/acsnano.5b08045>

L

Landmann, L. (2002). Deconvolution improves colocalization analysis of multiple fluorochromes in 3d confocal data sets more than filtering techniques. *Journal of Microscopy*, 208(2), 134–147. <https://doi.org/10.1046/j.1365-2818.2002.01068.x>

Lee, K. S., Chung, H. C., Im, S. A., Park, Y. H., Kim, C. S., Kim, S. B., Rha, S. Y., Lee, M. Y., & Ro, J. (2008). Multicenter phase II trial of Genexol-PM, a Cremophor-free, polymeric micelle formulation of paclitaxel, in patients with metastatic breast cancer. *Breast Cancer Research and Treatment*, 108(2), 241–250. <https://doi.org/10.1007/s10549-007-9591-y>

Lemke, A. J., Senfft von Pilsach, M. I., Lübbe, A., Bergemann, C., Riess, H., & Felix, R. (2004). MRI after magnetic drug targeting in patients with advanced solid malignant tumors. *European Radiology*, 14(11), 1949–1955. <https://doi.org/10.1007/s00330-004-2445-7>

Leung, Y. H., Yung, M. M. N., Ng, A. M. C., Ma, A. P. Y., Wong, S. W. Y., Chan, C. M. N., Ng, Y. H., Djurišić, A. B., Guo, M., Wong, M. T., Leung, F. C. C., Chan, W. K., Leung, K. M. Y., & Lee, H. K. (2015). Toxicity of CeO₂ nanoparticles - The effect of nanoparticle properties. *Journal of Photochemistry and Photobiology B: Biology*, 145, 48–59. <https://doi.org/10.1016/j.jphotobiol.2015.01.017>

Li, M., Shi, P., Xu, C., Ren, J., & Qu, X. (2013). Cerium oxide caged metal chelator: anti-aggregation and anti-oxidation integrated H₂O₂-responsive controlled drug release for

potential Alzheimer's disease treatment. *Chemical Science*, 4(6), 2536.
<https://doi.org/10.1039/c3sc50697e>

Li, X., Qian, J., Jiang, L., & He, S. (2009). Fluorescence quenching of quantum dots by gold nanorods and its application to DNA detection. *Applied Physics Letters*, 94(6), 94–97.
<https://doi.org/10.1063/1.3080662>

Li, Z., Aranda-Ramos, A., Güell-Grau, P., Tajada, J. L., Pou-Macayo, L., Lope Piedrafita, S., Pi, F., G. Roca, A., Baró, M. D., Sort, J., Nogués, C., Nogués, J., & Sepúlveda, B. (2018). Magnetically amplified photothermal therapies and multimodal imaging with magneto-plasmonic nanodomains. *Applied Materials Today*, 12, 430–440.
<https://doi.org/10.1016/j.apmt.2018.07.008>

Li, Z., Lopez-Ortega, A., Aranda-Ramos, A., Tajada, J. L., Sort, J., Nogues, C., Vavassori, P., Nogues, J., & Sepulveda, B. (2018). Simultaneous Local Heating/Thermometry Based on Plasmonic Magnetochromic Nanoheaters. *Small*, 14(24), 1800868.
<https://doi.org/10.1002/sml.201800868>

Lim, W. Q., Phua, S. Z. F., Xu, H. V., Sreejith, S., & Zhao, Y. (2016). Recent advances in multifunctional silica-based hybrid nanocarriers for bioimaging and cancer therapy. *Nanoscale*, 8(25), 12510–12519. <https://doi.org/10.1039/c5nr07853a>

Lintz, M., Muñoz, A., & Reinhart-King, C. A. (2017). The Mechanics of Single Cell and Collective Migration of Tumor Cells. *Journal of Biomechanical Engineering*, 139(2), 1–9. <https://doi.org/10.1115/1.4035121>

Liou, G.-Y., & Storz, P. (2010). Reactive oxygen species in cancer. *Free Radical Research*, 44(5), 479–496. <https://doi.org/10.3109/10715761003667554>

Loos, C., Syrovets, T., Musyanovych, A., Mailänder, V., Landfester, K., Ulrich Nienhaus, G., & Simmet, T. (2014). Functionalized polystyrene nanoparticles as a platform for studying bio-nano interactions. *Beilstein Journal of Nanotechnology*, 5(1), 2403–2412.
<https://doi.org/10.3762/bjnano.5.250>

Lübbe, A. S., Bergemann, C., Riess, H., Schriever, F., Reichardt, P., Possinger, K., Matthias, M., Dörken, B., Herrmann, F., Gürtler, R., Hohenberger, P., Haas, N., Sohr, R., Sander, B., Lemke, A. J., Ohlendorf, D., Huhnt, W., & Huhn, D. (1996). Clinical experiences with magnetic drug targeting: A phase I study with 4'-epidoxorubicin in 14 patients with advanced solid tumors. *Cancer Research*, 56(20), 4686–4693.

- Lupu, A. R., & Popescu, T. (2013). The noncellular reduction of MTT tetrazolium salt by TiO₂ nanoparticles and its implications for cytotoxicity assays. *Toxicology in Vitro*, 27(5), 1445–1450. <https://doi.org/10.1016/j.tiv.2013.03.006>
- Lyu, G. M., Wang, Y. J., Huang, X., Zhang, H. Y., Sun, L. D., Liu, Y. J., & Yan, C. H. (2016). Hydrophilic CeO₂ nanocubes protect pancreatic β -cell line INS-1 from H₂O₂-induced oxidative stress. *Nanoscale*, 8(15), 7923–7932. <https://doi.org/10.1039/c6nr00826g>

M

- MacDonald, C., Barbee, K., & Polyak, B. (2012). Force Dependent Internalization of Magnetic Nanoparticles Results in Highly Loaded Endothelial Cells for Use as Potential Therapy Delivery Vectors. *Pharmaceutical Research*, 29(5), 1270–1281. <https://doi.org/10.1007/s11095-011-0663-7>
- Madero-Visbal, R. A., Alvarado, B. E., Colon, J. F., Baker, C. H., Wason, M. S., Isley, B., Seal, S., Lee, C. M., Das, S., & Mañon, R. (2012). Harnessing nanoparticles to improve toxicity after head and neck radiation. *Nanomedicine: Nanotechnology, Biology, and Medicine*, 8(7), 1223–1231. <https://doi.org/10.1016/j.nano.2011.12.011>
- Maeda, H., Wu, J., Sawa, T., Matsumura, Y., & Hori, K. (2000). Tumor vascular permeability and the EPR effect in macromolecular therapeutics: A review. *Journal of Controlled Release*, 65(1–2), 271–284. [https://doi.org/10.1016/S0168-3659\(99\)00248-5](https://doi.org/10.1016/S0168-3659(99)00248-5)
- Masalov, A., Viagin, O., Maksimchuk, P., Seminko, V., Bespalova, I., Aslanov, A., Malyukin, Y., & Zorenko, Y. (2014). Formation of luminescent centers in CeO₂ nanocrystals. *Journal of Luminescence*, 145, 61–64. <https://doi.org/10.1016/j.jlumin.2013.07.020>
- Matuszak, J., Zaloga, J., Friedrich, R. P., Lyer, S., Nowak, J., Odenbach, S., Alexiou, C., & Cicha, I. (2015). Endothelial biocompatibility and accumulation of SPION under flow conditions. *Journal of Magnetism and Magnetic Materials*, 380, 20–26. <https://doi.org/10.1016/j.jmmm.2014.09.005>
- Mazzolini, J., Weber, R. J. M., Chen, H.-S., Khan, A., Guggenheim, E., Shaw, R. K., Chipman, J. K., Viant, M. R., & Rappoport, J. Z. (2016). Protein Corona Modulates Uptake and Toxicity of Nanocerium via Clathrin-Mediated Endocytosis. *The Biological*

Bulletin, 231(1), 40–60. <https://doi.org/10.1086/689590>

Mestre, R., Patiño, T., & Sánchez, S. (2021). Biohybrid robotics: From the nanoscale to the macroscale. *WIREs Nanomedicine and Nanobiotechnology*. <https://doi.org/10.1002/wnan.1703>

MG, K., V, K., & F, H. (2015). History and Possible Uses of Nanomedicine Based on Nanoparticles and Nanotechnological Progress. *Journal of Nanomedicine & Nanotechnology*, 06(06). <https://doi.org/10.4172/2157-7439.1000336>

Mittal, S., & Pandey, A. K. (2014). Cerium Oxide Nanoparticles Induced Toxicity in Human Lung Cells: Role of ROS Mediated DNA Damage and Apoptosis. *BioMed Research International*, 2014, 1–14. <https://doi.org/10.1155/2014/891934>

Miyazaki, H., Kato, J. I., Sakamoto, N., Wakiya, N., Ota, T., & Suzuki, H. (2010). Synthesis of CeO₂ nanoparticles by rapid thermal decomposition using microwave heating. *Advances in Applied Ceramics*, 109(2), 123–127. <https://doi.org/10.1179/174367509X12503626841631>

Montón, H., Nogués, C., Rossinyol, E., Castell, O., & Roldán, M. (2009). QDs versus Alexa: reality of promising tools for immunocytochemistry. *Journal of Nanobiotechnology*, 7, 4. <https://doi.org/10.1186/1477-3155-7-4>

Moore, C. (2016). Controlling the Synthesis , Characterisation , Formulation and Surface Properties of Dye- - - Doped Silica Nanoparticles for Biomedical Applications Colin Moore of the University of Kent and University of Greenwich for (Issue June).

Moore, C. J., Montón, H., O’Kennedy, R., Williams, D. E., Nogués, C., Crean (née Lynam), C., & Gubala, V. (2015). Controlling colloidal stability of silica nanoparticles during bioconjugation reactions with proteins and improving their longer-term stability, handling and storage. *Journal of Materials Chemistry B*, 3(10), 2043–2055. <https://doi.org/10.1039/C4TB01915F>

Moravej, M., Purnama, A., Fiset, M., Couet, J., & Mantovani, D. (2010). Electroformed pure iron as a new biomaterial for degradable stents: In vitro degradation and preliminary cell viability studies☆. *Acta Biomaterialia*, 6(5), 1843–1851. <https://doi.org/10.1016/j.actbio.2010.01.008>

Mukha, I., Chepurna, O., Vityuk, N., Khodko, A., Storozhuk, L., Dzhagan, V., Zahn, D. R. T., Ntziachristos, V., Chmyrov, A., & Ohulchanskyy, T. Y. (2021). Multifunctional magneto-

plasmonic fe₃o₄/au nanocomposites: Approaching magnetophoretically-enhanced photothermal therapy. *Nanomaterials*, 11(5). <https://doi.org/10.3390/nano11051113>

Murugadoss, S., Brassinne, F., Sebaihi, N., Petry, J., Cokic, S. M., Van Landuyt, K. L., Godderis, L., Mast, J., Lison, D., Hoet, P. H., & Van Den Brule, S. (2020). Agglomeration of titanium dioxide nanoparticles increases toxicological responses in vitro and in vivo. *Particle and Fibre Toxicology*, 17(1), 1–14. <https://doi.org/10.1186/s12989-020-00341-7>

Muthu, M. S., Leong, D. T., Mei, L., & Feng, S. S. (2014). Nanotheranostics - application and further development of nanomedicine strategies for advanced theranostics. *Theranostics*, 4(6), 660–677. <https://doi.org/10.7150/thno.8698>

N

Nanoparticles, B., Bouzigues, C., Gacoin, T., & Alexandrou, A. (2011). Biological Applications of Rare-Earth. 11, 8488–8505.

Nguyen, K., Nuß, B., Mühlberger, M., Unterweger, H., Friedrich, R. P., Alexiou, C., & Janko, C. (2020). Superparamagnetic iron oxide nanoparticles carrying chemotherapeutics improve drug efficacy in monolayer and spheroid cell culture by enabling active accumulation. *Nanomaterials*, 10(8), 1–21. <https://doi.org/10.3390/nano10081577>

Niederberger, M. (2009). Aqueous and Nonaqueous Sol-Gel Chemistry. In *Metal Oxide Nanoparticles in Organic Solvents* (pp. 7–18). https://doi.org/10.1007/978-1-84882-671-7_2

O

Obradors, X., & Puig, T. (2014). Coated conductors for power applications: materials challenges. *Superconductor Science and Technology*, 27(4), 044003. <https://doi.org/10.1088/0953-2048/27/4/044003>

Oei, A. L., Vriend, L. E. M., Crezee, J., Franken, N. A. P., & Krawczyk, P. M. (2015). Effects of hyperthermia on DNA repair pathways: One treatment to inhibit them all. *Radiation Oncology*, 10(1), 1–13. <https://doi.org/10.1186/s13014-015-0462-0>

Ong, K. J., MacCormack, T. J., Clark, R. J., Ede, J. D., Ortega, V. A., Felix, L. C., Dang, M. K. M., Ma, G., Fenniri, H., Veinot, J. G. C., & Goss, G. G. (2014). Widespread nanoparticle-assay interference: Implications for nanotoxicity testing. *PLoS ONE*. <https://doi.org/10.1371/journal.pone.0090650>

P

Pagliari, F., Mandoli, C., Forte, G., Magnani, E., Pagliari, S., Nardone, G., Licoccia, S., Minieri, M., Di Nardo, P., & Traversa, E. (2012). Cerium Oxide Nanoparticles Protect Cardiac Progenitor Cells from Oxidative Stress. *ACS Nano*, 6(5), 3767–3775. <https://doi.org/10.1021/nn2048069>

Panyam, J., & Labhasetwar, V. (2003). Dynamics of endocytosis and exocytosis of poly(D,L-lactide-co-glycolide) nanoparticles in vascular smooth muscle cells. *Pharmaceutical Research*, 20(2), 212–220. <https://doi.org/10.1023/A:1022219003551>

Park, E.-J., Choi, J., Park, Y.-K., & Park, K. (2008). Oxidative stress induced by cerium oxide nanoparticles in cultured BEAS-2B cells. *Toxicology*, 245(1–2), 90–100. <https://doi.org/10.1016/j.tox.2007.12.022>

Patiño, T., Nogués, C., Ibáñez, E., & Barrios, L. (2012). Enhancing microparticle internalization by nonphagocytic cells through the use of noncovalently conjugated polyethyleneimine. *International Journal of Nanomedicine*, 7, 5671–5682. <https://doi.org/10.2147/IJN.S34635>

Patiño, T., Soriano, J., Barrios, L., Ibáñez, E., & Nogués, C. (2015). Surface modification of microparticles causes differential uptake responses in normal and tumoral human breast epithelial cells. *Scientific Reports*, 5(May), 11371. <https://doi.org/10.1038/srep11371>

Peer, D., Karp, J. M., Hong, S., Farokhzad, O. C., Margalit, R., & Langer, R. (2007). Nanocarriers as an emerging platform for cancer therapy. *Nature Nanotechnology*,

2(12), 751–760. <https://doi.org/10.1038/nnano.2007.387>

- Pelka, J., Gehrke, H., Esselen, M., Türk, M., Crone, M., Bräse, S., Muller, T., Blank, H., Send, W., Zibat, V., Brenner, P., Schneider, R., Gerthsen, D., & Marko, D. (2009). Cellular uptake of platinum nanoparticles in human colon carcinoma cells and their impact on cellular redox systems and DNA integrity. *Chemical Research in Toxicology*, 22(4), 649–659. <https://doi.org/10.1021/tx800354g>
- Perrigue, P. M., Murray, R. A., Mielcarek, A., Henschke, A., & Moya, S. E. (2021). Degradation of drug delivery nanocarriers and payload release: A review of physical methods for tracing nanocarrier biological fate. *Pharmaceutics*, 13(6). <https://doi.org/10.3390/pharmaceutics13060770>
- Petros, R. A., & Desimone, J. M. (2010). Strategies in the design of nanoparticles for therapeutic applications. *Nature Reviews Drug Discovery*, 9(8), 615–627. <https://doi.org/10.1038/nrd2591>
- Piehler, S., Wucherpfennig, L., Tansi, F. L., Berndt, A., Quaas, R., Teichgraeber, U., & Hilger, I. (2020). Hyperthermia affects collagen fiber architecture and induces apoptosis in pancreatic and fibroblast tumor hetero-spheroids in vitro: Hyperthermia affects collagen ECM and pancreatic tumor cells. *Nanomedicine: Nanotechnology, Biology, and Medicine*, 28, 102183. <https://doi.org/10.1016/j.nano.2020.102183>
- Pissuwan, D., Valenzuela, S. M., & Cortie, M. B. (2006). Therapeutic possibilities of plasmonically heated gold nanoparticles. *Trends in Biotechnology*, 24(2), 62–67. <https://doi.org/10.1016/j.tibtech.2005.12.004>
- Pistollato, F., Madia, F., Corvi, R., Munn, S., Grignard, E., Painsi, A., Worth, A., Bal-Price, A., Prieto, P., Casati, S., Berggren, E., Bopp, S. K., & Zuang, V. (2021). Current EU regulatory requirements for the assessment of chemicals and cosmetic products: challenges and opportunities for introducing new approach methodologies. In *Archives of Toxicology* (Vol. 95, Issue 6). Springer Berlin Heidelberg. <https://doi.org/10.1007/s00204-021-03034-y>
- Podolski-renic, A., Stojkovic, S., Matovic, B., Zmejkoski, D., Bogdanovic, G., Pavic, A., Mojovic, M., & Savic, A. (2015). Chemico-Biological Interactions Anti-cancer effects of cerium oxide nanoparticles and its intracellular redox activity. 232, 85–93. <https://doi.org/10.1016/j.cbi.2015.03.013>

- Polacheck, W. J., German, A. E., Mammoto, A., Ingber, D. E., & Kamm, R. D. (2014). Mechanotransduction of fluid stresses governs 3D cell migration. *Proceedings of the National Academy of Sciences*, 111(7), 2447–2452. <https://doi.org/10.1073/pnas.1316848111>
- Pons, T., Medintz, I. L., Sapsford, K. E., Higashiya, S., Grimes, A. F., English, D. S., & Mattoussi, H. (2007). On the quenching of semiconductor quantum dot photoluminescence by proximal gold nanoparticles. *Nano Letters*, 7(10), 3157–3164. <https://doi.org/10.1021/nl071729+>
- Prasad, N. K., Rathinasamy, K., Panda, D., & Bahadur, D. (2007). Mechanism of cell death induced by magnetic hyperthermia with nanoparticles of γ - $\text{MnxFe}_2\text{-xO}_3$ synthesized by a single step process. *Journal of Materials Chemistry*, 17(48), 5042–5051. <https://doi.org/10.1039/b708156a>
- Pratt, S. J. P., Lee, R. M., & Martin, S. S. (2020). The mechanical microenvironment in breast cancer. *Cancers*, 12(6), 1–25. <https://doi.org/10.3390/cancers12061452>
- Price, P. M., Mahmoud, W. E., Al-Ghamdi, A. A., & Bronstein, L. M. (2018). Magnetic drug delivery: Where the field is going. *Frontiers in Chemistry*, 6(DEC), 1–7. <https://doi.org/10.3389/fchem.2018.00619>
- Pulido-Reyes, G., Rodea-Palomares, I., Das, S., Sakthivel, T. S., Leganes, F., Rosal, R., Seal, S., & Fernández-Piñas, F. (2015a). Untangling the biological effects of cerium oxide nanoparticles: the role of surface valence states. *Scientific Reports*, 5, 15613. <https://doi.org/10.1038/srep15613>
- Pulido-Reyes, G., Rodea-Palomares, I., Das, S., Sakthivel, T. S., Leganes, F., Rosal, R., Seal, S., & Fernández-Piñas, F. (2015b). Untangling the biological effects of cerium oxide nanoparticles: the role of surface valence states. *Scientific Reports*, 5(1), 15613. <https://doi.org/10.1038/srep15613>
- Pustovit, V. N., & Shahbazyan, T. V. (2012). Fluorescence quenching near small metal nanoparticles. *Journal of Chemical Physics*, 136(20), 0–6. <https://doi.org/10.1063/1.4721388>

R

- R Core Team. (2020). R: A language and environment for statistical computing. R Foundation for Statistical Computing. <https://www.r-project.org/>
- Radon, P., Liebl, M., Pömpner, N., Stapf, M., Wiekhorst, F., Gitter, K., Hilger, I., Odenbach, S., & Trahms, L. (2015). Magnetic Particle Spectroscopy to Determine the Magnetic Drug Targeting Efficiency of Different Magnetic Nanoparticles in a Flow Phantom. *IEEE Transactions on Magnetics*, 51(2), 6000104. <https://doi.org/10.1109/TMAG.2014.2326889>
- Rajan, A., & Sahu, N. K. (2020). Review on magnetic nanoparticle-mediated hyperthermia for cancer therapy. *Journal of Nanoparticle Research*, 22(11). <https://doi.org/10.1007/s11051-020-05045-9>
- Rashkow, J. T., Patel, S. C., Tappero, R., & Sitharaman, B. (2014). Quantification of single-cell nanoparticle concentrations and the distribution of these concentrations in cell population. *Journal of the Royal Society, Interface / the Royal Society*, 11(94), 20131152. <https://doi.org/10.1098/rsif.2013.1152>
- Reineck, P., Gómez, D., Ng, S. H., Karg, M., Bell, T., Mulvaney, P., & Bach, U. (2013). Distance and wavelength dependent quenching of molecular fluorescence by Au@SiO₂ core-shell nanoparticles. *ACS Nano*, 7(8), 6636–6648. <https://doi.org/10.1021/nn401775e>
- REJMAN, J., OBERLE, V., ZUHORN, I. S., & HOEKSTRA, D. (2004). Size-dependent internalization of particles via the pathways of clathrin- and caveolae-mediated endocytosis. *Biochemical Journal*, 377(1), 159–169. <https://doi.org/10.1042/bj20031253>
- Reyes-Acosta, M. A., Torres-Huerta, A. M., Domínguez-Crespo, M. A., Flores-Vela, A. I., Dorantes-Rosales, H. J., & Andraca-Adame, J. A. (2015). Thermal, mechanical and UV-shielding properties of poly(methyl methacrylate)/cerium dioxide hybrid systems obtained by melt compounding. *Polymers*, 7(9), 1638–1659. <https://doi.org/10.3390/polym7091474>
- RF, S. (2005). Nanotechnology. Calls rise for more research on toxicology of nanomaterials.

Science (New York, N.Y.), 310(5754), 1609.
<https://doi.org/10.1126/SCIENCE.310.5754.1609>

Ribeiro, T., Baleizão, C., & Farinha, J. P. S. (2017). Artefact-free evaluation of metal enhanced fluorescence in silica coated gold nanoparticles. *Scientific Reports*, 7(1), 1–12. <https://doi.org/10.1038/s41598-017-02678-0>

Riching, K. M., Cox, B. L., Salick, M. R., Pehlke, C., Riching, A. S., Ponik, S. M., Bass, B. R., Crone, W. C., Jiang, Y., Weaver, A. M., Eliceiri, K. W., & Keely, P. J. (2015). 3D collagen alignment limits protrusions to enhance breast cancer cell persistence. *Biophysical Journal*, 107(11), 2546–2558. <https://doi.org/10.1016/j.bpj.2014.10.035>

Riebeling, C., Piret, J. P., Trouiller, B., Nelissen, I., Saout, C., Toussaint, O., & Haase, A. (2018). A guide to nanosafety testing: Considerations on cytotoxicity testing in different cell models. *NanoImpact*, 10, 1–10. <https://doi.org/10.1016/j.impact.2017.11.004>

Rothen-Rutishauser, B., Kuhn, D. A., Ali, Z., Gasser, M., Amin, F., Parak, W. J., Vanhecke, D., Fink, A., Gehr, P., & Brandenberger, C. (2014). Quantification of gold nanoparticle cell uptake under controlled biological conditions and adequate resolution. *Nanomedicine*, 9(5), 607–621. <https://doi.org/10.2217/nnm.13.24>

Roti, J. L. (2008). Cellular responses to hyperthermia (40-46°C): Cell killing and molecular events. *International Journal of Hyperthermia*, 24(1), 3–15. <https://doi.org/10.1080/02656730701769841>

S

Sadik, O. A., Zhou, A. L., Kikandi, S., Du, N., Wang, Q., & Varner, K. (2009). Sensors as tools for quantitation, nanotoxicity and nanomonitoring assessment of engineered nanomaterials. *Journal of Environmental Monitoring*, 11(10), 1782–1800. <https://doi.org/10.1039/b912860c>

Sanz-Ortega, L., Rojas, J. M., Portilla, Y., Pérez-Yagüe, S., & Barber, D. F. (2019). Magnetic nanoparticles attached to the NK cell surface for tumor targeting in adoptive transfer therapies does not affect cellular effector functions. *Frontiers in Immunology*, 10(AUG), 1–17. <https://doi.org/10.3389/fimmu.2019.02073>

- Sanz, B., Calatayud, M. P., Torres, T. E., Fanarraga, M. L., Ibarra, M. R., & Goya, G. F. (2017). Magnetic hyperthermia enhances cell toxicity with respect to exogenous heating. *Biomaterials*, 114, 62–70. <https://doi.org/10.1016/j.biomaterials.2016.11.008>
- Sathyamurthy, S., Leonard, K. J., Dabestani, R. T., & Paranthaman, M. P. (2005). Reverse micellar synthesis of cerium oxide nanoparticles. *Nanotechnology*, 16(9), 1960–1964. <https://doi.org/10.1088/0957-4484/16/9/089>
- Scarpa, E., Bailey, J. L., Janeczek, A. A., Stumpf, P. S., Johnston, A. H., Oreffo, R. O. C., Woo, Y. L., Cheong, Y. C., Evans, N. D., & Newman, T. A. (2016). Quantification of intracellular payload release from polymersome nanoparticles. *Scientific Reports*, 6(1), 29460. <https://doi.org/10.1038/srep29460>
- Schindelin, J., Arganda-Carreras, I., Frise, E., Kaynig, V., Longair, M., Pietzsch, T., Preibisch, S., Rueden, C., Saalfeld, S., Schmid, B., Tinevez, J. Y., White, D. J., Hartenstein, V., Eliceiri, K., Tomancak, P., & Cardona, A. (2012). Fiji: An open-source platform for biological-image analysis. *Nature Methods*, 9(7), 676–682. <https://doi.org/10.1038/nmeth.2019>
- Schmid, S. L., Sorkin, A., & Zerial, M. (2014). Endocytosis: Past, Present, and Future. *Cold Spring Harbor Perspectives in Biology*, 6(12), a022509–a022509. <https://doi.org/10.1101/cshperspect.a022509>
- Schroeder, A., Levins, C. G., Cortez, C., Langer, R., & Anderson, D. G. (2010). Lipid-based nanotherapeutics for siRNA delivery. *Journal of Internal Medicine*, 267(1), 9–21. <https://doi.org/10.1111/j.1365-2796.2009.02189.x>
- Schulz, H., Stark, W. J., Maciejewski, M., Pratsinis, S. E., & Baiker, A. (2003). Flame-made nanocrystalline ceria/zirconia doped with alumina or silica: structural properties and enhanced oxygen exchange capacity. *Journal of Materials Chemistry*, 13(12), 2979. <https://doi.org/10.1039/b307754c>
- Schweiger, C., Hartmann, R., Zhang, F., Parak, W. J., Kissel, T. H., & Rivera_Gil, P. (2012). Quantification of the internalization patterns of superparamagnetic iron oxide nanoparticles with opposite charge. *Journal of Nanobiotechnology*, 10(1), 28. <https://doi.org/10.1186/1477-3155-10-28>
- Seleci, M., Seleci, D. A., Scheper, T., & Stahl, F. (2017). Theranostic liposome–nanoparticle hybrids for drug delivery and bioimaging. *International Journal of Molecular Sciences*,

18(7). <https://doi.org/10.3390/ijms18071415>

- Sensenig, R., Sapir, Y., MacDonald, C., Cohen, S., & Polyak, B. (2012). Magnetic nanoparticle-based approaches to locally target therapy and enhance tissue regeneration in vivo. *Nanomedicine*, 7(9), 1425–1442. <https://doi.org/10.2217/nnm.12.109>
- Shamsi, M., Sedaghatkish, A., Dejam, M., Saghafian, M., Mohammadi, M., & Sanati-Nezhad, A. (2018). Magnetically assisted intraperitoneal drug delivery for cancer chemotherapy. *Drug Delivery*, 25(1), 846–861. <https://doi.org/10.1080/10717544.2018.1455764>
- Sherje, A. P., Jadhav, M., Dravyakar, B. R., & Kadam, D. (2018). Dendrimers: A versatile nanocarrier for drug delivery and targeting. *International Journal of Pharmaceutics*, 548(1), 707–720. <https://doi.org/10.1016/j.ijpharm.2018.07.030>
- Shetake, N. G., Kumar, A., Gaikwad, S., Ray, P., Desai, S., Ningthoujam, R. S., Vatsa, R. K., & Pandey, B. N. (2015). Magnetic nanoparticle-mediated hyperthermia therapy induces tumour growth inhibition by apoptosis and Hsp90/AKT modulation. *International Journal of Hyperthermia*, 31(8), 909–919. <https://doi.org/10.3109/02656736.2015.1075072>
- Shin, H. R., Kwak, M., Lee, T. G., & Lee, J. Y. (2020). Quantifying the level of nanoparticle uptake in mammalian cells using flow cytometry. *Nanoscale*, 12(29), 15743–15751. <https://doi.org/10.1039/d0nr01627f>
- Skehan, P., Storeng, R., Scudiero, D., Monks, A., McMahon, J., Vistica, D., Warren, J. T., Bokesch, H., Kenney, S., & Boyd, M. R. (1990). New Colorimetric Cytotoxicity Assay for Anticancer-Drug Screening. *JNCI Journal of the National Cancer Institute*, 82(13), 1107–1112. <https://doi.org/10.1093/jnci/82.13.1107>
- Skorodumova, N. V., Ahuja, R., Simak, S. I., Abrikosov, I. A., Johansson, B., & Lundqvist, B. I. (2001). Electronic, bonding, and optical properties of CeO₂ and Ce₂O₃ from first principles. *Physical Review B - Condensed Matter and Materials Physics*, 64(11), 1151081–1151089. <https://doi.org/10.1103/physrevb.64.115108>
- Sobhani, Z., Behnam, M. A., Emami, F., Dehghanian, A., & Jamhiri, I. (2017). Photothermal therapy of melanoma tumor using multiwalled carbon nanotubes. *International Journal of Nanomedicine*, 12, 4509–4517. <https://doi.org/10.2147/IJN.S134661>

- Solano, E., Frontera, C., Puig, T., Obradors, X., Ricart, S., & Ros, J. (2014). Neutron and X-ray diffraction study of ferrite nanocrystals obtained by microwave-assisted growth. A structural comparison with the thermal synthetic route. *Journal of Applied Crystallography*, 47(1), 414–420. <https://doi.org/10.1107/S1600576713032895>
- Solano, E., Perez-Mirabet, L., Martinez-Julian, F., Guzmán, R., Arbiol, J., Puig, T., Obradors, X., Yañez, R., Pomar, A., Ricart, S., & Ros, J. (2012). Facile and efficient one-pot solvothermal and microwave-assisted synthesis of stable colloidal solutions of MFe₂O₄ spinel magnetic nanoparticles. *Journal of Nanoparticle Research*, 14(8), 1034. <https://doi.org/10.1007/s11051-012-1034-y>
- Spill, F., Reynolds, D. S., Kamm, R. D., & Zaman, M. H. (2016). Impact of the physical microenvironment on tumor progression and metastasis. *Current Opinion in Biotechnology*, 40, 41–48. <https://doi.org/10.1016/j.copbio.2016.02.007>
- Sreeremya, T. S., Thulasi, K. M., Krishnan, A., & Ghosh, S. (2012). A Novel Aqueous Route To Fabricate Ultrasmall Monodisperse Lipophilic Cerium Oxide Nanoparticles. *Industrial & Engineering Chemistry Research*, 51(1), 318–326. <https://doi.org/10.1021/ie2019646>
- Sung Eun Kim^{1,2}, Li Zhang³, Kai Ma⁴, M. R., Feng Chen³, Irina Ingold⁵, M. C., Melik Ziya Turker⁴, M. G., Xuejun Jiang^{1,2}, Sebastien Monette⁶, M. P., Mithat Gonen⁷, Pat Zanzonico⁸, Thomas Quinn⁹, Ulrich Wiesner⁴, Michelle S. Bradbury³, 10*†, & and Michael Overholtzer¹, 2*†. (2016). Ultrasmall nanoparticles induce ferroptosis in nutrient-deprived cancer cells and suppress tumour growth. *Nature Nanotechnology*, September. <https://doi.org/10.1038/NNANO.2016.164>
- Sung, H., Ferlay, J., Siegel, R. L., Laversanne, M., Soerjomataram, I., Jemal, A., & Bray, F. (2021). Global cancer statistics 2020: GLOBOCAN estimates of incidence and mortality worldwide for 36 cancers in 185 countries. *CA: A Cancer Journal for Clinicians*, 71(3), 209–249. <https://doi.org/10.3322/caac.21660>

T

- Tapeinos, C., Tomatis, F., Battaglini, M., Larrañaga, A., Marino, A., Telleria, I. A., Angelakeris, M., Debellis, D., Drago, F., Brero, F., Arosio, P., Lascialfari, A., Petretto, A., Sinibaldi, E., & Ciofani, G. (2019). Cell Membrane-Coated Magnetic Nanocubes with a Homotypic Targeting Ability Increase Intracellular Temperature due to ROS Scavenging and Act as a Versatile Theranostic System for Glioblastoma Multiforme. *Advanced Healthcare Materials*, 8(18). <https://doi.org/10.1002/adhm.201900612>
- Torrano, A. A., Blechinger, J., Osseforth, C., Argyo, C., Reller, A., Bein, T., Michaelis, J., & Bräuchle, C. (2013). A fast analysis method to quantify nanoparticle uptake on a single cell level. *Nanomedicine*, 8(11), 1815–1828. <https://doi.org/10.2217/nnm.12.178>
- Tripathy, N., Hong, T. K., Ha, K. T., Jeong, H. S., & Hahn, Y. B. (2014). Effect of ZnO nanoparticles aggregation on the toxicity in RAW 264.7 murine macrophage. *Journal of Hazardous Materials*, 270, 110–117. <https://doi.org/10.1016/j.jhazmat.2014.01.043>

U

- Urries, I., Muñoz, C., Gomez, L., Marquina, C., Sebastian, V., Arruebo, M., & Santamaria, J. (2014). Magneto-plasmonic nanoparticles as theranostic platforms for magnetic resonance imaging, drug delivery and NIR hyperthermia applications. *Nanoscale*, 6(15), 9230–9240. <https://doi.org/10.1039/c4nr01588f>

V

- Vance, M. E., Kuiken, T., Vejerano, E. P., McGinnis, S. P., Hochella, M. F., Rejeski, D., & Hull, M. S. (2015). Nanotechnology in the real world: Redeveloping the nanomaterial consumer products inventory. *Beilstein Journal of Nanotechnology*, 6(1), 1769–1780. <https://doi.org/10.3762/bjnano.6.181>

- Vassie, J. A., Whitelock, J. M., & Lord, M. S. (2017a). Endocytosis of cerium oxide nanoparticles and modulation of reactive oxygen species in human ovarian and colon cancer cells. *Acta Biomaterialia*, 50, 127–141. <https://doi.org/10.1016/j.actbio.2016.12.010>
- Vassie, J. A., Whitelock, J. M., & Lord, M. S. (2017b). Endocytosis of cerium oxide nanoparticles and modulation of reactive oxygen species in human ovarian and colon cancer cells. *Acta Biomaterialia*, 50, 127–141. <https://doi.org/10.1016/j.actbio.2016.12.010>
- Villalta, J. I., Galli, S., Iacaruso, M. F., Arciuch, V. G. A., Poderoso, J. J., Jares-Erijman, E. A., & Pietrasanta, L. I. (2011). New algorithm to determine true colocalization in combination with image restoration and time-lapse confocal microscopy to map Kinases in mitochondria. *PLoS ONE*, 6(4), 1–16. <https://doi.org/10.1371/journal.pone.0019031>
- Vtyurina, N., Åberg, C., & Salvati, A. (2021). Imaging of nanoparticle uptake and kinetics of intracellular trafficking in individual cells. *Nanoscale*, 13(23), 10436–10446. <https://doi.org/10.1039/d1nr00901j>

W

- Walkey, C., Das, S., Seal, S., Erlichman, J., Heckman, K., Ghibelli, L., Traversa, E., McGinnis, J. F., & Self, W. T. (2015). Catalytic properties and biomedical applications of cerium oxide nanoparticles. *Environmental Science: Nano*, 2(1), 33–53. <https://doi.org/10.1039/c4en00138a>
- Wang, M., & Thanou, M. (2010). Targeting nanoparticles to cancer. *Pharmacological Research*, 62(2), 90–99. <https://doi.org/10.1016/j.phrs.2010.03.005>
- Wang, R., Liu, J., Liu, Y., Zhong, R., Yu, X., Liu, Q., Zhang, L., Lv, C., Mao, K., & Tang, P. (2020). The cell uptake properties and hyperthermia performance of Zn_{0.5}Fe_{2.5}O₄/SiO₂ nanoparticles as magnetic hyperthermia agents. *Royal Society Open Science*, 7(1). <https://doi.org/10.1098/rsos.191139>
- Wang, Y., Sun, Y., Wang, J., Yang, Y., Li, Y., Yuan, Y., & Liu, C. (2016). Charge-Reversal

APTES-modified Mesoporous Silica Nanoparticles with High Drug Loading and Release Controllability. *ACS Applied Materials & Interfaces*, acsami.6b05370. <https://doi.org/10.1021/acsami.6b05370>

Wilhelm, S., Tavares, A. J., Dai, Q., Ohta, S., Audet, J., Dvorak, H. F., & Chan, W. C. W. (2016). Analysis of nanoparticle delivery to tumours. *Nature Reviews Materials*, 1(5), 16014. <https://doi.org/10.1038/natrevmats.2016.14>

Wong, A. D., DeWit, M. A., & Gillies, E. R. (2012). Amplified release through the stimulus triggered degradation of self-immolative oligomers, dendrimers, and linear polymers. *Advanced Drug Delivery Reviews*, 64(11), 1031–1045. <https://doi.org/10.1016/j.addr.2011.09.012>

Wörle-Knirsch, J. M., Pulskamp, K., & Krug, H. F. (2006). Oops they did it again! Carbon nanotubes hoax scientists in viability assays. *Nano Letters*, 6(6), 1261–1268. <https://doi.org/10.1021/nl060177c>

Wu, C. H., Cook, J., Emelianov, S., & Sokolov, K. (2014). Multimodal magneto-plasmonic nanoclusters for biomedical applications. *Advanced Functional Materials*, 24(43), 6862–6871. <https://doi.org/10.1002/adfm.201401806>

X

Xu, C., & Qu, X. (2014). Cerium oxide nanoparticle: a remarkably versatile rare earth nanomaterial for biological applications. *NPG Asia Materials*, 6(3), e90–e90. <https://doi.org/10.1038/am.2013.88>

Y

Yan, G., Elbadawi, M., & Efferth, T. (2020). Multiple cell death modalities and their key features (Review). *World Academy of Sciences Journal*, 39–48. <https://doi.org/10.3892/wasj.2020.40>

- Ye, D., Bramini, M., Hristov, D. R., Wan, S., Salvati, A., Åberg, C., & Dawson, K. A. (2017). Low uptake of silica nanoparticles in Caco-2 intestinal epithelial barriers. *Beilstein Journal of Nanotechnology*, 8(1), 1396–1406. <https://doi.org/10.3762/bjnano.8.141>
- Yoo, D., Jeong, H., Preihs, C., Choi, J. S., Shin, T. H., Sessler, J. L., & Cheon, J. (2012). Double-effector nanoparticles: A synergistic approach to apoptotic hyperthermia. *Angewandte Chemie - International Edition*, 51(50), 12482–12485. <https://doi.org/10.1002/anie.201206400>
- Yu, S.-H., Cölfen, H., & Fischer, A. (2004). High quality CeO₂ nanocrystals stabilized by a double hydrophilic block copolymer. *Colloids and Surfaces A: Physicochemical and Engineering Aspects*, 243(1–3), 49–52. <https://doi.org/10.1016/j.colsurfa.2004.05.006>

Z

- Zhang, X., Zhang, X., Wang, S., Liu, M., Tao, L., & Wei, Y. (2013). Surfactant modification of aggregation-induced emission material as biocompatible nanoparticles: Facile preparation and cell imaging. *Nanoscale*, 5(1), 147–150. <https://doi.org/10.1039/C2NR32698A>
- Zhang, Z., & Baerns, M. (1991). Hydrogen formation by steam-reforming and water-gas shift reaction in the oxidative methane coupling reaction over calcium oxide-cerium dioxide catalysts. *Appl. Catal.*, 5, 299–310.
- Zhao, H., Zeng, Z., Liu, L., Chen, J., Zhou, H., Huang, L., Huang, J., Xu, H., Xu, Y., Chen, Z., Wu, Y., Guo, W., Wang, J. H., Wang, J., & Liu, Z. (2018). Polydopamine nanoparticles for the treatment of acute inflammation-induced injury. *Nanoscale*, 10(15), 6981–6991. <https://doi.org/10.1039/C8NR00838H>
- Zholobak, N. M., Shcherbakov, A. B., Vitukova, E. O., Yegorova, A. V., Scripinets, Y. V., Leonenko, I. I., Baranchikov, A. Y., Antonovich, V. P., & Ivanov, V. K. (2014). Direct monitoring of the interaction between ROS and cerium dioxide nanoparticles in living cells. In *RSC Advances* (Vol. 4, Issue 93). <https://doi.org/10.1039/c4ra08292c>
- Zhou, H., Zou, F., Koh, K., & Lee, J. (2014). Multifunctional magnetoplasmonic nanomaterials and their biomedical applications. *Journal of Biomedical*

